TEL AVIV UNIVERSITY
RAYMOND AND BEVERLY SACKLER
FACULTY OF EXACT SCIENCES
SCHOOL OF PHYSICS & ASTRONOMY

אוניברסיטת תל-אביב
הפקולטה למדעים מדוייקים
ע"ש ריימונד ובברלי סאקלר
בית הספר לפיסיקה ואסטרונומיה

Search for massive neutral gauge bosons decaying into muon pairs in pp collisions at $\sqrt{s} = 7$ TeV with the ATLAS detector at the LHC

Thesis submitted for the degree "Doctor of Philosophy"

by

Noam Tal Hod

Submitted to the senate of Tel Aviv University

September 24, 2012

Supervisors:

Prof. Erez Etzion and Dr. Gideon Bella

This research was carried out under the supervision of Prof. Erez Etzion and Dr. Gideon Bella.

Abstract

A search is performed for deviations from the standard model (SM) prediction in the invariant mass distribution of muon pairs produced in pp collisions at a center of mass energy of $\sqrt{s} = 7$ TeV at the LHC. This search is based on 5 fb^{-1} of data collected by the ATLAS experiment in 2011. The main contribution to muon pair production in the SM is the Drell-Yan process, with additional small contributions from diboson and $t\bar{t}$ production and decay. No significant deviation from the SM expectation has been observed and therefore, direct limits at the 95% confidence level are set on two benchmark hypotheses. The first hypothesis assumes the simplest scenario where the SM is extended to five dimensions and a single spatial extra dimension (ED) is compactified on a S^1/Z_2 orbifold. As a result, a Kaluza-Klein (KK) tower of heavy resonant copies of the SM γ/Z particles is expected. However, this model also predicts each new massive resonance to be preceded, at much lower masses, by a large deficit with respect to the SM prediction. This is due to a strong destructive interference with the γ/Z particles, and this feature is found to have a very large exclusion power. Another hypothesis which is considered here, consists of a class of purely resonant Z' models, inspired by higher-symmetry breaking, such as the E_6 group. The Z' bosons also interfere with the γ/Z particles although this effect is much smaller than for the KK. The direct limits are set on the KK and Z' masses, where the KK mass is equivalent to the inverse of the ED compactification scale. Two methods are used to set limits on the masses M_{KK} and $M_{Z'}$. In the first method, which is valid only for the Z' case, the limit calculation uses the cross section times branching fraction (σB) as a free parameter, while neglecting the interference with the γ/Z. In the second method, the interference is taken into account by introducing a coupling-strength parameter, g. For a single ED, the lower limit on M_{KK} is 3.93 TeV from dimuons, and it extends to 4.71 TeV when dielectrons are included. This is the first direct limit on this model and it is almost 1 TeV higher than previous indirect limits. The limit on $M_{Z'}$ is ranging between 1.79 TeV and 2.25 TeV depending on the Z' model assumed.

Preface

A search for heavy gauge bosons produced in pp collisions and decaying into muon pairs is presented in this thesis. Large parts of this work have been performed within the ATLAS experiment at the large hadron collider (LHC) at CERN, while some studies within the context of this subject, were conducted independently throughout my Ph.D. studies in Tel Aviv University as well as during my short term studentship in University College London (UCL) as an early state researcher in MCnet [1].

The search for heavy neutral gauge bosons presented here is mainly motivated by a natural extension of the standard model into five dimensions. The thesis describes a complete path from developing the exact phenomenological properties of the model [2], implementation of this model in one of the most common tools used in high energy physics (HEP), the Pythia8 event generator [3] where I am a contributor-developer[1] (see reference [4]), and the search for this model signatures in ATLAS [5].

The experimental search in the two dilepton decay channels, $\mu^+\mu^-$ and e^+e^-, is ready for publication by ATLAS [5]. The thesis describes in details my contribution to this publication, which consists of the search performed in the dimuon channel as well as of extracting the limits from the combination of the two channels. As a member of the "ATLAS Z'-analysis-team", I performed trigger efficiency studies, pile-up studies, an attempt to obtain the W+jets background estimation using a data driven method, various Monte Carlo (MC) analyses, angular distribution and forward-backward asymmetry studies, etc. I was also responsible for the production of the Drell-Yan (DY) main background sample, and for the preparation of final figures and tables.

In the preparation for the ATLAS publication [5], several new approaches and methods had to be developed in order to set limits on the Kaluza-Klein (KK) mass, $M_{\rm KK} \sim 1/R$, where R is the compactification scale. I was responsible for all the aspects concerning the KK signature and for the combination of the two dilepton channels.

[1] The current "TeV^{-1}-Sized Extra Dimensions" implementation within Pythia8 is done and maintained by me. This also included few enhancements done to the Pythia8 core.

All the final results given for muons throughout the experimental part of this thesis, will be accompanied by the electron results, as well as the combined results, where applicable. The specific details of the dielectron analysis will be skipped and the reader is referred to [5] for more details.

In addition to my physics analysis studies, I have also worked on the design and implementation of the ATLAS TGC online monitoring system, and for the past few years I was in charge of its maintenance and upgrade. The TGC subsystem was mainly built and tested in Israel and the maintenance of this subsystem is one of the respectabilities of the Israeli community within ATLAS. This contribution is described in appendix I.

Noam Tal Hod

Acknowledgements

Of the many people who deserve thanks, some are particularly prominent. First of all, I would like to express my deepest thanks, to my supervisors Prof. Erez Etzion and Dr. Gideon Bella who accepted me as a M.Sc. student in 2007 and since then, they are there for the tiniest questions or the largest problems with greatest possible patience and deepest insight on physics and life. Special thanks are also given to

- the Tel Aviv University high energy physics group leader and staff, Prof. Halina Abramowicz, Dr. Yan Benhammou and Meny Ben Moshe, for taking care of everything and making a second home for all of us.
- Prof. Yaron Oz and Evgeny Yurkovsky from Tel Aviv University, Dr. Mark Sutton from Sheffield University and Prof. Torbjörn Sjöstrand from Lund University, for the work done on Pythia8 and the KK phenomenology part.
- the ATLAS Z'-analysis-team and especially the conveners of the 2011 analysis round, Simon Viel (TRIUMF), Sarah Heim (MSU), Fabienne Ledroit (IN2P3), Wojciech T. Fedorko (MSU), Oliver Stelzer-Chilton (TRIUMF) and Henri Bachacou (Saclay). Special thanks are given to Yiftah Silver from Tel Aviv University, who went through the stressful experimental work on the inclusion of the KK model along with me while concentrating on the e^+e^- channel, without which this analysis would not have been published eventually.
- the people from the TGC and ATLAS-DAQ community, Nimrod Taiblum and Omer Ben Ami from Tel Aviv University, Prof. Daniel Lellouch and Prof. Lorne Levinson from the Weizmann institute and Prof. Masaya Ishino from Kyoto University.
- all my colleagues from the Tel Aviv University HEP office, for the fruitful discussions, the mental and professional support over the past 5 years.
- the management, the senior academic staff, the secretariat and staff of the School of physics and astronomy in Tel Aviv University, for all the professional and cheerful help over the 10 years I have spent in the university.

Finally, I want to thank to my wife Efrat, my son Dan, my mother Nima, my sister Nitzan and the entire family without the support of which I could not have done anything.

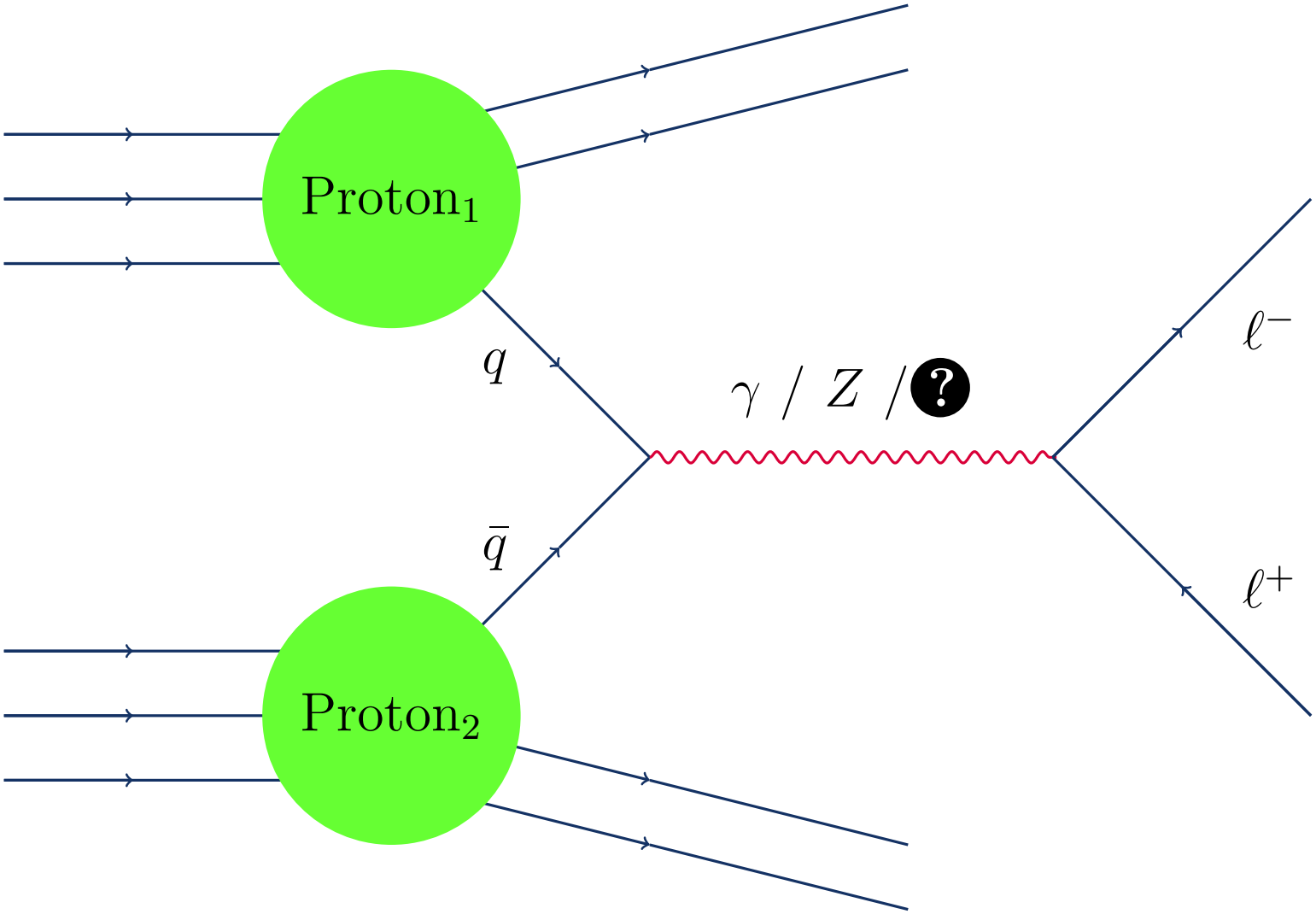
Proton$_1$
Proton$_2$
q
$\bar{q}$
γ / Z / ?
ℓ^-
ℓ^+

Contents

Chapter 1.

Introduction

The standard model of high energy physics has been proven to be the best theory to describe the fundamental particles and interactions up to the weak scale and even above it. With the observation of a Higgs-like boson in 2011-2012 [6,7] at the LHC, and with many experimental verifications prior to that, this has become even more compelling. However, there are some open questions because of which the standard model (SM) cannot be entirely complete. A certainly not comprehensive list includes the hierarchy problem, quantum description of gravity, dark matter and more.

New theories have been developed to address the hierarchy problem, i.e., the large gap between the electroweak scale and the traditional scale of gravity defined by the Planck scale. The recent approach to this long-standing problem is that the geometry of extra spatial dimensions may be responsible for the hierarchy. If new dimensions do indeed offer a solution to the hierarchy problem, then they should provide detectable signatures at or slightly above the electroweak scale in particle colliders. A certain physics scenario with additional dimension is studied in this thesis in the context of the LHC.

Another motivation to search for physics beyond the SM, is related to new extended or alternative electroweak gauge theories that have been developed to address the unification of the coupling constants at high energies. Grand unified theories (GUTs), predicting additional $U(1)'$ symmetry groups, such as those based on $SO(10)$ or E_6 [8, 9] have been developed. These can eventually break to the SM gauge group and they afford concrete and distinctive phenomenological predictions for particle colliders, see e.g. reference [10]. Few of these possibilities will be considered in this thesis as well, while emphasizing the differences with respect to the predictions from extra dimensions.

The work presented in this thesis summarizes a five-year effort concentrated around the search for evidence for the existence of extra dimensions. This effort has started with the examination of the phenomenological characteristics of the specific model [2], done within one of the most common MC simulation software tools used in high energy physics (HEP), PYTHIA8 [3]. The focus of this work was on the *five dimensional* S^1/Z_2 *Kaluza-Klein extension of the standard model* where a single spatial extra dimension is compactified on a S^1/Z_2 orbifold. The predicted signature of this model in a particle colliders is resonant, equivalent to many other exotic models predicting the appearance of heavy resonances in a color- and flavor-singlet difermion final state. In this specific model the new resonances are heavy copies of the SM γ and Z, with specific couplings to leptons and quarks.

This work concentrates on the dilepton final states, $\mu^+\mu^-$ and e^+e^-, which provide the cleanest experimental channel. This type of analysis is usually done in comparison with the DY prediction of the SM. The uniqueness of this model, however, is that when examining the invariant mass distribution of the dileptons, it predicts each resonant copy of the γ/Z particles to be preceded by a relatively large deficit with respect to the DY prediction, due to the negative interference with the DY [2, 11]. The facts that this deficit appears already at much lower dilepton masses and that it can be very pronounced, naturally imply that it should be considered in searches, along with the resonance itself. These underlying theory and its phenomenological concepts will be thoroughly explained in section 2.4 and particularly in section 2.4.4.

With proton beams colliding at the highest center of mass energy ever achieved in laboratory, and at the highest instantaneous luminosity ever recorded by a hadron collider, it has become possible to probe the presence of such heavy particles, coming from the extension of the spacetime to five dimensions. So far, there have been no searches for these particles and only indirect lower limits[1] exist on their mass at around $M_{\mathrm{KK}} \sim 1/R \leq 4$ TeV [12–14]. This makes LHC the best place to look for their presence even if they are lying above its direct reach, due to the strong deficit starting far below the resonance. Hereafter this model will be referred to as the "KK" model[2].

This search took place in the context of a wider search in ATLAS within the dilepton-resonance search group. It was done along with several other models all of which are purely resonant, where the most common one that will serve as another benchmark model throughout this work is the widely known Z'. This is actually a class of models, some of which will be presented

[1] These constraints were obtained from electroweak precision measurements.
[2] The exact features of this KK model be found also in [2] and in the corresponding implementation within PYTHIA8 [3].

in section 2.3. While the KK comes from the extension of the SM to five dimensions, the Z' is motivated by grand unification. However, the two selected models (KK and Z') for this experimental work, are essentially the most minimal *effective* models motivated from the above distinct physics scenarios. These can be called "sequential standard models" (SSMs) in the sense that the characters of the new particles are kept SM-like. For example, the couplings of the $Z'_{\rm SSM}$ are assumed to be the same as the Z couplings to fermions. Concerning the Z' interpretation, this analysis is an update of the publication based on the first 1 fb^{-1} of 2011 data, prepared for the EPS2011 conference [15], and the conference note based on the full 2011 dataset prepared for Moriond2012 [16]. ATLAS has excluded a $Z'_{\rm SSM}$ with mass lower than 1.83 TeV (2.21 TeV with the full dataset). The corresponding CMS result (EPS2011 analysis) has excluded a mass lower than 1.94 TeV for a $Z'_{\rm SSM}$ [17]. Direct searches at the TEVATRON set a limit on the $Z'_{\rm SSM}$ mass of 1.071 TeV [18, 19]. LEP results on Z' searches can be found in the following references [20–24].

These Z' and KK models are described in chapter 2 in terms of their basic properties, their basic phenomenology in the LHC and the ways to discriminate between them. This is done in comparison with the DY which does not only interfere with the exotic models but also serves as their light ancestor in terms of their basic properties.

The experimental considerations in the baseline analysis, i.e. the event-selection, the backgrounds and the systematic uncertainties are common to both searches in this thesis with several small differences. The main differences are, (1) the different signals themselves and the way they are simulated and (2) the way the statistical analysis is performed and interpreted. The analysis presented here is dealing only with the $\mu^+\mu^-$ final state, but the final $\mu^+\mu^-$ results are accompanied by the equivalent e^+e^- results and their combination. The input for the search analysis is solely the dilepton invariant mass distribution and its associated uncertainty. The baseline analysis, which is described in details in chapter 4 and in the appendices, is driven by the principle of obtaining the cleanest dilepton sample and can be summarized by the following:

- The analysis is based on a dataset of an integrated luminosity of 5 fb^{-1}, corresponding to the entire 2011 data taking period with pp collisions at 7 TeV center of mass energy. This is discussed briefly in section 4.1. The data has been taken by the ATLAS detector and a brief description of the LHC machine and the ATLAS detector are given in chapter 3 with an emphasis on the muon spectrometer, the muon trigger system and the TGC subsystem[3].

[3]The detailed description of the TGC is needed for the presentation of its on-line monitoring system that is described in appendix I

- To obtain a clean sample of dimuon events, muons are required to pass stringent identification criteria, be isolated, have high transverse momentum and invariant mass in the range of 70-3000 GeV. The event selection is described in section 4.4.
- Z'_{SSM} and KK events are simulated by MC generators followed by a full detector simulation. Variations within each model are obtained by reweighting techniques, based on the matrix element squared calculated for each event for each specific variation of the model parameters. This is described in section 4.2.2.
- The backgrounds are different for the $\mu^+\mu^-$ and the e^+e^- channels but they are the same for the KK and Z'_{SSM} models except for the treatment of the DY background. For the Z'_{SSM}, the DY can be viewed as a background or as a part of the signal, depending on the decision whether or not to account for the interference of the Z'_{SSM} with the DY, which is anyhow small and can be neglected. In the KK case, the interference between the heavy KK states and the DY is very strong so the DY is considered as a part of the signal. This approach is used as a second alternative also for the Z'_{SSM} case. The other backgrounds come from the diboson production channels, ZZ, WZ and WW and from $t\bar{t}$ production with subsequent leptonic decays. These non-DY backgrounds are at least one order of magnitude lower than the DY throughout the entire dimuon mass range. Possible contributions from QCD multi-jet with two fake leptons, and from W+jets production with one real (from the W decay) and one fake lepton, are shown to be negligible for the $\mu^+\mu^-$ case. The various contributions are described in sections 4.2, 4.7 and in appendix B.
- The transverse momentum, p_{T}, of all the muons in a given MC event has to be corrected for the resolution difference between data and MC. This is done by applying a p_{T}-smearing procedure on the MC muons, as described in section 4.5.
- The different pileup conditions between data and MC (see table table 4.2) must be corrected. This is described in sections 4.2 and 4.8.
- Higher order corrections to the leading order simulations are also applied, see section 4.3.1.
- There are few systematic uncertainties associated with the MC simulations and with the applied corrections. The main source is the uncertainty on the parton distribution functions (PDF) used in the MC simulation. Chapter 5 deals with all aspects of the systematic uncertainties.

The bare outcome of this analysis is shown as a set of single muon or dimuon histograms where the data is compared to the SM prediction and to the signals from both models. The most important histograms are the invariant mass distributions shown in figures 4.13 and 4.14 for the Z'_{SSM} and the KK respctively.

The statistical analysis and its interpretation are technically different between the KK and the Z' models. In practice this is reduced to the difference between the two approaches mentioned earlier - whether or not the DY is considered as a part of the signal. In all cases, the Bayesian [25] approach is adopted. In chapter 6 the search for the signal is performed where few basic considerations are explained. Specifically, the likelihood functions that are used for both the search and the limit-setting are listed with all the consideration taken per model.

In the case where the DY is considered as one of the background sources, the statistical analysis follows exactly the same lines as in previous analyses done in ATLAS [15, 16]. This approach is also similar to what has been done by other experiments e.g. [26, 27]. Namely, in the absence of a signal the limit is set on the cross section times branching fraction, σB, of the pure resonance versus its mass. The σB analysis is described in detail in chapter 7. The results are given for the Z' only where the interference with the DY is ignored.

In the case where the DY is considered as a part of the signal, the statistical treatment is different as the interpretation of σB is meaningless for a signal that interferes with the DY. Therefore, a new approach had to be developed. In the absence of a signal, instead of putting limits on σB, the limit is set on a different parameter which characterizes the signal. A coupling strength, g, is introduced as this parameter. This g multiplies the couplings of the new particles to the SM fermions as predicted by the underlying theory. The limit is then set on this parameter versus the mass of the new particle. The statistical analysis is significantly different due to the interference of the DY with what is called throughout this work the X signal where X stands for either the KK excitation of the γ/Z or the Z'_{SSM}. The fact that this g parameter affects not only the relative strength of the X signal with respect to the DY part but also the width of the X signal, has to be taken into account. The coupling limit analysis is described in detail in chapter 8. The issue of the Bayesian prior is discussed in details in this chapter where the results are given for the KK and for the Z'_{SSM}.

In both approaches, the limit derivation is using signal templates obtained via two different reweighting techniques where a different baseline MC sample is used for each. The treatment in the case of interfering signals is somewhat more complex due to the coupling strength parameter, g. This is described initially in section 4.2.2. The systematic uncertainties treatment is also more complex in the case of the interfering signals and requires the preparation of systematic uncertainty templates in addition to the nominal ones. This is described in section 5.4. Finally, it can be seen exactly how these nominal and uncertainty templates are entering the likelihood function in chapters 6, 7 and 8.

The outcome of this analysis is summarized in chapter 9.

All appendices but the last one, support the experimental analysis itself from the baseline, through the signal search and to the limits.

My analysis code is largely available under my private svn repository [28], except for files that contain ATLAS data or full simulation results.

The last appendix, I, deals with my work on the TGC on-line monitoring system. Brief explanation on the design and implementation are given as well as few examples of the histograms and data quality algorithms used.

Chapter 2.

Theory

2.1. Introduction

In the late 1960s and early 1970s, the electromagnetic and weak interactions were unified into an electroweak interaction, described by a nonabelian gauge theory based on the group $SU(2)_L \times U(1)_Y$. Somewhat later, in the early 1970s, it was realized that the strong interaction can be described by a nonabelian gauge theory based on the group $SU(3)$. But when the nonabelian gauge theory was first proposed in 1954 by Young and Mills, it seemed to be totally inconsistent with the existing experimental observations as they were interpreted at that time. The theory predicts several massless spin 1 particles, which were not known experimentally. It would seem that there are only two logical solutions to the difficulty that massless spin 1 particles were not experimentally seen except for the photon: (1) the Yang-Mills particles somehow acquire mass, or (2) the Yang-Mills particles are in fact massless but are somehow not observed. It is now known that the first possibility was realized in the electroweak interaction (the $W^{\pm}$ and the Z) and the second in the strong interaction (the gluons), forming together the standard model [29].

Soon after the proposal of the electroweak $SU(2)_L \times U(1)_Y$ model there were many suggestions for extended or alternative electroweak gauge theories, some of which involved additional $U(1)'$ symmetry groups [10]. An especially compelling motivation came from the development of GUTs as those based on $SO(10)$ or E_6 [8,9]. These had rank larger than four and could break to $G_{\rm SM} \times U(1)'^n$ where $n \geq 1$ and where $G_{\rm SM} = SU(3)_C \times SU(2)_L \times U(1)_Y$ is the SM gauge group.

Similarly, theories were suggested which are based on superstring constructions, often involving large gauge symmetries which break to $G_{\rm SM} \times U(1)'^n$ in the effective four-dimensional

theory [30]. In string theories and in supersymmetric versions of grand unification with extra $U(1)'$ below the string or GUT scale, both the $U(1)'$ and the $SU(2)_L \times U(1)_Y$ breaking scales are generally tied to the soft supersymmetry breaking scale [30]. Therefore, if supersymmetry is observed at the LHC there is a strong motivation that a string or GUT induced Z' would also have a mass at an observable scale.

In recent years, many TeV scale extensions to the SM have been proposed in addition to supersymmetry, often with the motivation of resolving the fine tuning associated with the quadratic divergence in the Higgs mass. These include various forms of dynamical symmetry breaking [31] and little Higgs models [32], which typically involve extended gauge structures, often including new Z' gauge bosons at the TeV scale.

Some versions of theories with large extra dimensions allow the standard model gauge bosons to propagate in the extra dimensions, implying Kaluza-Klein (KK) excitations [33] of the γ/Z and other standard model gauge bosons, with effective masses of order $R^{-1} \sim 1$ TeV where R is the scale of the extra dimension. Similar excitations can also occur in Randall-Sundrum (RS) models [34].

The possibility of indirectly observing the effects of Z'-like particles with electroweak strength couplings in the DY channel at the LHC with masses above the direct search reach is also considered here. It can be shown that, mostly due to statistical limitations, this is very unlikely in almost all classes of models, independently of the spin of the resonance. The one possible exception to this general result is the case of degenerate Kaluza-Klein excitations of the photon and Z that occur in some extra-dimensional models such as the S^1/Z_2 model which will be introduced later. In this special case, the strong destructive interference with the SM exchanges below the resonance mass leads to a significant suppression of the cross section and thus increased sensitivity to this particular new physics scenario [2, 11].

This chapter will concentrate on two benchmark possibilities of spin-1 models in the LHC, namely, the Z' and the KK γ/Z. Although not the most theoretically justified, the focus will be mainly on the SSM extensions. This will be practically expressed in the assumption that couplings of the new spin-1 particles will be SM-like.

In the next section, the SM γ/Z, having analogous terms in the new physics parts, will be introduced. In the cases considered here, the γ/Z is interfering with the new physics or is at least the main source of background for this new physics. Few other models will be introduced in the the later sections.

Throughout this chapter, PYTHIA8 [3] has been used together with the MRSTCal [35] PDF set for the generation of all the MC samples used for the basic analysis (at the generator-level) shown in section 2.2. These MC samples were generated with the LHC conditions for 2011, i.e. for pp collisions at $\sqrt{s} = 7$ TeV with integrated luminosity of about ~ 5 fb^{-1}. For illustration, the focus will be only on the (cleanest) dimuon decays of both the SM γ/Z, the Z's or the KK γ/Z.

2.2. The Z boson

2.2.1. The Z boson theory in a nutshell

Before introducing new heavy resonances, it is essential to write down few properties of the SM γ/Z since these will eventually interfere with the new spin-1-like resonances or at the very least be their main background in searches.

For the extension of the gauge symmetry to $SU(2)_L \times U(1)_Y$, one can start by denoting the generator of $U(1)$ by $\frac{1}{2}Y$ (called the hypercharge) and the associated gauge potential by B_μ (and their counterparts T^a and W^a_μ for $SU(2)$). The the covariant derivative is

$$D_\mu = \partial_\mu - igW^a_\mu T^a - ig' B_\mu \tfrac{Y}{2} \tag{2.2.1}$$

where g and g' are the $SU(2)$ and $U(1)$ gauge couplings respectively [29].

The next step is to introduce the Higgs field, $\phi = \begin{pmatrix} \phi^+ & \phi^0 \end{pmatrix}$, with its vacuum expectation value (VEV) being $\begin{pmatrix} 0 & \upsilon \end{pmatrix}$. If the couplings of the gauge bosons to the various fields, in particular, the Higgs field, are determined, the mass spectrum of the gauge bosons can be worked out. Upon spontaneous symmetry breaking $\phi \to \frac{1}{\sqrt{2}} \begin{pmatrix} 0 & \upsilon \end{pmatrix}$, and the Higgs kinetic part of the Lagrangian turns into,

$$\mathcal{L} = (D_\mu \phi)^\dagger (D^\mu \phi) \to \frac{g^2 \upsilon^2}{4} W^+_\mu W^{-\mu} + \frac{\upsilon^2}{8} \left(g W^3_\mu - g' B_\mu \right)^2 \tag{2.2.2}$$

Thus, the linear combination $gW^3_\mu - g'B_\mu$ becomes massive while the orthogonal combination remains massless and is identified with the photon. It is convenient to define the mixing angle, θ_W, using the relation $\tan\theta_W = g'/g$. Then, the following combination,

$$Z_\mu = \cos\theta_W W^3_\mu - \sin\theta_W B_\mu \tag{2.2.3}$$

describes a massive gauge boson known as the Z boson, while the electromagnetic potential is given by $A_\mu = \sin\theta_W W^3_\mu - \cos\theta_W B_\mu$. Combining Z_μ and A_μ, it can be seen that the mass squared of the Z boson is $M_Z^2 = \frac{v^2}{4}(g^2 + g'^2)$, where $M_W = M_Z \cos\theta_W$ and $M_A = 0$.

Rewriting the covariant derivative in terms of the physically observed Z and A, one can obtain the familiar electric charge $e = g\sin\theta_W = g'\cos\theta_W$. This determines the coupling of the Z boson to an arbitrary fermion field ψ in the theory;

$$\mathcal{L} = \frac{g}{\cos\theta_W} Z_\mu \bar{\psi}\gamma^\mu \left(T^3 - \sin^2\theta_W Q\right)\psi \tag{2.2.4}$$

where $Q = T^3 + \frac{1}{2}Y$ and where T^3 is the weak isospin. For example, using equation 2.2.4 one can write the coupling term of the Z to leptons;

$$\mathcal{L} = \frac{g}{\cos\theta} Z_\mu \left[\tfrac{1}{2}\left(\bar{\nu}_L\gamma^\mu\nu_L - \bar{e}_L\gamma^\mu e_L\right) + \sin^2\theta_W \bar{e}\gamma^\mu e\right] \tag{2.2.5}$$

It is possible to express the observed neutral currents (NC),

$$\begin{aligned} j^{em}_\mu &= J^3_\mu + \tfrac{1}{2} j^Y_\mu \\ J^{NC}_\mu &= J^3_\mu - \sin^2\theta_W j^{em}_\mu \end{aligned} \tag{2.2.6}$$

in terms of the weak isospin current, J^3_μ, and the hypercharge current, j^Y_μ, belonging to the symmetry groups $SU(2)$ and $U(1)$ respectively. The right-handed component of J^3_μ has been arranged to cancel with that in $\sin^2\theta_W j^{em}_\mu$ to leave a pure left-handed J^3_μ of $SU(2)$, where $\sin^2\theta_W$ is to be determined by experimental data. The NC interaction is given by,

$$-i\frac{g}{\cos\theta_W}\left(J^3_\mu - \sin^2\theta_W j^{em}_\mu\right) Z^\mu = -i\frac{g}{\cos\theta_W}\bar{\psi}_f\gamma^\mu\left[\tfrac{1}{2}\left(1+\gamma^5\right)T^3 - \sin^2\theta_W Q\right]\psi_f Z_\mu \tag{2.2.7}$$

for the coupling $Z \to f\bar{f}$. It is customary to express the vertex factor in the general form as seen in figure 2.1, where the vector and axial-vector couplings, g_V, and g_A, are determined in

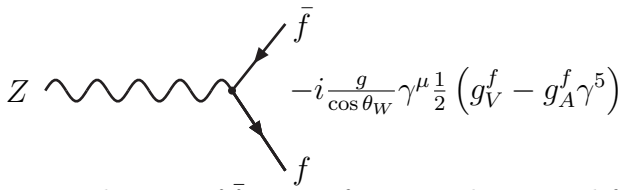

Figure 2.1.: The $Z \to f\bar{f}$ vertex factor in the general form

the standard model (given the value of $\sin^2\theta_W$) [29]. Recall that the electromagnetic current

Table 2.1.: The $Z \to f\bar{f}$ vertex factors in the SM

f	Q_f	g_A^f	g_V^f
ν_e, ν_μ,...	0	$\frac{1}{2}$	$\frac{1}{2}$
e^-, μ^-,...	-1	$-\frac{1}{2}$	$-\frac{1}{2} + 2\sin^2\theta_W$
u, c,...	$\frac{2}{3}$	$\frac{1}{2}$	$\frac{1}{2} - \frac{4}{3}\sin^2\theta_W$
d, s,...	$-\frac{1}{3}$	$-\frac{1}{2}$	$-\frac{1}{2} + \frac{2}{3}\sin^2\theta_W$

in QED is $-ie\,(j^{em})^\mu\,A_\mu = -ie\left(\bar{\psi}\gamma^\mu Q_f \psi\right) A_\mu$ and the corresponding vertex factor is realized in figure 2.2.

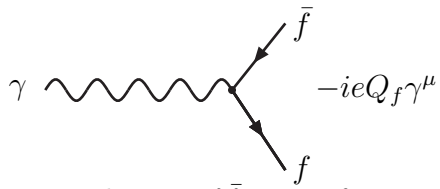

Figure 2.2.: The $\gamma \to f\bar{f}$ vertex factor in the general form

The vector and axial-vector couplings values are:

$$\begin{aligned} g_V^f &= T_f^3 - 2\sin^2\theta_W Q_f \\ g_A^f &= T_f^3 \end{aligned} \tag{2.2.8}$$

where T_f^3 and Q_f are, respectively, the third component of the weak isospin and the charge of fermion f. These are written in table 2.1. It is possible to transform the listed $V-A$ couplings into the chiral $L-R$ (left-right) couplings where $g_V = g_L + g_R$ and $g_A = g_L - g_R$. In that case, the vertex functions seen in figure 2.1 are,

$$\begin{aligned} V-A &: -i\tfrac{g}{\cos\theta_W}\gamma^\mu \tfrac{1}{2}\left(g_V^f - g_A^f\gamma^5\right) \\ L-R &: -i\tfrac{g}{\cos\theta_W}\gamma^\mu \left(g_L^f P_L + g_R^f P_R\right) \end{aligned} \tag{2.2.9}$$

where $P_{L,R} = \frac{1}{2}\left(1 \mp \gamma^5\right)$ are the chiral projection operators.

2.2.2. Basic phenomenology of Z-bosons

The Z is in principle interfering with the photon and this needs to be taken into account in scattering processes such as $f\bar{f} \to Z/\gamma \to F\bar{F}$. The amplitude in the $L-R$ formalism may

be written as [36, 37]

$$\mathcal{M}(\lambda, \lambda', s) = \frac{Q_f Q_F}{s} + \frac{g_\lambda^f g_{\lambda'}^F / \sin^2\theta_W \cos^2\theta_W}{s - M_Z^2 + iM_Z\Gamma_Z}. \tag{2.2.10}$$

where s is the square of the $f\bar{f}(F\bar{F})$ system invariant mass, $\lambda(\lambda')$ is the incoming(outgoing) fermion helicity and Γ_Z is the total Z width. The partial decay width in Lowest Order (LO) following the notation of [36] is,

$$\Gamma_{Z\to\mathcal{F}\bar{\mathcal{F}}} = \frac{N_C^{\mathcal{F}}\alpha_{em}M_Z}{6}\left(\left|g_R^{\mathcal{F}}\right|^2 + \left|g_L^{\mathcal{F}}\right|^2\right)\frac{1}{\sin^2\theta_W\cos^2\theta_W} \tag{2.2.11}$$

with $\mathcal{F}$ being a general fermion and $\Gamma_Z = \sum_{\mathcal{F}} \Gamma_{Z\to\mathcal{F}\bar{\mathcal{F}}}$. The first term in equation 2.2.10 stands for the photon and the second term is the Z. Here, the Z couplings to the fermions in the $L-R$ formalism are [36],

$$g_\lambda^{\mathcal{F}} = \begin{cases} -Q_{\mathcal{F}}\sin^2\theta_W & \text{if } \lambda = +1/2 \\ T_{\mathcal{F}}^3 - Q_{\mathcal{F}}\sin^2\theta_W & \text{if } \lambda = -1/2 \end{cases} \tag{2.2.12}$$

with $\lambda = \pm\frac{1}{2}(=\text{R or L})$. The differential cross section in LO takes the form,

$$\frac{d\sigma(f, F; s, \cos\theta^*)}{dt} = \frac{2}{s}2\pi\frac{\alpha_{em}^2}{4s}\frac{N_C^F}{N_C^f}\frac{s^2}{4}\sum_{\lambda=\pm\frac{1}{2}}\sum_{\lambda'=\pm\frac{1}{2}}\left|\mathcal{M}(\lambda, \lambda', s)\right|^2(1 + 4\lambda\lambda'\cos\theta^*)^2 \tag{2.2.13}$$

where θ^* is the angle of the outgoing F relative to the incoming f as measured in the $f\bar{f}(F\bar{F})$ system center of mass frame. The azimuthal angle ϕ is distributed uniformly. The summation over the incoming helicities, λ, comes from averaging over all the helicity states of the incoming fermions corresponding to their unpolarized state. This must be divided by the number of possible incoming helicity states which can be expressed in terms of the spins of the interacting particles: $\left(2S_{\bar{f}} + 1\right)(2S_f + 1) = 4$. The second summation over all the outgoing helicity states, λ', correspond to the unmeasured polarization state of the outgoing fermions. From helicity conservation, it is not needed to sum over the helicities of the incoming and outgoing anti-fermions since their helicities are always opposite to those of the corresponding fermions. The parameter $N_C^{f(F)}$ is the number of colors of $f(F)$. The overall color factor $\frac{1}{N_C^f}$ arises from to the fact that in the case of $q\bar{q}$ annihilation, only when the color of the quark matches the color of the antiquark can annihilation into a color-singlet state take place. The differential cross section is given with respect to the the invariant Mandelstam variable $t = -\frac{s}{2}(1 - \cos\theta^*)$. The

transformation from $\frac{d\sigma}{d\cos\theta^*}$ to $\frac{d\sigma}{dt}$ introduces a $\frac{2}{s}$ factor in the cross section where this has to be omitted if one is to measure $\frac{d\sigma}{d\cos\theta^*}$ [37].

Contrary to the pure QED case, it can be shown that the resulting $\cos\theta^*$ distribution will be asymmetric due to the presence of the Z boson and its $L-R$ (or $V-A$) couplings structure. This gives rise to forward-backward asymmetry, $A_{\rm fb}$, in the Z decay where,

$$A_{\rm fb} = \frac{\sigma_{\rm f} - \sigma_{\rm b}}{\sigma_{\rm f} + \sigma_{\rm b}} \quad \text{with} \quad \sigma_{\rm f} = \int_0^1 \frac{d\sigma}{d\cos\theta^*} d\cos\theta^* \quad \text{and} \quad \sigma_{\rm b} = \int_{-1}^0 \frac{d\sigma}{d\cos\theta^*} d\cos\theta^* \tag{2.2.14}$$

In terms of $A_{\rm fb}$, the $\cos\theta^*$ distribution for a given value of s can be written as,

$$\frac{d\sigma}{d\cos\theta^*} \propto \frac{3}{8}\left(1+\cos^2\theta^*\right) + A_{\rm fb}\cos\theta^* \tag{2.2.15}$$

Note that in the LO QED result ($A_{\rm fb} = 0$) the angular distribution is totally symmetric. The $A_{\rm fb}$ can in fact be measured where it is closely related to the couplings structure and in principle, it enables to distinguish between different scenarios of angular distributions. This is mostly common in the context of distinguishing between different spin-1 scenarios (e.g. between the DY and any of the possible Z's). Because the $A_{\rm fb}$ is an integrated quantity, then it has to be examined along with the examination of the angular distribution itself [2, 37]. The angular distribution, in the cases of enough statistics, can be in principle used also to distinguish between a spin-0 (neutralino), a spin-1 (Z-like) or a spin-2 (RS graviton).

2.2.3. Remarks about the hadronic level (LHC)

In the LHC, the process under examination is the DY process, $pp \to Z/\gamma + X \to F\bar{F} + X$ where the incoming fermions $f\bar{f}$ are quark and anti-quark originating from the two protons. The DY cross section for $q\bar{q}$ annihilation to a fermion pair via an intermediate massive γ/Z can be obtained from equation 2.2.13 with few modifications. Two quantities, $\hat{s}$ and $\hat{t}$ which will be introduced below are the partonic Mandelstam variables while s and t are these defined for the incoming hadrons. In general, the incoming quark and antiquark will have a spectrum of energies (in the center of mass frame) and it is more appropriate to consider the hadronic differential cross section $\frac{d\sigma}{d\hat{t}}$. In order to obtain this, one can start from the center of mass (CM) frame of the two incoming hadrons. In this frame, the four momenta, p_1 and p_2 of the

incoming partons may be written as [37],

$$\begin{aligned} p_1 &= \tfrac{\sqrt{s}}{2}\,(x_1, 0, 0, x_1) \\ p_2 &= \tfrac{\sqrt{s}}{2}\,(x_2, 0, 0, -x_2)\,, \end{aligned} \tag{2.2.16}$$

where the Bjorken x_i variable is the fraction of the hadron momentum carried by the parton i. The square of the parton CM energy $\hat{s}$ is related to the corresponding hadronic quantity by $\hat{s} = x_1 x_2 s$. Folding in the parton distribution functions for the initial state quarks, gives the hadronic differential cross section in terms of x_1 and x_2,

$$\frac{d^3\sigma}{dx_1 dx_2 d\hat{t}} = \sum_q \frac{d\sigma\,(q, F; \hat{s}, \cos\theta^*)}{d\hat{t}}\,[\mathrm{PDF}_q(x_1, Q)\cdot \mathrm{PDF}_{\bar{q}}(x_2, Q) + \{1 \leftrightarrow 2\}] \tag{2.2.17}$$

where PDF_q is the parton density function of species q. The quantity Q is the factorization scale, usually taken to be the invariant mass, $\sqrt{\hat{s}}$. From beam symmetry, the substitution $\{1 \leftrightarrow 2\}$ is equivalent to simply multiplying the whole expression by 2. To obtain the hadronic differential cross section one has to integrate over all possible values of x_1 and x_2. The transformation from x_1 and x_2 to $\hat{s}$ and the $q\bar{q}$ system rapidity, y, enables to reduce the double integration to a single one on y;

$$\begin{aligned} \hat{s} &= s x_1 x_2 \\ y &= \tfrac{1}{2}\ln\left(\tfrac{x_1}{x_2}\right) \end{aligned} \tag{2.2.18}$$

This transformation involves a Jacobian which reduces to the constant $\frac{1}{s}$. The problem reduces to integrating over all possible rapidity values. By knowing the value of s (7 TeV in 2011 in the LHC), the hadronic differential cross section can be written as,

$$\frac{d^2\sigma}{d\hat{s}d\hat{t}} = \int_{-y_0}^{+y_0} \frac{dy}{s} \sum_q \frac{d\sigma\,(q, F; \hat{s}, \cos\theta^*)}{d\hat{t}} \cdot 2 \cdot \mathrm{PDF}_q\left(x_1(y, \hat{s}), \sqrt{\hat{s}}\right) \cdot \mathrm{PDF}_{\bar{q}}\left(x_2(y, \hat{s}), \sqrt{\hat{s}}\right) \tag{2.2.19}$$

where the boundaries $\pm\, y_0$ are determined from both x_1 and x_2 being constrained between 0 and 1 so that $y_0 = \frac{1}{2}\ln\left(\frac{s}{\hat{s}}\right)$ [37]. It is sometimes useful to replace the transformation Jacobian with the equivalent expression, $\frac{1}{s} = \frac{x_1 x_2}{\hat{s}}$. The factor 2 in equation 2.2.19 reflects the beam symmetry.

The conventional DY forward-backward asymmetry in the LHC, cannot be calculated directly as in equation 2.2.14 since the direction of the incoming quark ($f = q$) is unknown and

therefore $\cos\theta^*$ cannot be calculated. That can be solved as follows; Neglecting higher order processes, the $F\bar{F}$ system is in general boosted along the beam axis. The z-axis is arbitrarily chosen as the direction of one of the beams. Under this definition, there is a sign ambiguity in the measurement of $\cos\theta^*$, since for a particular event, there is no information about whether the incoming quark comes from the positive or negative z directions. Instead, it is useful to consider the quantity $\cos\theta^*_{\vec{\beta}}$, the angle between the $F\bar{F}$ system boost vector $\vec{\beta} = \frac{\vec{p}_F + \vec{p}_{\bar{F}}}{E_F + E_{\bar{F}}}$ and the outgoing fermion direction as measured in the $F\bar{F}$ center of mass frame ($\vec{p^*}_F$),

$$\cos\theta^*_{\vec{\beta}} = \frac{\vec{p^*}_F \cdot \vec{\beta}}{\left|\vec{p^*}_F\right| \cdot |\vec{\beta}|} \tag{2.2.20}$$

This is equivalent to transforming to what is called the Helicity frame where the outgoing fermion F direction is measured relative to the outgoing difermion $F\bar{F}$ boost vector. Neglecting higher order processes, the boost is confined to the $|z|$ direction, that is, $\vec{\beta} = \pm\beta\hat{z}$, and can be measured so that there is no sign ambiguity in determining $\cos\theta^*_{\vec{\beta}}$. Taking the $F\bar{F}$ system boost instead of the (unknown) incoming quark direction can be justified by the fact that the quark will be, on average, more energetic than the anti-quark due to the difference in the q and $\bar{q}$ PDFs. Therefore, the boost direction will, on average, coincide with the incoming quark direction and the sensitivity to the Z couplings will not be significantly harmed. The measured quantity will be A^{β}_{fb}, to denote the fact that it is done with respect to the boost direction [37]. These concepts will be demonstrated in the next section.

2.3. $U(1)'$ models

2.3.1. The Z' extensions to the SM

In the extension of the SM $SU(2)_L \times U(1)_Y$ to $SU(2)_L \times U(1)_Y \times U(1)'^n$ ($n \geq 1$), the neutral current Lagrangian becomes [10]

$$-\mathcal{L} = e j^{\mu}_{em} A_{\mu} + g_1 J^{\mu}_1 Z_{1\mu} \longrightarrow e j^{\mu}_{em} A_{\mu} + \sum_{\alpha=1}^{n+1} g_{\alpha} J^{\mu}_{\alpha} Z_{\alpha\mu} \tag{2.3.1}$$

where the subscript "1" denotes the SM quantities, i.e. $Z_{1\mu}$ is the SM Z boson, $g_1 = g/\cos\theta_W$ is the SM coupling constant and J^{μ}_1 is the SM Z current. Similarly, the index $\alpha = 2, ..., n+1$ stands for the additional $U(1)'$s. The currents in equation 2.3.1 can be also written in the

$V-A$ or $L-R$ formalism as in the SM case:

$$\begin{aligned} J^\mu_\alpha &= \bar{\psi}\gamma^\mu \tfrac{1}{2}\left(g^\alpha_V(f) - g^\alpha_A(f)\gamma^5\right)\psi \\ &= \bar{\psi}\gamma^\mu \left(g^\alpha_L(f)P_L + g^\alpha_R(f)P_R\right)\psi \end{aligned} \tag{2.3.2}$$

The chiral couplings, $g^\alpha_{L,R}(f)$, which may be unequal for a chiral gauge symmetry, are the $U(1)'_\alpha$ charges of the left- and right-handed components of fermion f where $g^\alpha_{V,A}(f)$ are the corresponding vector and axial couplings. The previous connections between the two representations, for a given α, still hold. Frequently however, it is more convenient to specify the $U(1)'_\alpha$ charges of the left chiral components of both the fermion f and the anti-fermion (conjugate) f^c denoted $Q_{\alpha f}$ and $Q_{\alpha f^c}$, respectively. The two sets of charges are simply related,

$$\begin{aligned} g^\alpha_L(f) &= Q_{\alpha f} \\ g^\alpha_R(f) &= -Q_{\alpha f^c} \end{aligned} \tag{2.3.3}$$

For example, in the SM one has $Q_{1u} = \frac{1}{2} - \frac{2}{3}\sin^2\theta_W$ and $Q_{1u^c} = +\frac{2}{3}\sin^2\theta_W$. The additional gauge couplings and charges, as well as the gauge boson masses and mixings, are model dependent.

In a general theory the Z' and the SM Z are not true mass eigenstates due to mixing[1]. The interaction actually generates a mass (squared) matrix in the $Z-Z'$ basis,

$$\mathcal{M}^2 = \begin{pmatrix} M_Z^2 & \beta M_Z^2 \\ \beta M_Z^2 & M_Z'^2 \end{pmatrix} \tag{2.3.4}$$

where β, the symmetry breaking dependent parameter can be argued to be $\mathcal{O}(1)$ or less. Since this matrix is real, the diagonalization of $\mathcal{M}^2$ proceeds via a simple rotation through a mixing angle ϕ, i.e., by writing $Z = Z_1\cos\phi - Z_2\sin\phi$, etc., which yields the mass eigenstates $Z_{1,2}$ with masses $M_{1,2}$; given present data one may expect that $r = M_1^2/M_2^2 \leq 0.01$. $Z_1 \simeq Z$ is the state presently produced at colliders, i.e., $M_1 \simeq 90$ GeV, and thus one might also expect that ϕ must be quite small for the SM to work as well as it does. Defining $\rho = M_Z^2/M_1^2$, with M_Z being the would-be mass of the Z if no mixing occurred, one can approximate,

$$\begin{aligned} \phi &= -\beta r[1 + (1+\beta^2)r + O(r^2)] \\ \delta\rho &= \beta^2 r[1 + (1+2\beta^2)r + O(r^2)] \end{aligned} \tag{2.3.5}$$

[1] In principle, this can arise from different mechanisms [38]

Table 2.2.: E_6 inspired Z's couplings to fermions in the PYTHIA convention [42]

f	$g_V^f(\theta_{E_6})$	$g_A^f(\theta_{E_6})$
$\nu_e,\ \nu_\mu,\ \nu_\tau$	$\frac{\sqrt{10}\cos\theta_{E_6}-3\sqrt{6}\sin\theta_{E_6}}{6}\sin\theta_W$	$\frac{\sqrt{10}\cos\theta_{E_6}-3\sqrt{6}\sin\theta_{E_6}}{6}\sin\theta_W$
$e^-,\ \mu^-,\ \tau^-$	$-\frac{4\sin\theta_{E_6}}{\sqrt{6}}\sin\theta_W$	$\frac{\sqrt{10}\cos\theta_{E_6}-\sqrt{6}\sin\theta_{E_6}}{3}\sin\theta_W$
$u,\ c,\ t$	0	$\frac{\sqrt{10}\cos\theta_{E_6}+\sqrt{6}\sin\theta_{E_6}}{3}\sin\theta_W$
$d,\ s,\ b$	$+\frac{4\sin\theta_{E_6}}{\sqrt{6}}\sin\theta_W$	$\frac{\sqrt{10}\cos\theta_{E_6}-\sqrt{6}\sin\theta_{E_6}}{3}\sin\theta_W$

where $\delta\rho \equiv \rho - 1$, so that β determines the sign of ϕ. It can be expected that both $\delta\rho, |\phi| < 10^{-2}$. In fact, if one is *not* dealing with issues associated with precision measurements [39], then $Z - Z'$ mixing is expected to be so small that it can be safely neglected [38]. It is important to note that non-zero mixing modifies the predicted SM Z couplings where this can lead to many important effects. For example, the partial width for $Z_1 \to f\bar{f}$ to lowest order will be modified.

2.3.2. Benchmark Z' models

There are many Z' models falling into two rather broad categories depending on whether or not they arise in a GUT scenario. The most popular GUT scenario is the one coming from E_6 grand unification [40, 41]. In that case, the symmetry breaking pattern can be realized as $E_6 \to SO(10) \times U(1)_\psi \to SU(5) \times U(1)_\chi \times U(1)_\psi$. Then, $SU(5)$ breaks to the SM and only one linear combination $U(1)_{\theta_{E_6}} = \cos\theta_{E_6} U(1)_\psi - \sin\theta_{E_6} U(1)_\chi$ remains light at the TeV scale. The mixing angle, θ_{E_6} is treated as a free parameter[2] and the particular values $\theta_{E_6} = 0,\ -\frac{\pi}{2}$ and $\tan^{-1}\left(-\sqrt{5/3}\right) + \frac{\pi}{2}$, correspond to 'special' models called ψ, χ and η, respectively. The couplings of any of these possibilities to the SM fermions for a given θ_{E_6} are listed in table 2.2 in the PYTHIA6 convention [42].

The partial Z' decay width in LO, in analogy to equation 2.2.11 is,

$$\Gamma_{Z'_{E_6} \to \mathcal{F}\bar{\mathcal{F}}} = \frac{N_C^{\mathcal{F}} \alpha_{em} M_{Z'_{E_6}}}{6} \left(\left| g_L^{\mathcal{F}}(\theta_{E_6}) \right|^2 + \left| g_R^{\mathcal{F}}(\theta_{E_6}) \right|^2 \right). \tag{2.3.6}$$

[2] There are several different definitions of this mixing angle in the literature, i.e., $Z' = Z_\chi \cos\beta + Z_\psi \sin\beta$ occurs quite commonly.

where $g^{\mathcal{F}}_{L,R}(\theta_{E_6})$ are linear combinations of the couplings given in table 2.2, and where decays such as $Z'_{E_6} \to W^+W^-$ are not included. The transformation to the $L-R$ formalism under the PYTHIA convention is,

$$\begin{aligned} g^{\mathcal{F}}_L &= \frac{1}{2\sin\theta_W\cos\theta_W}\frac{g^{\mathcal{F}}_V + g^{\mathcal{F}}_A}{2} \\ g^{\mathcal{F}}_R &= \frac{1}{2\sin\theta_W\cos\theta_W}\frac{g^{\mathcal{F}}_V - g^{\mathcal{F}}_A}{2} \end{aligned} \tag{2.3.7}$$

Another example is a Z' that has couplings which are exactly the same as those of the SM Z, but is just heavier. This is often referred to as sequential standard model, i.e. Z'_{SSM}. It is not a real model but is very commonly used as a "standard candle" in experimental Z' searches. In that cases, to obtain the total width of the Z', one simply has to scale the known width of the Z by the ratio of the masses and add the possibility of a $t\bar{t}$ decay which is kinematically forbidden for the Z, i.e.,

$$\Gamma_{Z'_{\mathrm{SSM}}} = \sum_{\mathcal{F}} \Gamma_{Z'_{\mathrm{SSM}}\to\mathcal{F}\bar{\mathcal{F}}} = \Gamma_Z \times \frac{M_{Z'_{\mathrm{SSM}}}}{M_Z} + \Gamma_{Z'_{\mathrm{SSM}}\to t\bar{t}} \tag{2.3.8}$$

A more realistic variant of this model is one in which a Z' has no couplings to SM fermions in the weak basis but the couplings are then induced in the mass eigenstate basis $Z-Z'$ via mixing [38]. In this case the relevant couplings of the Z' are those of the SM Z but scaled down by a factor of $\sin\phi$. If the couplings of the Z' are those of the SM Z but scaled down by a factor of $\sin\phi$, then the width should be also scaled down by a factor of $\sin^2\phi$, as can be seen from the relationship given in equation 2.2.11. In general, the possibility to scale the strength of the Z' couplings is usually ignored in the conventional Z' direct searches where only the cross-section is allowed to float while the width remains fixed at the SSM value. In these searches, that are based only on the $F\bar{F}$ mass distribution, the $\gamma/Z/Z'$ interference is usually neglected.

2.3.3. Some Z' observables

Apart from the appearance of a heavy resonance above the SM DY shape, the Z' also exhibits a different A_{fb} behavior because of the presence of the new heavy state [2, 37, 43, 44]. The p_{T} distribution of the Z' decay products will also differ from the pure DY one. There are of course more differences but these are the most pronounced and most easy to use. These differences between the few Z' benchmark-models discussed above are shown in figures 2.3 and 2.4.

In the following, only the differences between the DY, the $Z'_{\rm SSM}$ and a few of the E_6 inspired Z' models will be shown. The focus will be on a dimuon final state in pp collisions at $\sqrt{s} = 7$ TeV, with integrated luminosity of about 5 fb^{-1}. Any detector and background effects will be ignored as the detector signature of muons is rather clear, the acceptance for these channels is usually high and the background rates are usually very low comparing to the DY throughout the available phase-space. Higher order QCD and EW corrections will be also ignored in the following illustrative MC analysis.

The dimuon channel is extremely useful for these studies. However, an experimental feature which cannot be easily ignored while doing a proper experimental analysis (even at the generator level) is the modeling of the detector resolution for high-$p_{\rm T}$ muons imposed by the muon spectrometer. For a dimuon analysis this may be crucial but it will be ignored in this generator-level analysis.

In a dielectron channel, the background cannot be easily ignored while the high resolution for high-$p_{\rm T}$ electrons will not require to correct for the calorimeter measurement of the electron energy. However, different difficulty arises in the case of electrons in the determination of the electron-object charge. This difficulty makes a selection requirement as the opposite-charge requirement to be very problematic. It is also imposing difficulties in calculating $\cos\theta^*$ as one of the inputs for that calculation is the lepton charge.

The first and most important observable in that context is the new, heavy resonance in the dilepton invariant mass distribution as can be seen in figure 2.3(a). The shape seen is for the full $\gamma/Z/Z'$ interference starting from below the Z peak at 50 GeV and going up to 5000 GeV. The Z's signals (generated with mass of 1000 GeV) and the DY background are normalized to 5 fb^{-1}. It can be seen that although it is visible, the interference just below the Z' peak is very small. Indeed it can be shown to be negligible for "ordinary" Z' searches but this is not always the case, as it will be shown in the next section. Even after applying QCD and EW higher-order corrections and after taking into account experimental effects such as momentum smearing, acceptance and efficiencies, the shapes at the resonance should remain very distinctive given sufficient statistics. Naturally, this is the baseline for almost all the past and present experimental Z' searches except for precision measurements done on the Z peak [39]. The latter are considered *indirect* searches while searching for deviations from the DY shape along the invariant mass distribution is considered *direct*. With the LHC reach and even with the TEVATRON, the sensitivity of the latest direct searches should be greater.

Figure 2.3(b) shows the the $p_{\rm T}$ distributions for the same samples. The small "shoulder" above the DY contribution starting from $\sim$300 GeV, may also have a discriminating power. Both

features, namely the resonance in $m_{\mu\mu}$ and the p_{T} shoulder, are rather local and should be visible but the mass resonance is more prominent.

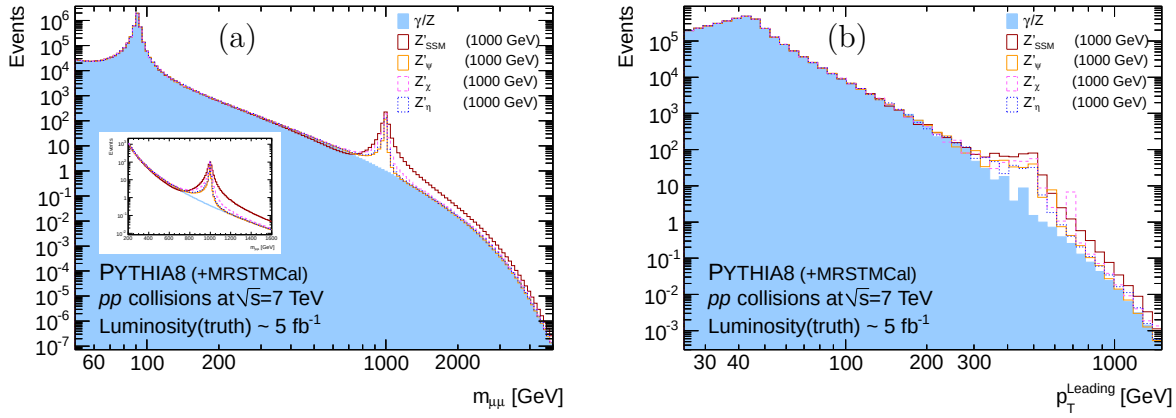

Figure 2.3.: The dimuon invariant mass distribution in (a) and the leading muon p_{T} distribution in (b) of the DY, the Z'_{SSM} and few E_6 inspired Z's at $M_{Z'} = 1000$ GeV. The MC samples are normalized to 5 fb^{-1} with no selection criteria or higher order corrections applied.

Another kinematic variable which can help in the discovery of a possible Z' signal is the forward-backward asymmetry, A_{fb}. Figure 2.4(a) shows A_{fb} versus $m_{\mu\mu}$. A clear deviation from the DY behavior is observed near the mass of the resonance. However, this A_{fb}, where the forward and backward directions are defined with respect to the incoming quark, cannot be practically measured because the incoming quark direction is experimentally unknown and therefore the A_{fb} has to be calculated e.g. in the Helicity frame as discussed in the previous section. This measured A_{fb}^{β} shown in figure 2.4(b), appears less pronounced than the true A_{fb} from figure 2.4(a). It is possible to correct the measured A_{fb}^{β} in order to recover the true A_{fb}. The correction is related to our knowledge of how well the boost vector is collinear with the incoming quark. It is common to expect that on average, the dilepton boost vector will be collinear with the incoming quark rather than the incoming anti-quark, which originates entirely from the sea and thus is less energetic on average. However, this is not always the case for every event. This can be demonstrated by looking on the probability, $\mathcal{P}(y_{\ell\ell})$, that the boost will be anti-parallel to the quark direction as a function of the dilepton rapidity, $y_{\ell\ell}$ (see figure 2.4(c)). The dilepton rapidity is closely related to the z-component of the boost which is the dominant component even in the presence of higher orders effects. For small values of $|y_{\ell\ell}|$ the determination of the true quark direction in the center of mass frame is less reliable. Since the momentum of the incoming quark and anti-quark are very close to each other, and then the more energetic one does not necessarily have to be the quark, there is a higher probability to get the wrong sign of $\cos\theta^*$. This $\mathcal{P}(y_{\ell\ell})$ can be calculated

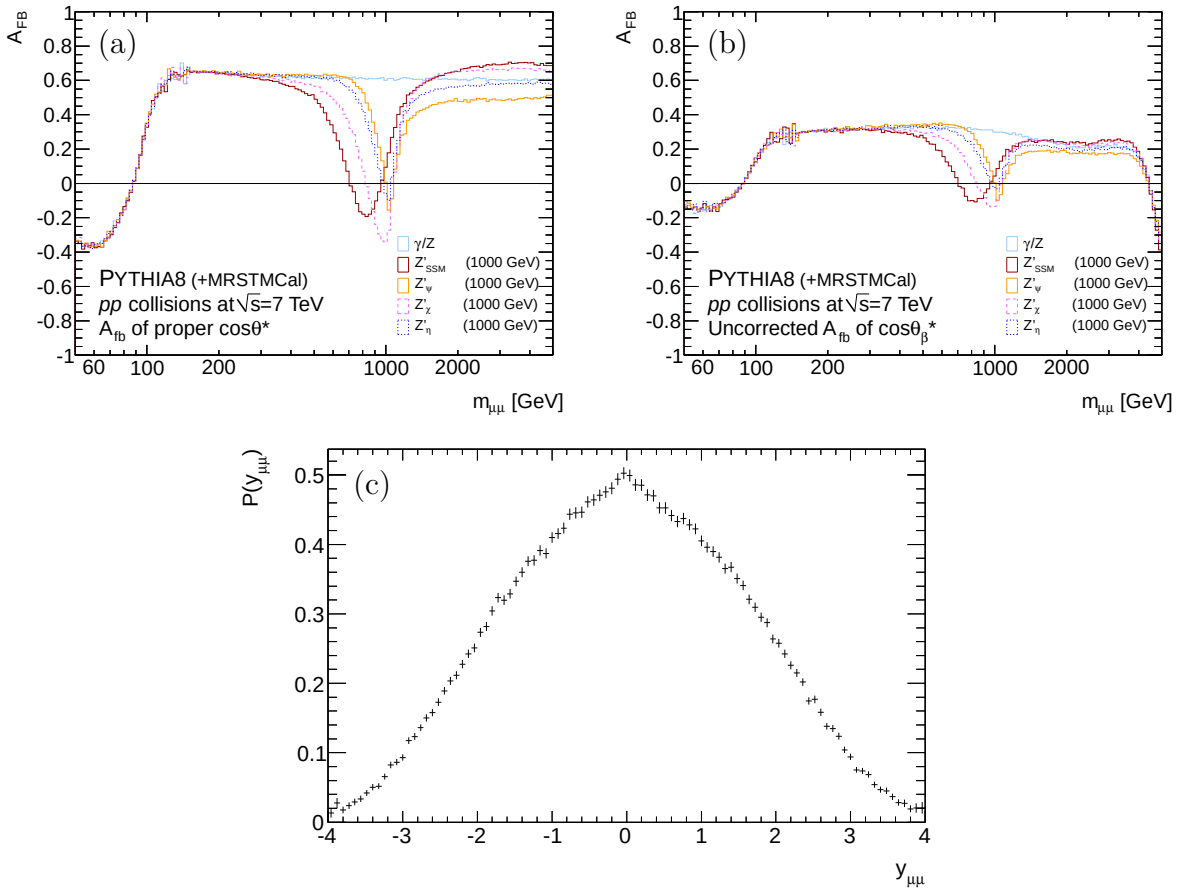

Figure 2.4.: The A_{fb} as calculated relative to the incoming quark direction in (a) and to the dilepton boost in (b) vs. the dimuon invariant mass of the DY, the Z'_{SSM} and few E_6 inspired Z's at $M_{Z'} = 1000$ GeV. Shown in (c) is the wrong $\cos\theta^*$ sign assignment probability. These figures are based on events generated with PYTHIA8 (LO) without any detector effects and selection cuts.

by dividing the MC $y_{\ell\ell}$ distribution for which the dilepton boost component along the true incoming quark direction is anti-parallel to the quark direction (i.e. when $\vec{\beta} \cdot \vec{p}_q \leq 0$), by the inclusive $y_{\ell\ell}$ distribution. The resulting $\mathcal{P}(y_{\ell\ell})$ can be seen in figure 2.4(c). It is clear that this probability should peak at $y_{\ell\ell} \simeq 0$ and that the peak value should be $\frac{1}{2}$ since without a boost there is a total uncertainty in determining the sign of $\cos\theta^*_\beta$. It is important to note that after detector reconstruction, $\mathcal{P}(y_{\ell\ell})$ is expected to have a slightly different shape than what is shown in figure 2.4(c) because mis-measurement of the muon tracks can affect both the measured $y_{\ell\ell}$ and the probability $\mathcal{P}$.

In practice, the A_{fb} can be extracted from a fit to the $\cos\theta^*_\beta$ distribution in bins of invariant mass (like the bins in e.g. figure 2.4), by first correcting for the experimental acceptance and efficiencies and then accounting for the $\cos\theta^*_\beta$ wrong sign assignment probability using the

following expression for events with a given $y_{\ell\ell}$ value,

$$\frac{1}{\sigma}\frac{d\sigma}{d\cos\theta^*_\beta}\left(\cos\theta^*_\beta|y_{\ell\ell}\right) = \frac{3}{8}\left(1+\cos^2\theta^*_\beta\right) + \left[1-2\mathcal{P}\left(y_{\ell\ell}\right)\right]A_{fb}\cos\theta^*_\beta. \tag{2.3.9}$$

It can be concluded that the effect of wrong $\cos\theta^*$ sign assignment can only reduce the "effective" asymmetry, defined on event-by-event basis as,

$$A^{\text{eff}}_{\text{fb}}\left(y_{\ell\ell}\right) = \left[1-2\mathcal{P}\left(y_{\ell\ell}\right)\right]A_{\text{fb}} \tag{2.3.10}$$

where the right-hand side is the true asymmetry (corresponding to figure 2.4(a)) multiplied by the wrong sign assignment factor, and where the left-hand side is the effective, uncorrected asymmetry as seen in figure 2.4(b).

The strong deviation of any of the Z' forward-backward asymmetries from the DY asymmetry seen in figure 2.4(a) and 2.4(b), can potentially serve as a discriminant measurable-quantity between a possible Z' and the DY process and also between the various Z' scenarios (although this is much further ambitious). It is also tempting to say that a DY-Z' discrimination can potentially happen using the A_{fb} measurement, even at masses below the Z' resonance mass, where the Z' itself might be beyond the experimental reach. However, this kind of precision measurement, is much more complicated to preform in a hadron collider. It also requires a much better understanding of the detector and in particular, its inherent geometrical and kinematic asymmetries. This knowledge is usually not needed in robust searches for deviation from the DY invariant mass shape. In addition, it requires a lot more data (than for a "simple" resonance search) in order to measure the asymmetry in the range of $m_{\ell\ell} \gtrsim 500$ GeV with sufficient precision, regardless of the new resonance model.

2.4. Higher dimensional models

2.4.1. Kaluza-Klein γ/Z excitations in five dimensions

In particle physics, the (3+1)-dimensional Minkowski spacetime is the underlying fundamental framework under which the laws of nature are formulated and interpreted. Early attempts to extend general relativity in order to unify gravity and electromagnetism within a common geometrical framework trace back to Gunnar Nordström (1914) [45], Theodor Kaluza (1921) and Oscar Klein (1926) [46, 47]. They proposed that unification of the two forces occurred when spacetime was extended to a five dimensional manifold and imposed the condition that

the fields should not depend on the extra dimension. A difficulty with the acceptance of these ideas at the time was a lack of both experimental implications and a quantum description of gravitational dynamics.

Today, one of the most striking requirements of modern string theory, which incorporates both gauge theories and gravitation, is that there must be six or seven extra spatial dimensions. Otherwise the theory is anomalous. Concepts developed within string theory have led to new phenomenological ideas which relate the physics of extra dimensions to observables in a variety of physics experiments.

These new theories have been developed to address the hierarchy problem, i.e., the large gap between the electroweak scale (where electroweak symmetry breaking occurs) and the traditional scale of gravity defined by the Planck scale ($M_{\rm P} \sim 10^{19}$ GeV).

The source of physics which generates and stabilizes this huge difference between the two scales is unknown and represents one of the most puzzling aspects of nature. The novel approach to this long-standing problem proposed in these recent theories is that the geometry of extra spatial dimensions may be responsible for the hierarchy: the gravitational field lines spread throughout the full higher dimensional space and modify the behavior of gravity.

The first scenario of this type to be proposed [48–50] suggested that the apparent hierarchy between these two important scales of nature is generated by a large volume of the extra dimensions, while in a later theoretical framework [34, 51] the observed hierarchy results from a strong curvature of the extra dimensional space. If new dimensions are indeed relevant to the source of the hierarchy, then they should provide detectable signatures at or slightly above the electroweak scale. These physics scenarios with additional dimensions hence afford concrete and distinctive phenomenological predictions for particle colliders.

The new dimensions must be sufficiently small such that these have escaped our detection so far. The compactification, where additional dimensions are considered to be compact manifolds of a characteristic size R (e.g. an n dimensional torus with common radius R), provides a mechanism which can successfully hide them.

Although gravity is not the main concern here, it can be easily demonstrated why n extra, flat dimensions with a large radius R can lower the gravitational scale. This observation [48–50] has triggered most of the research on extra dimensions over the past 10-15 years. At distances small compared to R, the gravitational potential simply changes according to the Gauss law

in $n+4$ dimensions, i.e.,

$$V(r) \sim \frac{m_1 m_2}{M_G^{n+2}} \frac{1}{r^{n+1}} \tag{2.4.1}$$

where $r \ll R$ and M_G is the true gravitational scale to be distinguished from the Planck Scale M_{P}. At $r \gg R$, the potential again looks effectively four-dimensional, i.e.,

$$V(r) \xrightarrow{r \gg R} \frac{m_1 m_2}{M_G^{n+2}} \frac{1}{R^n r} = \frac{m_1 m_2}{M_{\mathrm{P}}^2} \frac{1}{r} \tag{2.4.2}$$

Hence, one finds the important relation among the parameters M_{P}, M_G and R,

$$M_{\mathrm{P}}^2 = M_G^{n+2} R^n \tag{2.4.3}$$

The apparent weakness of gravity is not due to the enormity of the Planck scale M_{P} but due to the presence of a large volume factor R^n. As a result, the true fundamental gravity scale M_G can be much smaller than M_{P}. Thus, the so-called gauge hierarchy problem is solved if M_G is of the order of the electroweak scale. For example, extra dimensions of size,

$$R \sim \frac{1}{M_G} \left(\frac{M_{\mathrm{P}}}{M_G} \right)^{\frac{2}{n}} \sim \begin{cases} \mathcal{O}(1 \text{ mm}) & \text{if } n = 2 \\ \mathcal{O}(10 \text{ fm}) & \text{if } n = 6 \end{cases} \tag{2.4.4}$$

are needed for M_G in the TeV range.

Although the original hierarchy problem disappears in this setup, the question arises why there is another physical scale which is also pretty remote from the electroweak scale and set by the compactification radius around a mm.

Let us now turn to the SM of particle physics in the context of extra dimensions. A mm size extra dimension for the photon is excluded by experiment. An electromagnetic potential in analogy to equation 2.4.1 is clearly falsified by atomic physics. Nevertheless, there is a possibility to embed the SM in such an extra-dimensional setup again provided by string theory. In string theory, there is the concept of branes which allow to locate degrees of freedom in a subspace of the full space-time [48–50, 52–55]. Hence, it is possible to have gravity propagating in large extra dimensions, while the SM is confined to a brane and hardly affected until gravity becomes strong in or beyond the TeV region.

As the mentioned branes may be higher-dimensional as well, in addition to gravitons the SM fields could also propagate within at least a single extra dimension. No matter if the gravi-

tational scale is not around the experimental corner at the TeV-scale, nature could reveal an extra dimension populated by SM fields already in the LHC. An extra dimension reflects itself in a tower of heavy copies of any bulk field, i.e. any field propagating in the extra dimension. The masses of these so-called Kaluza-Klein (KK) modes are found to be multiples of the compactification scale $M_{\mathrm{KK}} = 1/R$ in the simplest models. Consequently, the extra dimension becomes visible when the heavy particles can be produced in high-energy experiments or at least leave their fingerprints in observables.

This work concentrates on the possibility of a single extra dimension to avoid problems in models with more than five dimensions. In six or more dimensions, already tree-level amplitudes are generally not well-defined because the infinite sums over diagrams, where towers of KK modes are exchanged, diverge. Thus, an explicit cut-off has to be introduced.

The simplest 5D extension of the SM uses the simplest orbifold S^1/Z_2 which possesses two branes where parts of the SM spectrum can be localized. After compactifying the extra dimension on S^1/Z_2, one obtains an effective 4-dimensional theory for the usual SM states and the corresponding infinite towers of massive KK modes. In the setup considered here, the fermionic matter content of the SM is localized on a brane, i.e. fermions live in the usual Minkowski space.

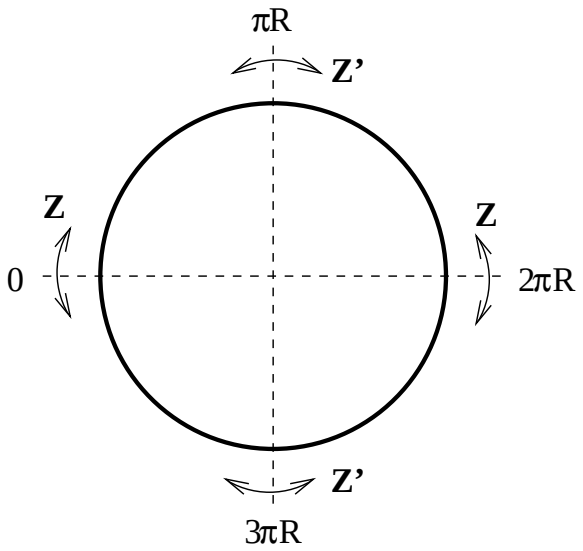

Figure 2.5.: The action of the two Z_2 reflections in the extended circle picture. The fundamental domain of the S^1/Z_2 orbifold is just the interval between 0 and πR, and the theory can be equivalently formulated on this line segment as well.

At this point, one can rephrase the introductory question in more physical terms: How large can a possible extra dimension in such a framework be so that it is not in conflict with present experimental data? Localized fermions are shown to couple to each KK mode of gauge

fields in the bulk. Hence, KK excitations mediate interactions between light SM fermions already at tree-level. These effective interactions imply that the compactification scale M_{KK} is constrained to lie in the TeV region.

The strength of the higher dimensional fields is an additional free parameter of the theory. Therefore, one has to reconsider the derivation of the effective 4D theory in the presence of these new terms. The spectrum of mass eigenstates and their coupling to fermions as well as the quantization procedure with an appropriate gauge fixing will be derived in the next subsection.

2.4.2. 5-Dimensional QED

The gauge part of the Lagrangian of 5-dimensional Quantum Electrodynamics (5D-QED) is given by,

$$\mathcal{L}(x,y) = -\frac{1}{4}F_{MN}(x,y)F^{MN}(x,y) + \mathcal{L}_{\mathrm{GF}}(x,y) \tag{2.4.5}$$

where,

$$F_{MN}(x,y) = \partial_M A_N(x,y) - \partial_N A_M(x,y) \tag{2.4.6}$$

denotes the 5-dimensional field strength tensor, and $\mathcal{L}_{\mathrm{GF}}(x,y)$ is the gauge-fixing term. The notation for the Lorentz indices and space-time coordinates is: $M,N = 0,1,2,3,5$; $\mu,\nu = 0,1,2,3$; $x = (x^0,\vec{x})$; and $y = x^5$ denotes the coordinate of the additional dimension [56].

In this case, the 5D gauge boson, A_M, will decompose into an infinite series of 4D gauge bosons $A_\mu^{(n)}$ and 4D scalars $A_5^{(n)}$ with index $n \geq 1$ as it will be shown shortly. Since there is a quadratic term mixing A_μ and A_5, one needs to add a gauge fixing term that eliminates this cross term [57].

The structure of the conventional QED Lagrangian is simply carried over to the five-dimensional case. The field content of the theory is given by a single gauge boson A_M transforming as a vector under the Lorentz group $SO(4,1)$. In the absence of the gauge-fixing, the 5D-QED Lagrangian from equation 2.4.5 is invariant under a $U(1)$ gauge transformation,

$$A_M(x,y) \longrightarrow A_M(x,y) - \partial_M \Theta(x,y) \tag{2.4.7}$$

Hence, the defining features of conventional QED are present in 5D-QED as well. So far, the spatial dimensions were treated on the same footing. To hide the additional dimension at low energies, the extra dimension has to be compactified, i.e., one has to replace the infinitely extended extra dimension by a compact object. The simplest compact one dimensional manifold is a circle, denoted by S^1, with radius R. However, compactification on a circle would introduce a massless scalar to QED. Hence, one should require an additional internal reflection symmetry Z_2 with respect to the origin $y = 0$. So, one is led to the so-called orbifold S^1/Z_2 (see figure 2.5) which turns out to be especially well suited for higher-dimensional physics. The extra dimensional coordinate y runs only from 0 to $2\pi R$ where these two points are identified. Moreover, according to the Z_2 symmetry, the points y and $-y = 2\pi R - y$ are identified in the following sense: knowing the field content for the segment $y \in [0, \pi R]$ implies the knowledge of the whole system. In other words, each 5D field has a particular Z_2 parity, so it is either even or odd with respect to the extra dimension. The fixed points $y = 0$ and $y = \pi R$, which do not transform under Z_2, are also called boundaries of the orbifold.

Thus, the compactification on S^1/Z_2 is reflected in restrictions for the fields. The above property of gauge symmetry leads to additional constraints. In order to meet all requirements, one has demand the fields to satisfy the following equalities:

$$\begin{aligned} A_M(x,y) &= A_M(x, y + 2\pi R) \\ A_\mu(x,y) &= A_\mu(x, -y) \\ A_5(x,y) &= -A_5(x, -y) \\ \Theta(x,y) &= \Theta(x, y + 2\pi R) \\ \Theta(x,y) &= \Theta(x, -y) \end{aligned} \tag{2.4.8}$$

The field $A_\mu(x, y)$ is taken to be even under Z_2, so as to embed conventional 4D-QED with a massless photon into the 5D-QED. Notice that the reflection properties of the field $A_5(x, y)$ and the gauge parameter $\Theta(x, y)$ under Z_2 in equation 2.4.8 follow automatically if the theory is to remain gauge invariant after compactification.

Making the periodicity and reflection properties of $A_\mu(x, y)$ and $\Theta(x, y)$ in equation 2.4.8 explicit, one can expand these quantities in Fourier series as,

$$\begin{aligned} A^\mu(x,y) &= \tfrac{1}{\sqrt{2\pi R}} A^\mu_{(0)}(x) + \sum_{n=1}^{\infty} \tfrac{1}{\sqrt{\pi R}} A^\mu_{(n)}(x) \cos\left(\tfrac{ny}{R}\right) \\ \Theta(x,y) &= \tfrac{1}{\sqrt{2\pi R}} \Theta_{(0)}(x) + \sum_{n=1}^{\infty} \tfrac{1}{\sqrt{\pi R}} \Theta_{(n)}(x) \cos\left(\tfrac{ny}{R}\right) \end{aligned} \tag{2.4.9}$$

where the Fourier coefficients $A^{\mu}_{(n)}(x)$ are the so-called Kaluza-Klein (KK) modes. The extra component A^5 of the gauge field is odd under the reflection symmetry and its expansion is given by,

$$A^5(x,y) = \sum_{n=1}^{\infty} \frac{1}{\sqrt{\pi R}} A^5_{(n)}(x) \sin\left(\frac{ny}{R}\right) \tag{2.4.10}$$

Note that for A^5 there is no zero mode, a phenomenologically important fact.

Using equations 2.4.9 and 2.4.10, one can now derive an effective 4D field theory for the four-dimensional fields, the KK modes. The dependence of the Lagrangian density on the extra coordinate y is parameterized by simple Fourier functions so that it can be completely removed by integrating out the extra dimension. From now on, the quantity of interest will be,

$$\mathcal{L}(x) = \int_0^{2\pi R} \mathcal{L}(x,y)dy \tag{2.4.11}$$

where in $\mathcal{L}(x)$ the higher-dimensional physics is reflected by the infinite tower of KK modes for each field component. A simple calculation yields,

$$\begin{aligned} \mathcal{L}(x) = \; & -\tfrac{1}{4} F_{(0)\mu\nu} F^{(0)\mu\nu} \\ & -\tfrac{1}{4} \sum_{n=1}^{\infty} F_{(n)\mu\nu} F^{(n)\mu\nu} \\ & +\tfrac{1}{2} \sum_{n=1}^{\infty} \left[\left(\tfrac{n}{R} A_{(n)\mu} + \partial_\mu A_{(n)5} \right) \left(\tfrac{n}{R} A^{\mu}_{(n)} + \partial^\mu A_{(n)5} \right) \right] \\ & +\mathcal{L}_{\mathrm{GF}}(x) \end{aligned} \tag{2.4.12}$$

where $\mathcal{L}_{\mathrm{GF}}(x)$ is defined in analogy to equation 2.4.11. The first term in equation 2.4.12 represents conventional QED involving the massless field $A^{\mu}_{(0)}$. Note that the other vector excitations $A^{\mu}_{(n)}$ from the infinite tower of KK modes come with mass terms where their mass is an integer multiple of the inverse compactification radius. Therefore, a small radius leads to a large mass or compactification scale $M_{\mathrm{KK}} = 1/R$. It is this large scale which is responsible for the fact that an extra dimension, if it exists, has not yet been discovered yet. The extra dimension is, therefore hidden by its compactness.

Moreover, the absence of $A^5_{(0)}$ due to the odd Z_2 symmetry of $A^5(x,y)$ allows to recover conventional QED in the low-energy limit of the model. For $n \geq 1$, the KK tower $A^5_{(n)}$ for the additional component of the five-dimensional vector field mixes with the vector modes.

The Lagrangian in equation 2.4.12 is still manifestly gauge invariant under the transformation given in equation 2.4.7 which in terms of the KK modes reads,

$$\begin{aligned} A_{(n)\mu}(x) &\longrightarrow A_{(n)\mu}(x) + \partial_\mu \Theta_{(n)}(x) \\ A_{(n)5}(x) &\longrightarrow A_{(n)5}(x) + \tfrac{n}{R}\Theta_{(n)}(x) \end{aligned} \tag{2.4.13}$$

The gauge-fixing condition can be shown to take the form,

$$\mathcal{L}_{\mathrm{GF}}(x) = -\frac{1}{2\xi}\left(\partial^\mu A_\mu - \xi \partial_5 A_5\right)^2 \tag{2.4.14}$$

in the generalized R_ξ gauge [56, 58] where upon integration over the extra dimension, the terms mixing $A^\mu_{(n)}\partial_\mu A^5_{(n)}$ in equation 2.4.12 drop out apart from irrelevant total derivatives. Thus, the effective gauge-fixed four-dimensional Lagrangian of 5D-QED,

$$\begin{aligned} \mathcal{L}(x) = \; & -\tfrac{1}{4}F_{(0)\mu\nu}F^{(0)\mu\nu} - \tfrac{1}{2\xi}\left(\partial^\mu A_{(0)\mu}\right)^2 \\ & + \sum_{n=1}^{\infty}\left[-\tfrac{1}{4}F_{(n)\mu\nu}F^{(n)\mu\nu} + \tfrac{1}{2}\left(\tfrac{n}{R}\right)^2 A^\mu_{(n)}A_{(n)\mu} - \tfrac{1}{2\xi}\left(\partial^\mu A_{(n)\mu}\right)^2\right] \\ & + \sum_{n=1}^{\infty}\left[\tfrac{1}{2}\left(\partial^\mu A_{(n)5}\right)\left(\partial_\mu A_{(n)5}\right) - \tfrac{1}{2}\xi\left(\tfrac{n}{R}\right)^2\left(A_{(n)5}\right)^2\right] \end{aligned} \tag{2.4.15}$$

explicitly shows the different degrees of freedom in the model. Gauge-fixed QED is accompanied with a tower of its copies for massive gauge bosons. From this Lagrangian, it is seen that the corresponding propagators take on their usual form given in figure 2.6. From now on, the $A^5_{(n)}$ fields will be referred to as Goldstone modes.

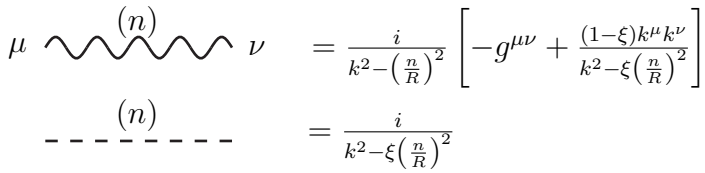

Figure 2.6.: Propagators for the gauge boson and Goldstone modes in 5D-QED

Having established the five-dimensional gauge sector, one should now introduce fermions. As mentioned above, the S^1/Z_2 orbifold has the feature that there are fixed points $y = 0$ and $y = \pi R$ not transforming under the Z_2 symmetry. Borrowing a concept from string theory, these special points can be considered as branes. The branes can host localized fields which cannot penetrate the extra dimension. Using this idea for the fermions, it can be formalized

by introducing a δ-function in the Lagrangian

$$\mathcal{L}_{\text{Fermions}}(x,y) = \delta(y)\bar{\Psi}(x)\left(i\gamma^{\mu}D_{\mu} - m_f\right)\Psi(x) \tag{2.4.16}$$

where the covariant derivative

$$D_{\mu} = \partial_{\mu} + ie_5 A_{\mu}(x,y) \tag{2.4.17}$$

contains the bulk gauge field A_{μ} and e_5 denotes the coupling constant of 5D-QED. The generalization for the usual $U(1)$ gauge-transformation properties of fermion fields reads,

$$\Psi(x) \longrightarrow e^{-ie_5\Theta(x,0)}\Psi(x) \tag{2.4.18}$$

Again integrating out the fifth dimension, one is are left with an effective four-dimensional interaction Lagrangian,

$$\mathcal{L}_{\text{Interaction}}(x) = -e\bar{\Psi}\gamma^{\mu}\Psi\left(A_{(0)\mu} + \sqrt{2}\sum_{n=1}^{\infty}A_{(n)\mu}\right) \tag{2.4.19}$$

which couples all KK modes to the fermion field on the brane (the fixed points). The coupling constant,

$$e = \frac{e_5}{\sqrt{2\pi R}} \tag{2.4.20}$$

is the QED coupling constant as measured by experiment. The factor $\sqrt{2}$ in equation 2.4.19 is a typical enhancement factor for the coupling of brane fields to heavy KK modes ($n \geq 1$) due to their wave-function normalization in equation 2.4.9.

Note that the scalar modes $A^5_{(n)}$ do not couple to brane fermions even if D^{μ} is replaced by D^M in equation 2.4.16 because their wave functions vanish at $y = 0$ according to the odd Z_2-symmetry. These interaction terms together with completely standard kinetic terms for the fermion field complete 5D-QED. The corresponding Feynman rules for the electron-photon vertex and the analogous interaction of the heavy KK modes are shown in figure 2.7.

To fully extend the standard model by an extra dimension one has to understand spontaneous symmetry breaking in this context in order to explain the fermion and gauge boson masses of the standard model particles. This will be briefly shown in section 2.4.3.

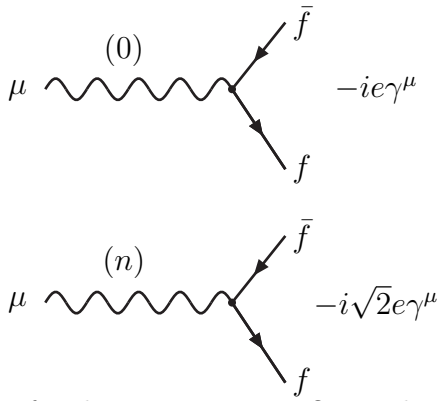

Figure 2.7.: Feynman rules for the vertices in 5D-QED where contrary to figure 2.2, the charge of fermion f (Q_f) is swallowed in the last definition of e.

An exemplary experimental signature of 5D-QED in experiments would be a series of s-channel resonances in lepton-pair production at colliders, as shown in figure 2.9(a) for a KK tower of the γ/Z bosons. The generic signatures of extra dimensions in the discussed setup are quite similar to figure 2.9, also in more realistic theories.

In this basic S^1/Z_2 setup with the fixed branes, the momentum is not conserved in the 5th dimension because the fermions are localized in the regular 4 dimensions. However, the "non-conservation" in each vertex of the interaction cannot be observed since the 5th dimension cannot be sensed. Note that in the overall process, i.e. looking on the two vertices, the momentum is conserved. If instead one allows also the fermions to move in the extra dimension, then there must be momentum conservation in 5D. In this universal extra dimension case, if one starts with momentum only in 4 dimensions (as in particle colliders) then it implies that the KK particles can only be produced in pairs (this is often called KK-parity). There are several models where the fermion fields are not constrained to the fixed branes ($y = 0, \pi R$) and the predictions of these models can be very different from the ones of the model considered here.

2.4.3. 5-Dimensional non-Abelian extension of the SM

In the following discussion, the minimal 5-dimensional extension of the SM compactified on an S^1/Z_2 orbifold will be briefly studied. It will be assumed that the chiral fermions are localized on a brane at the $y = 0$ fixed point of the S^1/Z_2 orbifold. The most frequently investigated model in the context of the S^1/Z_2 setup, is where all electroweak gauge fields propagate in the bulk and couple to both a brane and a bulk Higgs doublets. The Lagrangian

of the gauge-Higgs sector of this 5D SM is given by,

$$\begin{aligned}\mathcal{L}(x,y) = &-\frac{1}{4}\,B_{MN}\,B^{MN} \;-\; \frac{1}{4}\,F^{a}_{MN}F^{aMN} \;+\; (\,D_M\,\Phi_1\,)^\dagger\left(\,D^M\,\Phi_1\,\right)\\ &+\,\delta(y)(\,D_\mu\,\Phi_2\,)^\dagger\,(\,D^\mu\,\Phi_2\,) \;-\; V\,(\Phi_1,\Phi_2)\\ &+\,\mathcal{L}_{\rm GF}(x,y) + \;\mathcal{L}_{\rm FP}(x,y)\end{aligned} \tag{2.4.21}$$

where B_{MN} and F^a_{MN} ($a = 1,2,3$ for $SU(2)_L$) are the field strength tensors of the $U(1)_Y$ and $SU(2)_L$ gauge fields, respectively. In equation 2.4.21, the gauge-fixing term $\mathcal{L}_{\rm GF}$ and the induced Faddeev–Popov Lagrangian $\mathcal{L}_{\rm FP}$ can be determined as done e.g. in [56]. As usual, the covariant derivative D_M is,

$$D_M \;=\; \partial_M \;-\; i\,g_5\,A^a_M\,\tau^a \;-\, i\,\frac{g'_5}{2}\,B_M \tag{2.4.22}$$

where τ^a are the $SU(2)_L$ generators. The Higgs potential of this $SU(2)_L \times U(1)_Y$–bulk model is $V\,(\Phi_1,\Phi_2)$, where $\Phi_1(x,y)$ is a bulk Higgs doublet and $\Phi_2(x)$ a brane one. The most general Higgs potential allowed by gauge invariance is,

$$\begin{aligned}V(\Phi_1,\Phi_2) = &\;\mu_1^2\,(\Phi_1^\dagger\Phi_1) \;+\; \lambda_1\,(\Phi_1^\dagger\Phi_1)^2\\ &+\,\delta(y)\left[\,\frac{1}{2}\,\mu_2^2\,(\Phi_2^\dagger\Phi_2) \;+\; m_{12}^2\,(\Phi_1^\dagger\Phi_2) \;+\; \frac{1}{2}\,\lambda_2\,(\Phi_2^\dagger\Phi_2)^2\right.\\ &+\,\frac{1}{2}\,\lambda_3\,(\Phi_1^\dagger\Phi_1)(\Phi_2^\dagger\Phi_2) + \frac{1}{2}\,\lambda_4\,(\Phi_1^\dagger\Phi_2)(\Phi_2^\dagger\Phi_1) + \;\lambda_5\,(\Phi_1^\dagger\Phi_2)^2\\ &+\,\left.\lambda_6\,(\Phi_1^\dagger\Phi_1)(\Phi_1^\dagger\Phi_2) + \lambda_7\,(\Phi_2^\dagger\Phi_2)(\Phi_1^\dagger\Phi_2) + \;\text{h.c.}\,\right]\end{aligned} \tag{2.4.23}$$

Note that all terms involving the brane field Φ_2 are multiplied by a δ-function. Here, the discussion restricted to a CP-conserving Higgs sector, i.e. the parameters m_{12}^2, λ_5, λ_6 and λ_7 in equation 2.4.23 are real. Furthermore, it is assumed here that both complex scalar fields acquire real VEVs. After spontaneous symmetry breaking, the Higgs doublets will linearly be expanded about their VEVs, i.e.,

$$\Phi_1(x,y) = \begin{pmatrix} \chi_1^+ \\ \frac{1}{\sqrt{2}}\left(\,\frac{v_1}{\sqrt{2\pi R}} \;+\; h_1 \;+\; i\chi_1\right)\end{pmatrix}, \quad \Phi_2(x) = \begin{pmatrix} \chi_2^+ \\ \frac{1}{\sqrt{2}}\,(v_2 \;+\; h_2 \;+\; i\chi_2)\end{pmatrix} \tag{2.4.24}$$

The calculation steps for determining the particle mass spectrum of the $SU(2)_L \times U(1)_Y$-bulk model will not be repeated here, as they are analogous to those of the Abelian model discussed in the previous subsection. In fact, the above analogy in the derivation of the particle mass spectrum becomes rather explicit if the bulk gauge fields are written in terms of their higher-

dimensional mass eigenstates:

$$\begin{aligned} W_M^{\pm} &= \frac{1}{\sqrt{2}}\left(A_M^1 \mp i\, A_M^2\right), \\ Z_M &= \frac{1}{\sqrt{g_5^2 + g_5'^2}}\left(g_5\, A_M^3 - g_5' B_M\right) \\ A_M &= \frac{1}{\sqrt{g_5^2 + g_5'^2}}\left(g_5'\, A_M^3 + g_5 B_M\right) \end{aligned} \tag{2.4.25}$$

In this minimal 5D extension of the SM, it is assumed that all the SM fermions are localized at the $y = 0$ fixed point of the S^1/Z_2 orbifold. Therefore, upon integrating out the y dimension, both the effective kinetic terms of fermions and the effective Yukawa sector take on the usual 4D SM structure. Clearly, the SM fermions do not have KK modes. Under a gauge transformation, the left- and right- handed fermions transform according to,

$$\begin{aligned} \Psi_L(x) &\longrightarrow \exp\left(i g_5\, \Theta^a(x,0)\, \tau^a + i g_5'\, Y^L\, \Theta(x,0)\right) \Psi_L(x) \\ \Psi_R(x) &\longrightarrow \exp\left(i g_5'\, Y^R\, \Theta(x,0)\right) \Psi_R(x) \end{aligned} \tag{2.4.26}$$

The corresponding covariant derivatives that couple the chiral fermions to the gauge fields are given by,

$$\begin{aligned} D_\mu^L &= \partial_\mu - i\, g_5\, A_\mu^a\, \tau^a - i\, g_5'\, Y^L\, B_\mu\,, \\ D_\mu^R &= \partial_\mu - i\, g_5'\, Y^R\, B_\mu\,. \end{aligned} \tag{2.4.27}$$

It can be shown that the effective coupling of a fermion to a gauge boson which is restricted to the same brane $y = 0$ has its SM value. On the other hand, the effective interaction Lagrangian describing the coupling of a fermion to a gauge boson living in the bulk has the generic form,

$$\mathcal{L}_{\rm int}(x) = \overline{\Psi}\,\gamma^\mu\left(g_V + g_A\gamma^5\right)\Psi\left(A_{(0)\mu} + \sqrt{2}\sum_{n=1}^{\infty} A_{(n)\mu}\right). \tag{2.4.28}$$

Again, the coupling parameters g_V and g_A are set by the quantum numbers of the zero KK gauge mode and receive their SM values. Because the KK mass eigenmodes generally differ from the Fourier modes, their couplings to fermions $g_{V(n)}$ and $g_{A(n)}$ have to be calculated for each model individually by taking into account the appropriate weak-basis transformations. The masses, couplings and Feynman rules for the interactions of the KK gauge mass eigen-

modes to fermions and the propagators for the KK gauge in the R_ξ gauge can be found in [56].

There are some attempts to utilize the extra dimension itself for spontaneous symmetry breaking [57, 59] in order to explain the fermion and gauge boson masses of the standard model particles.

2.4.4. The sequential standard model in 5 dimensions

Hereafter, only the sequential standard model scenario will be considered, based on the non-Abelian case for the $SU(2)_L \times U(1)_Y$–bulk model in the S^1/Z_2 setup that was presented in section 2.4.3. The SSM simplification here practically reduces to the assumption of SM-like couplings and a simplified form of the KK masses. The assumption on the couplings will be somewhat generalized in the limit setting procedure where the couplings will still have the SM-like structure but will be allowed to scale (see section 8). For the masses of the heavy neutral KK gauge bosons, it is usually assumed that,

$$M^2_{\gamma^{(n)}_{\rm KK}/Z^{(n)}_{\rm KK}} = M^2_{\rm SM} + \left(\frac{n}{R}\right)^2 = M^2_{\rm SM} + n^2 M^2_{\rm KK} \tag{2.4.29}$$

where for the SM($n = 0$) γ or Z, the masses are $M_{\rm SM} = 0$ and $M_{\rm SM} = M_Z$ respectively. Note that the exact features of the $SU(2)_L \times U(1)_Y$–bulk model in the S^1/Z_2 setup can be found in [56].

The LO KK tower diagram for the non-Abelian case for the $SU(2)_L \times U(1)_Y$ group, in terms of the $L - R$ couplings for a $q\bar{q}$ initial state and an $\ell^+\ell^-$ final state manifests as shown in figure 2.8.

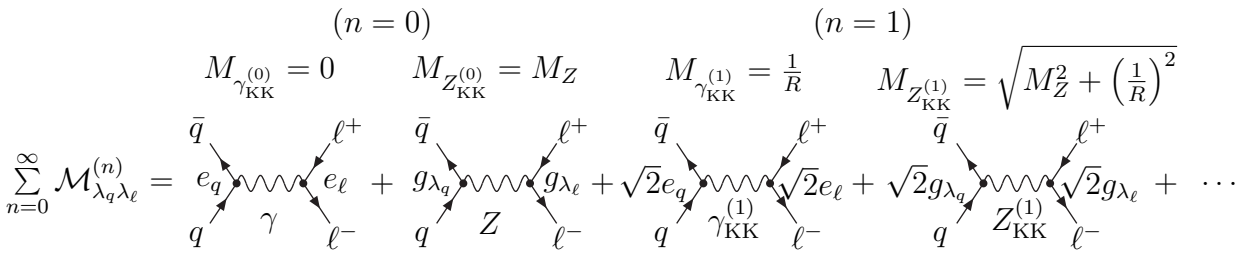

Figure 2.8.: The KK excitations tower of the gauge bosons γ/Z starting from the 0^{th} SM state. Note the couplings and masses (which affect also the widths) of each level.

For $n > 0$, the KK amplitude, $\mathcal{M}^{(n)}_{\lambda_q\lambda_\ell}$, has the same form as in equation 2.2.10, i.e.,

$$\mathcal{M}^{(n>0)}_{\lambda_q\lambda_\ell} = \frac{2Q_qQ_\ell}{\hat{s} - M^2_{\gamma^{(n)}_{\rm KK}} + iM_{\gamma^{(n)}_{\rm KK}}\Gamma_{\gamma^{(n)}_{\rm KK}}} + \frac{2g^q_\lambda g^\ell_\lambda / \sin^2\theta_W \cos^2\theta_W}{\hat{s} - M^2_{Z^{(n)}_{\rm KK}} + iM_{Z^{(n)}_{\rm KK}}\Gamma_{Z^{(n)}_{\rm KK}}} \tag{2.4.30}$$

and where the $n = 0$ term is identical to the equation 2.2.10 replacing s with $\hat{s}$ which is the square of the invariant mass of the $q\bar{q}(\ell^+\ell^-)$ system, ignoring the effect of initial and final state radiation (ISR and FSR). The incoming(outgoing) helicities notation, $\lambda_q(\lambda_\ell)$, is the same as before and $\Gamma_{X^{(n)}_{\rm KK}}$ is the total width of the $n^{\rm th}$ KK excitation for $X = \gamma, Z$. The partial decay widths in LO are:

$$\begin{aligned}
\Gamma_{Z^{(n)}_{\rm KK}\to F\bar{F}} &= \frac{N^F_C\alpha_{em}}{6} M_{Z^{(n)}_{\rm KK}} \left(\left|\sqrt{2}g^F_R\right|^2 + \left|\sqrt{2}g^F_L\right|^2 \right) \frac{1}{\sin^2\theta_W\cos^2\theta_W} \\
\Gamma_{\gamma^{(n)}_{\rm KK}\to F^+F^-} &= \frac{N^F_C\alpha_{em}}{6} M_{\gamma^{(n)}_{\rm KK}} 2 \left(\sqrt{2}Q_F\right)^2 \frac{1}{\sin^2\theta_W\cos^2\theta_W}
\end{aligned} \tag{2.4.31}$$

and where Q_F and $g^F_{L/R}$ are the SM couplings to fermions of the γ and Z respectively (see equation 2.2.12). Like for the Z', possible decays such as $Z^{(n)}_{\rm KK} \to W^+W^-$ are ignored here and and the sum runs only on the SM fermions including the neutrinos in the $Z^{(n)}_{\rm KK}$ case, and the top-quark pair in both cases.

This description (equations 2.4.30, 2.4.31 and figure, 2.8) is the basis for the study shown in [2], the implementation in Pythia8 for this process as done by myself and the interpretation of the ATLAS dimuon data described in this thesis.

2.4.5. Some KK observables

The discussion held in the section about the Z' observables, is mostly relevant also for the KK case in terms of the analysis setup. While the basic experimental analysis techniques should be the same in terms of selection, background, efficiencies etc., the interpretation is different due to several features that are very distinct from the Z' ones.

Like in the Z' case, there is a resonance but it is about twice as wide and also higher than any of the Z' resonances. This is due to the enhancement of the KK couplings by a factor of $\sqrt{2}$ and the appearance of the KK photon almost at the same mass. Perhaps, the most important feature of this class of models, is the strong destructive interference with the DY imposed by the presence of the KK photon (which does not appear in the Z' models) and the KK couplings structure. As mentioned in the introduction, this can serve as a discriminant feature in searches for deviations from the DY line-shape. The strong KK-DY interference

manifests itself at low invariant masses where at higher masses (above the first KK excitation), the rest of the KK tower appears as a series of equally-spaced resonances as can be seen in figure 2.9.

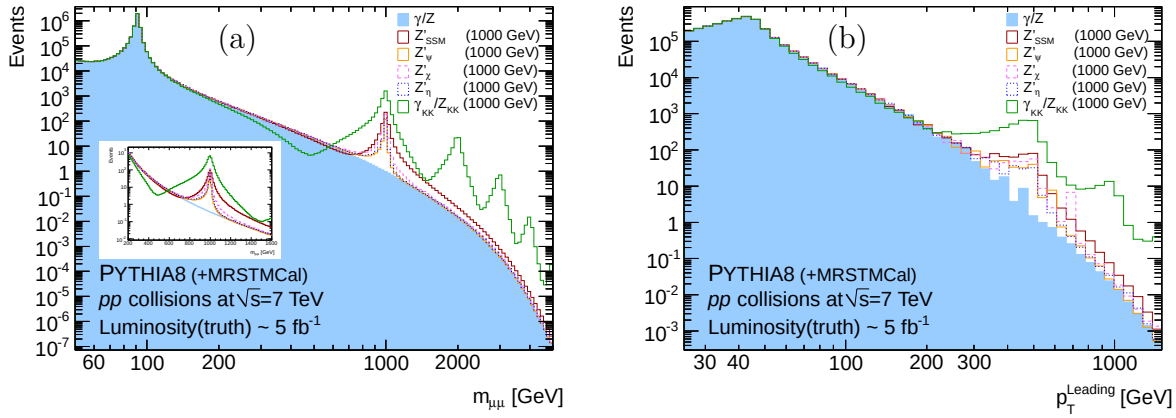

Figure 2.9.: The dimuon invariant mass distribution in (a) and the leading muon p_T distribution in (b) of the DY, KK, Z'_{SSM} and few E_6 inspired Z's at $M_X = 1000$ GeV. The samples are normalized to 5 fb^{-1} with no selection criteria or higher order corrections.

In the simplest S^1/Z_2 setup, the maximum destructive interference appears always exactly between the resonances - as can be seen in figure 2.9(a) for $M_{\mathrm{KK}} = 1000$ GeV, the maximum interference is at 500 GeV. At early stages of data taking in the LHC, this allows either to detect a possible negative deviation from the DY shape, or to set a strong limit on $M_{\mathrm{KK}} = 1/R$ in case the data are consistent with the DY shape.

The KK p_{T} distribution also shows the "shoulder" above 300 GeV as seen in the Z' case, but it is higher and there is a slight deficit with respect to the DY (and any of the Z's) between 60 GeV and 300 GeV.

Unlike for the Z' cases, the KK forward-backward asymmetry is consistent with the DY A_{fb} within the expected LHC measurement accuracy. This can be seen in figure 2.10.

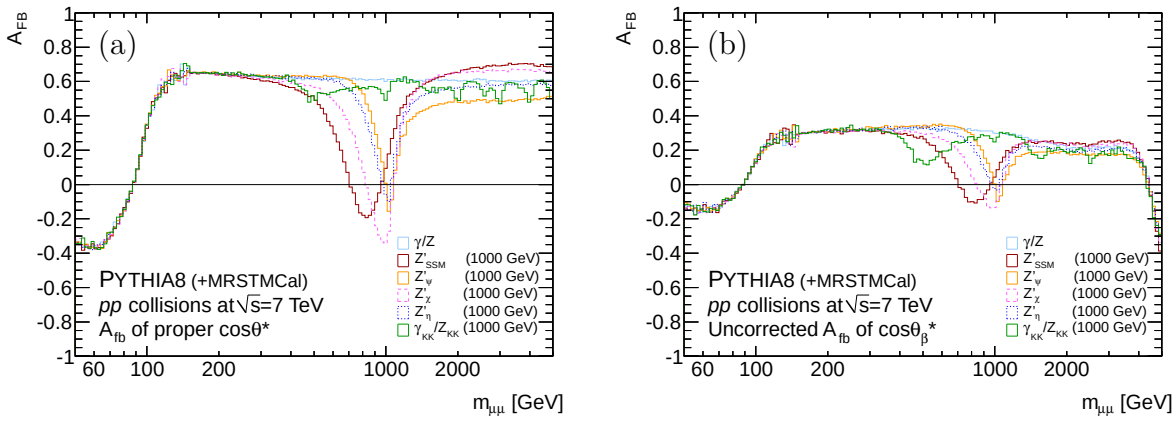

Figure 2.10.: The A_{fb} as calculated relative to the incoming quark direction in (a) and to the dilepton boost in (b) vs. the dimuon invariant mass of the DY, KK, Z'_{SSM} and few E_6 inspired Z's at $M_X = 1000$ GeV. These figures are based on events generated with PYTHIA8 (LO) without any detector effects and selection cuts.

Chapter 3.

Experimental setup

The LHC [60] at CERN near Geneva is the world's most powerful tool for Particle Physics research. It is a two-ring-superconducting-proton accelerator and collider installed in the existing 26.7 km tunnel (lying between 45 m and 170 m below the surface) that was constructed between 1984 and 1989 for the CERN LEP machine, see figure 3.1. There are two transfer tunnels, each approximately 2.5 km in length, linking the LHC to the CERN accelerator complex that act as injector. Around the LHC tunnel, Points 1 and 5 were built during the construction of the LHC for the two new general purpose detectors ATLAS and CMS, respectively, while those for ALICE and LHCb, at Points 2 and 8, respectively, were originally built for LEP.

3.1. The LHC machine

The LHC has two high luminosity experiments, ATLAS and CMS [61]. There are also two low luminosity experiments: LHCb [62] for B-physics, and TOTEM [63] for the detection of protons from elastic scattering at small angles. In addition to the proton beams, the LHC also operates with heavy ion beams and therefore, it has one dedicated heavy ion experiment, ALICE [64] for nominal lead-lead ion operation.

3.1.1. The LHC design

The LHC is designed to collide proton beams with a CM energy of 14 TeV and an unprecedented luminosity of 10^{34} $\mathrm{cm}^{-2}\mathrm{s}^{-1}$. The maximum total integrated luminosity per year is 80-120 fb^{-1}, assuming the machine can be operated for 200 days per year. The maximal

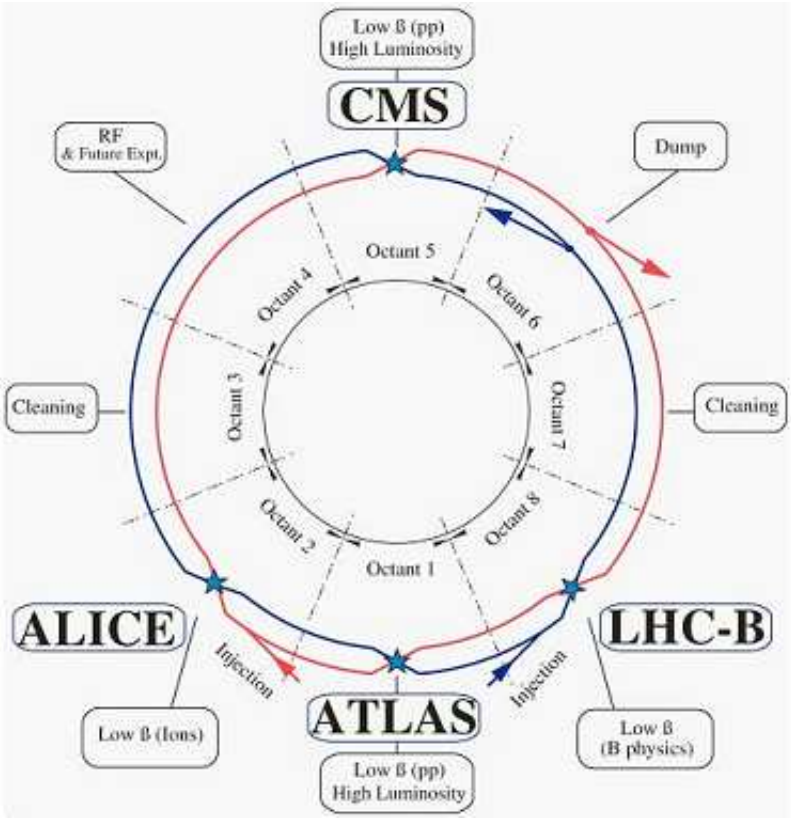

Figure 3.1.: Schematic layout of the LHC (Beam 1–clockwise, Beam 2–anti clockwise).

number of bunches instantaneously circulating at the tunnel is 2808 per beam (there are 3564 bunch slots), where the minimum nominal bunch spacing is 25 ns. This corresponds to a maximum bunch crossing frequency of 40 MHz. The maximum bunch intensity is $\sim 10^{11}$ protons per bunch. The peak beam energy depends on the integrated dipole field around the storage ring, which implies a peak dipole field of 8.33 T for the 7 TeV in the LHC machine. The LHC ring accommodates 1232 such main superconducting dipoles magnets to keep the beam circulating in it.

3.1.2. The LHC operation in 2011

During the *pp* running in 2011, the LHC operated at the nominal energy of 3.5 TeV for both beams. The nominal bunch spacing in 2011 proton run was 50 ns, i.e. every second slot was filled.

The number of injected bunches (at 450 GeV) varied from around 200 in early 2011 to 1380 during the final phases of the 2011 *pp* run. Typically, 95% of the bunches were colliding in

ATLAS. The average bunch intensities in normal physics operation evolved over the year from $\sim 1.0 \times 10^{11}$ to $\sim 1.6 \times 10^{11}$ protons per bunch. The beam current at the end of the year was around 300 mA and the peak luminosity in ATLAS was 3.5×10^{33} cm^{-2}s^{-1}. In 2011 the full beam crossing angle was 240 μrad in the vertical plane.

At the high-luminosity experiments the number of interactions is maximized by the "β-squeeze" (beam size), where in 2011 the value of β^* was 1.5 m initially and was reduced to 1.0 m in mid-September 2011. This resulting increase in luminosity typically leads to several proton-proton interactions occurring in the same bunch crossing. Consequently, every interaction which was registered by the detector is accompanied by several minimum bias events from the same bunch crossing (in-time pile-up) and previous bunch crossing (out-of-time pile-up). The in-time pileup results in additional reconstructed primary vertices. The increased average number of vertices can influence the efficiency of the event selection through the effect on lepton isolation criteria, measurement of the missing transverse energy, etc. The different β^* values in 2011 resulted in very different in- and out-of-time pile-up conditions throughout the year. The luminosity weighted average number of interactions per bunch crossing, $\langle\mu\rangle$, was 6.3 in the first half of the collected data and 11.6 in the second half.

In 2011, the integrated luminosity of the pp collisions at $\sqrt{s} = 7$ TeV, as recorded by ATLAS was 5 fb^{-1}. The total integrated luminosity as delivered by the LHC and as recorded by the ATLAS detector can be seen in figure 3.2. For a comparison, the previously running TEVATRON $p\bar{p}$ collider center of mass energy was 1.96 TeV and its integrated luminosity was almost 10 fb^{-1} [65].

3.2. Detecting challenges and benchmark physics

The high LHC luminosity and the resulting interaction rate are useful because of the small cross-sections expected for many of the benchmark physics processes. However, with an inelastic proton-proton cross-section of 80 mb at the design center of mass energy, the LHC will produce a total rate of 10^9 inelastic events/s at design luminosity [66]. This presents a serious experimental difficulty as it implies that every candidate event for new physics will on the average be accompanied by 23 interactions per bunch crossing, i.e. $\langle\mu\rangle$ twice as large as in 2011. The nature of proton-proton (pp) collisions imposes another difficulty. QCD jet production cross-section dominates over the rare processes. It is therefore more difficult select clean samples of these rare processes. Candidate events coming from rare processes can be identified mostly by the presence of isolated leptons or photons, and by momentum

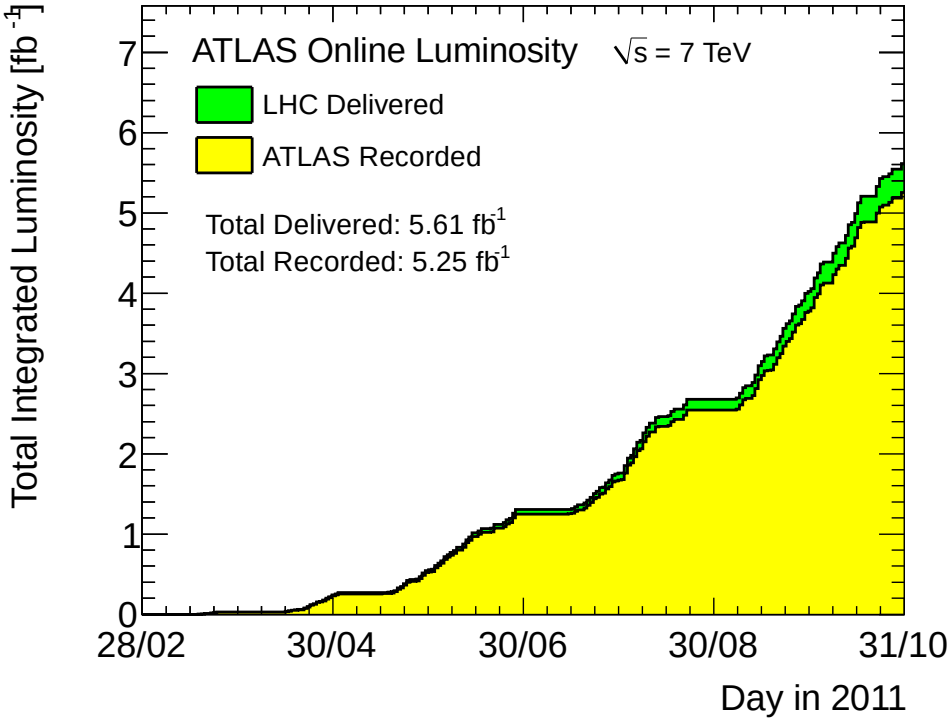

Figure 3.2.: Delivered and recorded luminosity for pp collisions at $\sqrt{s} = 7$ TeV , as seen by the LHC and ATLAS respectively in 2011.

imbalance in the transverse plane[1]. Tagging such experimental signatures characteristic of the physics processes in question in an event, requires an excellent separation between leptons, photons and hadrons. This is achieved by a high granularity of the detector, ensuring good angular separation between the leptons or the photon and the hadrons that are concentrated in the jets. It also requires hermetic coverage of calorimeters with high energy and position resolution. Viewed in this context, these benchmark physics goals can be turned into a set of general requirements for the LHC detectors.

Remarkably, until July 2012, the absence of direct experimental evidence for the existence of the Higgs boson and the importance of the search for it, were the first physics goals to be mentioned. However, in July 2012 it was announced independently by ATLAS [6] and CMS [7] that a standard model Higgs-like boson has been observed with mass of about 126 GeV at the level of 5σ. This discovery came in very early after the start of the LHC operation, with about only 5 fb^{-1} for 2011 ($\sqrt{s} = 7$ TeV) and 6 fb^{-1} in 2012 ($\sqrt{s} = 8$ TeV). This is now

[1] This kind of imbalance is a possible indication of an emission of a neutrino or a stable heavy neutral particle predicted by various theories beyond the standard model.

turned into a quest for confronting more data with the standard model predictions for the Higgs properties.

The LHC physics program is much wider than just the Higgs search and the study of its properties. A certainly non-exhaustive list of the physics scenarios and their characteristic signature in the detectors is given below.

New heavy gauge bosons W' and Z' could be accessible for masses up to $\sim$6 TeV. To study their leptonic decays, high-resolution lepton measurements and charge identification are needed in the transverse momentum, p_{T} range of a few TeV.

Another class of signatures of new physics may be provided by very high-p_{T} jets and high mass dijet measurements. As a benchmark scenario, quark compositeness has been used, where the signature would be a deviation in the jet cross-sections from the QCD expectations, at high energies.

The decays of hypothetical supersymmetric particles, such as squarks and gluinos, would involve cascades which, if R-parity is conserved, always contain the lightest supersymmetric particle (LSP) which is expected to be stable. As the LSP would interact very weakly with the detector, the experiment would measure a significant missing transverse energy, E_T^{miss}, in the final state. The rest of the cascade would result in a number of leptons and jets. In schemes where the LSP decays into a photon and a gravitino, an increased number of hard isolated photons is expected.

The emission of TeV-scale RS gravitons which escape into extra dimensions and therefore generate E_T^{miss} can also be tested.

Other experimental signature could be production of miniature black-holes decaying into a mixture of fundamental final states such as jets, leptons, photons, neutrinos, W's, and Z's and more.

In view of these possibilities, the multi-purpose detectors need to be able to measure the reconstructed particles with excellent momentum resolution, and they need to have a very fine granularity to be able to separate between adjacent particles emitted in near directions, and to have a low occupancy per channel to be able to detect the large number of emitted hadrons from the main process and from pile-up. In addition, the calorimeters need to have high energy and position resolution in order to obtain accurate measurements of electrons, photons, jets and E_T^{miss}.

3.3. The ATLAS detector

The coordinate system and nomenclature used to describe the ATLAS detector and the particles emerging from the pp collisions are briefly summarized here. The nominal interaction point is defined as the origin of the coordinate system, while the beam direction defines the z-axis and the $x-y$ plane is transverse to the beam direction. The positive x-axis is defined as pointing from the interaction point to the centre of the LHC ring and the positive y-axis is defined as pointing upwards. The side-A of the detector is defined as that with positive z and side-C is that with negative z. The azimuthal angle ϕ is measured around the beam axis, and the polar angle θ is the angle from the beam axis. The pseudorapidity is defined as $\eta = -\ln\tan\theta/2$ (in the case of massive objects such as jets, the rapidity $y = \frac{1}{2}\ln\frac{E+p_z}{E-p_z}$ is used). The transverse momentum p_{T}, the transverse energy E_{T}, and the missing transverse energy E_T^{miss} are defined in the $x-y$ plane unless stated otherwise. The distance ΔR in the pseudorapidity-azimuthal angle space is defined as $\Delta R = \sqrt{\Delta\eta^2 + \Delta\phi^2}$.

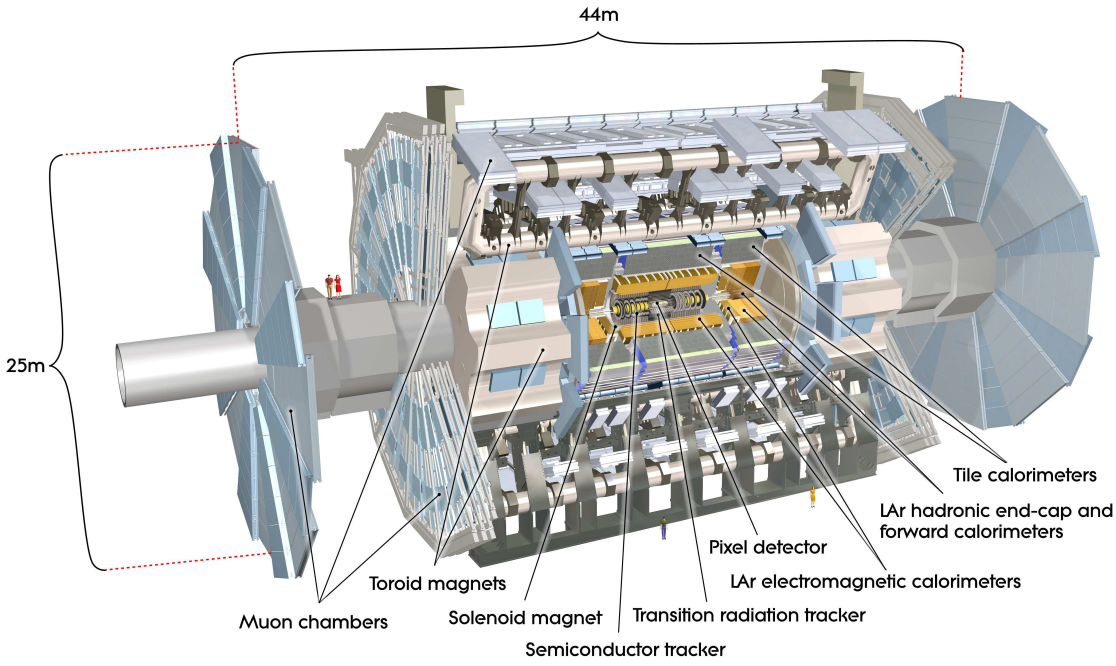

Figure 3.3.: Cut-away view of the ATLAS detector. The dimensions of the detector are 25 m in height and 44 m in length. The overall weight of the detector is approximately 7000 tones.

The overall ATLAS detector layout is shown in figure 3.3 [66]. Its shape is a 44 m long cylinder with a diameter of 25 m and it is nominally forward-backward symmetric with respect to the interaction point. Like most of its ancestors, it has an onion-like structure and it can be divided into three major sub-systems; the inner detector (ID), the calorimeters and the

muon spectrometer surrounding the calorimeters. The magnet configuration comprises a thin superconducting solenoid surrounding the ID cavity and supplying a 2 T magnetic field for the measurement of the track momentum in the ID, and three large superconducting air core toroids, one long barrel and two end-caps, arranged with an eight-fold azimuthal symmetry around the calorimeters and generating a strong bending power in a large volume within a light and open structure. This magnetic system is 22 m in diameter and 26 m in length, with a stored energy of 1.6 GJ.

As this work deals with high-p_{T} muons, then the emphasis in the remainder of this discussion will be on the muon spectrometer.

3.3.1. Inner detector

Approximately 1000 particles, on average, emerge from the collision point every bunch crossing within $|\eta| < 2.5$, creating a large track density in the detector. The benchmark physics processes impose a fine detector granularity to achieve high resolution measurements. The ATLAS ID is designed to provide hermetic and robust pattern recognition, excellent momentum resolution and both primary and secondary vertex measurements for charged tracks above a given p_{T} threshold (nominally $\sim$0.5 GeV) and within the pseudorapidity range $|\eta| < 2.5$. It also provides electron identification over $|\eta| < 2.0$ and a wide range of energies (between 0.5 GeV and 150 GeV). In the ID, the Pixel and silicon microstrip (SCT) trackers, used in conjunction with the straw tubes of the Transition Radiation Tracker (TRT), offer these features.

A detailed conceptual layout of the ID can be seen in figure 3.4. This layout will be of importance in the discussion on the muon identification and event selection in section 4.4.

3.3.2. Calorimetry

The calorimeters cover the range $|\eta| < 4.9$, using different techniques suited to the widely varying requirements of the physics processes of interest. The fine granularity of the electromagnetic (EM) calorimeter is ideally suited for precision measurements of electrons and photons. The coarser granularity of the rest of the calorimeter is sufficient to satisfy the physics requirements for jet reconstruction and E_T^{miss} measurements. The calorimeters closest to the beam-line are housed in three cryostats, one barrel and two end-caps. These calorimeters use liquid argon as the active detector medium. The precision electromagnetic calorimeters

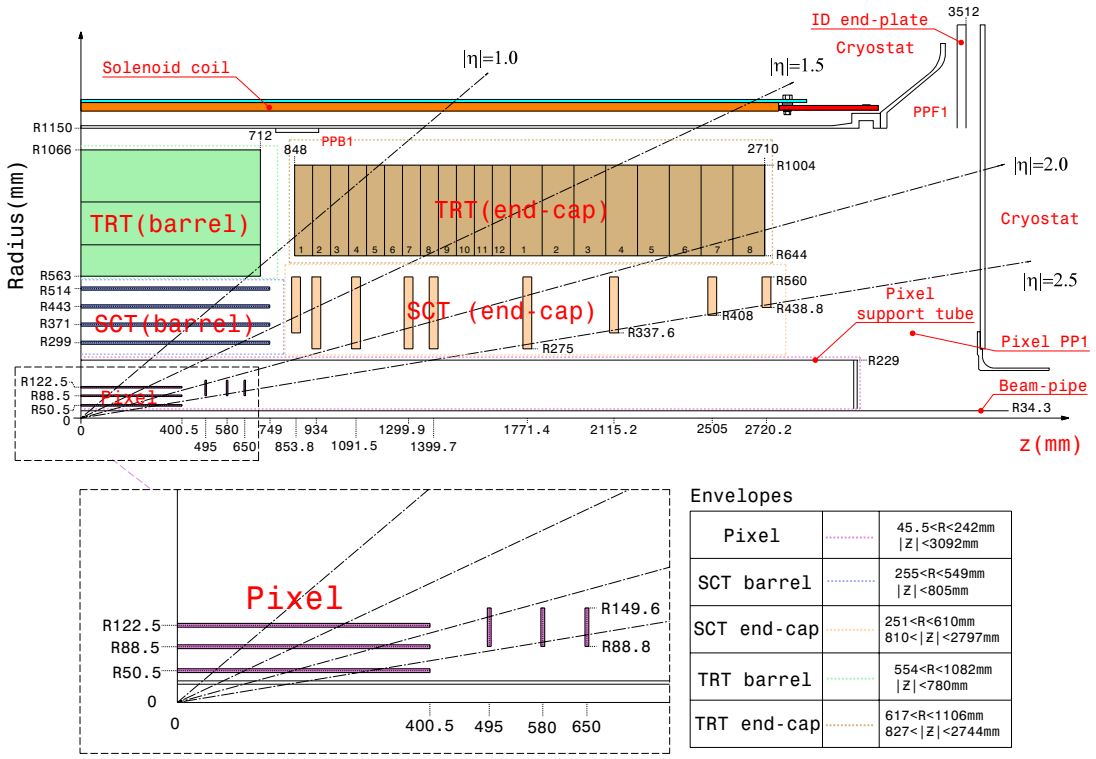

Figure 3.4.: Plan view of a quarter-section of the ATLAS inner detector showing each of the major detector elements with its active dimensions and envelopes. The labels PP1, PPB1 and PPF1 indicate the patch-panels for the ID services..

are lead-liquid argon detectors with accordion-shape absorbers and electrodes. This geometry allows the calorimeters to have several active layers in depth. For the outer barrel hadronic calorimeter, the sampling medium consists of scintillator tiles and the absorber medium is steel. The tile calorimeter is composed of three parts, one central barrel and two extended barrels. The choice of this technology provides maximum radial depth.

3.3.3. Muon spectrometer

The conceptual layout of the muon spectrometer is shown in figure 3.5 where a more detailed layout can be seen in figure 3.6. It is instrumented with high-precision tracking chambers measuring the coordinate in the bending plane, and separate trigger and second coordinate chambers. The muon spectrometer forms the outer part of the ATLAS detector and is designed to detect charged particles exiting the barrel and end-cap calorimeters. It is designed to measure the muons momentum in the pseudorapidity range $|\eta| < 2.7$ and to trigger on these in the region $|\eta| < 2.4$. The driving performance goal is a stand-alone transverse momentum resolution of approximately 10% for a 1 TeV muon, which translates into a sagitta along the z

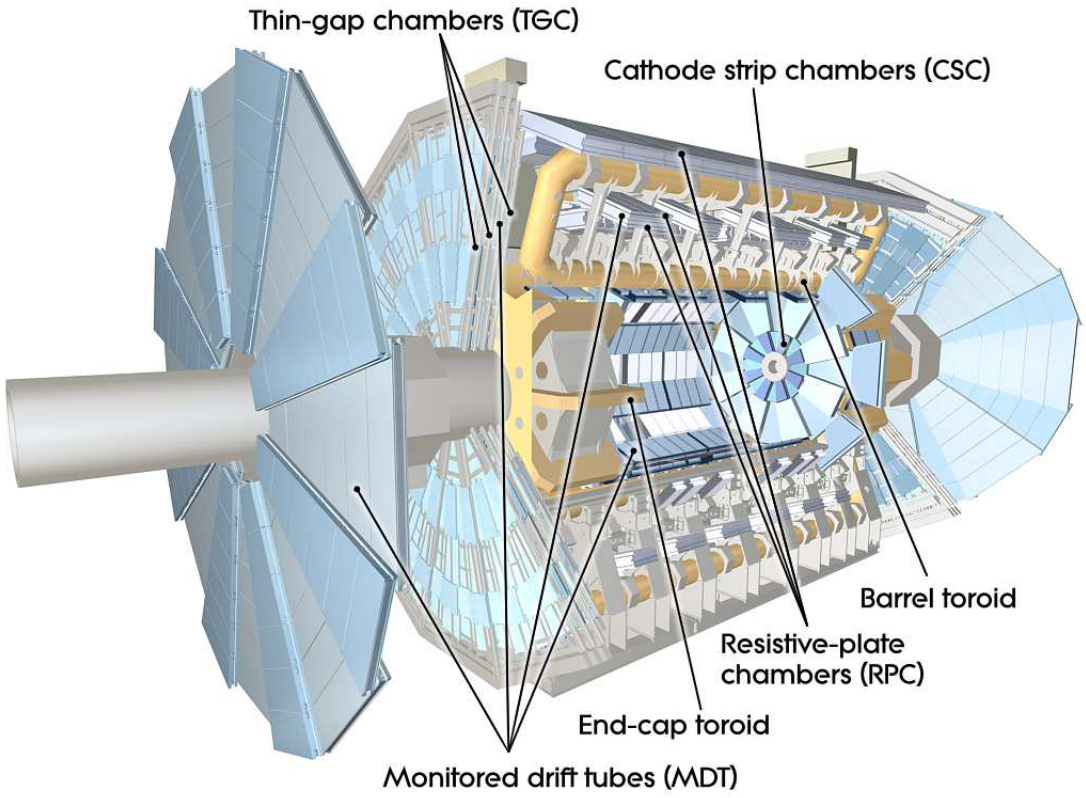

Figure 3.5.: Cut-away view of the ATLAS muon system.

(beam) axis of about 500 μm, to be measured with a resolution of ≤ 50 μm. Muon momenta down to a few GeV may be measured by the spectrometer alone. Even at the high end of the accessible range ($\sim$3 TeV), the stand-alone measurements still provide adequate momentum resolution and excellent charge identification.

A system of three large air-core toroids generates the magnetic field for the muon spectrometer. The performance in terms of bending power is characterized by the field integral $\int B \cdot dl$, where B is the field component normal to the muon direction and the integral is computed along an infinite-momentum muon trajectory, between the innermost and outermost muon-chamber planes. The barrel toroid provides 1.5 to 5.5 Tm of bending power in the pseudorapidity range $0 < \eta < 1.4$, and the end-cap toroids approximately 1 to 7.5 Tm in the region $1.6 < \eta < 2.7$. Multiple-scattering effects are thereby minimized, and excellent muon momentum resolution is achieved with three layers of high precision tracking chambers. This concept would be of importance later when the muon selection criteria will be discussed (see section 4.4).

Over most of the η-range, a precision measurement of the track coordinates in the principal bending direction of the magnetic field is provided by the monitored drift tubes (MDTs). At

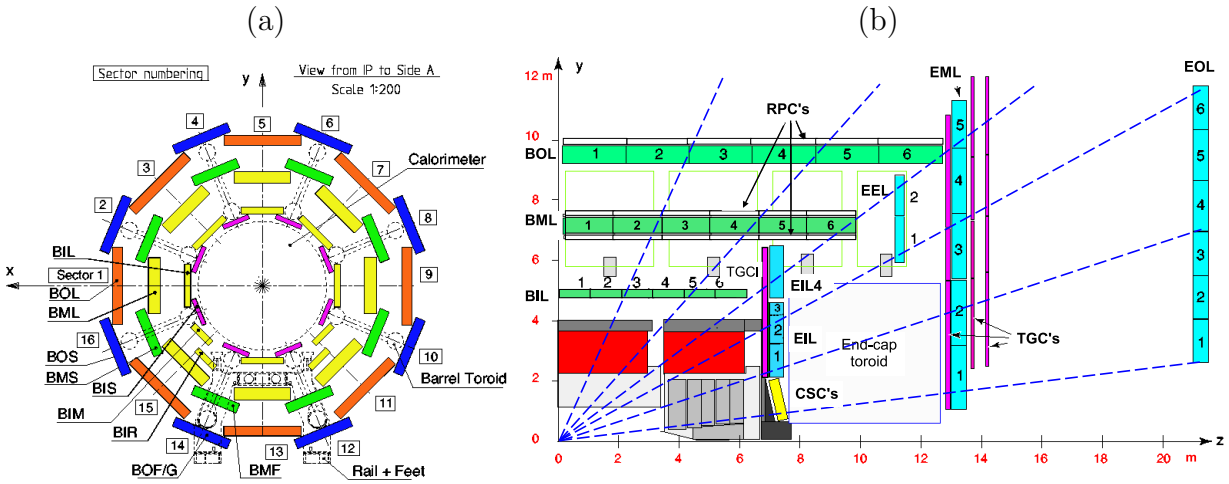

Figure 3.6.: In (a), The cross-section of the barrel muon system perpendicular to the beam axis (non-bending plane), showing three concentric cylindrical layers of eight large and eight small chambers. The outer diameter is about 20 m. In (b), the cross-section of the muon system in a plane containing the beam axis (bending plane). Infinite-momentum muons would propagate along straight trajectories which are illustrated by the dashed lines and typically traverse three muon stations.

large pseudorapidities, cathode strip chambers (CSCs) with higher granularity are used in the innermost plane over $2 < \eta < 2.7$, to withstand the demanding rate and background conditions. In the trigger system, resistive-plate chambers (RPC) are used in the barrel ($|\eta| < 1.05$) and thin-gap chambers[2] (TGCs) in the end-cap regions ($1.05 < \eta < 2.4$). The trigger chambers for the muon spectrometer serve a threefold purpose: provide bunch-crossing identification due to their excellent timing resolution, provide well-defined p_{T} thresholds for the trigger system, and measure the muon coordinate in the direction orthogonal to that determined by the precision-tracking chambers. Due to my work on the TGC subsystem, it will be described in more details in section 3.5.

3.4. Triggering and data acquisition

This triggering and data acquisition system will be described here in more details because it is the framework where the TGC online monitoring system is integrated (see appendix I).

The proton-proton interaction rate at the design luminosity of the LHC is approximately 1 GHz, while the event data recording, based on technology and resource limitations, is limited

[2]The TGCs were mainly constructed and tested in Israel

to about 200 Hz. This requires an overall rejection factor of 5×10^6 against minimum-bias processes, while maintaining maximum efficiency for new physics.

The trigger system has three distinct levels: L1 and the subsequent two levels, L2, and the event filter. The L2 and event filter together form the high-level trigger (HLT). Each trigger level refines the decisions made at the previous level and, where necessary, applies additional selection criteria. The data acquisition system receives and buffers the event data from the detector-specific readout electronics, at the L1 trigger accept rate, over 1600 point-to-point readout links. The first level uses a limited amount of the total detector information to make a decision in less than 2.5 μs, reducing the rate to about 75 kHz (limited by the bandwidth of the readout system). The two higher levels access more detector information and they provide the reduction to a final data-taking rate of approximately 200 Hz with an average event size (on disk) of approximately 1.5 Mb.

The L1 trigger uses the muon trigger chambers (TGC and RPC) to search for high p_T muons, and all the calorimeter sub-systems to search for electromagnetic clusters (electrons and photons), jets, τ-leptons (decaying into hadrons), E_T^{miss} and E_T^{total} (large missing and total transverse energy). Its selection is based on information from a subset of detectors. High transverse-momentum muons are identified using trigger chambers in the barrel and end-cap regions of the spectrometer. Calorimeter selections are based on reduced-granularity information from all the calorimeters. Decision results from the L1 muon and calorimeter triggers are processed by the Central Trigger Processor (CTP), which implements a trigger 'menu' made up of combinations of trigger selections. Events passing the L1 trigger selection are transferred to the next stages of the detector-specific electronics and subsequently to the data acquisition via point-to-point links. The trigger decision, together with the 40.08 MHz clock and other signals, is distributed to the detector front-end and readout systems via the Timing, Trigger and Control (TTC) system, using an optical-broadcast network.

An essential function of the L1 trigger is unambiguous identification of the bunch-crossing of interest. The very short (25 ns) bunch-crossing interval makes this a challenging task. In the case of the muon trigger, the physical size of the muon spectrometer implies times-of-flight exceeding the bunch-crossing interval. For the calorimeter trigger, a serious complication is that the width of the calorimeter signals extends over many (typically four) bunch-crossings.

While the trigger decision is being formed, the information for all detector channels has to be retained in pipeline memories. The L1 latency, which is the time from the pp collision until the L1 trigger decision, must therefore be kept as short as possible. The design of the trigger and front-end systems requires the L1 latency to be less than 2.5 μs, with a target latency of

2.0 μs. About 1 μs of this time is accounted for by cable-propagation delays alone. To achieve this aim, the L1 trigger is implemented as a system of purpose-built hardware processors.

While the L1 trigger decision is based only on the multiplicity of trigger objects (or flags indicating which thresholds were passed), information about the geometric location of trigger objects is retained in the muon and calorimeter trigger processors. Upon the event being accepted by the L1 trigger this information is sent to the L2 trigger as one or more regions-of-interest (ROIs). An ROI is the geographical coordinates in η and ϕ, of those regions within the detector where its selection process has identified interesting features. The ROI data include information on the type of feature identified and the criteria passed, e.g. a threshold. This information is subsequently used by the HLT system.

The L2 selection is seeded by the ROI information provided by the L1 trigger over a dedicated data path. L2 selections use, at full granularity and precision, all the available detector data within the ROIs (approximately 2% of the total event data). The L2 menus are designed to reduce the trigger rate to approximately 3.5 kHz, with an event processing time of about 40 ms, averaged over all events.

The final stage of the event selection is carried out by the event filter, which reduces the event rate to roughly 200 Hz. Its selections are implemented using offline analysis procedures within an average event processing time of the order of four seconds.

After an event is accepted by the L1 trigger, the data from the pipe-lines are transferred off the detector to the read-out drivers (RODs). Digitized signals are formatted as raw data prior to being transferred to the trigger data acquisition (TDAQ) system. The ROD's follow some general ATLAS rules, including the definition of the data format of the event, the error detection/recovery mechanisms to be implemented, and the physical interface for the data transmission to the DAQ system. The first stage of the DAQ, the readout system, receives and temporarily stores the data in local buffers. It is subsequently solicited by the L2 trigger for the event data associated to ROIs. Those events selected by the L2 trigger are then transferred to the event-building system and subsequently to the event filter for final selection. Events selected by the event filter are moved to permanent storage at the CERN computer center. In addition to the transfer of data, the data acquisition also provides for the configuration, control and monitoring of the hardware and software components which together provide the data-taking functionality.

3.5. The TGC subsystem

The TGC subsystem will be described in this section in more details to precede the discussion on the TGC online monitoring system in appendix I.

3.5.1. Overview of the TGC detector

Thin gap chambers operate on the principle of multi-wire proportional chambers and they provide good time resolution and high rate capability. The TGC chambers main characteristic is that the wire-to-cathode distance of 1.4 mm is smaller than the wire-to-wire distance of 1.8 mm. Their spatial resolution is mainly determined by the readout channel granularity, which can be adjusted to the needs by wire ganging. Crucial for the end-cap region of ATLAS is their larger rate capability of more than 20 kHz/cm^2. To reduce the probability of accidental triggers caused by random combinations of converted γ's, the coincidence condition in both types of trigger chambers is established separately in the η and ϕ-projection, a valid trigger requiring a coincidence of both. This also suppresses fake triggers from curling tracks, i.e. multi-MeV electrons from γ-conversions, spiraling in the magnetic field, potentially creating correlated hits in the trigger chambers.

The structure consists of wire planes (anode), cathode planes, strip planes, shields and honeycomb support structures. Two of the cladding copper layers in the triplet and doublets are segmented into readout strips to read the azimuthal coordinate (marked "Cu strips" in figure 3.7). On the outside of the triplet and doublet chambers the honeycomb stiffeners are covered by 0.5 mm thick plates for rigidity and mechanical protection. A gas volume containing a wire plane and two cathodes is called a chamber, while the entirety of three or two chambers in a triplet or doublet arrangement is called a unit. Figure 3.7 shows the cross-section of a TGC triplet and doublet.

The radial, bending coordinate is measured by the TGC wire groups, the azimuthal coordinate by the radial strips. The TGCs need fine granularity to provide a sufficiently sharp cut-off in the momentum of the triggering muon. To match the granularity to the required momentum resolution, the size of the wire groups varies from 6 to 31 as a function of η, corresponding to a variation in width from 10.8 mm to 55.8 mm. The alignment of wire groups in consecutive layers is staggered to optimize the position resolution for a given number of electronics channels. The radial strips are staggered in a similar way to achieve an azimuthal granularity of 2–3 mrad, as seen from the interaction point.

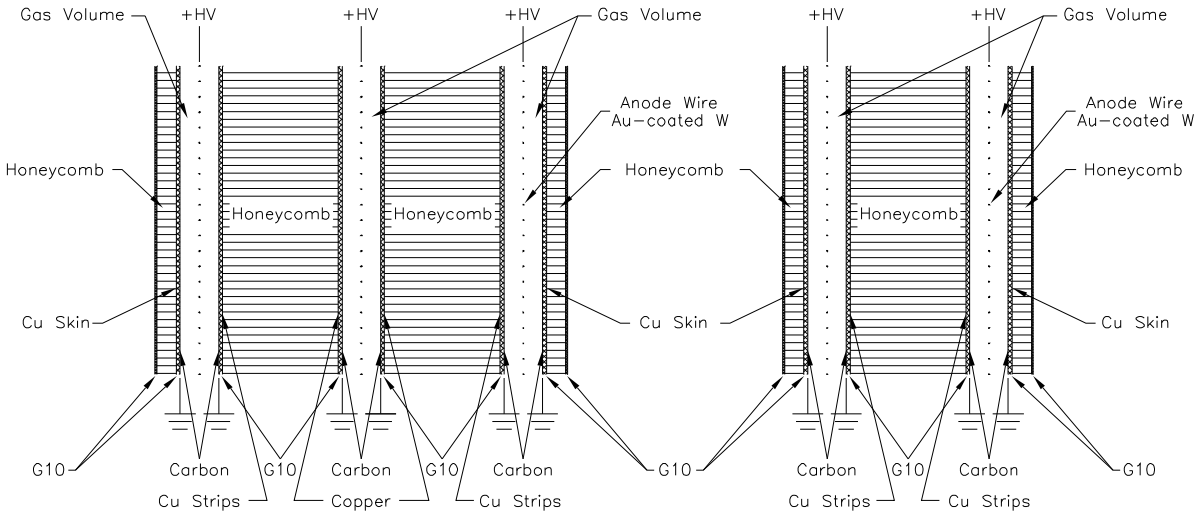

Figure 3.7.: Cross-section of a TGC triplet and doublet module. The triplet has three wire layers but only two strip layers. The dimensions of the gas gaps are enlarged with respect to the other elements.

The TGCs are arranged in nine layers of gas volumes grouped into four planes in z. The TGC inner station (I) at $|z| \sim 7$ m is segmented radially into two non-overlapping regions: end-cap (EI) and forward (FI), also known as the small wheel. At $|z| \sim 14$ m seven layers are arranged in one plane of triplet chambers (TGC1, closest to the interaction point) and two planes of doublet chambers (TGC2, TGC3). The doublet forming the plane farthest from the interaction point in each end-cap (TGC3) is referred to as the pivot plane, and its chamber layout and electronics are arranged such that, to a good approximation, there are no overlaps or holes in this plane.

The seven detector layers in the middle layers (big wheels, TGC1,TGC2,TGC3) are arranged in one triplet (TGC1) and two doublets(TGC2,TGC3). The triplet is to cope with false coincidences from background hits, which are more likely in the end-cap region than in the barrel. The trigger detectors, forming circular disks, are mounted in two concentric rings, an outer or end-cap one covering the rapidity range $1.05 \leq \eta \leq 1.92$ and an inner or forward one covering the rapidity range $1.92 \leq \eta \leq 2.4$. In the outer ring four or five chambers in triplet and doublets, respectively, are mounted in the way of a ladder forming modules. All TGCs in the big wheel are segmented into 12 sectors of 30° in the azimuthal direction. Thus, a sector in the outer ring comprises four modules of 7.5°, while the inner ring has two modules of 15°. Altogether there are 744 units in the big wheels, corresponding to 1704 chambers. The TGC wheel in the innermost layer has a slightly different geometrical structure, containing 45 units and 90 chambers on each side.

3.5.2. The muon trigger

The schematic layout of the trigger system is shown in figure 3.8. The trigger detectors must provide acceptance in the range $|\eta| \leq 2.4$ and over the full ϕ-range. The resolution requirements in barrel and end-cap are quite different. One obvious reason being that muon momenta, corresponding to a given p_{T}, are strongly increasing with η. At $|\eta| = 2.4$, for example, p is about 5.8 times larger than p_T, while the integrated bending power is only about twice the value as at $\eta = 0$. This leads to the necessity of an increased and η-dependent granularity in the end-cap trigger system, if the p_{T}-resolution is to match the one in the barrel. The fact that the three trigger layers in the end-cap are outside the magnetic field, seeing no curvature, and that their respective distances are smaller than the ones in the barrel (see figure 3.8) also calls for a finer granularity of the end-cap trigger readout. Furthermore, radiation levels in the end-cap region reach a factor of 10 higher than in the barrel.

The trigger in both the barrel and the end-cap regions is based on three trigger stations each. The basic principle of the algorithm is to require a coincidence of hits in the different trigger stations within a road, which tracks the path of a muon from the interaction point through the detector. The width of the road is related to the p_{T} threshold to be applied.

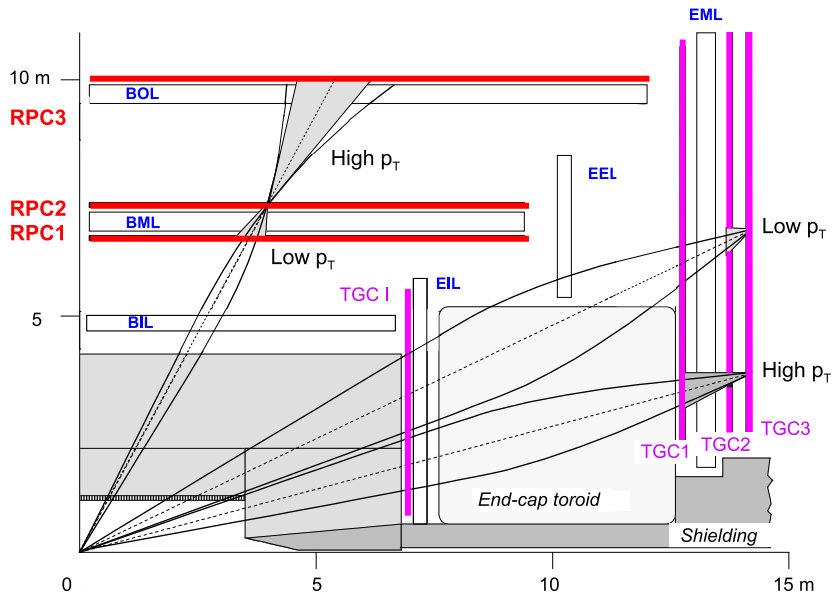

Figure 3.8.: Schematics of the muon trigger system. RPC2 and TGC3 are the reference (pivot) planes for barrel and end-cap, respectively.

In the end-cap, the three layers are in front (TGC1) and behind (TGC2 and TGC3) the second MDT wheel, while the fourth layer is located in front of the innermost tracking layer

(see figure 3.8). The trigger information is generated by a system of fast coincidences between the three last layers along the trajectory of the muon.

Each coincidence pattern corresponds to a certain deviation from a straight line, i.e. curvature of the track, which is used as a criterion for the track to have passed a predefined momentum threshold. The deviation from a straight line is the deviation of the slope of the track segment between two trigger chambers from the slope of a straight line between the interaction point and the hit in a reference layer called the pivot plane, which is the second layer in the barrel (RPC2) and the last layer in the end-cap (TGC3), as illustrated in figure 3.8. For the low- (high-) p_{T} trigger in the end-cap, for example, the slope between TGC3 and TGC2 (TGC1) is compared to the slope between the interaction point and TGC3. For the low- (high-) p_{T} trigger in the barrel, the slope between RPC2 and RPC1 (RPC3) is compared to the slope between the interaction point and RPC2.

A system of programmable coincidence logic allows concurrent operation with a total of six thresholds, three associated with the low-p_{T} trigger (threshold range approximately 6–9 GeV) and three associated with the high-p_{T} trigger (threshold range approximately 9–35 GeV). The trigger signals from the barrel and the muon end-cap trigger are combined into one set of six threshold multiplicities for each bunch-crossing in the muon to CTP interface, before being passed on to the CTP itself. Thus, the L1 muon trigger searches for patterns of hits consistent with low and high-p_{T} muons originating from the interaction region in the six independently-programmable p_{T} thresholds. The information (for each bunch-crossing) used in the L1 trigger decision is the multiplicity of muons for each of the p_{T} thresholds where muons are not double-counted across the different thresholds.

After sketching the TGC technology, structure and basic operation scheme, the online monitoring framework for the TGC subsystem can now be introduced. This framework is briefly discussed in appendix I.

3.6. ATLAS software

The ATLAS software version that was used for this analysis is labeled release 17.

3.6.1. The ATHENA framework

The ATLAS experiment is recording approximately 1 PB of data per year. The analysis of this enormous amount of data is a great challenge for the collaboration. To address this challenge a standard framework for simulation, reconstruction and physics analyses in ATLAS has been developed named ATHENA [67, 68]. It is an implementation of the component-based architecture responsible for handling the configuration and execution of several C++ packages through python scripts. It takes care of the execution order, data flow and persisting issues.

The data formats handled by ATHENA in the ATLAS event data model are the following:

- RAW data: contains the output of the ATLAS detector, produced by real or simulated events after the HLT. It comes in the "bytestream" format as they are delivered from the detector, rather than object-oriented format. The average size of each event is approximately 1.5 MB.
- Event summary data (ESD): holds the output of the reconstruction process. Both detector information and combined reconstruction objects like muons, electrons and jets are stored at this stage. An object-oriented format based on ROOT [69] objects is adopted, and the typical event size is 1 MB.
- Analysis object data (AOD): a subset of the ESD, with the physical objects used in analysis and few detector objects to allow track-refitting, isolation studies and others. The AOD is also stored in ROOT format and the nominal event size is of the order of 100 KB.
- Derived physics data (DPD): contains a small subset derived from the AOD / ESD, specific for an analysis or performance group. More than one derivation is possible, in which the data is reduced by removing unnecessary physics blocks (e.g. jets, photons etc.), selecting only some objects and dropping irrelevant information from those objects. User-data can be added in the process, and in the final stage of derivation a flat ROOT tuple can be produced.

In this analysis, the format used is a version of the last format in the list, i.e. the D3PD. The D3PD is essentially a flat ROOT ntuple.

3.6.2. ATLAS simulation

A fully detailed simulation of the ATLAS experiment [67] has been implemented using the GEANT4 [70] toolkit. The simulation program, built within the ATHENA framework, is being

used for large-scale production of events. The simulation software requires many components, ranging from generators packages for simulation of particle collisions, to packages simulating the response of the various detectors and triggers. All of these components are steered by the ATLAS simulation infrastructure. The simulation process is generally divided into three steps, (1) event generation (2) physics and detector response (3) digitization of physics quantities with production of final output.

The event generation is provided by about 40 different generators interfaced to the ATHENA framework, all of which are continually tuned and validated for physics performance. These generators cover a wide range of the LHC physics processes, as well as configurable "particle guns". Each event contains particles from a single interaction with vertex at the interaction point. All the beam properties are applied at a later stage before being passed through GEANT4. The physical construction parameters and conditions are contained in databases to allow an identical description for simulation digitization and reconstruction processes and they are connected at runtime.

A description of the full ATLAS detector has been made available to simulation. Misalignments in the realization of the detector, material distortions and extra materials are described as well. The ATLAS digitization software transforms the hits into detector responses. The peculiarities of each subdetector charge collection including cross-talk, electronic noise and channel-dependent variations are modeled in subdetector-specific digitization software. Dead channels and noise rate are read from a database to reproduce run-dependent conditions.

To simulate in-time pile-up, minimum bias events are simulated and added to the main event by mixing their hits. Other types of events such as beam-gas, beam-halo, cavern background (neutron haze) and out-of-time pile-up interactions from previous bunch crossings are also overlaid to the hard scattering events.

3.6.3. Flagging data for physics analysis

Since not all of the recorded collision data are "good" for physics analysis, it is essential to identify which collisions are good and which are not. To define a good collision, DQ information is needed, as assessed by the DQ group. The use of this DQ information in a physics analysis is done via the use of dedicated lists of runs and luminosity blocks, known as "good run lists" (GRLs). A luminosity block (LB) is the unit of time for data-taking, and lasts about two minutes. A good run list is formed by applying DQ criteria, and possibly other criteria, to the list of all valid physics runs and LBs. The DQ flags are simple indicators of data

quality, and act much like a traffic light. They are set per LB for each sub-detector and for each physics object. Each sub-system is responsible for filling in their DQ flags (see also appendix I). The most low-level flag, filled automatically, is based on detector control conditions (DCS), such as nominal voltages, temperature, humidity, etc. Detector sub-systems fill in flags at a number of different stages, flagging possible hardware and data-taking problems. Automatic "online" flags are set during data taking; these can be overwritten by the detector shifter at the ATLAS control room during data taking. To form a GRL, a query of DQ flags is required to be green, i.e. indicating good data. In a physics analysis, the requirement of good runs and luminosity blocks needs to be included in the event selection, to skip events from bad runs and luminosity blocks.

Chapter 4.

The experimental analysis

The basic steps of the experimental analysis are described in this chapter, where as mentioned earlier, the final muon results will be accompanied by the electron ones where appropriate.

The general motivation is the search for resonances such as Z' or a relatively low-mass $\gamma_{\rm KK}/Z_{\rm KK}$, or non-resonant deviations from the standard model in the $\mu^+\mu^-$ invariant mass spectrum due to the presence of a high-mass $\gamma_{\rm KK}/Z_{\rm KK}$ beyond the LHC reach. The most important feature in this study is the shape of the $m_{\ell\ell}$ distribution and its possible deviations from the expected DY and other backgrounds shape. Therefore, the event selection, the background estimations, the shape corrections and other considerations that will be presented later, are adjusted to obtain the most reliable shape information. In practice, this is realized in stringent requirements on the muon objects and relatively conservative systematic uncertainties. These result in a relatively low acceptance times efficiency (at the level of $\sim 40\%$). Such considerations will not necessarily be appropriate for precision measurements, e.g. a cross section measurement.

4.1. Data samples

The data sample used for this analysis was collected in 2011, and corresponds to an integrated luminosity of about 5.0 fb^{-1} (4.9 fb^{-1} for electrons). In general the format used for the analysis is the D3PD[1]. The "D3PD" is essentially a flat and compact ROOT [69] ntuple where almost all the event properties are kept while allowing various analyses to be done using this convenient format.

[1]The format is NTUP_SMWZ and the D3PDMaker tag is p716

The data used in the analysis span all periods from B through M of the 2011 data-taking (without period C). The data-taking periods and the corresponding run numbers are visualized in figure 4.2.

The GRL used is the one recommended by the muon combined performance (MCP) group. The data from the ntuple is further skimmed requiring the presence of at least one combined muon with $p_{\mathrm{T}} > 20$ GeV. All information in the ntuple is kept in the skimming. Muons from the following four categories were reconstructed:

- Combined muons reconstructed from tracks in both ID and MS;
- segment tagged muons to recover efficiency in poorly covered regions of the MS and at low transverse momenta;
- muon spectrometer stand-alone muons to extend the muon acceptance to $|\eta| < 2.7$[2];
- calorimeter tagged muons to recover efficiency in the region around $|\eta| \sim 0$ which is not covered well by the MS.

For the spectrometer-based types the MCP group considers both muon algorithm chains (*Staco* [71] or *Muid* [72]) suitable for physics analyses where for this analysis, only *Muid* combined muons have been used.

The luminosity as computed by the ATLAS luminosity calculator [73, 74] corresponding to the GRL used in the analysis is 5.0 fb^{-1}. The relative uncertainty on the luminosity scale is determined to be 3.7% [73].

4.2. Monte Carlo samples

All samples are generated and fully simulated (using GEANT [70]) in the ATHENA software framework, with reconstruction in release 17. Table 4.1 lists some of the relevant software tools/generators.

The MC samples were produced using 50 ns LHC bunch spacing, which is consistent with the bulk of the 2011 data. The detector and pile-up conditions varied in the simulation according to the real conditions[3] (details in table 4.2) and because of using two different generators for pile-up simulation: The MC bulk productions campaigns MC11a and MC11b used PYTHIA8

[2] an additional request on the number of muon chamber stations used in the track fit should be applied to achieve a reliable momentum measurement

[3] About half of the data (periods B to K) was taken with average number of interactions per crossing, $< \mu > \sim 6.3$ and the other half (periods L and M) was taken with $< \mu > \sim 11.6$.

Table 4.1.: Simulation software.

Program	Version	References
ATHENA	17	[67, 68]
PYTHIA6	6.425	[75]
PYTHIA8	8.1	[3]
HERWIG	6.520	[76, 77]
JIMMY	4.31	[78]
CompHEP	4.4.3	[79]
MadGraph	4	[80]
MC@NLO	4.01	[81]
ALPGEN	2.13	[82]

whereas MC11c used PYTHIA6, which reproduces the data better. The analysis is done with MC11c samples[4]. The ATLAS official 2011 pile-up re-weighting tool recovers the same

Table 4.2.: Pile-up simulation conditions. The integrated luminosities and fractions of data are computed with the EGamma GRL.

Period Name	L_{int} [pb^{-1}]	$\langle\mu\rangle$	fraction of data	fraction in MC11a	fraction in MC11b/c
B-D	181.2	low	3.7%	7%	3.3%
E-H	993.4	low	20.2%	41%	17.8%
I-K	1229.8	low	25.0%	41%	24.2%
L-M	2509.9	high	51.1%	10%	54.7%

distribution of the number of primary vertices in MC as measured in data.

4.2.1. Simulated background processes

The full list of simulated background samples is given in section A.3.

Drell Yan samples are generated with PYTHIA6 and, as all other PYTHIA6 samples, use the "ATLAS Underlying Event Tune 2B" (AUET2B) [83] and MRST2007LO** (LHAPDF set

[4] D3PDMaker tag p833

number 20651, also known as MRSTMCal) [35] parton distribution functions (PDFs). An inclusive $Z \to \mu^+\mu^-$ sample covering masses above 60 GeV is used. To ensure adequate statistics at high invariant mass (i.e. above 250 GeV), additional samples are generated in kinematic windows of the true dilepton invariant mass (150, 200 or 250 GeV-wide ranges, see details in appendix A.3), which are used instead of the high mass tail of the inclusive sample. The cross section calculation is detailed later (section 4.3.1). An inclusive $Z \to \tau\tau$ sample was also examined to show that its contribution is completely negligible.

The W + jets background is generated with ALPGEN to generate the hard process using the CTEQ6L1 [84] PDF set. The parton showering and hadronization are done by HERWIG and the multiple parton interactions is done by JIMMY using the AUET2 [85] tune.

Diboson samples are generated with HERWIG (same tune and PDFs as PYTHIA6) with a filter requiring at least one lepton. Additional samples are generated in two bins of high dilepton invariant mass using a lepton filter and a dilepton mass filter[5], in order to obtain enough statistics for masses above 400 GeV.

The $t\bar{t}$ background is generated with MC@NLO to generate the hard process using the CT10 [86] PDF set. The parton showering and hadronization are done by HERWIG and the multiple parton interactions is done by JIMMY using the AUET2 tune. The top mass is set to 172.5 GeV.

The $t\bar{t}$ and diboson samples have insufficient statistics, therefore their contribution to the dimuon invariant mass distribution is extrapolated for masses above 400 GeV and 1.4 TeV respectively. The details of this extrapolation and the associated systematic uncertainty are described in appendix B.

The QCD background was evaluated using a data-driven method (see section 4.7).

4.2.2. Simulated signal processes

Few fully simulated signal samples are used in the analysis, mainly for validation purpose. The full list of simulated signal samples is given in appendix A. For the limit-setting, two types of signal templates are made as described below.

[5] For the WW sample, both Ws are forced to decay leptonically, and for the WZ and ZZ samples, only one boson is forced to decay leptonically.

Fully simulated signal samples Small Z'_{SSM} signal samples are simulated for a few pole masses up to $M_{Z'_{\mathrm{SSM}}} = 2$ TeV (see table A.1). The PYTHIA6 generator is used, with full interference structure with the DY switched on. These samples have a generator level mass cut at half the resonance pole mass to restrict the lower mass range of the γ/Z. These samples are used for dedicated studies and for the figures whenever hypothetical signal is shown.

A single KK signal sample was simulated for $M_{\mathrm{KK}} = 2$ TeV using the PYTHIA8 generator [3] for validation purpose. The sample was generated in bins of (generator-level) dilepton invariant mass above $m_{\ell\ell} = 120$ GeV (see table A.2 in appendix A). This was enabled due to my implementation of the KK process in PYTHIA8.

Non interfering signal template samples A "flat" sample is used for the Z'_{SSM}, obtained using a modified version of PYTHIA6 in which the differential cross section is multiplied by the inverse Breit-Wigner and divided by an exponential:

$$\frac{d\sigma}{dm} \rightarrow \frac{d\sigma}{dm} \times ((m^2 - M(Z')^2)^2 + m^2\Gamma(Z')^2) / \exp(-0.00195m) \tag{4.2.1}$$

where all mass and width terms are in units of GeV and the exponential is tuned to remove the effect of the parton luminosity. This allows to build as many fully simulated signal templates as needed, by reweighting the events according to the desired invariant mass shape. These templates are used only in the σB limit setting procedure (see section 7), since the σB parameter scales the signal. Since these templates simulate the Z'_{SSM} signal only, i.e. without taking into account the interference with the DY part, this procedure is approximated. However, when comparing the output templates with a dedicated Z'_{SSM} samples at few mass points generated with proper interference (see previous paragraph), the agreement is satisfying - see appendix G for the validation procedure.

Interfering signal template samples If the interference of the heavy states with the DY is taken into account, then it is not possible to set limits on σB, since this is practically meaningless and technically impossible. This is true in principle even if the interference is very small, as in the Z'_{SSM} case. Moreover, if the interference is strong and destructive as in the KK case, the cross-section approach is even less appropriate. Instead, a different approach has been developed for this analysis. Namely, limits will be set on the fermion coupling strength versus the mass of the heavy state (see chapter 8).

The KK and the interfering-Z'_{SSM} signal templates are produced by reweighting the binned DY samples with the analytical (3+1)-dimensional weighting function, based on helicity am-

plitudes as the one introduced in equation 2.4.30 for the KK case, with summation over the first 10 KK excitations. For the interfering-Z'_{SSM} case, the KK tower in equation 2.4.30 should be replaced by the Z'_{SSM} term where the rest remains the same. The weighting function reads,

$$\mathcal{W}_0\left(m_{\ell\ell}, \cos\theta^*, q; g\right) = \frac{\left|\mathrm{DY} + X(g)\right|^2}{\left|\mathrm{DY}\right|^2} \tag{4.2.2}$$

where DY and X are the amplitudes for DY or X with X being either the KK tower or the Z'_{SSM}. Both the DY and the X parts are calculated in terms of the truth dilepton invariant mass, $m_{\ell\ell}$, the incoming quark flavor, q and the truth lepton $\cos\theta^*$ measured in the $\ell^+\ell^-$ center of mass frame with respect to the truth incoming quark direction. For simplicity, the summation of the squared amplitude over the helicity states has been omitted in both numerator and denominator of the weight function. The last parameter, g, is a numeric coupling scale (or "strength"). The introduction of this new parameter and a discussion of its impact on the rest of the analysis will be performed in more details later in chapter 5 and in the context of the limit on the couplings in chapter 8.

For the Z'_{SSM} model, this approach is more accurate than the one described in equation 4.2.1 since it contains the full amplitude with interference. A comparison between the resulting Z'_{SSM} templates of the two approaches with respect to a fully simulated Z'_{SSM} samples, is given in appendix G.

Few of the KK templates are shown with respect to the backgrounds and data at the end of this chapter, in figure 4.14 for g fixed to 1, corresponding to the SSM case. Some of the full $m_{\mu\mu}$ versus g^N templates of both Z'_{SSM} and $\gamma_{\mathrm{KK}}/Z_{\mathrm{KK}}$ signals (for $N = 2$ or 4), are shown in the next chapter in section 5.4 and in appendix G, where a validation against the fully simulated Z'_{SSM} is also done. While in the non-interfering case the σB parameter scales the differential cross section of the signal when it is added to the DY, the parameter that scales the differential cross section in the interfering cases are either g^2 or g^4, as it will be shown in section 8.1.

4.3. Cross sections used in the analysis

4.3.1. Signal and Drell Yan cross sections

The signal and SM background cross sections are typically generated using leading-order (LO) matrix elements and the corresponding parton distribution functions (PDFs). The normaliza-

tion and the shape of these differential cross sections are modified by higher-order QCD and electroweak corrections. However, next-to-leading order (NLO) or next-to-next-to-leading order (NNLO) calculations are typically not available for all the processes of interest. The usual procedure of using NNLO QCD calculations of the DY process, to compute a mass-dependent K-factor is followed. This K-factor is defined as a function of the invariant mass which, when used to multiply the LO differential cross section, yields the NNLO differential cross section. It is conventional to assume that all colorless final states produced from initial $q\bar{q}$ state have similar QCD radiation in the initial state, and therefore the K-factor derived for the Drell Yan process can be applied to the signal (Z' and γ_{KK}/Z_{KK}) processes as well.

The details of the NNLO cross section and the NNLO QCD K-factor calculations using the PHOZPR [87] programme are provided in appendix C. Since the simulation samples have been generated using PYTHIA6 and the LO** PDFs, the K^{**}_{NNLO} set of K-factors for various $m_{\ell\ell}$ values is used to weight the simulated signal and DY background events as a function of the dilepton invariant mass. Some representative values of K^{**}_{NNLO} are shown in table 4.3.

Table 4.3.: QCD K-factor for several dimuon masses obtained with PYTHIA6 (LO) and PHOZPR (NNLO) using the central value of MSTW2008 NNLO PDF.

$m_{\mu\mu}$ [GeV]	250	500	750	1000	1250	1500	1750	2000	2250	2500
$K^{**}_{NNLO} = \frac{\sigma(NNLO)}{\sigma(LO**)}$	1.152	1.136	1.121	1.100	1.069	1.025	0.973	0.914	0.853	0.791

Similarly, a mass-dependent electroweak (EW) correction is defined to take into account the effects of higher order electroweak corrections. The PYTHIA6 simulated samples already include real photon emission via the PHOTOS program. The HORACE [88, 89] program is used to calculate the weak K-factor due to virtual gauge boson loops. The EW K-factor is discussed in detail in appendix D and shown in figure D.2. For convenience, some representative values are shown in table 4.4.

Table 4.4.: Electroweak K-factor for for several dimuon masses obtained with HORACE using MRST2004QED PDF set, as described in appendix D.

$m_{\mu\mu}$ [GeV]	500	750	1000	1250	1500	1750	2000	2250	2500
K^{**}_{EW}	1.030	1.014	0.999	0.984	0.969	0.953	0.931	0.898	0.859

In principle, the EW K-factor that was derived for the DY sample, is not necessarily the same for the new boson (Z'_{SSM} or $\gamma_{\text{KK}}/Z_{\text{KK}}$) since it depends on the couplings of that boson to the SM particles. Usually, higher order model dependent corrections are not applied in search analyses. However, in cases where the full interference structure has to be considered, and the EW corrections are anyhow relevant for the interference of the heavy bosons with the DY amplitude, one prefers to apply the DY EW K-factor on the whole DY+X cross section and the EW K-factor is multiplying the event weight[6], $\mathcal{W}_0$, given in equation 4.2.2,

$$\mathcal{W}\left(m_{\ell\ell}, \cos\theta^*, q; g\right) = K_{\text{EW}}\mathcal{W}_0 \tag{4.3.1}$$

In this way, not only the DY and the interference term are modified, but also the pure KK term. This approximation is made because this is the most conservative option and because it is also consistent with the ATLAS contact interaction analysis [90] which is another non-resonant search in a dilepton final state where the interference with the DY amplitude cannot be neglected.

A better approximation could be to subtract the pure DY part and re-add it with the EW correction,

$$\mathcal{W}\left(m_{\ell\ell}, \cos\theta^*, q; g\right) = \frac{|\text{DY} + X(g)|^2 + (K_{\text{EW}} - 1) \times |\text{DY}|^2}{|\text{DY}|^2} = \mathcal{W}_0 + (K_{\text{EW}} - 1) \tag{4.3.2}$$

where in this way, neither the new X state nor the interference term are modified and only the DY part is corrected. However this leads to non-physical negative weights because of the strong destructive interference.

The two approaches were tested. While the latter was found to be problematic for some pole masses in few specific phase-space ranges, it could still be used throughout the rest of the phase-space where the weights are non-negative. The impact of switching between the two approaches, in the region where both of them work, was found to have a negligible effect on the results. Therefore, the procedure described in equation 4.3.1 was safely adopted.

Note that for the σB limits, where the interference is not taken into account (see chapter 7), the EW K-factor is not applied to the signal.

While the mass window for this analysis ends at 3 TeV, this analysis uses also a DY sample with a generator-level mass above at 3 TeV. This is important mainly for the KK search where the information at the high-end tail of the invariant mass shape should be modeled correctly.

[6] This is done only in the context of the coupling-limits where the interference is taken into account.

This tail may contain events migrating from *truth* masses above 3 TeV, down into the mass window below 3 TeV, via effects such as detector resolution or final state radiation (FSR). In the context of the K-factors, this imposes a difficulty since the EW K-factor dependence on $m_{\mu\mu}$ which is described by a parabolic behavior is valid only up to 3 TeV (see appendix D) and since the QCD K-factor fit is valid only up to 5 TeV (see appendix C). Since there are no calculations of the EW K-factor beyond 3 TeV, the parabolic behavior of the EW K-factor is extrapolated to higher masses. However, around 5 TeV both EW and QCD K-factors become negative. The solution taken in this analysis was to demand that at all times the K-factors will be kept above a certain "ad-hoc" value taken to be 0.5[7]. This is eventually a very small effect since it deals with relatively very few DY events, most of which have *true* mass between 3 and 4 TeV. The uncertainties on the QCD and EW K-factors at $m_{\mu\mu} = 2$ TeV are 3% and

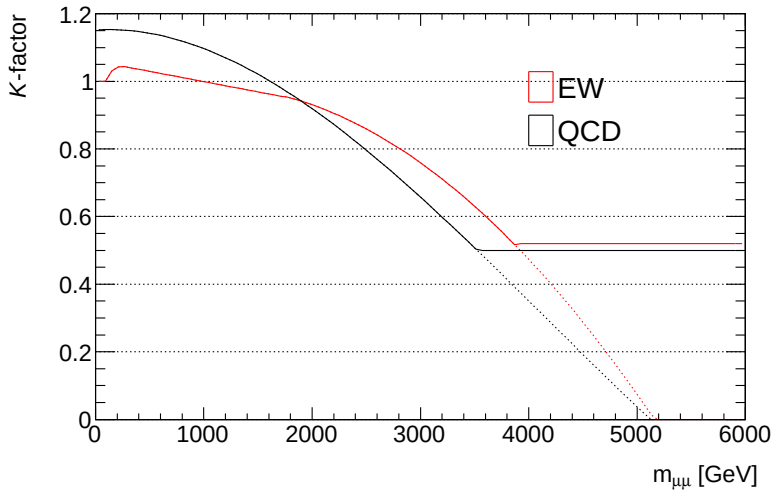

Figure 4.1.: The EW and QCD K-factors used in this analysis for the DY and the signals. The dotted lines represent the original fits (see appendix D and C) and the solid lines represent the actual K-factors used in the analysis.

4.5% respectively.

4.3.2. Other background cross sections

Cross section calculations for W/Z are described in references [91] and [92]. They are performed at NLO and normalized to NNLO in the case of W+jets. The theoretical uncertainties are 5% for inclusive diboson production and about 27.6 % for $W + n$ jets ($n > 0$) produc-

[7] This is certainly ad-hoc, but the PDF uncertainty is exploding at large masses so the overall uncertainty here is anyhow very large.

tion. Cross section calculations for $t\bar{t}$ are performed at approximate-NNLO as described in reference [91]. The related uncertainty is 8.3%.

4.4. Muon identification and event selection

A series of selection cuts are applied in order to select Z'_{SSM} or $\gamma_{\mathrm{KK}}/Z_{\mathrm{KK}}$ candidates decaying into muon pairs from pp collisions at 7 TeV. These are chosen to preserve the efficiency of potential signals, while minimizing background processes. It was mentioned in the introduction that the emphasis is given to the quality of the muon objects. As can be expected, the most outstanding shortcoming of this approach is the relatively large loss in acceptance times efficiency. However, it ensures that the muon candidates are properly identified and measured in order to form the invariant mass shape with as little distortions as possible. The selection criteria are listed below.

- The event is in the good runs list (GRL);
- The event passes the trigger:
  - ⋆ EF_mu22 or EF_mu22_MG or EF_mu40_MSonly_barrel, before the start of period J (run 186516). These EF triggers were seeded by the L1_MU10 trigger.
  - ⋆ EF_mu22_medium or EF_mu22_MG_medium or EF_mu40_MSonly_barrel_medium, from period J and on. These EF triggers were seeded by the L1_MU11 trigger, since the L1_MU10 trigger got prescaled;
- The event has at least one primary vertex (PV) with more than two tracks and $|z_{\mathrm{PV}}| < 200$ mm;
- There are at least two combined *Muid* muons in the event;
- Each muon must have $p_{\mathrm{T}} > 25$ GeV;
- Each muon must pass the muon combined performance (MCP) requirements for ID hits (explanation below);
- Each muon must pass stringent requirements on the MS hits, and a cut on the significance of the difference between the standalone momentum measurements from the ID and MS (more details below);
- For each muon, the impact parameter in the transverse plane, d_0, with respect to the primary vertex must be less than 0.2 mm;
- For each muon, the impact parameter along the beam axis, z_0, with respect to the primary vertex must be less than 1.0 mm;

- Each muon must be isolated: the sum of the p_{T} of all tracks in a cone of size $\Delta R < 0.3$ relative to the muon combined p_{T} must be less than 0.05.

To select well-reconstructed muons, the 2011 MCP guidelines are followed. These require each muon used in the analysis to satisfy the following set of cuts:

ID hits requirements: The ID conceptual layout can be seen for convenience in figure 3.4.

- At least one BLayer[8] hit, if one is to be expected;
- At least two Pixel hits. A dead Pixel sensor crossed by the track is also considered as a hit;
- At least six SCT hits. A dead SCT sensor crossed is also considered as a hit;
- At most two Pixel or SCT holes along the track;
- If η <1.9: at least six TRT hits, including TRT outliers, with outlier[9] fraction <0.9;
- If $\eta \geq$1.9: only if at least six TRT hits, including TRT outliers, are observed with outlier fraction below 0.9

MS hits requirements: The MS conceptual layout can be seen for convenience in figure 3.6. This analysis considers two categories of muons. The first category consists of the so-called *three-station* muons which are required to pass the following criteria:

- At least three hits in each of the three layers, Inner, Middle and Outer of the precision MS chambers (MDT/CSC) in the Barrel or Endcap with no Barrel-Endcap overlap[10];
- At least one phi hit in two different RPC/TGC/CSC layers;
- No hit in the BEE, EE or BIS78 MDT chambers which are not properly aligned;
- For each muon, the difference between the standalone momentum measurements from the ID and MS must not exceed five times the error on that difference.

The second category consists of *two-station* muons which are kept if they pass the following criteria:

[8] The BLayer is the innermost barrel layer of the Pixel detector, as can be seen in the bottom left part of figure 3.4 (denoted by R50.5). This structure ensures that there are three hits per track up to $|\eta| = 2.5$, one in the BLayer and two in outer layers (barrel or endcap).

[9] TRT outlier is either a straw tube with a signal but not crossed by the nearby track, or a set of TRT measurements around the track extrapolation which, however, fail to form a smooth trajectory together with the pixel and SCT measurements.

[10] In practice this is already very rare with the imposed geometry of the MS hits cut, but even if such a track manage to survive the other requirements, it is discarded due to misalignments between the barrel and the endcap.

- At least five hits in each of the Barrel Inner and Outer MDT precision layers (no hit in Barrel Middle layer, no Barrel-Endcap overlap);
- At least one phi hit in one RPC layer;
- No hit in the BEE, EE or BIS78 MDT chambers (misalignments);
- No hit in the MS chambers in sector 13 with $0.00 < \eta < 0.65$, or in sector 2 with $\eta > 0.85$
- For muons in large MDT sectors, $|\eta| < 0.85$; for muons in small MDT sectors, $|\eta| < 1.00$;
- For each muon, the difference between the standalone momentum measurements from the ID and MS must not exceed three times the error on that difference.

The muons that pass the selection criteria described above are used to build opposite-sign muon pairs. First, if two opposite-sign muons passing the *three-station* selection are found, they are used to make the pair, and the event is said to pass the *tight dimuon selection*. If more than one tight dimuon candidate is found in an event, the one with the highest transverse momentum sum is selected.

If no tight dimuon candidate is found, pairs can be built with one *three-station* muon, and a *two-station* muon of opposite-sign. Events with such pairs are said to pass the *loose dimuon selection*. Similarly, if more than one loose dimuon candidate is found in an event, the one with the highest transverse momentum sum is selected.

Tables 4.5 and 4.6 list the kinematic properties of the highest mass and highest momentum data events passing the selection.

Table 4.5.: Properties of the dimuon events with $m_{\mu\mu} > 900$ GeV in 2011 data

			Leading Muon			Subleading Muon			Event		
Run	Event	Selection	p_T [GeV]	η	ϕ	p_T [GeV]	η	ϕ	$m_{\mu\mu}$ [GeV]	MET [GeV]	ϕ_{MET}
190975	26669226	loose	648	-0.75	0.49	583	-0.36	-2.60	1252	67	-2.83
187763	10145376	tight	669	0.44	-0.74	498	-0.35	2.23	1242	117	2.53
179710	33299833	loose	698	0.79	-1.91	460	0.90	1.20	1135	230	1.32
190256	98768839	tight	595	0.28	-1.42	450	-0.40	1.73	1095	96	1.78
186216	10126855	tight	300	-0.42	-0.55	256	1.91	2.62	975	44	-3.06
183780	72206332	tight	533	0.37	3.01	409	0.72	-0.12	949	138	-0.25

A 3D event-display of the highest invariant mass event is available in appendix H.

Table 4.6.: Properties of the dimuon events having a muon with $p_T > 600$ GeV in 2011 data.

			Leading muon, CB			Leading muon, ID & MS				Event			
Run	Event	Selection	p_T [GeV]	η	ϕ	p_{ID} [GeV]	p_{MS} [GeV]	MS/ID	Diff. Sig.	$m_{\mu\mu}$ [GeV]	Dimuon p_T [GeV]	MET [GeV]	ϕ_{MET}
187219	69080640	tight	812	0.15	3.10	688	720	1.05	0.16	103	853	182	0.01
179710	33299833	loose	698	0.79	-1.91	591	410	0.69	1.03	1135	239	230	1.32
187763	10145376	tight	669	0.44	-0.74	680	858	1.26	0.84	1242	197	117	2.53
190975	26669226	loose	648	-0.75	0.49	707	1629	2.30	1.29	1252	74	67	-2.83
186216	2639314	tight	634	0.42	0.83	651	659	1.01	0.06	95	670	80	-2.02
189822	51196769	tight	618	-0.29	-2.43	715	671	0.94	0.24	88	695	36	-2.57

It has been checked that no event from the 2011 debug stream[11] passes this selection.

Figure 4.2 shows the event yield per run of the full muon selections, normalized to 1 pb^{-1}. There are two important characteristics related to the following: (i) the change from nominal (L1_MU10 seeded) to "_medium" (L1_MU11 seeded) triggers at the start of period J (run 186516), and (ii) Periods L3-L4 (runs 189205–189610) have a known RPC timing problem. Both effects resulted in efficiency losses.

4.5. Resolution Smearing

At high transverse momentum, the muon momentum resolution in the ID and the MS can be parameterized [93] as

$$\frac{\sigma(p)}{p} = P_1 \oplus P_2 \cdot p_{\mathrm{T}}, \tag{4.5.1}$$

where P_1 and P_2 are resolution parameters related to the contribution of multiple scattering and intrinsic curvature resolution, respectively. At very high momentum, the resolution is dominated by P_2, and the values obtained for data and MC are shown in tables 4.7 and 4.8, respectively. As can be see from these tables, some discrepancies exist between data and MC simulations. To adjust the muon momentum resolution in simulations to the data, a Gaussian smearing of the track ID and MS p_{T} measurements is performed, randomly shifting q/p_{T} by

$$\delta(q/p_T) = S_1 \cdot g_1 \cdot (q/p_T) + S_2 \cdot g_2, \tag{4.5.2}$$

[11] There are four streams of data generated based on the trigger decision: physics stream, calibration stream, express stream and debug stream. The debug stream contains events for which the trigger was not able to make a decision because those events caused failures in some part of the online system.

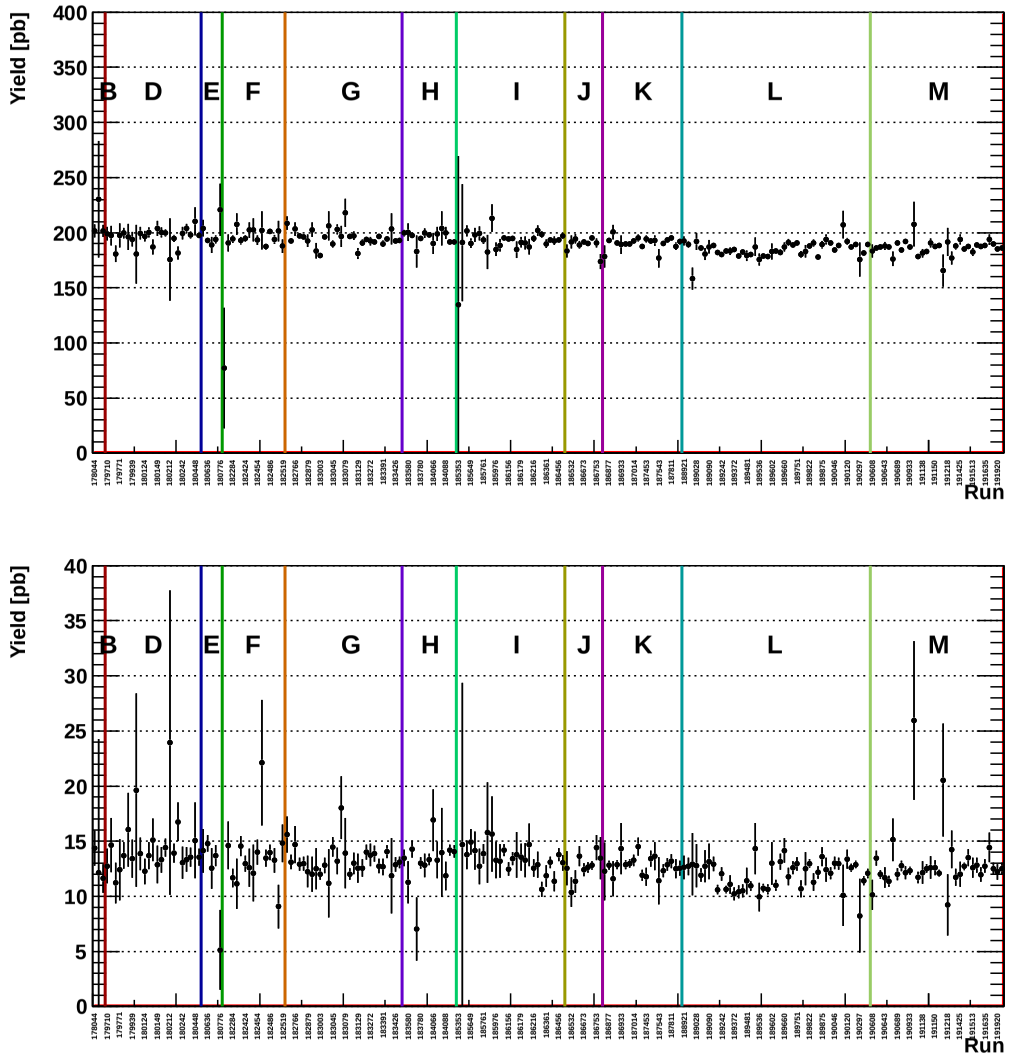

Figure 4.2.: Yield per 1 pb^{-1}, shown run by run, for the tight (top) and loose(bottom) dimuon selection.

where $q = \pm 1$ is the track charge, g_1 and g_2 are random Gaussian variables with mean = 0 and $rms = 1$, and where S_1 and S_2 are smearing constants. These smearing constants are determined by computing the quadratic differences in the resolution parameters between data and simulations as $S_i = P_i^{\text{data}} \ominus P_i^{\text{MC}}$. The smearing constants S_2 are shown in table 4.9. Finally, the corrected combined p_{T} is the weighted average of the smeared p_{T} from the ID and the MS.

In the case of combined muons with hits in all three stations of the muon spectrometer, the MS dominates the momentum measurement at high p_{T} and the resolution ranges from about 10% to 20%. In the case of the *two-station* muons, the resolution from the ID dominates.

Smearing for the *three-station* muons is handled by the official MCP smearing tool [93][12], whereas for *two-station* muons, a different set of resolution constants are used for the MS which were determined in a dedicated *two-station* muon analyses (see table 4.9).

The resolution parameters for the *three-station* muons in data are calculated from the intrinsic resolution of the detectors and the known spectrometer geometry and magnetic field integrals; The intrinsic resolution of the muon spectrometer chambers is measured from straight collision tracks that were recorded in dedicated runs with the toroidal magnetic field switched off. For *two-station* muons, the momentum resolution is derived from the measured angular resolution of the inner and outer MS stations.

Table 4.7.: Intrinsic muon p_{T} resolution parameters P_2 see equation 4.5.1. The $P_2^{\mathrm{MS*}}$ corresponds to the category of the *two-station* muons.

Region	P_2^{ID} (TeV^{-1})	P_2^{MS} (TeV^{-1})	$P_2^{\mathrm{MS*}}$ (TeV^{-1})
$\lvert\eta\rvert < 1.05$	0.36 ± 0.01	0.14 ± 0.01	0.54 ± 0.02
$1.05 < \lvert\eta\rvert < 1.7$	0.41 ± 0.02	0.51 ± 0.01	—
$1.7 < \lvert\eta\rvert < 2.0$	0.66 ± 0.01	0.22 ± 0.01	—
$2.0 < \lvert\eta\rvert < 2.5$	$(0.044 \pm 0.002)\sinh^2\eta$	0.16 ± 0.02	—

Table 4.8.: Intrinsic muon p_{T} resolution parameters P_2 for MC simulations. The $P_2^{\mathrm{MS*}}$ corresponds to the category of the *two-station* muons.

Region	P_2^{ID} (TeV^{-1})	P_2^{MS} (TeV^{-1})	$P_2^{\mathrm{MS*}}$ (TeV^{-1})
$\lvert\eta\rvert < 1.05$	0.31	0.10	0.43
$1.05 < \lvert\eta\rvert < 1.7$	0.33	0.19	—
$1.7 < \lvert\eta\rvert < 2.0$	0.44	0.08	—
$2.0 < \lvert\eta\rvert < 2.5$	$0.042\sinh^2\eta$	0.05	—

A systematic uncertainty that arises from a curvature offset is also considered. It has been evaluated by comparing the transverse momentum spectra of positively and negatively charged muons from Z boson decays. Upper limits on the curvature offset have been derived by MCP and are listed in table 4.10. The measured offsets are consistent with zero, and it has been verified that propagating the uncertainties on the offsets (which represent an upper bound)

[12] In this reference, this is demonstrated for release 15

Table 4.9.: Smearing constants S_2 used in the analysis. The $S_2^{\mathrm{MS}*}$ corresponds to the category of the *two-station* muons.

Region	S_2^{ID} (TeV^{-1})	S_2^{MS} (TeV^{-1})	$S_2^{\mathrm{MS}*}$ (TeV^{-1})
$\lvert\eta\rvert < 1.05$	0.19 ± 0.01	0.10 ± 0.02	0.35 ± 0.04
$1.05 < \lvert\eta\rvert < 1.7$	0.24 ± 0.03	0.47 ± 0.02	—
$1.7 < \lvert\eta\rvert < 2.0$	0.50 ± 0.02	0.20 ± 0.01	—
$2.0 < \lvert\eta\rvert < 2.5$	$(0.015 \pm 0.004)\sinh^2\eta$	0.15 ± 0.05	—

results in a negligible systematic uncertainty. The fit to the $Z \to \mu\mu$ mass peak also constrains the track momentum scale. The Z boson mass measurements are consistent with the world-average value, indicating that there is no systematic bias in the momentum measurement.

Table 4.10.: Bounds on the standalone muon momentum bias for 2011 data

Eta Region	Standalone Muon Momentum Bias in TeV^{-1}
$\eta < -1.05$	-0.006 ± 0.043
$-1.05 < \eta < 1.05$	-0.009 ± 0.008
$\eta > 1.05$	0.017 ± 0.045

4.6. Signal efficiencies

The relative and absolute efficiencies of the selection criteria calculated from the fully simulated 2 TeV Z'_{SSM} MC sample are listed in table 4.11. The overall acceptance times efficiency of the final selection for the flat signal sample, is displayed in figure 4.3 as a function of $m_{\mu\mu}$. The gain in acceptance with the inclusion of the loosely selected events is about 0.04.

The trigger and reconstruction efficiencies in the data are obtained using a "tag-and-probe" methods which are described in appendix E and F respectively. The corresponding scale factors (SF) and systematic uncertainties are also described in these two appendices. It is found that both the trigger and reconstruction SFs between data and MC are very close to unity and that they are flat in p_{T}. This implies that their influence is independent of $m_{\mu\mu}$

Table 4.11.: Cut flow for the tight dimuon selection for a 2 TeV Z'_{SSM} sample with 20000 events (run 105349). Numbers on the last row in parenthesis refer to the loose dimuon selection.

Cut description	Events	Relative efficiency	Absolute efficiency
Trigger	18409	0.920	0.920
PV	18217	0.990	0.911
2 Combined muons	15960	0.876	0.798
p_{T}	15817	0.991	0.791
ID Hits	15291	0.967	0.765
d_0	15288	1.000	0.764
z_0	15278	0.999	0.764
Isolation	14931	0.977	0.747
MS Hits, Opposite-sign	7878 (787)	0.528 (0.053)	0.394 (0.039)

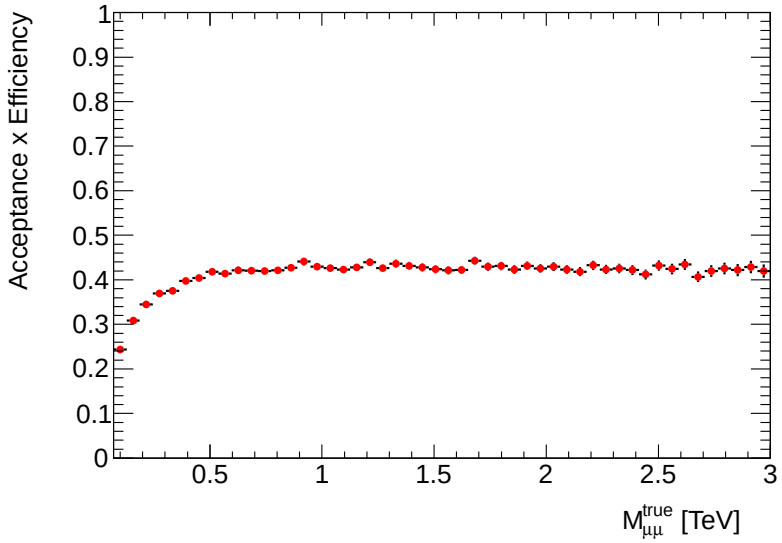

Figure 4.3.: Total acceptance times efficiency as a function of the generated $m_{\mu\mu}$ for the flat sample.

and thus is vanishing upon normalizing to the Z peak. Therefore, these SFs are not applied to the MC samples in this analysis. Systematic uncertainties are assigned on these efficiency estimations, however.

4.7. Background estimation

The main background source is from DY production. This background is modeled using simulated MC samples, and the same smearing and corrections applied to the signal events are also applied to DY events.

Background due to $t\bar{t}$, WW, WZ and ZZ production, are estimated using simulated samples as well. The momentum smearing is also applied to these background samples. Background from W production in association with jets was shown to be negligible in the previous cycles of this analysis [16], therefore it is not considered in the current analysis.

The QCD multijet background is due to $b\bar{b}$ and $c\bar{c}$ production and their subsequent decays to muons. The contribution from this background is estimated from a sample of non-isolated dimuon events in data, using the track-isolation variable $\sum p_T^{\mathrm{trk}}/p_T^{\mu}$, where the sum is over the tracks in a cone with size $\Delta R < 0.3$ around the muon track. Events from data in which both muons fall in the region 0.1–1.0 in this isolation variable are used to obtain the shape of the QCD background. In order to estimate the number of QCD events passing the selection, this shape (data points in figure 4.4(c)) is then scaled using the fraction of isolated (0.00–0.05) to non-isolated (0.1–1.0) dimuons in simulated $b\bar{b}$ and $c\bar{c}$ events. With the current MC statistics, this scale factor is $5/212 = 0.024 \pm 0.012$ per muon. After overlaying the resulting QCD scaled shape with the other backgrounds, the distribution peaks at 70 GeV with about 0.3 events / 5 GeV and falls to 0 events already at 400 GeV (see reference [16]). Therefore, this background will be neglected in the following discussion. The distribution of the isolation variable is shown in figure 4.4(a), and also in figure 4.4(b) where the bins and range are wider. The distribution in figure 4.4(b) shows the QCD dominated region which is removed by the isolation requirement. These histograms show that the isolation variable used in the analysis is well modeled by MC. Figure 4.4(c) shows the dimuon invariant mass for data and MC for non-isolated muon pairs, demonstrating that this constitutes a pure sample of QCD background.

Cosmic ray background can cause a muon to be reconstructed as two back-to-back muons while it traverses the ATLAS detector in the presence of the magnetic field. The contamination of high-mass dimuon collision events from this source of background as a function of $m_{\mu\mu}$ can be estimated using data from the same triggers as the final analysis but with a different set of cuts. Namely, all analysis requirements except the ones that have a low efficiency for cosmic muons. In particular, the invariant mass requirement, primary vertex, track d_0 and z_0 requirements are relaxed. Furthermore, discrimination variables between collision and cosmic

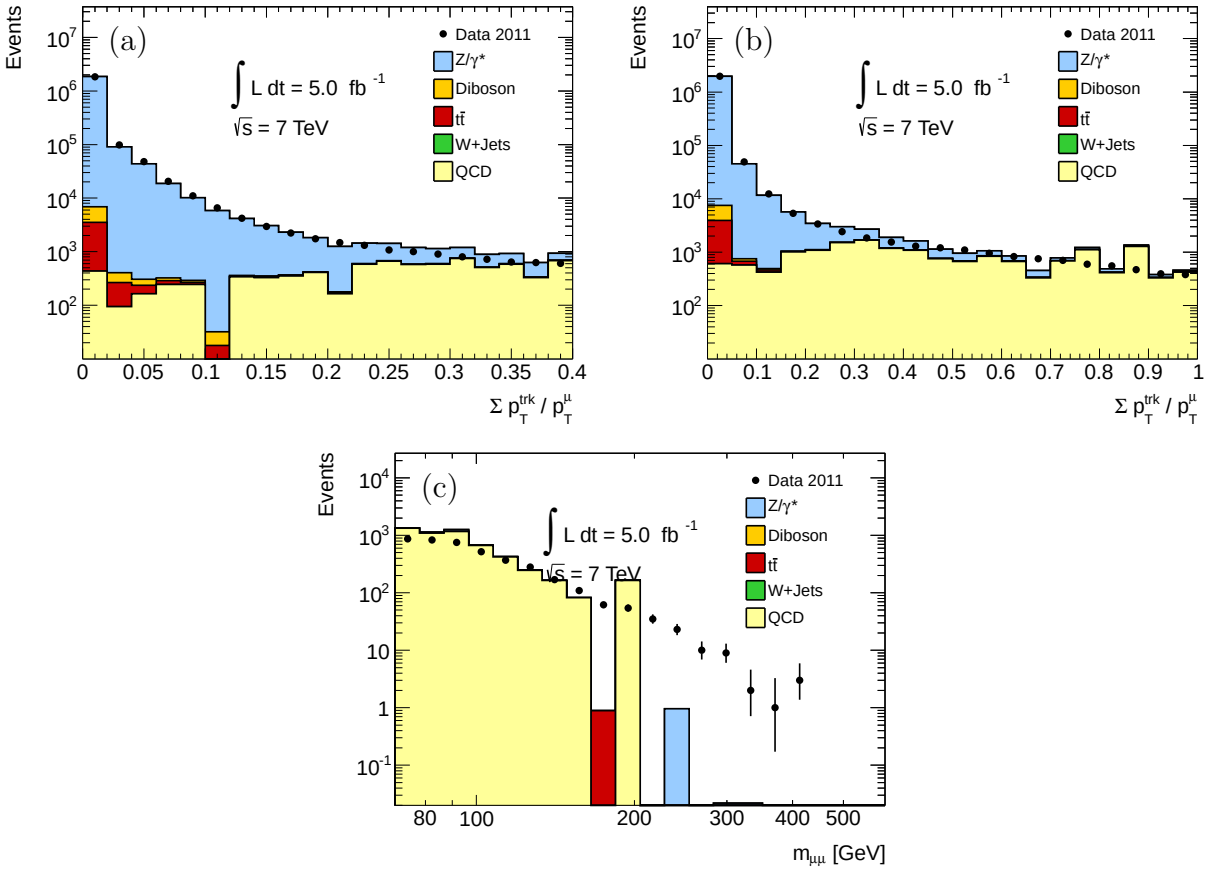

Figure 4.4.: Muon isolation for dimuon events, for the low isolation region (a) and the full region (b). The invariant mass distribution of dimuon events failing the isolation cut is given in (c) before the scaling to the fraction of isolated to non-isolated dimuons in the $b\bar{b}$ and $c\bar{c}$ MC.

muons events can be used. For example, the distribution of $\sum_{\text{trk}} \eta$ of the two tracks is expected to peak at 0 for cosmic muons since the reconstructed tracks must be back-to-back. The cosmic ray background was estimated for the EPS analysis [15] using the first 1 fb^{-1} in 2011 to be $(18.8 \pm 13.3) \cdot 10^{-3}$ events, centered between 200 and 300 GeV and was therefore neglected. The cosmic background scales with trigger live-time and not with the integrated luminosity. As the bulk of the 2011 data has been collected at higher instantaneous luminosity, compared with the first 1 fb^{-1}, the relative contribution of cosmic muons for the full 2011 dataset is expected to be even lower, and therefore completely negligible.

4.8. Estimate of pile-up effects

In order to match the different data pile-up conditions throughout 2011 data-taking periods, the MC samples need to be reweighed (see table 4.2)). This is done as a function of the average number of pile-up interactions $\langle\mu\rangle$ using the ATLAS official pile-up reweighting tool. The flat sample was used to calculate the acceptance times efficiency as a function of the pole mass, with and without pile-up reweighting. Figure 4.5 shows the ratio of acceptance computed without pileup, to the acceptance computed with pileup. The ratio shows negligible deviation from unity. To conclude, this analysis is insensitive to pile-up effects.

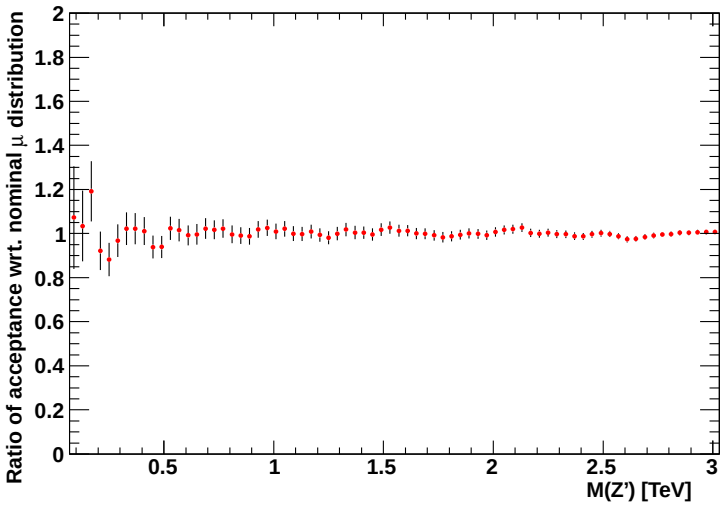

Figure 4.5.: The ratio as a function of the Z'_{SSM} pole mass, of the Z'_{SSM} acceptance times efficiency without pile-up reweighting to with pile-up reweighting.

4.9. Data - Monte Carlo Comparison

Tables 4.12, 4.13 and 4.14 show the number of observed events in bins of reconstructed dimuon invariant mass, along with the expectation from various background sources for the full, tight and loose dimuon selection, respectively. The normalization between data and MC is done based on the number of entries in the Z mass region (70–110 GeV); the data to MC ratio in this region is found to be 1.013. The number of observed events in the normalization region is 985180. The sum of MC tight (table 4.13) plus loose (table 4.14) events at high mass does not match *exactly* the number of MC tight+loose events in table 4.12 because the $t\bar{t}$ and diboson backgrounds at high mass are evaluated from a fit to the combined channel case, whereas for

the separate tight and loose channels they were taken directly from MC without a fit (see appendix B).

Table 4.12.: Expected and observed number of events in the combined selection (tight+loose). The errors quoted include both statistical and systematic uncertainties. The $t\bar{t}$ and diboson background are from the fit results at high mass.

$m_{\mu\mu}$ [GeV]	110 - 200	200 - 400	400 - 800	800 - 1200	1200 - 3000
γ/Z	21246 ± 1200	2095 ± 230	173 ± 15	7.7 ± 0.8	0.98 ± 0.16
$t\bar{t}$	863 ± 100	268 ± 50	18 ± 11	0.32 ± 0.07	0.019 ± 0.007
Diboson	289 ± 32	97 ± 24	11.8 ± 2.7	0.59 ± 0.26	0.087 ± 0.016
Total	22405 ± 1200	2463 ± 240	203 ± 19	8.7 ± 0.9	1.09 ± 0.16
Data	21945	2294	197	10	2

Table 4.13.: Expected and observed number of events in the tight selection. The errors quoted include both statistical and systematic uncertainties. The $t\bar{t}$ and diboson background do not use fit results at high mass.

$m_{\mu\mu}$ [GeV]	110 - 200	200 - 400	400 - 800	800 - 1200	1200 - 3000
γ/Z	19920 ± 1100	1967 ± 220	161 ± 14	7.1 ± 0.8	0.88 ± 0.14
$t\bar{t}$	795 ± 90	248 ± 50	17 ± 11	0.1 ± 0.4	0.000 ± 0.000
Diboson	270 ± 31	91 ± 23	11.3 ± 2.6	0.55 ± 0.25	0.066 ± 0.020
Total	20992 ± 1100	2309 ± 230	189 ± 18	7.7 ± 0.9	0.94 ± 0.14
Data	20545	2144	187	9	1

Figures 4.6 and 4.7 show the p_{T} distributions of the leading p_{T} and sub-leading p_{T} muon. The tail of the p_{T} distributions shows a slight excess in the data. An event by event examination shows that many of the high p_{T} events also show high jet activity, indicating highly boosted topologies. For illustration, this is apparent in table 4.6: of the six events with $p_{\mathrm{T}} > 600$ GeV, three come from highly boosted Z (seen also figure 4.11). The excess in data is then due to the fact that PYTHIA6 underestimates the amount of very-high-energy jets produced in association with Z bosons. It has been verified that ALPGEN describes the high-p_{T} tails better.

Table 4.14.: Expected and observed number of events in the loose selection. The errors quoted include both statistical and systematic uncertainties. The $t\bar{t}$ and diboson background do not use fit results at high mass.

$m_{\mu\mu}$ [GeV]	110 - 200	200 - 400	400 - 800	800 - 1200	1200 - 3000
γ/Z	1339 ± 200	134 ± 50	12.1 ± 3.1	0.61 ± 0.18	0.10 ± 0.04
$t\bar{t}$	66 ± 15	20 ± 10	1.3 ± 1.4	0.03 ± 0.03	0.000 ± 0.000
Diboson	18 ± 7	6 ± 4	0.5 ± 0.3	0.04 ± 0.03	0.005 ± 0.004
Total	1425 ± 200	160 ± 50	14 ± 3.4	0.67 ± 0.19	0.11 ± 0.04
Data	1400	150	10	1	1

Figure 4.8 shows the η and ϕ distributions of the two muons. The p_{T} and rapidity of the dimuon system are shown in figure 4.9 for the combined selection (tight+loose). The missing transverse energy (denoted as MET or E_T^{miss}) distributions after event selection is shown in figure 4.10. The agreement between data and MC is good; this indicates that the muon reconstruction performance is well modeled. There is no excess above expectation at high missing transverse energies observed in data. The 2D histograms in figures 4.11 and 4.12 show the absence of correlation between missing transverse energy and the dimuon invariant mass or between missing transverse energy and the transverse momentum of the leading muon.

Looking at the E_T^{miss} vs. $m_{\mu\mu}$ distribution for the loose selection in figure 4.12 (left), it can be seen that the second highest mass event has $E_T^{\mathrm{miss}} > 200$ GeV. Looking closer at the event properties, the MET direction points directly away from the leading muon, a clear sign of mis-measurement, and upon further inspection one sees that for this muon the p_{T} is measured to be (ID, MS, CB): (591, 410, 926) by *Muid* vs. (591, 404, 600) by *Staco* (in GeV). The diagnosis is that the CB momentum of the *two-station* muon of the pair, has been overestimated by misalignment of the MS causing the track to appear more straight than it really is. In that case, the "more reliable" momentum measurement is that given by the ID alone, resulting a high p_{T} muon but with 25% measurement error. Obviously, that problem cannot be simply "fixed" after the event selection has been frozen.

The invariant mass distributions of the selected dimuon data events can be seen in figure 4.13 with respect to the stacked sum of all backgrounds, and with few overlaid Z'_{SSM} signals. Finally, the same is shown for few KK signals (with full interference structure) in figure 4.14. It can be clearly seen that the presence of a KK resonance at a mass of 3.03 TeV, just outside the mass window for this analysis, is visible as a deficit already above dimuon masses of about 1.5 TeV.

This remarkable feature, which was discussed in the theory chapter 2 (see e.g. figure 2.9(a)), remains visible even after the application of all the experimental considerations.

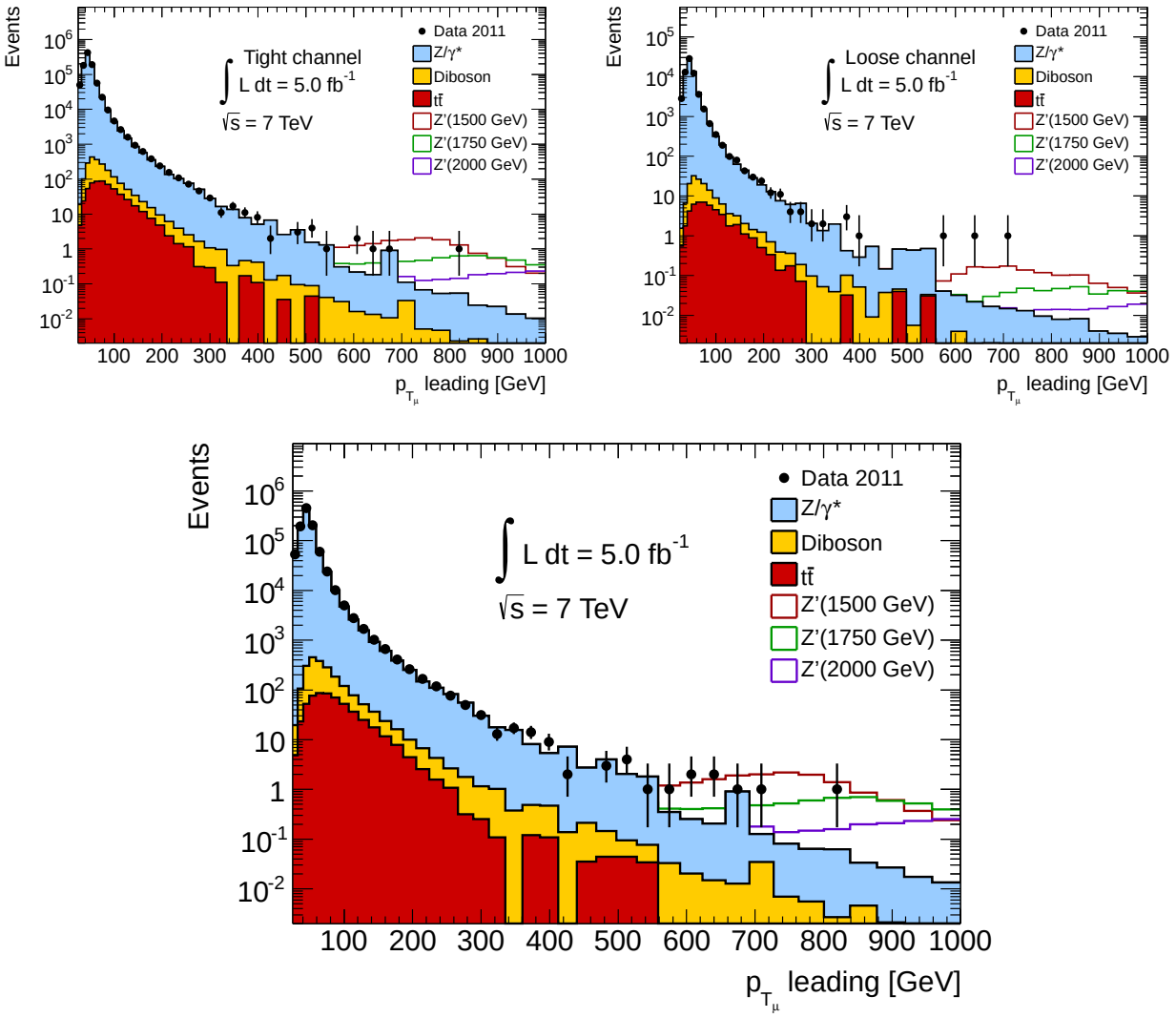

Figure 4.6.: The p_{T} distribution for the leading muon for tight (top left), loose (top right) and combined (bottom) dimuon selection. As described in appendix A, the signal shapes come from dedicated samples generated at a given mass point. This holds for the subsequent figures.

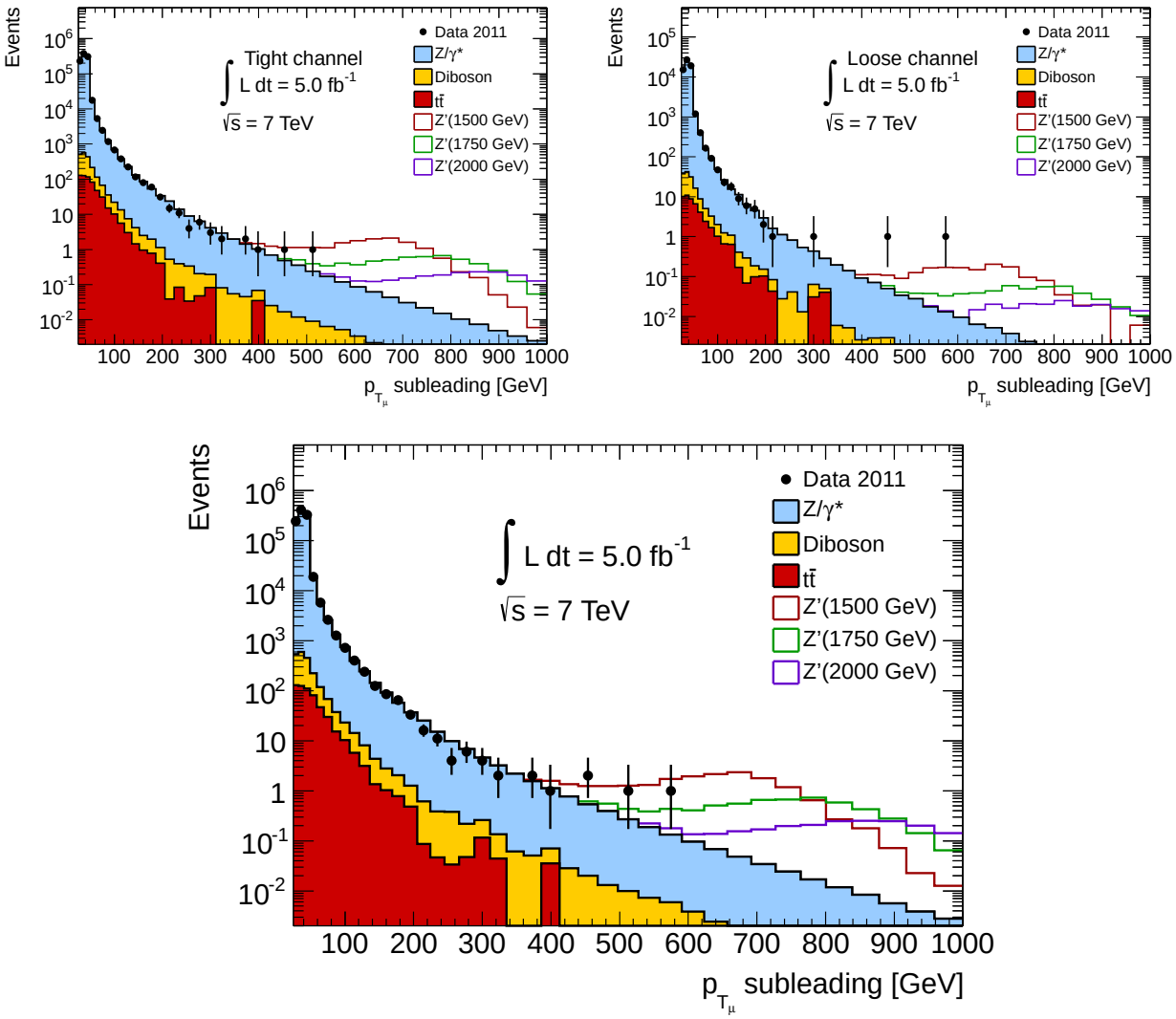

Figure 4.7.: The p_{T} distribution for the sub-leading muon for tight (top left), loose (top right) and combined (bottom) dimuon selection.

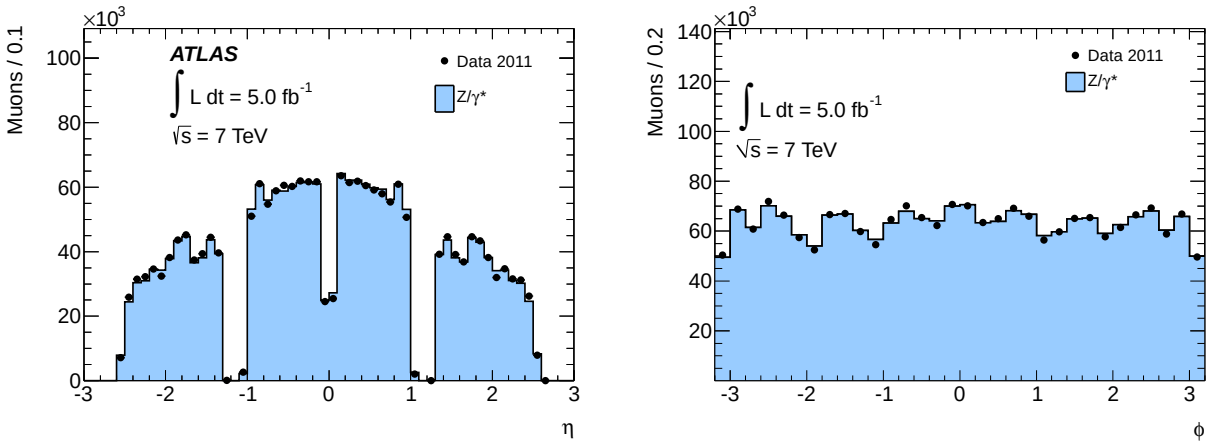

Figure 4.8.: The η and ϕ distributions of the combined dimuon sample.

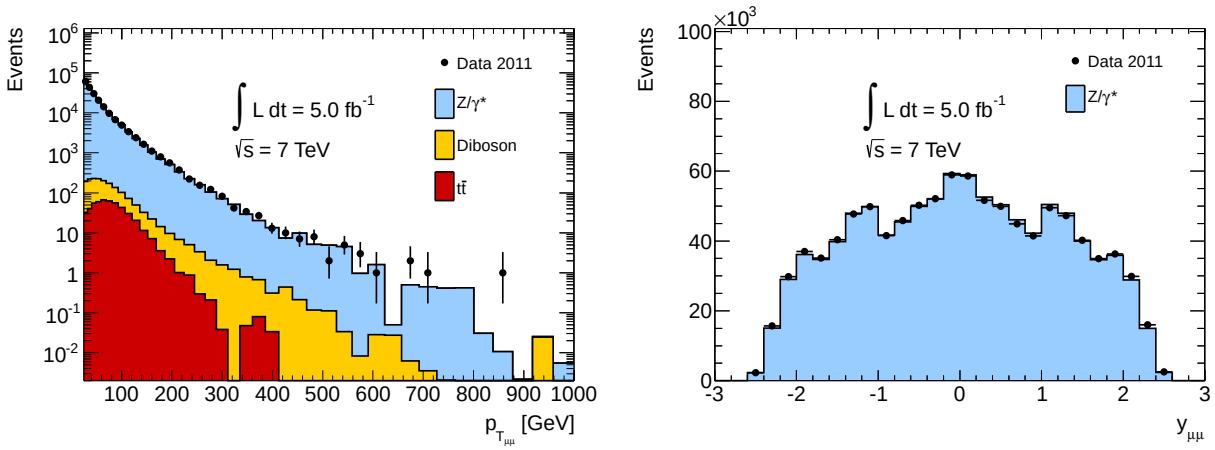

Figure 4.9.: The dimuon p_{T} and rapidity after the combined selection for data (dots) and MC (solid histogram).

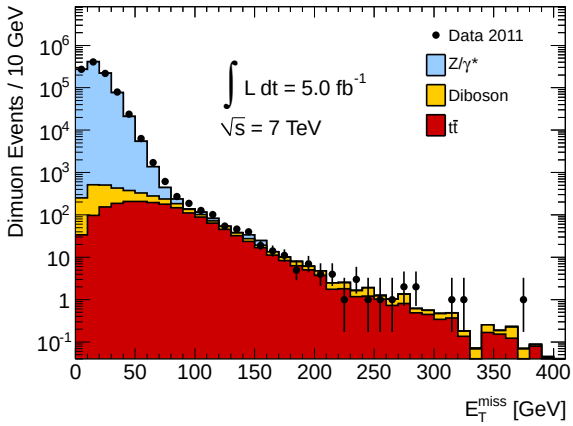

Figure 4.10.: The missing transverse energy of the combined dimuon sample.

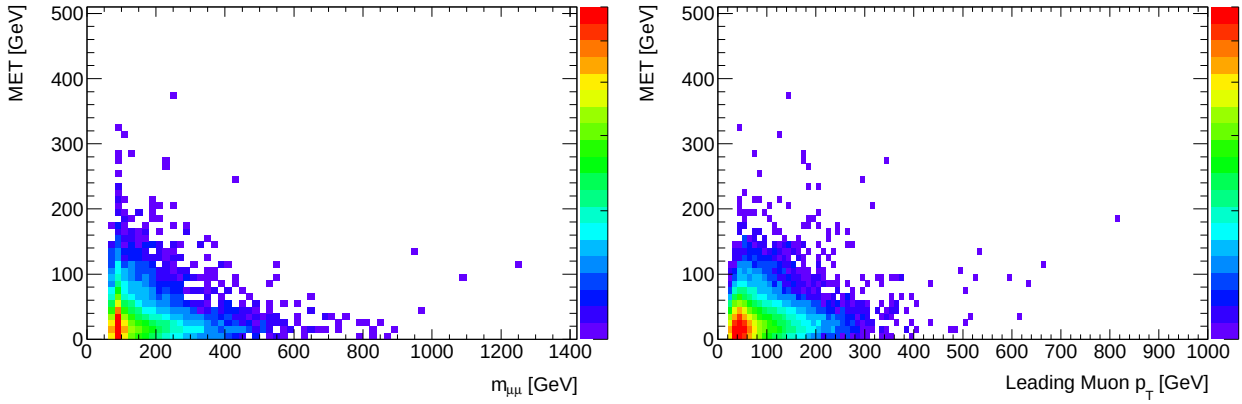

Figure 4.11.: The missing transverse energy after the tight selection in data, against the invariant mass (left) and the transverse momentum of the leading muon (right).

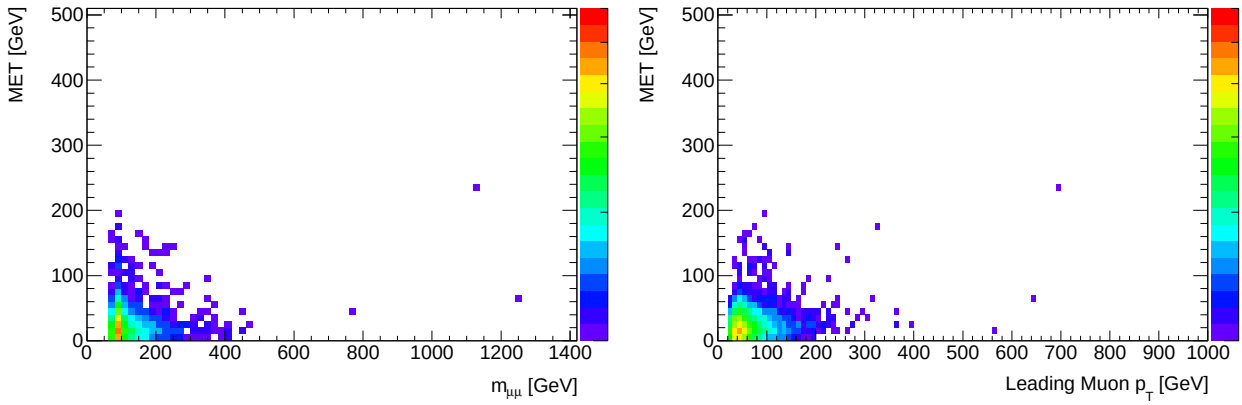

Figure 4.12.: The missing transverse energy after the loose selection in data, against the invariant mass (left) and the transverse momentum of the leading muon (right). See comment about the highest mass events in the text.

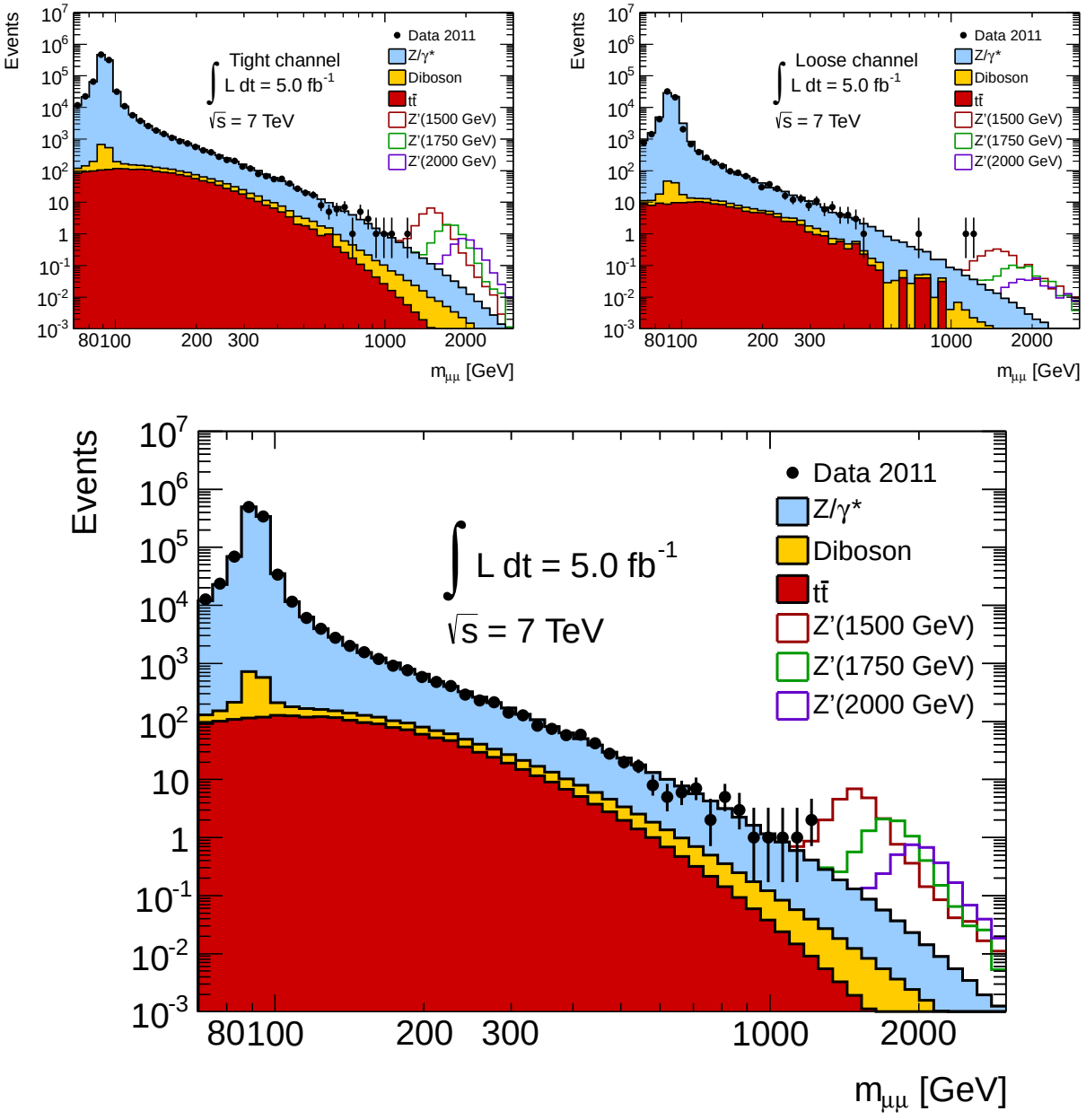

Figure 4.13.: The dimuon invariant mass distribution after the tight (top left), loose (top right) and combined (bottom) selection. The data (dots) are compared to the background sum and selected Z'_{SSM} signals for illustration.

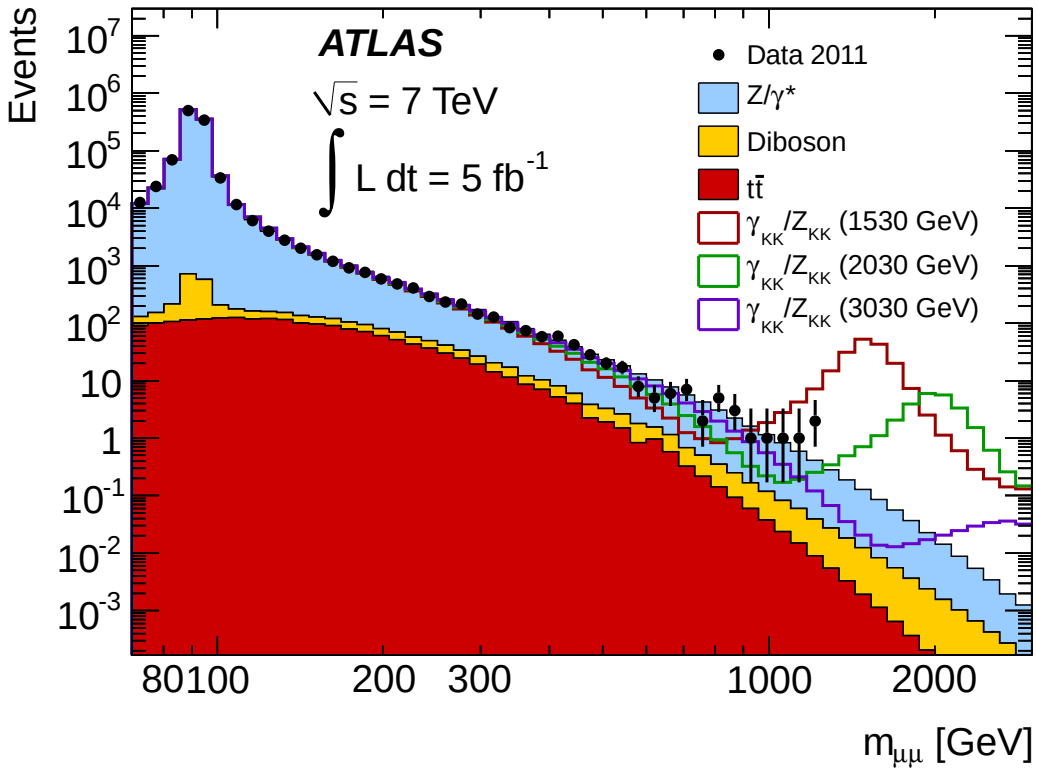

Figure 4.14.: The dimuon invariant mass distribution after the combined selection. The data (dots) are compared to the background sum and selected $\gamma_{\mathrm{KK}}/Z_{\mathrm{KK}}$ signals for illustration.

Chapter 5.

Systematic uncertainties

The systematic uncertainties in this analysis are reduced by the fact that the expected $m_{\mu\mu}$ distribution, both for the DY as a background and for the DY+X as a signal, are normalized to the data in a narrow region around the Z peak. The search (or limit-setting) is then started above $m_{\mu\mu} \sim 130$ GeV to avoid biases due to this normalization procedure. This choice of normalization makes the analysis insensitive to the uncertainty on the integrated luminosity as well as other mass-independent systematic uncertainties. In the signal search and limit setting, mass-dependent systematic uncertainties are incorporated as nuisance parameters whose variation is integrated over in the computation of the likelihood function [25]; most of these are small at low mass and grow at high mass.

Following the discussion started in section 4.2.2, the systematic uncertainties must be considered separately for the σB and for the coupling limit-setting approaches. The sources of these uncertainties are the same in both cases but the way these are interpreted is different between the two. Namely, for the σB limit-setting, where the interference is neglected and the DY is part of the backgrounds, the systematic uncertainties are essentially one-dimensional, i.e. they depend only on the dimuon mass, and most of them are applied to the backgrounds only with one exception. This is explained in sections 5.1, 5.2 and 5.3. For the coupling limit-setting, where the DY is treated as a part of the signal due to interference with the heavy states (Z'_{SSM} or $\gamma_{\mathrm{KK}}/Z_{\mathrm{KK}}$), the templates themselves and consequently also the systematic uncertainties must be two-dimensional, i.e. they depend on the dimuon mass but also on the coupling strength g (see equation 4.2.2). In other words, to use these systematic uncertainties later on, they must be parametrized with respect to g as well as the dimuon mass. To do so, it is essential to artificially separate the DY and X contributions of the 2D template (DY+X) and apply the systematic uncertainty separately for each part. The separation is done simply by subtraction of the DY part from the nominal DY+X 2D template. This is explained in 5.4.

The main systematic uncertainties of this analysis are listed in table 5.1 and figure 5.3. They include theoretical effects due to the PDF, QCD and electroweak corrections, as well as experimental effects, namely efficiency and resolution. It is assumed that the experimental uncertainties are correlated between signal and all types of backgrounds. According to the ATLAS-Exotics group convention, no theoretical uncertainties are applied on the signal expectation when setting limits. This has one exception in the case of the the coupling limit-setting. In that case, the uncertainty on the EW K-factor, which is applied to the entire DY + X template, is taken into account.

A more detailed description of the uncertainties is listed below.

5.1. Theoretical uncertainties

On the theoretical side, the systematic effects are as follows.

An uncertainty of 5% is associated with the DY γ/Z cross section, independent of $m_{\ell\ell}$. Due to the normalization by the number of events in the Z region, this uncertainty cancels out for the DY contribution and is valid only for the signal. The uncertainty of the electroweak corrections is 4.5% at $m_{\ell\ell} = 2$ TeV, and includes the effects of neglecting real boson emission, the difference in the electroweak scheme definition between PYTHIA6 and HORACE, and higher order electroweak and $\mathcal{O}(\alpha\alpha_s)$ corrections.

The following uncertainties on the NNLO cross section for the production of γ/Z or Z' bosons, which can be interpreted as uncertainties on the QCD K-factor, were studied (see also Table C.3). As the couplings to quarks differ for Z bosons and photons, K^{**}_{NNLO} was reevaluated assuming only Z (or Z') couplings. The relative difference between K^{**}_{NNLO} for Z (or Z') and γ/Z production is found to be within 1% for 70 GeV $< m_{\ell\ell} <$ 2250 GeV. The scale uncertainties are estimated by varying the renormalization (μ_R) and factorization scales (μ_F) independently up and down by a factor of two, but with the constraint $0.5 \leq \mu_F/\mu_R \leq 2$. The resulting maximum variations are taken as the uncertainties. They are within 1% for 70 GeV $< m_{\ell\ell} <$ 900 GeV and within 2.1% up to 2 TeV. The α_S and PDF uncertainties are evaluated using the MSTW2008NNLO eigenvector PDF sets and the PDF sets corresponding to variations of α_S, both at the 68% and 90% C.L. The α_S uncertainties at 68% (90%) C.L. are within 1.7% (4.6%) up to 2 TeV and are found to be considerably smaller than the PDF uncertainties. The PDF uncertainties were also evaluated for the envelope of the uncertainty

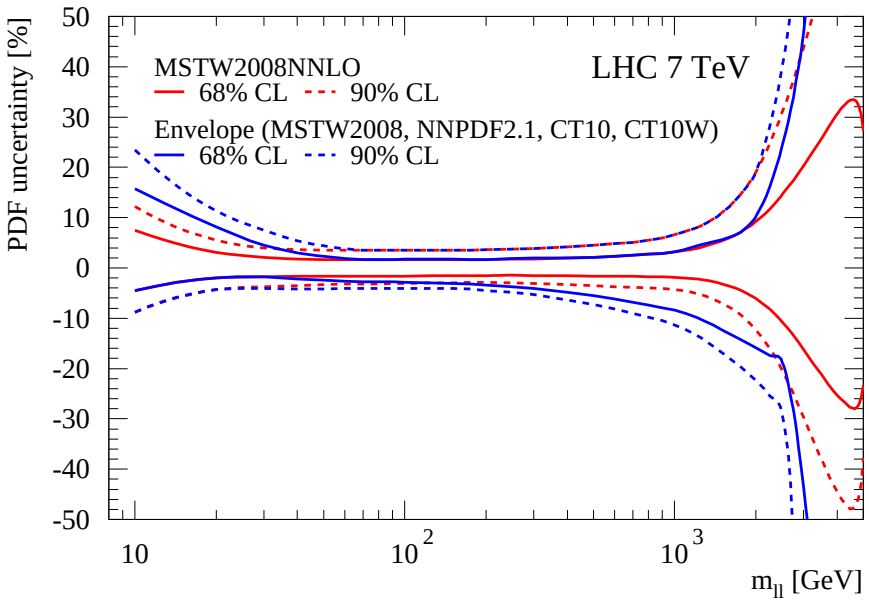

Figure 5.1.: PDF uncertainty (at 68% and 90% C.L.) on the NNLO DY lepton-pair production cross section $m_{\ell\ell}^2 \mathrm{d}\sigma_{\mathrm{NNLO}}/\mathrm{d}m_{\ell\ell}^2$ as function of dilepton mass $m_{\ell\ell}$. The 68% and 90% C.L. uncertainties are shown based on the MSTW2008 PDF error sets and based on the envelope of the PDF uncertainties using the MSTW2008, NNPDF2.1, CT10, and CT10W PDF sets.

bands of MSTW2008, NNPDF2.1, CT10, and CT10W at both 68% (90%) C.L.[1] As CT10 and CT10W only include NLO PDF sets, the envelope of MSTW2008, CT10, and CT10W was determined for the NLO cross section and used to rescale the MSTW2008 uncertainty band at NNLO. Over a wide mass region (about 70 GeV $< m_{\ell\ell} <$ 2 TeV) the envelope method reproduces the positive PDF uncertainty derived with MSTW2008 alone, whereas the lower uncertainty band is significantly increased. For masses beyond 2 TeV, the envelope method results in largely increased uncertainty regions. The relative PDF uncertainties are also shown in figure 5.1. Figure 5.2 shows the PDF uncertainties as well as the different contributions to the uncertainty of the QCD K-factor.

5.2. Experimental uncertainties

On the experimental side, the systematic effects are as follows.

[1] Since CT10 and CT10W only provide PDF uncertainty sets at 90% C.L., the corresponding uncertainty bands were rescaled by 1/1.645 for 68% C.L. regions.

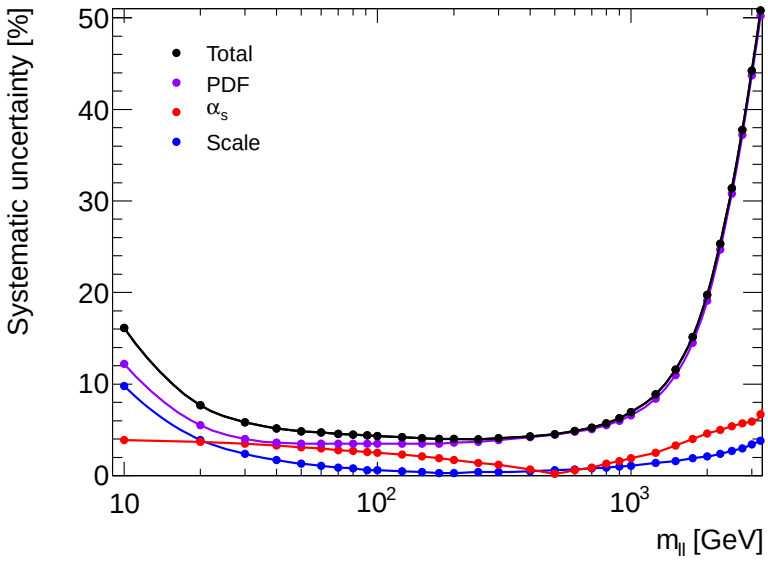

Figure 5.2.: Non EW theoretical systematic uncertainties on Drell Yan prediction (see appendix C for details). The PDF and α_s uncertainties are evaluated using the MSTW2008NNLO sets. The PDF uncertainty is given at 90% C.L.

One source of systematic uncertainty is the trigger and reconstruction efficiencies. The tag-and-probe method used to determine these efficiencies (see appendices E and F respectively) is based on events constrained in a narrow region around the Z peak. Therefore, it is sensitive for muons with $p_{\mathrm{T}} \leq 100$ GeV and shows that the efficiencies are independent of p_{T}. However, at much higher p_{T} values, the probability of muon Bremsstrahlung becomes non-negligible. In this case, the muon might lose a large fraction of its momentum, which might affect its trigger and reconstruction efficiency. A simulation-level study carried for the (equivalent) 2010 analysis [94], shows a systematic uncertainty increasing with dimuon mass with a rate of 3% per TeV. For a dimuon mass of 2 TeV, the overall systematic error on the trigger and reconstruction efficiency is estimated then to be 6%.

The uncertainty on the resolution due to residual misalignments in the muon spectrometer propagates to a change in the observed width of the signal line-shape, and affects the sensitivity of the search. This uncertainty is calculated using the nominal DY sample with all the corrections, including the smearing (see section 4.5) and the same sample, but with smearing parameters increased by $+1\sigma$. Both of these samples (nominal and oversmeared) are obtained using the MCP smearing tool. This effect leads to a loss of less than 3% of the events in the Z'_{SSM} signal peak at 2 TeV, within ± 1 RMS, and therefore it is neglected in the σB limit-setting. It will be shown in the next section that this uncertainty cannot be neglected in the coupling limit-setting.

The muon momentum scale is calibrated with a statistical precision of 0.1% using the $Z \to \ell\ell$ mass peak. Therefore, the momentum calibration uncertainty has negligible impact on the search.

The effect of pileup on the total signal acceptance has been studied and found to be negligible (see section 4.8).

Finally, the relative systematic uncertainty due to the diboson and $t\bar{t}$ background shape extrapolation in the tails of the distributions is also considered. This uncertainty has two sources; the choice of the fit function and the fit range variation. For the case of the coupling limit-setting, where the DY is not part of the background, this relative uncertainty is ranging between 10%-40% in the $m_{\mu\mu}$ range of 2-3 TeV. For the case of the σB limit-setting, where the DY is a part of the background, this relative uncertainty is 1.3% below 2 TeV and rises to 5% only at 3 TeV, which is negligible compared to the theoretical error at this mass, and therefore is neglected. That can be seen in figure 5.3.

5.3. All uncertainties

The main relative systematic uncertainties in this analysis are shown in in table 5.1 at $m_{\mu\mu} =$ 2 TeV and in figure 5.3 for the entire mass window of the search/limit-setting. In table 5.1, the contributions are divided into "Signal", "Drell-Yan" and "Other backgrounds" since the procedure allows to separate the influences of the different systematic uncertainties on these three parts. For the σB limit-setting, the "Drell-Yan" and "Other backgrounds" parts are treated as one part, simply "All backgrounds".

As mentioned above, no theoretical uncertainties are used for the signal in the limit setting. However, in the σB limit plots, their size is illustrated by the theoretical curves on the limit plots, where their thickness represents the uncertainties. In that context, for most of the other Z' models (few are also shown in the σB limit plots), these theoretical uncertainties are assumed to be the same as for the Z'_{SSM}, even though, strictly speaking, the PDF errors might be slightly different since the couplings to u- and d-type quarks vary between the different models.

Table 5.1.: Summary of systematic uncertainties on the expected numbers of events at $m_{\mu\mu} = 2$ TeV. NA indicates that the uncertainty is not applicable. The uncertainty on the PDF includes the QCD corrections uncertainty.

	With interference (coupling strength)			No interference (σB)	
Uncertainty source	Signal	Drell-Yan	Other backgrounds	Signal	All backgrounds
Normalization	5%	NA	NA	5%	NA
PDF/α_s /scale	NA	19%	19%	NA	19%
Electroweak corrections	4.5%	4.5%	NA	NA	4.5%
Efficiency	6%	6%	6%	6%	6%
Resolution	4.5%	4.5%	4.5%	4.5%	4.5%
Diboson and $t\bar{t}$ tail fit	NA	NA	12%	NA	1.3%
Total	9%	21%	24%	9%	21%

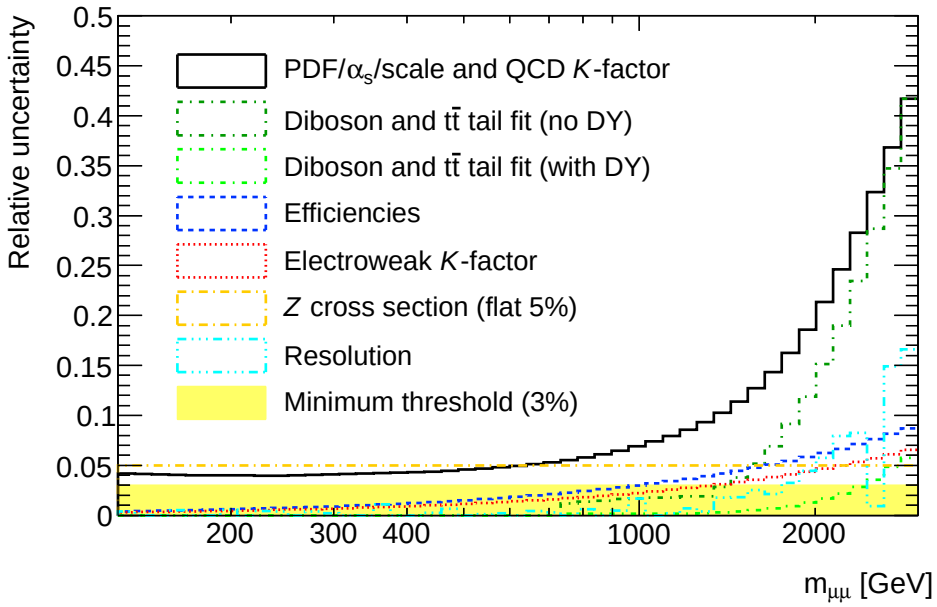

Figure 5.3.: The relative systematic uncertainties for this analysis, given in the $m_{\mu\mu}$ binning used for the search and limit setting.

5.4. Implementation of systematic uncertainties for the interfering signals

In this section it must be first shown how the coupling strength, g, is incorporated in the helicity amplitude of the $Z'_{\rm SSM}$ or $\gamma_{\rm KK}/Z_{\rm KK}$ signals. This will serve the basis of the discussion on how the relative systematic uncertainties for the coupling limit-setting are made.

5.4.1. Two dimensional signal templates

As mentioned in the introduction of chapter 4, if the interference of the heavy states with the DY is taken into account, then it is not possible to set limits on σB.

Instead, a coupling strength g is introduced and the signal templates for the coupling limit-setting can be then derived (per pole mass) using a four-dimensional analytic function with one free parameter, namely the strength g (see equation 4.2.2). The baseline for the reweighting are the binned DY samples (see table A.4). This is done for all the dimuon masses from that binned sample in the search window (130 GeV to 3 TeV), so the signal template is essentially two dimensional. For the remaining of this discussion, let us use the generic notation X for either $Z'_{\rm SSM}$ or $\gamma_{\rm KK}/Z_{\rm KK}$.

The coupling strength g simply multiplies the the fermion helicity couplings, $\mathcal{g}^f_\lambda$, to the heavy X state. In the case of the $Z'_{\rm SSM}$, these couplings $\mathcal{g}^f_\lambda$ are the $L-R$ couplings of the SM Z (see section 2.3.2). In the KK case, these are again the $L-R$ couplings of the SM Z, but enhanced by a factor of $\sqrt{2}$ for $Z_{\rm KK}$ or the enhanced charges ($\sqrt{2}Q_f$) for $\gamma_{\rm KK}$ (see section 2.4.4).

For simplicity, a general heavy X state will be considered and the notations will slightly differ from the ones used in the theory chapter 2. The resulting differential cross section, after the couplings scaling transformation, $\mathcal{g}^f_\lambda \longrightarrow g \times \mathcal{g}^f_\lambda$, is

$$\frac{d\sigma}{ds_{\ell\ell}} \propto \left|\mathrm{DY} + \frac{\mathcal{g}^q_\lambda \mathcal{g}^\ell_\lambda}{s_{\ell\ell} - M_X^2 + i\Gamma_X M_X}\right|^2 \longrightarrow \left|\mathrm{DY} + g^2 \frac{\mathcal{g}^q_\lambda \mathcal{g}^\ell_\lambda}{s_{\ell\ell} - M_X^2 + ig^2\Gamma_X M_X}\right|^2 \tag{5.4.1}$$

where $s_{\ell\ell} = m^2_{\ell\ell}$ is the square of the dilepton invariant mass. In the KK case, the X resonance breaks into two towers, i.e. $X = \sum_{n=1}^{\infty} Z^{(n)}_{\rm KK} + \sum_{n=1}^{\infty} \gamma^{(n)}_{\rm KK}$ as shown in section 2.4.4 with the appropriate replacements. The g^2 factor in the denominator is due to the X resonance width variation with g, i.e. $\Gamma_X(g) = g^2\Gamma_X$ (see e.g. equation 2.4.31). In this illustration, the angular

term and the summation over spins (helicities) is omitted for convenience where the full form can be seen e.g. in equation 2.2.13.

The full version of the DY+X differential cross section, that is simplified in equation 5.4.1, is the one used in the numerator of the weight function from equation 4.2.2, where the denominator is the same with only the DY part. In this parametrization, the value of g itself is allowed to float between 0 and $\sim$100.

It will be shown in section 8.1 that on certain circumstances, which are different between a Z'_{SSM} and a $\gamma_{\mathrm{KK}}/Z_{\mathrm{KK}}$, the cross-section factorizes as g^4 or as g^2 to a good approximation. Therefore, the derivation of the templates will be done in a grid of equally spaced values of either g^2 or g^4. These choices are related to the Bayesian approach [25] that is used in this analysis as will be thoroughly explained in chapter 8.

It is clear that the choice $g = 0$ returns the pure DY part and that the $g = 1$ choice returns the SSM scenario for the heavy X state. This will be of importance later on in the discussion on the limit itself since the limits are quoted for this ($g = 1$) choice.

Few examples of the templates are shown in figures 5.4 and 5.5 for a 2 TeV and 4 TeV X mass. Note that unlike in figure 5.4 for 2 TeV, the 4 TeV Z'_{SSM} is not shown in figure 5.5 since it is essentially the same as the DY($g = 0$) for any value $g^4 > 0$ in the range of dimuon masses up to 3 TeV (the high end in this analysis).

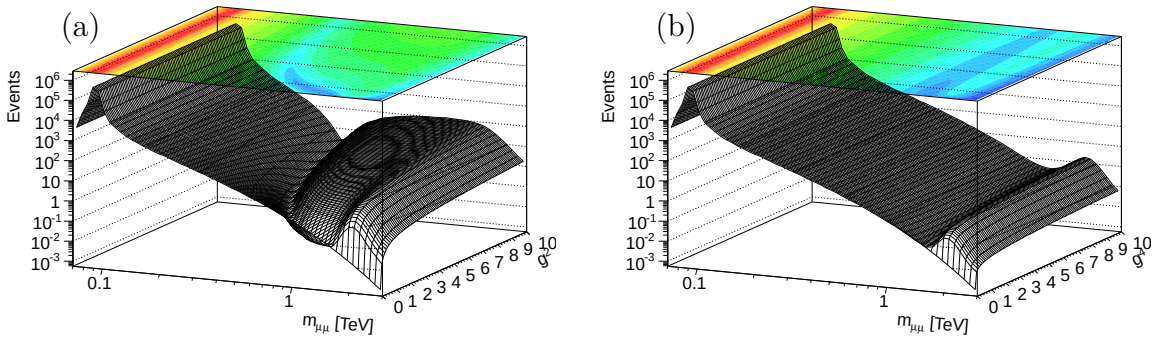

Figure 5.4.: Nominal 2D templates ($m_{\mu\mu}$ vs. g^N) for a resonance mass at 2 TeV. The KK template for g^2 in (a) and the Z'_{SSM} template for g^4 in (b).

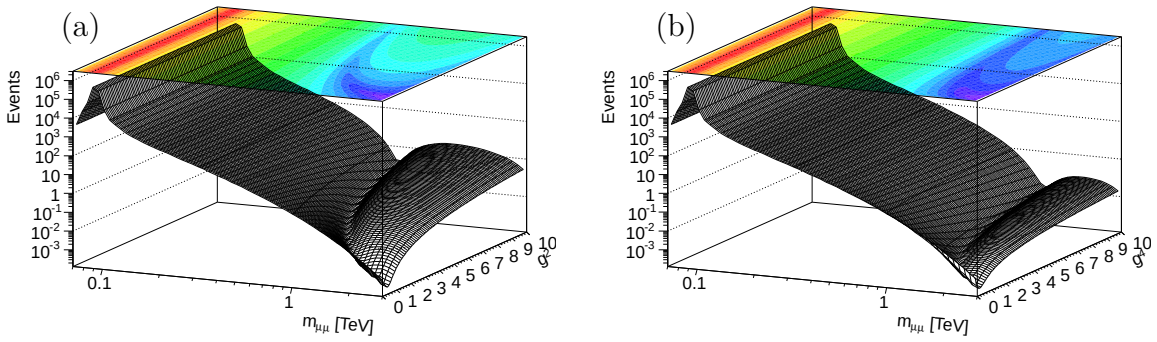

Figure 5.5.: Nominal KK 2D templates (a) for g^2 and (b) for g^4 for a KK mass at 4 TeV.

5.4.2. Two dimensional uncertainty templates

Since in the coupling limit-setting the DY is an integral part of the signal, it implies that the systematic uncertainties must also be parametrized with respect to the coupling strength g. Therefore, these are two-dimensional like the signal templates.

However, there are systematic uncertainties that should be applied only on the DY part of the template, while others should be applied only on the new physics part of the templates. This can be done by defining the relative systematic uncertainty (2D) template,

$$T_{\text{syst.}} = \frac{T^{\text{DY}+X}_{\text{syst.up}}}{T^{\text{DY}+X}_{\text{nominal}}} - 1 \tag{5.4.2}$$

where X is the new physics part, $T^{\text{DY}+X}_{\text{syst.up}}$ is the modified 2D template corresponding to an increase by $(+1\sigma)$ from a given source of systematic error and $T^{\text{DY}+X}_{\text{nominal}}$ is the nominal 2D template. This is of course done bin-by-bin in the two dimensions, $g^N - m_{\mu\mu}$, with $N = 2$ or 4.

The way to correctly obtain the modified 2D template ($T^{\text{DY}+X}_{\text{syst.up}}$) is as follows.

- for a DY-only uncertainty, subtract the nominal DY part from the nominal template and re-add the DY $+1\sigma$ overestimate
- for a new-physics-only uncertainty, subtract the DY part from the nominal DY+X template, modify the remaining part to get its modified $(+1\sigma)$ shape. This corresponds to modifying the $|\text{DY} + X|^2 - |\text{DY}|^2$ signal-only shape. Then, the nominal DY part has to be re-added.
- For the resolution systematic uncertainty, $T^{\text{DY}+X}_{\text{syst.up}}$ is simply the over-smeared, DY+X template

The modification of the DY+X part is done for every g^N-slice of the template, whereas the standard DY-only part is independent of g, as for the σB limit-setting (see section 5.3).

Few examples of the relative systematic uncertainty templates are shown in figures 5.6, 5.7 for a 2 TeV X mass and 5.8, 5.9 for a 4 TeV X mass.

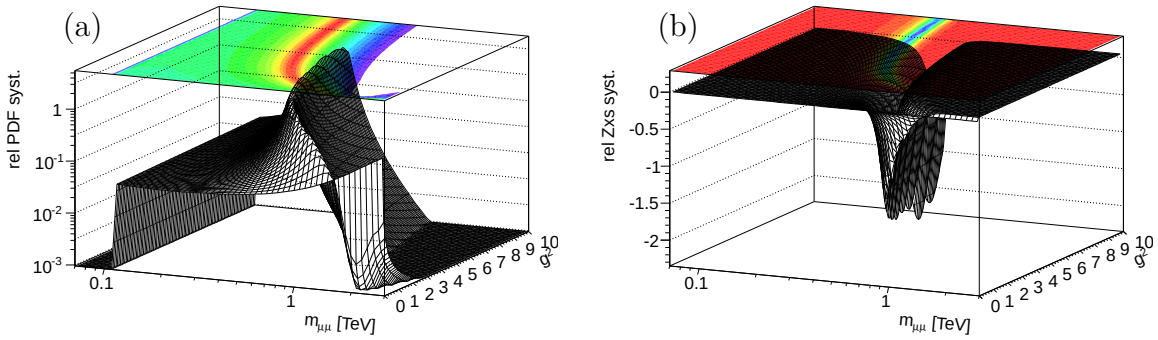

Figure 5.6.: Examples of two relative systematic uncertainty 2D templates ($m_{\mu\mu}$ vs. g^2) for a KK mass of 2 TeV. The PDF relative uncertainty template where only the DY part was modified in (a) and the Z cross section relative uncertainty template where only the KK part was modified in (b).

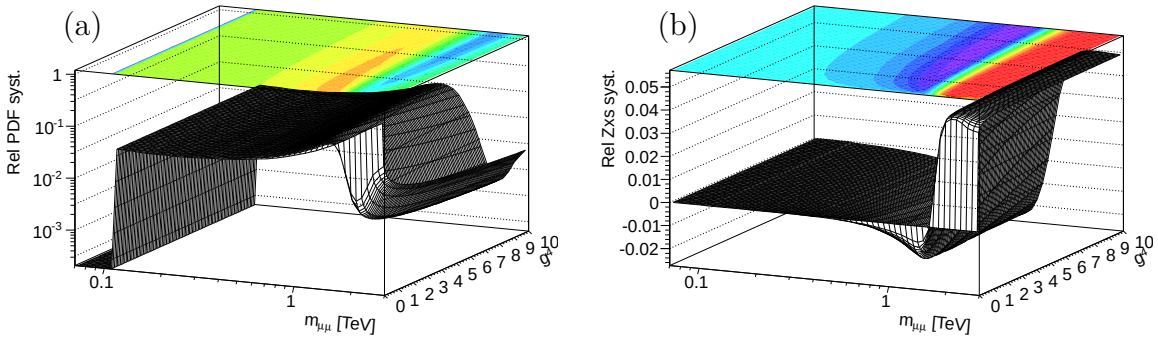

Figure 5.7.: Examples of two relative systematic uncertainty 2D templates ($m_{\mu\mu}$ vs. g^4) for a Z'_{SSM} mass of 2 TeV. The PDF relative uncertainty template where only the DY part was modified in (a) and the Z cross section relative uncertainty template where only the Z'_{SSM} part was modified in (b).

5.4.3. Remarks on the resolution uncertainty

Since in the KK case, the analysis is more sensitive to shape distortions, especially at the high-end of the mass window (2.5-3 TeV), it has been decided to account also for the resolution systematic uncertainty in the coupling limit-setting (it is neglected in the σB limit-setting).

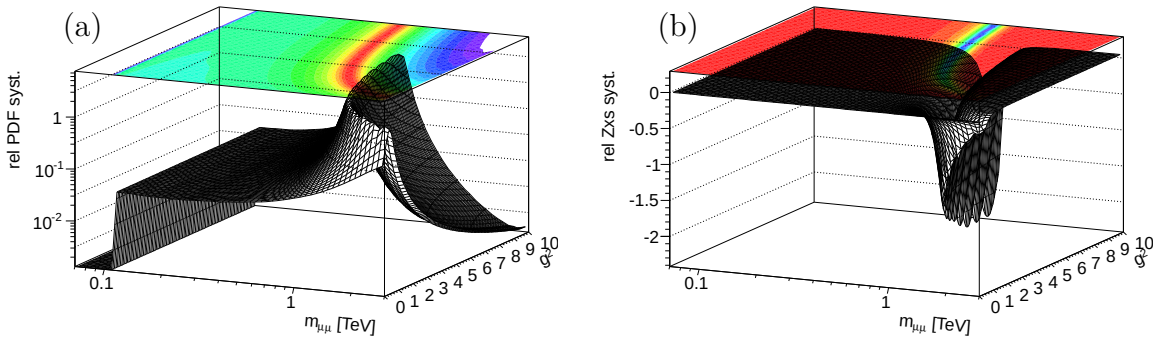

Figure 5.8.: Examples of two relative systematic uncertainty 2D templates ($m_{\mu\mu}$ vs. g^2) for a KK mas of 4 TeV. The PDF relative uncertainty template where only the DY part was modified in (a) and the Z cross section relative uncertainty template where only the KK part was modified in (b).

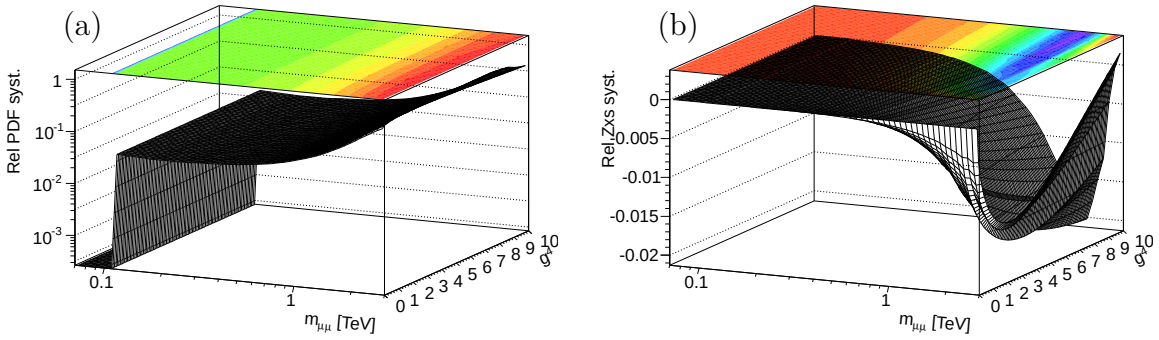

Figure 5.9.: Examples of two relative systematic uncertainty 2D templates ($m_{\mu\mu}$ vs. g^4) for a Z'_{SSM} mass of 4 Tev. The PDF relative uncertainty template where only the DY part was modified in (a) and the Z cross section relative uncertainty template where only the Z'_{SSM} part was modified in (b).

The resolution relative uncertainty for the DY scenario ($g = 0$) is mostly smaller than 3%-4% up to $m_{\mu\mu} \sim 2$ TeV. Above that, it increases up to 10%-15%. For the KK and the Z'_{SSM} cases ($g > 0$), it is mostly smaller than 5% but it can get up to 20%-30% above 2.5 TeV. It can be also seen that along the maximum KK negative-interference curve in the $g^N - m_{\mu\mu}$ space, the relative uncertainty is always higher than in the surrounding area. This can be seen in figures 5.10 and 5.11 for a 2 TeV and 4 TeV KK masses.

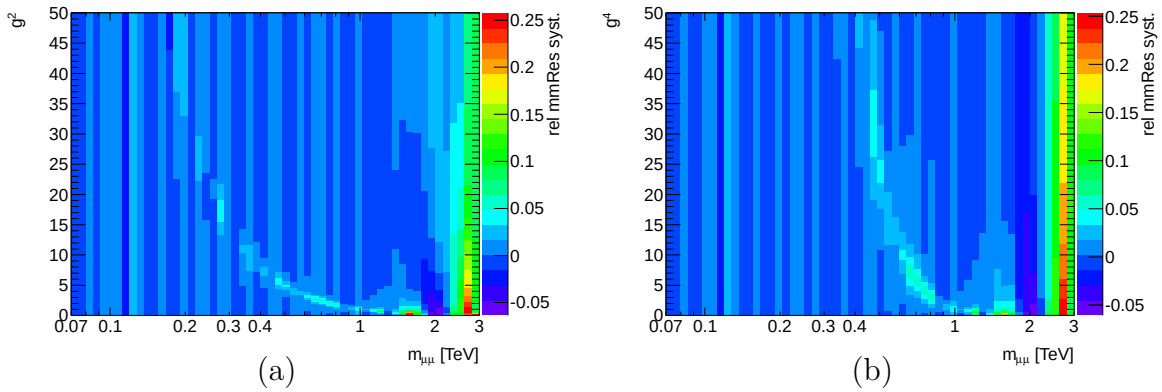

(a) (b)

Figure 5.10.: Resolution relative systematic uncertainty 2D templates for a KK mass of 2 TeV, (a) for g^2 and (b) for g^4. Note that the oversmearing is done for the entire template, i.e. without treating the DY and the KK parts separately.

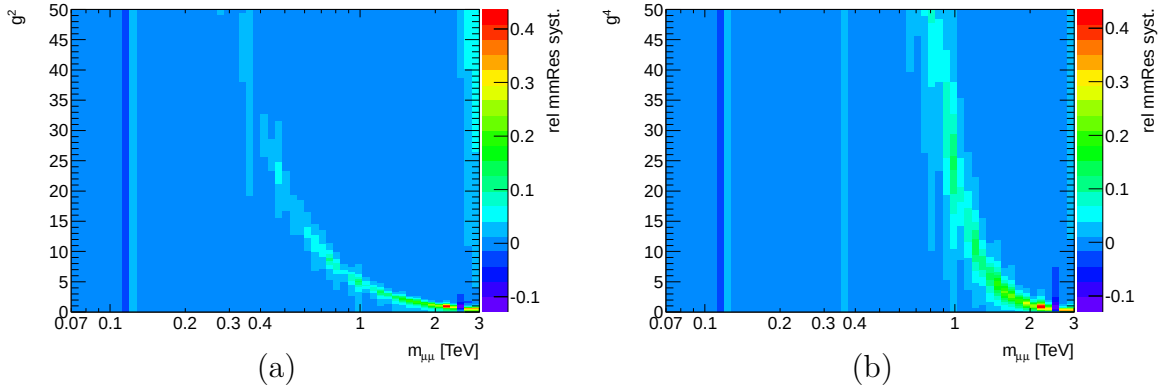

(a) (b)

Figure 5.11.: Resolution relative systematic uncertainty 2D templates for a KK mass of 4 TeV, (a) for g^2 and (b) for g^4. Note that the oversmearing is done for the entire template, i.e. without treating the DY and the KK parts separately.

Chapter 6.

Discovery statistics

6.1. Introduction

The consistency of the observed data with the standard model prediction is tested using several methods. The likelihood functions and test statistics are defined in this chapter and these are also used in the limit-setting that is described in the two subsequent chapters.

A signal search is first performed and in the absence of a signal, limits are calculated on the cross-section times branching fraction, σB (chapter 7) or the coupling strength, g (chapter 8). This is done in this analysis with the Bayesian approach, using the Bayesian analysis toolkit, BAT [25].

Hereafter, the final results will be shown for both the dilepton channels, dimuons and dielectrons, and for the combination when applicable.

6.2. Counting Experiment

In the presence of a signal, an excess or a deficit of candidate events is expected in the dilepton invariant mass distribution compared to background expectations, around or below the new particle pole mass, M_X, namely $M_{Z'_{\mathrm{SSM}}}$ or M_{KK} for this analysis. A single bin counting experiment can be used to analyze the data using the observed number of events above a kinematic threshold which depends on the mass hypothesis.

The expected number of events is the sum of expected background and signal, $N_{\mathrm{s+b}} = N_{\mathrm{s}} + N_{\mathrm{b}}$. Using Poisson statistics, the likelihood to observe N_{obs} events under the $N_{\mathrm{s+b}}$ hypothesis, for

a given X signal at mass M_X, is:

$$\mathcal{L}_{M_X}\left(N_{\rm s}, N_{\rm b}|\text{data}\right) = \frac{N_{\rm s+b}^{N_{\rm obs}} e^{-N_{\rm s+b}}}{N_{\rm obs}!} \times \text{Prior}\left(N_{\rm s}\right). \tag{6.2.1}$$

Uncertainties in any of the free parameters which are used to calculate $N_{\rm s}$ and $N_{\rm b}$ are included as nuisance parameters by multiplying by the probability density function (pdf) characterizing that uncertainty. If $n_{\rm syst.}$ such nuisance parameters $\theta_1, \ldots, \theta_{n_{\rm syst.}}$ are identified, then the likelihood becomes

$$\mathcal{L}_{M_X}\left(N_j, \theta_i|\text{data}\right) = \frac{\mu_k^{N_{\rm obs}} e^{-\mu_k}}{N_{\rm obs}!} \times \prod_{i=1}^{n_{\rm syst.}} G(\theta_i, 0, 1) \times \text{Prior}\left(N_{\rm s}\right) \tag{6.2.2}$$

where μ_k is Poisson mean representing the expected number of events,

$$\mu_k = \sum_{j={\rm s,b}} N_j \left(1 + \sum_{i}^{n_{\rm syst.}} \theta_i \epsilon_{ji}\right) \tag{6.2.3}$$

and where ϵ_{ji} is the relative change in normalization of process $j = {\rm s, b}$ (signal and background) for each source of systematic uncertainty i. The term $G(\theta_i, 0, 1)$ is the *prior* pdf for the nuisance parameters, θ_i, which is chosen to be Gaussian with unit width and mean 0.

The reduced likelihood, which is only a function of the parameter of interest ($N_{\rm s}$) is obtained by means of marginalization technique using Markov chain Monte Carlo (MCMC) as implemented in the BAT [25].

$$\mathcal{L}_{M_X}\left(N_j|\text{data}\right) = \int \mathcal{L}_{M_X}\left(N_j, \theta_1, \ldots, \theta_{n_{\rm syst.}}|\text{data}\right) d\theta_1 \cdots d\theta_{n_{\rm syst.}} \tag{6.2.4}$$

Note that instead of writing the likelihood function per pole mass (with a subscript M_X), it can be written with M_X being one of the function parameters, like e.g. N_j.

6.3. Template shape fitting

While a simple counting experiment can detect an overall excess or deficit of events, the details about the kinematic properties of these events will be lost.

Using template shape fitting, one can test the consistency of the standard model background-only hypothesis with the observed data over the entire spectrum of a sensitive search observable like the dilepton mass distribution. This provides additional information about the nature

of a potential signal detected by ATLAS. It is especially important to distinguish resonances or deficits originating from new physics, from possibly other sources like experimental biases, MC background mismodeling or "conservative" background (over) estimation. As a result, template fitting in a signal search is less sensitive to such systematic biases which are spread over large $m_{\mu\mu}$ range, compared to a simple counting experiment.

Template shape fitting is essentially a counting experiment in many bins of the $m_{\ell\ell}$ distribution and the likelihood function is the product of the single bin counting experiment likelihood function. The sensitivity of the search is enhanced over a single bin counting experiment, by the exclusive treatment of bins with different S/B ratios. The shape information helps to better constrain signal and background contribution of the candidate sample.

Like in the previous case, the reduced likelihood is obtained by means of marginalization technique using MCMC [25].

6.3.1. The likelihood function for non-interfering signals

In the case where the signal is not interfering with the DY, there is a clear distinction between the signal and the backgrounds which include the DY. This is typical for a narrow resonance signals and it will be deployed for the Z'_{SSM} later on.

The expected number of events in the invariant mass bin k is represented by the Poisson mean,

$$\mu_k = \sum_{j=\mathrm{s,b}} N_j T_{jk} \left(1 + \sum_{i}^{n_{\mathrm{syst.}}} \theta_i \epsilon_{jik}\right) \tag{6.3.1}$$

which is a sum of signal and total background plus their systematic shifts. Under this definition, T_{jk} are the (unit area) template shapes and ϵ_{jik} are the bin-by-bin systematic variations. As before, θ_i are the nuisance parameters. The binned likelihood function is a product of all Poisson terms corresponding to all of the invariant mass bins, n_{bins},

$$\mathcal{L}_{M_X}\left(N_j, \theta_i | \mathrm{data}\right) = \prod_{k=1}^{n_{\mathrm{bins}}} \frac{\mu_k^{N_{\mathrm{obs}}^k} e^{-\mu_k}}{N_{\mathrm{obs}}^k !} \times \prod_{i=1}^{n_{\mathrm{syst.}}} G(\theta_i, 0, 1) \times \mathrm{Prior}\left(N_{\mathrm{s}}\right) \tag{6.3.2}$$

where the signal and total background correspond to template numbers $j = \mathrm{s}$ and $j = \mathrm{b}$ respectively. Finally, $G(\theta_i, 0, 1)$ is the same unit width Gaussian *prior* pdf for nuisance parameters (θ_i) that control bin-by-bin systematic variations (ϵ_{jik}) of the template shapes (T_{jk}).

Note that N_j are simply the two overall-normalizations of the signal and the background where the (binned) shape information is stored in the normalized signal and background templates, T_{jk}. These (N_j) are the free parameters of interest in the likelihood function. Eventually, these would have to be extracted for any given M_X, especially $N_{\rm s}$ which can easily be converted into the equivalent σB value.

6.3.2. The likelihood function for interfering signals

In the case where the signal is strongly interfering with the DY, there is no clear distinction between the signal and the DY but between the signal+DY and the other (non-DY) backgrounds. This is typical for signals like the $\gamma_{\rm KK}/Z_{\rm KK}$ and it will be deployed for this case later on.

The likelihood function for a given M_X in that case is

$$\mathcal{L}_{M_X}\left(g, N^k_{\rm b,noDY}, \theta_i|{\rm data}\right) = \prod_k^{n_{\rm bins}} \frac{\mu_k^{N^k_{\rm obs}} \times e^{-\mu_k}}{N^k_{\rm obs}!} \times \prod_i^{n_{\rm syst.}} G\left(\theta_i, 0, 1\right) \times {\rm Prior}\left(g^N\right) \tag{6.3.3}$$

where instead of writing $N_{j=\rm b}$ as in equation 6.3.2, the background part ($j = \rm b$) is the same but binned, without the DY contribution and normalized to the ad-hoc luminosity (the sum of the contributions is always normalized to the data in the Z-peak area). Correspondingly, the signal parametrization (previously $N_{j=\rm s}$ in equation 6.3.2) is represented now by the coupling strength free parameter, g, that was introduced in the previous chapter. The templates contain both the overall-normalization and the shape information.

Note that the templates here are not normalized to unity as in the previous case but they are normalized to the data in the Z-peak range which is out of the search/limit mass range to avoid a potential bias. The free parameter of interest in the likelihood function here is g and not the number of signal/background events N_j as before. Eventually, this would have to be extracted for any given M_X.

The systematic uncertainties are again incorporated via nuisance parameters, θ_i, with $G\left(\theta_i, 0, 1\right)$ again being a Gaussian *prior* pdf in θ_i with mean 0 and $\sigma = 1$. Like in equation 6.3.1, the expected number of events (+ the systematic shifts) in the k'th $m_{\ell\ell}$ bin is

$$\mu_k = N^k_{\rm s}(g)\left(1 + \sum_i^{n_{\rm syst.}} \theta_i \cdot S^k_{i,\rm s}(g)\right) + N^k_{\rm b,noDY}\left(1 + \sum_i^{n_{\rm syst.}} \theta_i \cdot S^k_{i,\rm b}\right) \tag{6.3.4}$$

where $N_{\rm s}^k(g)$ is the nominal signal template value in the k'th $m_{\ell\ell}$ bin as a function of g that includes the DY interfering part, i.e. $|\mathrm{DY}(m_{\ell\ell}) + X(m_{\ell\ell}, g)|^2$, and where $N_{\rm b,noDY}^k$ is the nominal sum of other backgrounds (no DY) value in the k'th $m_{\ell\ell}$ bin.

Note that contrary to the previous case, where the shape information was stored in T_{ij} and the overall-normalization was N_j, the shape information here is stored in the full 2D template, $N_{\rm s}^k(g)$ and in the 1D background, $N_{\rm b,noDY}^k$.

Finally, the term $S_{i,\rm s}^k(g)$ is the relative systematic uncertainty template value of the interfering signal, in the k'th $m_{\ell\ell}$ bin as a function of g. It is obtained from the 2D relative systematic uncertainty templates that were shown in chapter 5. The term $S_{i,\rm b}^k$ is the standard 1D relative systematic uncertainty of the "other backgrounds" (no DY) that were also shown in chapter 5.

For practical reasons, the dependency of $N_{\rm s}^k$ in g for every $m_{\ell\ell}$ bin is transformed into a continuous function of g^2 or g^4 which is given as input to BAT.

6.4. Combination of analysis channels

The two independent analysis channels (dimuon and dielectron) are combined by means of extending the likelihood function. The joint likelihood for two independent channels is simply the product of Poisson probabilities of each individual bin in each channel. Since both channels differ in signal acceptance and data size (integrated luminosity) the likelihood function is rewritten in terms of the common variable of interest.

For example, in the non-interfering signals case as in section 6.3.1, it is namely the cross section of a potential X signal. This is done by the simple substitution of the X normalization parameter (e.g. $N_{Z'_{\rm SSM}}$) and expressing it in terms of the X cross section times branching ratio (e.g. $\sigma_{Z'_{\rm SSM}} B$):

$$\mathcal{L}_{M_X}\left((\sigma B)_X, \theta_i|\mathrm{data}\right) = \prod_{l=1}^{n_{\rm channels}} \prod_{k=1}^{n_{\rm bins}} \frac{\mu_{lk}^{N_{\rm obs}^{lk}} e^{-\mu_{lk}}}{N_{\rm obs}^{lk}!} \prod_{i=1}^{n_{\rm syst.}} G(\theta_i, 0, 1) \times \mathrm{Prior}\left((\sigma B)_X\right) \qquad (6.4.1)$$

where $\mu_{lk} \sim \sum_j T_{ljk}\left(1 + \sum_i^{n_{\rm syst.}} \theta_i \epsilon_{ljik}\right)$ and it is also proportional to $(\sigma B)_X$. Sources of systematic uncertainties are treated in the same way as in the single channel analysis but can be correlated across channel as well as across processes.

6.5. Signal scan

The template shape fitting technique is used to search for a Z'_{SSM} signal of unknown mass and unknown rate in ATLAS dilepton data. The significance of a potential Z'_{SSM} signal is summarized by a p-value.

6.5.1. The p-value

To define the p-value, the concept of the hypothesis tests needs to be introduced. To start with, the data is compared to null-hypothesis, H_0, and their difference is quantified by a single number. This number is called the *test statistic* and is denoted by t. For example, the test statistic can be a χ^2, namely

$$t = \sum_{k=1}^{n_{\mathrm{bins}}} \left(\frac{N_{\mathrm{obs}}^k - N_{\mathrm{b}}^k}{\sqrt{N_{\mathrm{b}}^k}} \right)^2 \tag{6.5.1}$$

where N_{obs}^k denotes the observed events in bin k, and N_{b}^k is the number of events expected by H_0 in the same bin.

The p-value is the probability that, when H_0 is assumed, the test statistic will be equal to or greater than the test statistic obtained by comparing the actual data to H_0: Pseudo-data are generated, following the expectation of H_0. In each pseudo-data spectrum, the same test statistic t is computed, comparing the pseudo-data to H_0. The distribution of test statistics from pseudo-experiments is made.

$$p\text{−value} = P\left(t \geq t_{\mathrm{obs}} | H_0\right) \tag{6.5.2}$$

where the test statistic t is a random variable depending on how pseudo-data fluctuate around H_0, and t_{obs} is the observed statistic from comparing the data to H_0. If the exact probability density function (pdf) of t under H_0 is known ($\rho(t|H_0)$), then the p-value is exactly computed as

$$p\text{−value} = \int_{t_{\mathrm{obs}}}^{\infty} \rho(t|H_0) dt \tag{6.5.3}$$

For example, under some assumptions of Gaussianity, the χ^2 statistic from equation 6.5.1 follows a χ^2-distribution which can be analytically integrated to obtain the p-value.

When $\rho(t|H_0)$ is estimated using pseudo-experiments, as in this analysis, then the p-value is estimated as a binomial success probability. Thus, the p-value is interpretable as a false-discovery probability.

In the context of this search, the p-value is the probability of observing an outcome of an analysis at least as signal-like as the one observed in data, assuming that a signal is absent. The common convention is that a p-value less than 1.35×10^{-3} constitutes evidence for a signal and a p-value less than 2.87×10^{-7} constitutes a discovery. These are one-sided integrals of the tails of a unit Gaussian distribution beyond $+3\sigma$ and $+5\sigma$, respectively.

6.5.2. The test statistic

For non-interfering signals, a natural choice for the test statistic is based on the Neyman-Pearson lemma which states that when performing a hypothesis test between two hypotheses - in this case one assuming the presence of signal and background (S+B) and the other one assuming only SM background (B) - the log-likelihood-ratio (LLR) $\mathrm{LLR} = -2\ln\frac{\mathcal{L}(\mathrm{S+B})}{\mathcal{L}(\mathrm{B})}$ is the best test to reject (B) in favor of (S+B). In the presence of nuisance parameters to account for systematic uncertainties, the LLR test statistic can be written more explicitly as:

$$t \equiv \mathrm{LLR} = -2\ln\frac{\mathcal{L}\left(\hat{N}_\mathrm{s}, \hat{M}_X, \hat{\theta}_i|\mathrm{data}\right)}{\mathcal{L}\left(N_\mathrm{s}=0, \hat{\hat{\theta}}_i|\mathrm{data}\right)} \tag{6.5.4}$$

where $\hat{N}_\mathrm{s}$ and $\hat{M}_X$ are the best-fit values of the X normalization and mass and $\hat{\theta}_i$ are the best-fit values of the nuisance parameters which maximize $\mathcal{L}$ given the data, assuming a X signal is present. For the background only hypothesis, $\hat{\hat{\theta}}_i$ are the best-fit values of the nuisance parameters which maximize $\mathcal{L}$, assuming that no X signal is present. Note that contrary to equation 6.3.2 or 6.3.3, there is no subscript M_X for the likelihood functions in 6.5.4. Instead, this is included as a parameter of the likelihood function in the numerator and is absent from the one in the denominator, as appropriate for H_0.

Since the mass and the rate of a hypothetical Z' is unknown *a-priori*, a likelihood fit is performed for the best-fit signal cross section ($\sigma_{Z'}$) and the best-fit mass of Z' ($M_{Z'}$) present in data. This approach accounts naturally for the "look elsewhere effect".

Figure 6.1 shows the marginalized posterior probability density as a function of $N_{Z'_{\mathrm{SSM}}}$ and $M_{Z'_{\mathrm{SSM}}}$ for the (S+B) hypothesis fit to ATLAS data in the electron (left) and muon (right) channels Figure 6.2 shows the same for their combination. The high-t regions support the

(S+B) hypothesis for particular values of $N_{Z'_{\mathrm{SSM}}}$ and $M_{Z'_{\mathrm{SSM}}}$ and correspond to localized excesses in the dilepton spectrum. The significance of the excess is quantified using the LLR test statistic.

The expected distribution of LLR assuming the background only (B) hypothesis is computed numerically performing pseudo-experiments varying all sources of systematic uncertainty as described in chapter 5.

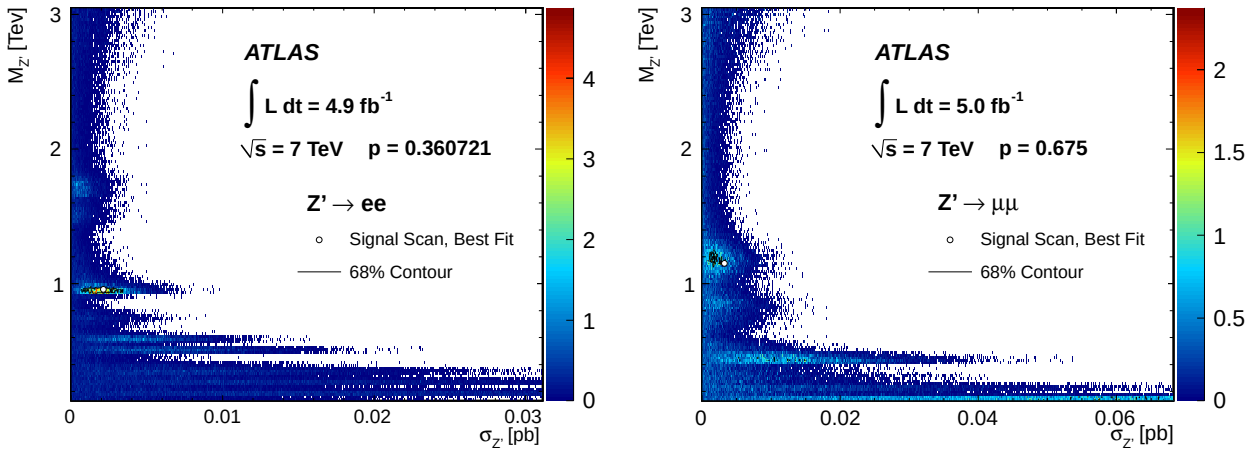

Figure 6.1.: Absolute value of the log-likelihood-ratio test statistic as a function of $\sigma_{Z'}$ and $M_{Z'}$ for the likelihood fit to ATLAS data in the dielectron (left) and dimuon channel (right).

For the dielectron sample, a p-value of 36% is observed where for the dimuon sample, the observed p-value is 68%. For the combination of both channels, the observed p-value is 40%.

6.6. Bump hunting

The presence of a resonance is also tested using the BumpHunter algorithm [95].

The BumpHunter is designed to address a different question than the one used in the previous section. For this question, only the data and H_0 are required, and no specific signal is assumed, hence it is model-independent.

The BumpHunter algorithm scans the spectrum of interest (in this case the dilepton invariant mass) in windows of progressively increasing width. In a given window the algorithm computes a negative logarithm of the Poisson probability for the background to fluctuate to, above or below the prediction. The largest value of the computation over all assumed search windows and all considered window widths is the final test statistic. The computation in a

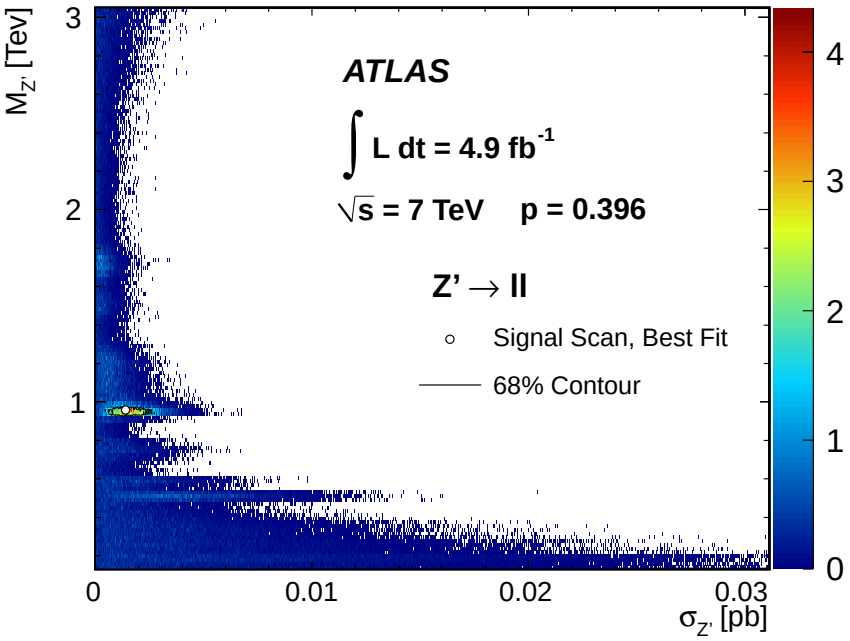

Figure 6.2.: Absolute value of the log-likelihood-ratio test statistic as a function of $\sigma_{Z'}$ and $M_{Z'}$ for the likelihood fit to ATLAS data for the combination of the dielectron and dimuon channel.

given window is only performed if there is an excess over prediction and when the sidebands show good agreement with the prediction. The algorithm is described in more detail in [95].

The reported p-value in the electron channel is 64% and in the muon channel 91%.

6.7. Local significances

Finally, the differences between data and expectation are displayed using the tool developed by G. Choudalakis and D. Casadei [96]. The result is shown in figure 6.3 for both electron and muon channels. The largest positive local significance is $< 2\sigma$ in the electron channel and $\sim 1\sigma$ in the muon channel, and the largest negative local significance is about -1.5σ and -2σ respectively).

In conclusion: the data are consistent with the standard model prediction in this search.

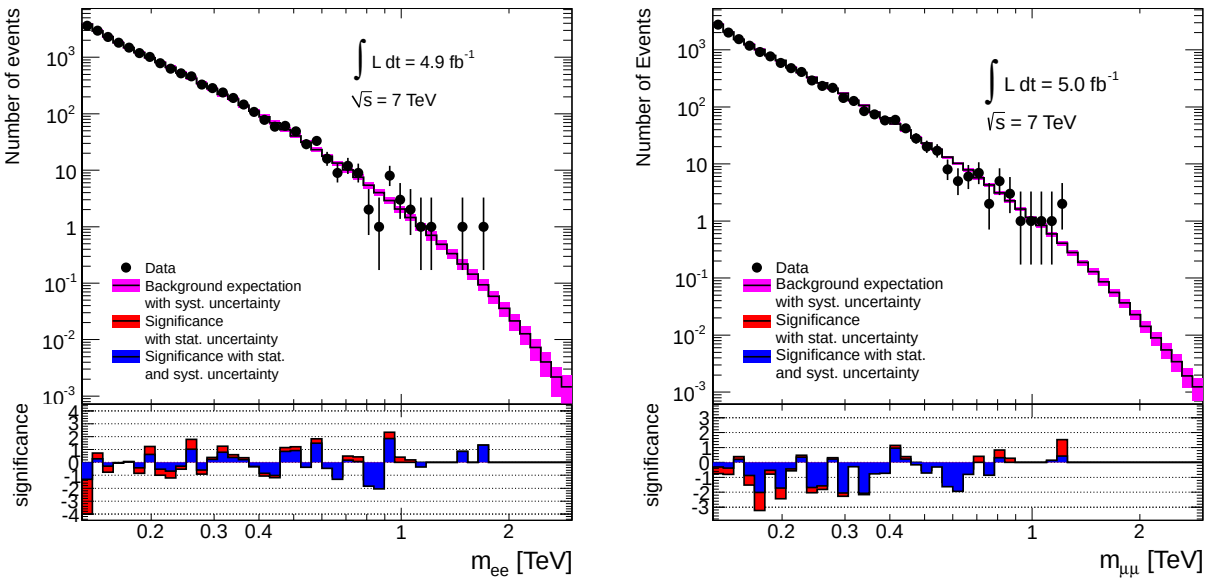

Figure 6.3.: Differences between data and expectation in the electron (left) and muon (right) channels. The mass range is from 128 GeV to 3 TeV.

Chapter 7.

Limits on the cross section

In the absence of a signal, an upper limit on the number of events N_X produced by the decay of a new resonance $X = Z'_{\text{SSM}}$ is determined at the 95% confidence level (C.L.) using a Bayesian approach [25].

The invariant mass distribution of the data is compared to templates of the expected backgrounds and varying amounts of signal at varying pole masses in the 0.13-3.0 TeV range[1]. The templates provide the expected yield of events (μ) in each $m_{\ell\ell}$ bin: $\mu = N_X(\lambda, \bar{\theta}) + N_{\text{DY}}(\bar{\theta}) + N_{\text{bg,noDY}}(\bar{\theta})$, where λ represents the model parameters, $\bar{\theta}$ the set of nuisance parameters and N_X, N_{DY}, $N_{\text{bg,noDY}}$ are respectively the number of events coming from the new resonance, DY and other backgrounds respectively. The separation of the backgrounds into a DY part and no DY part is due to the different treatment of systematic uncertainties.

The interference between signal and DY is neglected. In addition, the width of the Z'_{SSM} in each template is kept fixed although the entire template shape is allowed to scale up and down. Since the cross-section of such a Z'_{SSM} is fixed to some known value (see equation 2.3.8), this scaling can be viewed as variation of the couplings but then, also the width is expected to change accordingly. Thus, there is no a-priori physically-motivated reason to think the resonance can scale up and down while the width is kept fixed.

Some examples of signal templates are shown in appendix G.

A likelihood function is defined as the product of the Poisson probabilities over all mass bins in the search region, where the Poisson probability in each bin is evaluated for the observed number of data events given the expectation from the signal template and accounting for all

[1] The exact range actually starts at 128.05 GeV.

the systematic uncertainties as described in chapter 5. This likelihood function is given in equation 6.3.2 for an individual channel.

The total acceptance for signal as a function of mass is propagated into the expectation. For each X pole mass, a uniform prior in the X production cross-section times branching fraction, σB, is used.

The limit on N_X is converted into a limit on cross section times branching fraction $\sigma B(X \to \ell^+\ell^-)$ by scaling with the observed number of Z boson events and the known value of $\sigma B(Z \to \ell^+\ell^-)$:

$$\sigma B(X) = \sigma B(Z) \frac{N_X \, \mathcal{A}\epsilon(Z)}{N_Z \, \mathcal{A}\epsilon(X)} \tag{7.0.1}$$

where,

- $\sigma B(Z) = 0.989 \pm 0.049$ nb is the inclusive Z cross section for $m_{\ell\ell} > 60$ GeV [92];
- $\mathcal{A}\epsilon(Z)$, calculated with the inclusive Z MC sample, is the efficiency of requiring $70 < m_{\ell\ell} < 110$ GeV times the average selection efficiency for events with $m_{\ell\ell} > 60$ GeV:

$$\mathcal{A}\epsilon(Z) = \frac{N^{MC}(\text{selected events in } 70 < m_{\ell\ell} < 110 \text{ GeV})}{N^{MC}(\text{all events in } m_{\ell\ell} > 60 \text{ GeV})}$$

- N_Z is the number of Z events in the $70 < m_{\ell\ell} < 110$ GeV range;
- $\mathcal{A}\epsilon(X)$ is the acceptance times efficiency for a given X pole mass.

$\mathcal{A}\epsilon(X)$ is the ratio between the integral of each template after full selection, and the integral of the corresponding template without selection, i.e the truth template integral. This is done per X mass as shown in figure 7.1 for the Z'_{SSM}. The resulting shape is fitted to a sixth-order polynomial which is used later for translating N_X to σB according to equation 7.0.1. The luminosity normalization is replaced by a normalization to the data, using the Z number of events and acceptance above 0.13 TeV in order to cancel systematic uncertainties.

The expected exclusion limits are determined using simulated pseudo-experiments containing only standard model processes by evaluating the 95% C.L. upper limits for each pseudoexperiment for each fixed value of M_X. The median of the distribution of limits is chosen to represent the expected limit. The ensemble of limits is also used to find the 68% and 95% envelope of the expected limits as a function of M_X.

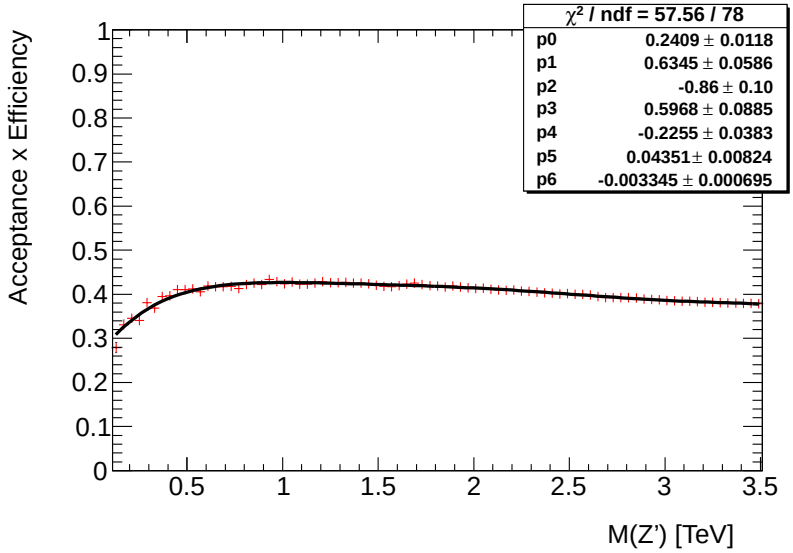

Figure 7.1.: Total acceptance times efficiency as a function of the pole mass for Z'_{SSM}.

The reduced likelihood function is obtained by a marginalization[2] technique used by BAT [25] and is then converted into a posterior probability density using Bayes' theorem, assuming a uniform positive prior in σB, i.e. $\mathrm{Prior}\,(\sigma B) = 1$. The maximum of the posterior probability density $P((\sigma B)_X|\mathrm{data})$ corresponds to the most likely signal content given the data. The 95% Bayesian upper limit, $(\sigma B)^{95}$, is obtained by integrating the posterior probability density:

$$0.95 = \frac{\int_0^{(\sigma B)^{95}} \mathcal{L}\,(\sigma B)\,d(\sigma B)}{\int_0^{\infty} \mathcal{L}\,(\sigma B)\,d(\sigma B)} \tag{7.0.2}$$

A combinations of the two dilepton channels (dimuon and dielectron) is performed by using a joint likelihood as the one given in equation 6.4.1.

Finally, lower limits on M_X are obtained by comparing the expected σB with the upper limits on σB as a function of M_X, i.e. the cross section limits are converted into mass limits using the theoretical σB dependence on the resonance mass.

[2]Marginalization means integrating out over irrelevant variables, e.g. the nuisance parameters, like it is done in equation 6.2.4.

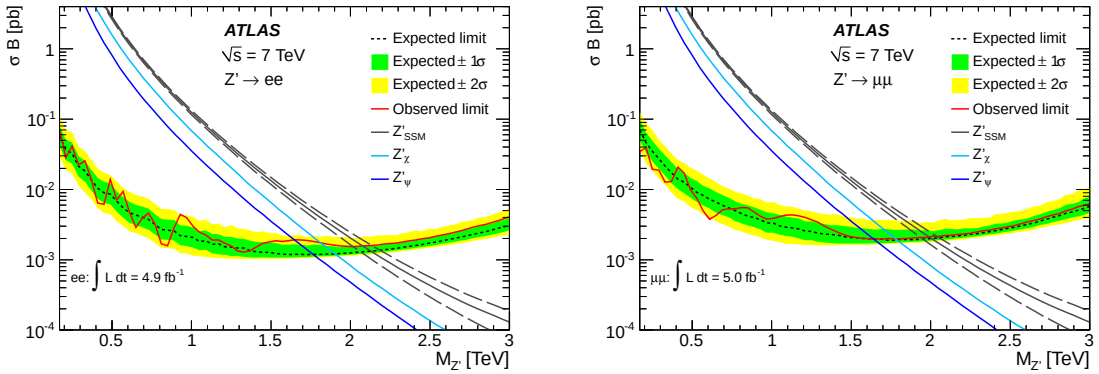

Figure 7.2.: Expected and observed 95% C.L. limits on σB and expected σB for Z'_{SSM} production and the two E_6-motivated Z' models with lowest and highest σB for the dielectron (left), and the dimuon selection (right). The two dashed lines forming a band around the Z'_{SSM} theory curve represent the theoretical uncertainty and holds for the other theory curves.

7.1. Limits on spin-1 Z'

Figure 7.2 (left) shows for the dielectron channel the 95% C.L. observed and expected exclusion limits on $\sigma B(Z' \to e^+e^-)$. It also shows the theoretical cross section times branching fraction for the Z'_{SSM} and for the lowest and highest σB of E_6-motivated Z' models. Similarly, Figure 7.2 (right) show the same results in the case of the dimuon selection. Figure 7.3 shows the 95% C.L. exclusion limit on σB for the combination of the electron and muon channels, and Figure 7.4 shows the ratio of this limit divided by the Z'_{SSM} cross section.

The 95% C.L. σB limit is used to set mass limits for each of the considered models. Mass limits obtained for the Z'_{SSM} are displayed in Table 7.1. The combined mass limit for the Z'_{SSM} is 2.22 TeV (observed) and 2.25 TeV (expected). The combined mass limits on the E_6-motivated models are given in Table 7.2.

Table 7.1.: The e^+e^-, $\mu^+\mu^-$ and combined 95% C.L. mass limits on Z'_{SSM}.

Channel	Observed limit mass [TeV]	Expected limit mass [TeV]
$Z'_{\mathrm{SSM}} \to e^+e^-$	2.08	2.13
$Z'_{\mathrm{SSM}} \to \mu^+\mu^-$	1.99	2.00
$Z'_{\mathrm{SSM}} \to \ell^+\ell^-$	2.22	2.25

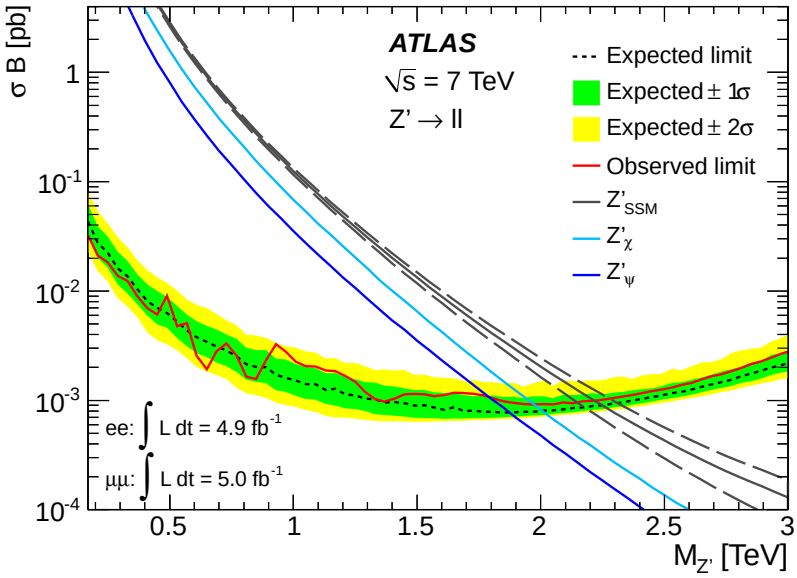

Figure 7.3.: Expected and observed 95% C.L. limits on σB and expected σB for Z'_{SSM} production and the two E_6-motivated Z' models with lowest and highest σB for the combination of the electron and muon channels. The two dashed lines forming a band around the Z'_{SSM} theory curve represent the theoretical uncertainty and holds for the other theory curves.

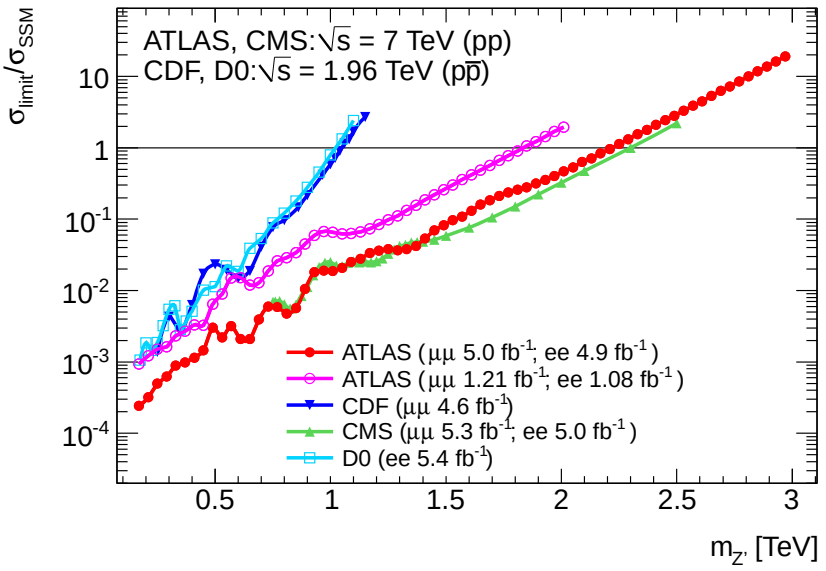

Figure 7.4.: Ratio of observed combined limit for the Z' search divided by the Z'_{SSM} cross section, using the combination of both channels.

Table 7.2.: The combined mass limits at 95% C.L. on the E_6-motivated Z' models.

Model	Z'_ψ	Z'_{N}	Z'_η	Z'_{I}	Z'_{S}	Z'_χ
Observed Mass limit [TeV]	1.79	1.79	1.87	1.86	1.91	1.97
Expected Mass limit [TeV]	1.87	1.87	1.92	1.91	1.95	2.00

Chapter 8.

Limits on the couplings

The motivation for developing the technique presented here is the unique signature of the already discussed S^1/Z_2 KK model. Although eventually, the statistical treatment is in principle identical to the one presented in the previous chapter (7), the interpretation and the actual mechanism is completely different. This is because of the strong destructive interference which makes it impossible and meaningless to set limits on the cross section. Note that the methods described here can be perfectly used also for any other signal, e.g. for a Z'_{SSM}, as it will be done later in this chapter to cross check the σB method.

8.1. The choice of the prior

A question arises concerning which variables should be assumed to have a flat prior. In the non-interfering Z'_{SSM} the natural choice was σB (see chapter 7). In the interfering case, instead of putting a limit on σB, a coupling strength g was introduced (see section 5.4) and the signals were derived (per X mass) using a four-dimensional analytic function (equation 4.2.2) with this coupling strength, g, as a free parameter. For convenience, the cross-section from equation 5.4.1 is duplicated here:

$$\frac{d\sigma}{ds_{\ell\ell}} \propto \left|\mathrm{DY} + \frac{\mathcal{g}^q_\lambda \mathcal{g}^\ell_\lambda}{s_{\ell\ell} - M_X^2 + i\Gamma_X M_X}\right|^2 \longrightarrow \left|\mathrm{DY} + g^2 \frac{\mathcal{g}^q_\lambda \mathcal{g}^\ell_\lambda}{s_{\ell\ell} - M_X^2 + ig^2\Gamma_X M_X}\right|^2 \qquad (8.1.1)$$

where the angular term and the summation over helicity amplitudes and over the higher KK excitations are omitted for convenience. Note that in the KK case, there are actually two resonances (γ_{KK} and Z_{KK}) but the following arguments will hold for both, in the same way as for a single X resonance.

Looking on equation 8.1.1 and on the typical behavior of Z'-like or KK-like signals as in figures 5.4 and 5.5, raises the question whether it is indeed possible to extract such a parameter that appropriately characterizes the outstanding features of the signals. The conclusion has to be approximated as follows. For very off-shell $s_{\ell\ell}$ values, namely $s_{\ell\ell} \ll M_X^2$, it is easy to see that the X width term can be neglected and the dependence on g is only due to the numerator of the X amplitude. Since g is allowed to vary between 0 and $\mathcal{O}(10)$, with its interesting range being $g \lesssim 1$, this is even more justified. Under these circumstances, it can be clearly seen that the pure resonance term is proportional to g^4 while the interference term is proportional to g^2.

For the $Z'_{\rm SSM}$ case, the interference with the DY is negligible[1] throughout the entire search range. In fact, g^4 in that case has almost[2] exactly the same effect as σB had in the non-interfering case and therefore, following the Bayesian approach, it is natural to take a flat prior in g^4 for this case.

For a KK signal, the question remains which of the two features - the KK resonance term or the KK interference term - is more powerful for discriminating the signal from the backgrounds (see e.g. figure 4.14). The correct choice depends on $M_{\rm KK}$. Previous experimental limits and the current data suggest that the minimum value of $M_{\rm KK}$ is such that the KK interference term will dominate over the resonance in the search range. For lower $M_{\rm KK}$ values, within the search range, it is not clear which of the two features will dominate since they will both be present. However, when viewed with respect to the data and backgrounds, then for $M_{\rm KK}$ values between 2 and 3 TeV the interference term will still dominate over the resonance term. Below $\sim$2 TeV the contributions will be similar. For the KK case, both flat priors in g^4 and g^2 will be used. The quoted choice is g^2 because of the already existing indirect limits at $M_{\rm KK} \sim 4$ TeV [12–14], and because it is clear that for a KK mass above $\sim 1.5 - 2$ TeV, the dominant feature is the interference, as will also be seen from the resulting limits which are above 3 TeV for both approaches (g^2 and g^4).

The individual-channel likelihood used for these limits is explicitly written in equation 6.3.3 where the statistical treatment of the systematic uncertainties is given in sections 5.4 and 6.3.2. The rest of the statistical treatment, including the combination of the two channels is equivalent to what has been presented in chapter 7 except that the lower limits on M_X are obtained by finding the intersection of the limit on g^N with of the horizontal $g^N = 1$ line (with $N = 2$ or 4).

[1] Although the interference can be clearly seen just below the resonance itself.
[2] Without the g^2 factor multiplying the X width in equation 8.1.1, it would have exactly the same effect as the σB.

8.2. Results for the couplings-limits

Two-dimensional templates are produced for pole masses, M_X, between 130 GeV and 6130 GeV. For each template, 47 slices in $\log m_{\ell\ell}$ for $128 \leq m_{\ell\ell} \leq 3000$ GeV are given to BAT [25] as functions of g^4 or g^2 and the limit is set on this parameter, versus the pole mass. Example templates are shown in appendix G.

For the limit-setting, the range in which g^4 or g^2 are allowed to vary is 0 to $\mathcal{O}(100)$. The resulting limits on g are shown in figures 8.1 and 8.2 for $\gamma_{\mathrm{KK}}/Z_{\mathrm{KK}}$ respectively with g^4 and g^2 as prior. Figure 8.3 shows the combination of dielectron and dimuon channels $\gamma_{\mathrm{KK}}/Z_{\mathrm{KK}}$ limits with the two prior choices.

Finally, lower limits on M_{KK} are derived from the $\gamma_{\mathrm{KK}}/Z_{\mathrm{KK}}$ SSM hypothesis ($g = 1$); they are displayed in table 8.1. Contrary to the non-interfering case, high-mass candidates in data induce observed limits which are higher than expected. This is because any bin in the $m_{\ell\ell}$ data histogram above the signal+background expectation (in the range where a deficit is expected), will cause the limit to be pushed upwards in mass in order to increase the $m_{\ell\ell}$ shape upwards such that the signal+background expectation will be compatible with the data.

The obtained mass limits for the combined $\ell^+\ell^-$ channel are higher than the indirect limits from electroweak precision measurements [12, 13].

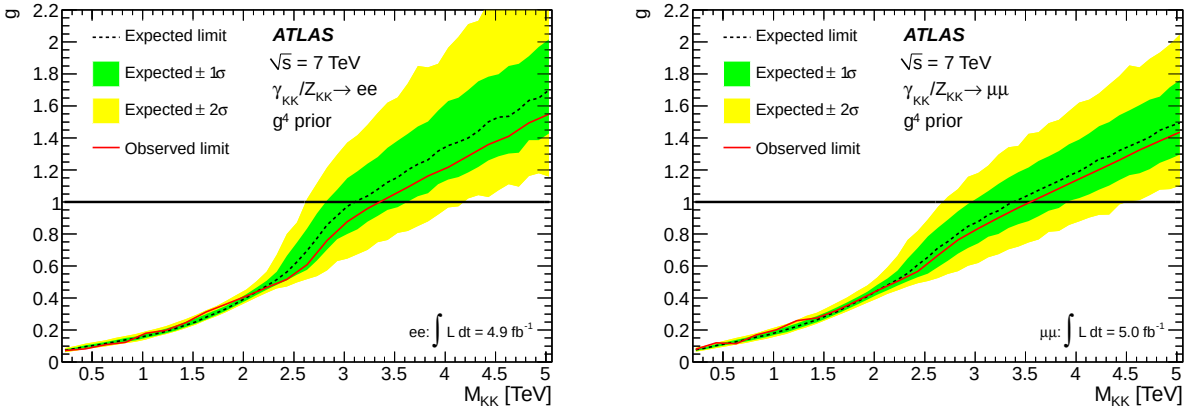

Figure 8.1.: Dielectron (left) and dimuon (right) limits on g in the $\gamma_{\mathrm{KK}}/Z_{\mathrm{KK}}$ hypothesis taking a prior flat in g^4. See explanations in the text for the behavior of the limits.

It should be mentioned that the g^4 limit result is somewhat less important because the search region goes up to 3 TeV with only few data events around $\sim$1.5 TeV (highest mass, see

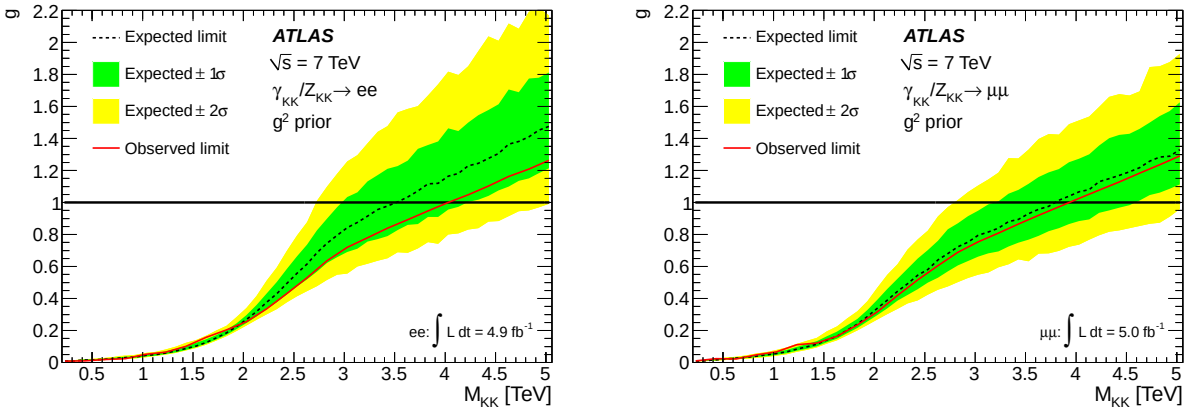

Figure 8.2.: Dielectron (left) and dimuon (right) limits on g in the $\gamma_{\rm KK}/Z_{\rm KK}$ hypothesis taking a prior flat in g^2. See explanations in the text for the behavior of the limits.

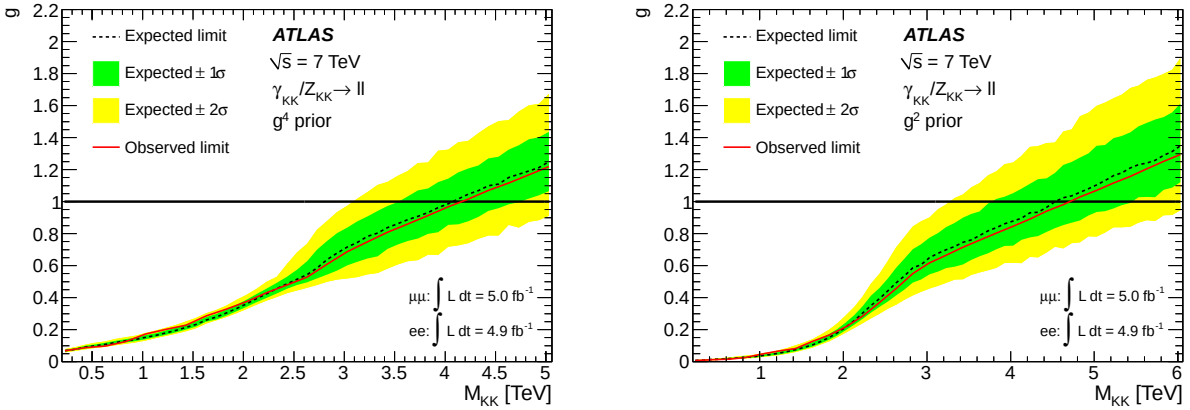

Figure 8.3.: The e^+e^- and $\mu^+\mu^-$ combined 95% C.L. mass limits on $\gamma_{\rm KK}/Z_{\rm KK}$ a flat prior in g^4 (left) and g^2 (right). See explanations in the text for the behavior of the limits.

Table 8.1.: The e^+e^-, $\mu^+\mu^-$ and combined 95% C.L. mass limits on $\gamma_{\rm KK}/Z_{\rm KK}$.

	g^4 prior		g^2 prior	
	Observed	Expected	Observed	Expected
Channel	[TeV]	[TeV]	[TeV]	[TeV]
$\gamma_{\rm KK}/Z_{\rm KK} \to e^+e^-$	3.35	3.11	4.03	3.52
$\gamma_{\rm KK}/Z_{\rm KK} \to \mu^+\mu^-$	3.55	3.38	3.93	3.79
$\gamma_{\rm KK}/Z_{\rm KK} \to \ell^+\ell^-$	4.16	4.07	4.71	4.53

figure 8.4), whereas all the limits are higher than 3 TeV[3]. Therefore, for $M_{\rm KK} \gtrsim 2-3$ TeV,

[3]This is the case for both priors flat in either g^4 or g^2, for every individual channel and for the combination.

the dominant feature within the search region ($m_{\ell\ell} \leq 3$ TeV) is the KK negative interference rather than the KK resonance, and it is more appropriate to use a prior that is flat in g^2. This is illustrated in figure 5.4(a) versus 5.5(a) where M_{KK} is 2 TeV and 4 TeV respectively, and in figure 8.4 for $\mu^+\mu^-$ (a) and e^+e^- (b). The $\mu^+\mu^-$ invariant mass distribution seen in figure 8.4(a) was shown earlier but is duplicated here for convenience and for a comparison with the corresponding e^+e^- result. Contrary to the Z' limit-logic, data points *above* the signal+background expectation will cause the KK limit to be pushed higher in mass where this is the case here due to the highest mass events in both $\mu^+\mu^-$ and e^+e^- channels - see figure 8.4.

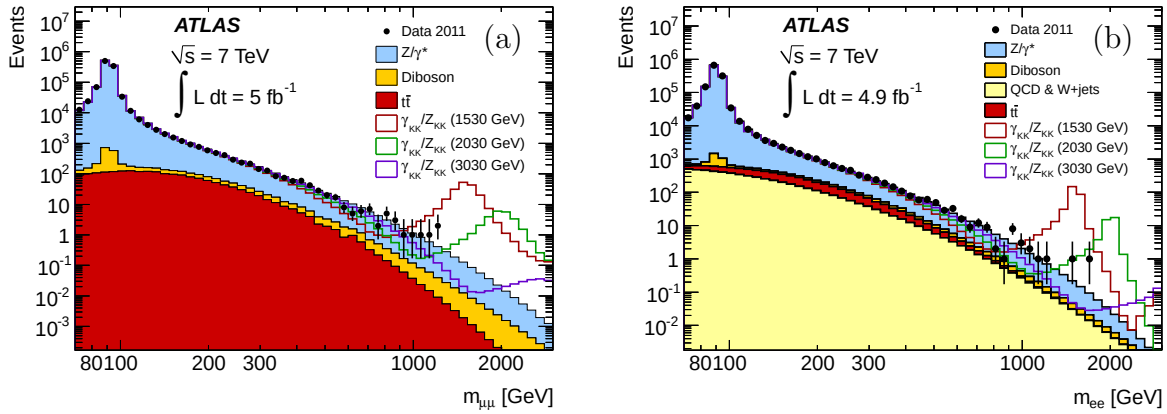

Figure 8.4.: Dimuon (a) and dielectron (b) invariant mass distributions after final selection, compared with the stacked sum of all expected backgrounds, with three example KK signals overlaid for $g = 1$ (SSM).

The KK limit curves and bands are somewhat different than in the Z' signal case, even if the Z' limits are calculated using a prior flat in g^4. Particularly, the most striking features are the rapid widening of the 1σ and 2σ bands for $M_{\mathrm{KK}} \gtrsim 2.5$ TeV for the g^4 limits only (figure 8.1 and 8.3) and the fact that both the g^2 and g^4 limits bands are becoming relatively very wide for high M_{KK} values.

There are two reasons for the relatively large width of the KK limit bands. First, the limit setting procedure is based on the negative interference which is a gradual feature that spreads over several hundreds of GeVs, rather than a sharp one (like a narrow local resonance as in the Z' case). Second, the limit setting procedure searches for a *valley*, so it is more sensitive to small fluctuations at both the low- and the high-end of the search window. These MC fluctuations in the number of events around the expected sum of the DY and the other backgrounds between the different pseudo-experiments in BAT [25], determine the spread of the limit bands.

Finally, the rapid widening occurring around 2.5 TeV in figure 8.1 and 8.3 (for g^4) is related to the fact that by using the flat prior in g^4, the analysis is actually more sensitive to a *peak* and not to a *valley*. This situation is reversed for KK masses around and above 2.5-3 TeV where the dominant KK discriminant is clearly the KK *valley* not the KK *peak* as can be seen in figures 5.4(a), 5.5(a) and 8.4. It has to be remembered that these two discriminants (*peak/valley*) are only relevant within the search window, i.e. up to exactly 3 TeV where the next deepest KK *valley* or the highest KK *peak* can be actually much further away than that.

8.3. Comparison of limits obtained with the two approaches

In the $\gamma_{\mathrm{KK}}/Z_{\mathrm{KK}}$ model parameterization described in this chapter, $g^N = 0$ simply returns the DY shape, whereas $g^N = 1$ gives the $\gamma_{\mathrm{KK}}/Z_{\mathrm{KK}}$ SSM scenario. It is also possible to get limits on the Z'_{SSM} within the $\gamma_{\mathrm{KK}}/Z_{\mathrm{KK}}$ framework by replacing the $\gamma_{\mathrm{KK}}/Z_{\mathrm{KK}}$ amplitude with the Z'_{SSM} one.

The expected limits on g for the Z'_{SSM} are shown in figures 8.5 and the mass limits are listed in table 8.2. The expected mass limits are lower than the ones obtained in the baseline analysis (σB) by 120 GeV ($\mu^+\mu^-$) and 130 GeV (e^+e^-) respectively. As a consistency check, the limits were computed again in the same framework but by

- neglecting the interference by adding the the DY to the *pure* 2D Z'_{SSM} signal template;
- not applying the EW K-factor to the signal but only on the DY part;
- fixing the width of the resonance to the SSM value corresponding only to the resonance mass and not to its coupling strength, i.e. $\Gamma_{Z'_{\mathrm{SSM}}}(g) = \Gamma_{Z'_{\mathrm{SSM}}}$;
- matching the systematic uncertainties with only the ones used in the σB analysis.

It was found that the interference had a small effect (within $\sim$10 GeV) compared to the width variation, and that fixing the width to the SSM value allowed to recover the baseline σB limits on Z'_{SSM} within 10 GeV. This can be seen in figure 8.6. It can also be seen that the limit curves and bands for the no-interference and no-width-scaling case in figure 8.6 are different than for those seen in figure 8.5.

It is clear that the coupling limit framework is more appropriately describing the specific Z'_{SSM} limit because in the σB framework, that was described in chapter 7, the whole Z'_{SSM} template shape is allowed to scale up and down while the width is fixed to the SSM value (for a given pole mass). Therefore, the σB framework is less adequate for the specific model with respect to the coupling limit framework which gives the "true" limit. In the Z'_{SSM} case,

the prior approximation problem is less crucial and it can be shown that the pure resonance is dominating such that the g^4 limit is indeed giving the correct value.

To conclude, it has been checked that the mass limits obtained in two completely different frameworks are consistent within $\sim$10 GeV once the resonance width is fixed to the SSM value.

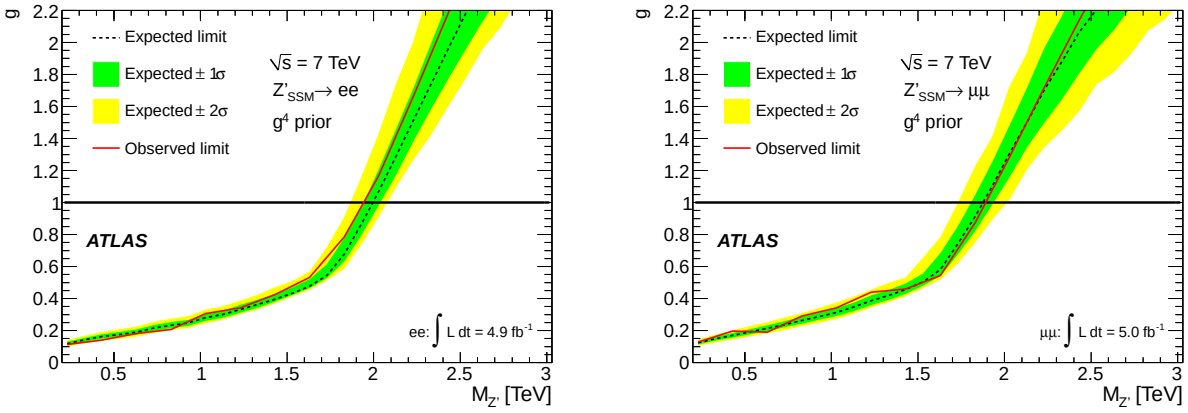

Figure 8.5.: Dielectron (left) and dimuon (right) limits on g in the Z'_{SSM} hypothesis (g^4 prior).

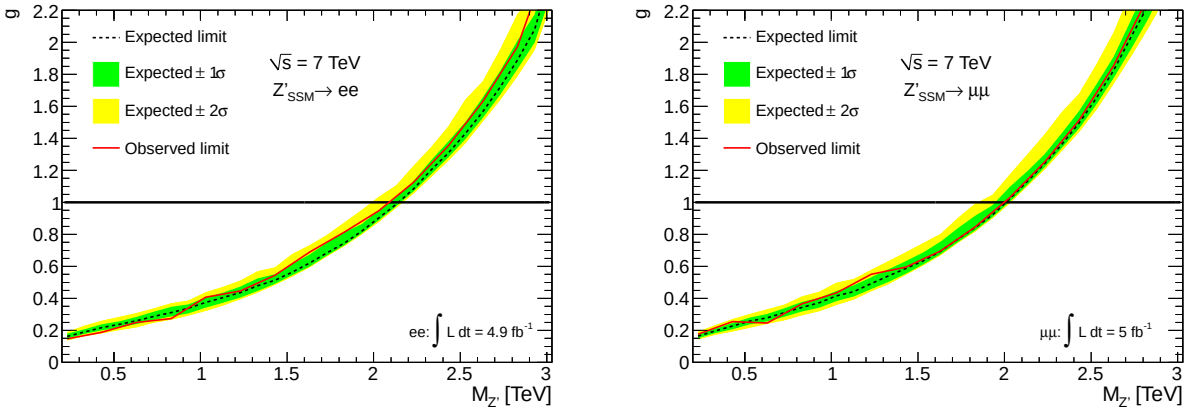

Figure 8.6.: Dielectron (left) and dimuon (right) limits on g in the Z'_{SSM} hypothesis (g^4 prior) without interference and width-scaling with the coupling strength.

Table 8.2.: Comparison of observed (expected) limits in the baseline Z'_{SSM} σB analysis and in the coupling limit framework with and without allowing the width to vary with g.

Method	e^+e^- [TeV]	$\mu^+\mu^-$ [TeV]
σB limit	2.08(2.13)	1.99(2.00)
Coupling limit, fixed width, no interference	2.09(2.14)	1.99(2.00)
Coupling limit, varying width, with interference	1.94(2.00)	1.89(1.88)

Chapter 9.

Summary

This thesis has outlined the basic features of few GUT-inspired Z' models as well as the two sequential standard models, Z'_{SSM} and the extra dimensional $\gamma_{\mathrm{KK}}/Z_{\mathrm{KK}}$ (in the minimal S^1/Z_2 setup). In general, this work covers two of the three classes of signatures in experimental terms, i.e. the resonant signatures, Z' and the negative interference signatures, KK. The third class, which is not covered here, is composed of non-resonant models predicting gradual enhancement *above* the SM expectation such as ADD models [48] or models with contact interactions [97].

The experimental procedures described in this work are eventually narrowed down to a very good understanding of the invariant mass shapes from data, backgrounds and signals throughout the entire search range and even below and above it. The overall systematic uncertainty is conservative and is being properly propagated on to the statistical analysis.

Some new approaches and methods had to be developed in order to consider the interference between the DY and the signals, and these were successfully validated. Already in the subsequent analysis of the ATLAS experiment with the 2012 data, some of these methods have been adopted as a part of the baseline analysis.

It has been shown that no significant deviation from the standard model has been observed. In the absence of any signal within the analyzed window of $0.07 \leq m_{\ell\ell} \leq 3$ TeV, lower limits on $M_{Z'}$ and M_{KK} are set at the ~ 2 TeV and ~ 5 TeV levels respectively. These limits are the highest to date where in the KK case, this is also the first and only direct search done so far. Particularly, the KK limits are higher than the ones computed a decade ago indirectly from electroweak precision measurements [12, 13]. Finally, it should be reminded that the lower limit on the KK mass is actually equivalent to an upper limit on the extra dimension compactification scale, R via the relation $R \sim 1/M_{\mathrm{KK}}$. Thus, for the current limit

on M_{KK}, this analysis has ruled out the existence of an S^1/Z_2 extra dimension up to a scale of ~ 0.000042 fm.

It should be reminded that many other spin-1 scenarios have not been studied here nor other models with different spins. For example, the spin-2 RS graviton belongs to the resonant class and although it is narrower and maybe higher than a Z', its resonance would appear essentially like a Z' in the LHC. This would hold until enough data are collected in order to study the (hypothetical) resonance's angular distribution and classify its spin. The second class, of negative-interference *below* the SM expectation, was covered in this analysis. However, even under the Z' or the S^1/Z_2 KK umbrella, there are a lot more models to study, more than can be possibly covered by one analysis.

With more integrated luminosity and with higher pp center of mass energy (already with the 2012 data), the probed KK masses can be extended to beyond 5 TeV, which is nearly the edge of the current LHC reach.

Appendix A.

Monte Carlo samples and LO cross sections

A.1. Signal samples

Table A.1 lists the characteristics of the MC samples for Z'_{SSM} . As already stated in the main text, the Z' samples are generated with PYTHIA6 with MRST2007LO**. The single mass Z'_{SSM} samples also include the Drell Yan contribution above a mass threshold of 0.5 times the pole mass. The cross section used in the σB limit computation is not the cross section of the generated samples due to this Drell Yan component; it is the cross section of the signal alone, shown in table A.3.

Table A.2 lists the characteristics of the MC samples for the $\gamma_{\mathrm{KK}}/Z_{\mathrm{KK}} \to \mu^+\mu^-$ (SSM) signal; these samples are not currently used due to the PDF mismatch with respect to the main (binned) Drell-Yan samples that are used for the signals reweighting.

A.2. Signal LO cross sections

Table A.3 displays the LO Z' cross sections used in the σB limit calculation for various masses. Contrary to the simulated sample cross section, which include Drell Yan production (and interference), these cross sections are for Z' production only. Another difference with simulated cross sections is that the MSTW2008lo90cl PDF is used, for consistency with the

Table A.1.: Full interference MC Z'_{SSM} samples (PYTHIA6) used for the study. The first four columns give the Z'_{SSM} mass, mass threshold (M_{min}), width and leptonic branching fraction. Next is the ATLAS MC run number followed by the cross section time branching fraction reported by the generator. The last columns give the number of generated events and the integrated luminosity $L_{\mathrm{int}} = N_{\mathrm{evt}}/(\sigma B)$ (not taking into account the pile-up reweighting).

$M_{Z'_{\mathrm{SSM}}}$	M_{min}	Γ	$B(Z'_{\mathrm{SSM}} \to \ell^+\ell^-)$	Run number		σB [fb]		L_{int}
[GeV]	[GeV]	[GeV]	[%]	e	μ	generated	N_{evt} [k]	[fb^{-1}]
250	125	6.87	3.36	115272	115269	35401.	20	0.48
500	250	14.56	3.20	115273	115270	2607.1	20	6.7
750	375	22.64	3.10	115274	115271	473.49	20	37.5
1000	500	30.64	3.06	105603	105601	124.66	20	143.
1250	625	38.60	3.05	105549	105534	39.88	20	469.
1500	750	46.55	3.04	105624	105625	14.38	20	1312.
1750	875	54.49	3.03	105554	105544	5.67	20	3597.
2000	1000	62.43	3.03	105409	105349	2.43	20	9091.

Table A.2.: Full interference MC $\gamma_{\mathrm{KK}}/Z_{\mathrm{KK}}$ samples (PYTHIA8) used for the study, for $M_{\mathrm{KK}} =$ 2 TeV for muons only. The first column gives the phase-space for the generation ($m_{\mu\mu}$ in GeV). The next two columns are the ATLAS MC run numbers, followed by the cross section times branching fraction reported by the generator. The last two columns give the number of generated events and the integrated luminosity $L_{\mathrm{int}} = N_{\mathrm{evt}}/(\sigma B)$ (not taking into account the pile-up reweighting.

$m_{\mu\mu}$ bin [GeV]	Run number	σB [fb]	N_{evt} [k]	L_{int} [fb^{-1}]
$120 - 450$	145016	7722.	40	0.00518
$450 - 850$	145017	21.91	10	0.456
$850 - 1300$	145018	0.2	10	49.
$1300 - 1800$	145019	1.358	10	7.36
$1800 - 2300$	145020	9.419	10	1.06
$2300 - 2800$	145021	0.0474	10	210.
$2800 - 3300$	145022	0.000298	10	33485.
> 3300	145023	0.0032	10	3115.

calculation of the Drell Yan cross section. The actual mass spacing used in the σB limits calculation is 40 GeV.

Table A.3.: The LO cross sections used in the σB limit calculation for all Z' models

$M_{Z'}$ [GeV]	σB (Z'_{SSM}) [fb]	σB (Z'_{ψ}) [fb]	σB (Z'_{χ}) [fb]	σB (Z'_{η}) [fb]
250	$2.735 \cdot 10^{4}$	$8.132 \cdot 10^{3}$	$1.589 \cdot 10^{4}$	$9.566 \cdot 10^{3}$
500	$2.038 \cdot 10^{3}$	596.8	$1.163 \cdot 10^{3}$	694.6
750	366.8	106.9	210.1	123.2
1000	94.77	26.90	51.83	31.40
1250	29.60	8.171	15.56	9.704
1500	10.33	2.732	5.064	3.229
1750	3.876	$9.833 \cdot 10^{-1}$	1.747	1.195
2000	1.579	$3.706 \cdot 10^{-1}$	$6.410 \cdot 10^{-1}$	$4.550 \cdot 10^{-1}$
2250	$6.935 \cdot 10^{-1}$	$1.422 \cdot 10^{-1}$	$2.493 \cdot 10^{-1}$	$1.775 \cdot 10^{-1}$
2500	$3.296 \cdot 10^{-1}$	$5.668 \cdot 10^{-2}$	$1.044 \cdot 10^{-1}$	$7.255 \cdot 10^{-2}$
2750	$1.729 \cdot 10^{-1}$	$2.395 \cdot 10^{-2}$	$4.888 \cdot 10^{-2}$	$3.083 \cdot 10^{-2}$
3000	$1.000 \cdot 10^{-1}$	$1.064 \cdot 10^{-2}$	$2.591 \cdot 10^{-2}$	$1.399 \cdot 10^{-2}$

A.3. Background samples

Tables A.4 to A.7 list the background samples that are used in this analysis. The binned DY samples ($e^{+}e^{-}$ and $\mu^{+}\mu^{-}$) are also used as a base for reweighting some of the signals and produce KK and Z' within the coupling limit approach.

Table A.4.: MC Drell Yan samples (PYTHIA6) used for the study. The first column gives the mass range [GeV] and the second, third and fourth are the ATLAS MC run numbers. The fifth column is the cross section time branching ratio reported by the generator. The next column is the number of generated events and the last is the integrated luminosity $L_{\text{int}} = N_{\text{evt}}/(\sigma B)$ for each lepton flavor (not taking into account the pile-up reweighting). Denoted by (*) are the mass binned $\tau\tau$ samples which have 5 times less integrated luminosity (20k events). The integrated luminosity in the last column does not hold for the mass binned $\tau\tau$ 20k-events samples. The cross section of the inclusive samples calculated at QCD NNLO is 989 pb.

	Run number			σB [pb]		
Process	e	μ	τ	generated	N_{evt} [k]	L_{int} [fb^{-1}]
$Z \to e^+e^-$	106046			834.6	9986	10.
$Z \to \mu^+\mu^-$		106047		834.6	9994	10.
$Z \to \tau\tau$			106052	834.6	495	0.5
$Z \to \ell^+\ell^-$						
75-120	105466	145001	105488*	798.36	100	0.12
120-250	105467	145002	105489*	8.53	100	11.7
250-400	105468	145003	105490*	0.410	100	243.
400-600	105469	145004	105491*	0.0664	100	1506.
600-800	105470	145005	105492*	0.01095	100	9128.
800-1000	105471	145006	105493*	0.002647	100	37778.
1000-1250	105472	145007	105494*	0.0008901	100	112340.
1250-1500	105473	145008	105495*	0.00023922	100	418025.
1500-1750	105474	145009	105496*	0.00007343	100	1361674.
1750-2000	105475	145010	105497*	0.00002464	100	4057947.
2000-2250	145263	145011	105498*	0.00000876	100	11413049.
2250-2500	145264	145012	105498*	0.00000322	100	31025068.
2500-2750	145265	145013	105498*	0.00000120	100	82829454.
2750-3000	145266	145014	105498*	0.00000045	100	223398789.
>3000	145267	145015	105498*	0.00000025	100	390838740.

Table A.5.: MC W background samples (ALPGEN) used for the study. The first column lists the physics process and the second is the ATLAS MC run number. The third column is the cross section times branching fraction reported by the generator. The next column is the number of generated events and the last is the integrated luminosity $L_{\text{int}} = N_{\text{evt}}/(\sigma B)$ (not taking into account the pile-up reweighting).

Process	Run number	σB [pb]	N_{evt} [k]	L_{int} [fb^{-1}]
$W \to \mu\nu$ + 0 parton	107690	6918.7	3466.5	0.4
$W \to \mu\nu$ + 1 parton	107691	1304.2	642	0.4
$W \to \mu\nu$ + 2 partons	107692	378.5	3769	8.3
$W \to \mu\nu$ + 3 partons	107693	101.6	1010	8.3
$W \to \mu\nu$ + 4 partons	107694	25.9	255	7.3
$W \to \mu\nu$ + 5 partons	107695	6.9	70	8.4

Table A.6.: Inclusive (first three rows) and mass binned (rest) MC diboson background samples used for the study. The first column lists the physics process and the second is the ATLAS MC run number. The third column is the filter efficiency. The fourth and fifth columns are the cross section times branching fractions (within the leptonic decays) times filter efficiency first reported by the generator, and second calculated as follows: the inclusive K-factor given by the ratio of calculated over generated cross sections of the inclusive samples are applied to the generated cross section of the high-mass bin samples. The next column is the number of generated events and the last is the integrated luminosity $L_{\text{int}} = N_{\text{evt}}/(\sigma B)$ (not taking into account the pile-up reweighting). The lepton filter is 1 lepton with $p_T > 10$ GeV, $|\eta| < 2.8$ for the inclusive mass samples, 1 muon with $p_T > 15$ GeV, $|\eta| < 2.8$ for the binned mass muon samples.

Process	Run number	ϵ_f (filter efficiency)	$\sigma B \times \epsilon_f$ [fb] generated	calculated	N_{evt} [k]	L_{int} [fb^{-1}]
WW (1 lepton filter)	105985	0.38947	12115.	17487.	1000	57.
WZ (1 lepton filter)	105987	0.31043	3565.	5743.	1000	180.
ZZ (1 lepton filter)	105986	0.21319	975.	1271.	250	198.
WW ($m_{\mu\mu} = 0.4 - 1$ TeV)	145490	0.00716	2.598	3.808	20	5252.
WW ($m_{\mu\mu} = 1 - 1.6$ TeV)	145491	0.0000739	0.027	0.039	20	508821.
WZ ($m_{\mu\mu} = 0.4 - 1$ TeV)	145496	0.00296	1.315	1.840	20	10869.
WZ ($m_{\mu\mu} = 1 - 1.6$ TeV)	145497	0.0000812	0.036	0.050	20	396317.
ZZ ($m_{\mu\mu} = 0.4 - 1$ TeV)	145502	0.00133	0.449	0.525	20	38116.
ZZ ($m_{\mu\mu} = 1 - 1.6$ TeV)	145503	0.0000237	0.0080	0.0093	20	2144458.

Table A.7.: MC $t\bar{t}$ background samples used for the study. The second column is the ATLAS MC run number. The third and fourth columns are the cross section time branching fractions reported by the generator and calculated as described in the text. The next column is the number of generated events and the last is the integrated luminosity $L_{\text{int}} = N_{\text{evt}}/(\sigma B)$ (not taking into account the pile-up reweighting).

Process	Run number	ϵ_f (filter efficiency)	$\sigma B \times \epsilon_f$ [pb] generated	calculated	N_{evt} [k]	L_{int} [fb^{-1}]
$t\bar{t} \to \ell X$	105200	0.54259	79.0	89.4	14995	168.

Appendix B.

Extrapolation of diboson and $t\bar{t}$ backgrounds at high masses

In the cases of the $t\bar{t}$ and diboson MC samples, statistics sufficient to gain information in the entire mass range explored in the analysis were not available.

The missing statistics can clearly be seen in figure B.1a, showing the reconstructed dimuon mass using the approximately 15M event $t\bar{t}$ sample, and figure B.1b, showing the same for all diboson processes (WW,WZ,ZZ). The diboson distribution is obtained by using unbinned, single-lepton filtered samples in the region $m_{\mu\mu} < 0.4$ TeV, and samples binned in dilepton mass in the regions $0.4 \leq m_{\mu\mu} \leq 1.0$ TeV, $1.0 \leq m_{\mu\mu} \leq 1.6$ TeV and $m_{\mu\mu} \geq 1.6$ TeV. However, the sample in generated dilepton mass bin $m_{\mu\mu} \geq 1.6$ TeV contains no generated events, due to very low event filter efficiency. This leads to the "knee" feature seen near 1.5 TeV in figure B.1 (b). This effect is clearly not physical.

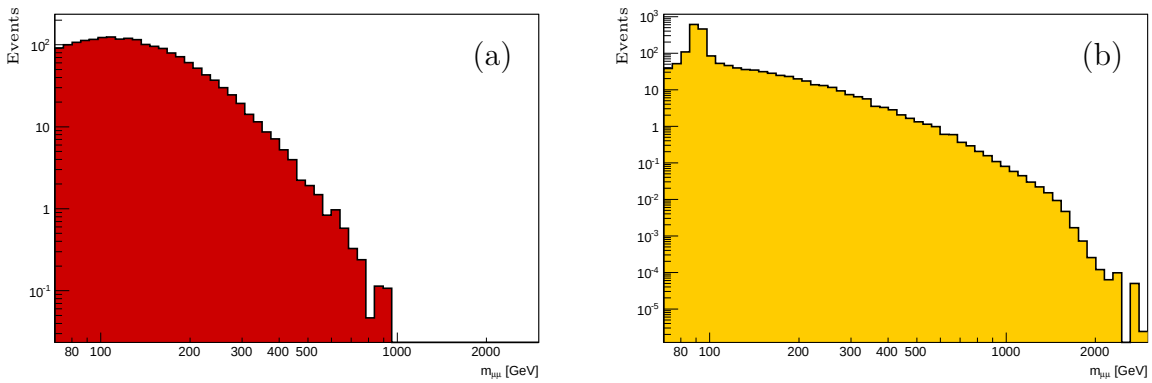

Figure B.1.: Reconstructed dimuon mass on (a) $t\bar{t}$ and (b) diboson MC samples, scaled to 5 fb^{-1}.

Due to the fact that reconstruction-level information is not available at high masses from these samples, $t\bar{t}$ and diboson background estimates at high mass are obtained via fits to the information that is available. As the distributions are weighted according to the pile-up information in the sample, a χ^2 fit, which can be used with weights, is performed. Two fitting functions are attempted for each distribution:

- "Dijet"[1] function: $a \times x^b \times x^{c \times \ln(x)}$,
- Inverse monomial function: $\frac{a}{(x+b)^c}$,

with $x \equiv m_{\mu\mu}$. The decision of which function to use is based on the stability of the function with variation of fit range, and the χ^2 fit probability in the optimal range tested. Variation in both the upper and lower boundaries of the fit are attempted, see figures B.2 and B.3.

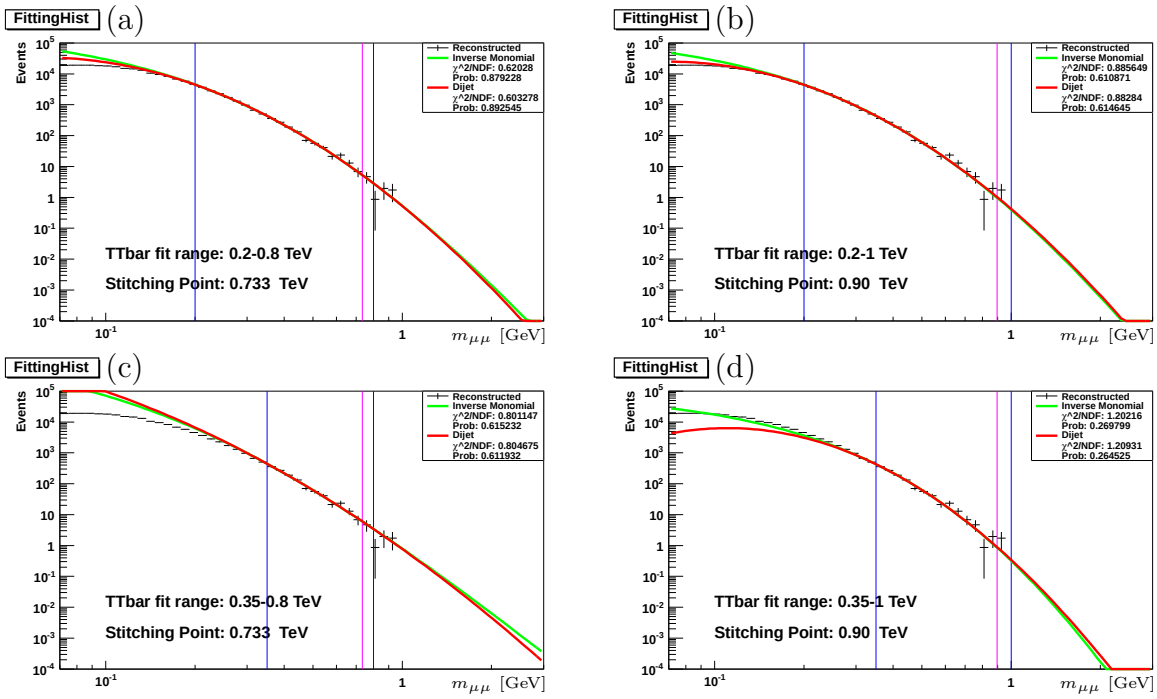

Figure B.2.: Fits to the $t\bar{t}$ tail. In (a) and (b) the variation of the fits when moving the upper boundary of the fit region between 0.8 and 1.0 TeV is shown, using a lower boundary of 0.2 TeV. In (c) and (d) the same is shown using a lower boundary of 0.350 TeV. The vertical blue lines indicate the fit range boundaries; the vertical magenta line indicates where the fit is used instead of the Monte-Carlo.

Upon varying the fit range, it was found that the most stable fitting function for both $t\bar{t}$ and diboson is the dijet function. Therefore, the fits using this function are taken as the central estimate for the background.

[1] The name is only borrowed from the dijet analysis

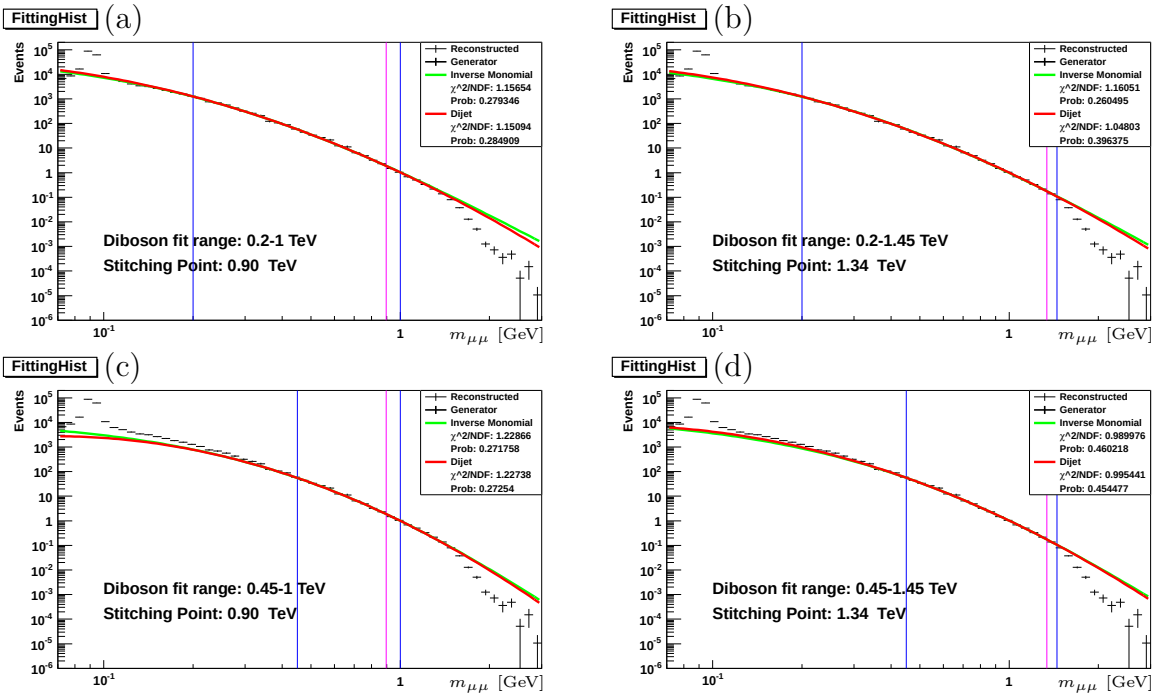

Figure B.3.: Fits to the diboson tail. In (a) and (b) the variation of the fits when moving the upper boundary of the fit region between 1.0 and 1.45 TeV is shown, using a lower boundary of 0.2 TeV. In (c) and (d) the same is shown using a lower boundary of 0.45 TeV. The vertical blue lines indicate the fit range boundaries; the vertical magenta line indicates where the fit is used instead of the Monte-Carlo.

In the $t\bar{t}$ case, the fit range is 0.2-0.8 TeV and the fit is used from 0.73 TeV onwards; in the diboson case, the fit range is 0.45-1.45 TeV and the fit is used from 1.34 TeV onwards. The fit result is converted into a binned histogram, which is used elsewhere in the analysis.

Two systematic uncertainties are assessed. The first is calculated by taking the difference between the dijet and inverse monomial functions. The second varies the starting and ending points of the dijet fit range, by 5 steps of 0.01 TeV above the starting value and 5 steps of 0.02 TeV below the ending value, resulting in 25 different fits. The error is estimated as the maximum difference between these fits and the central fit. The two systematic uncertainties are combined in quadrature and this is used to generate a $\pm 1\sigma$ systematic error band around the central estimate. This systematic uncertainty is neglected in the non-interfering case but not in the interfering ones as discussed in chapter 5.

Appendix C.

Drell Yan production cross section and QCD K-factors

The production of lepton pairs with an invariant mass $m_{\ell\ell}$ via photon and Z boson exchange has been calculated up to NNLO in QCD using various PDF sets and our modified version of PHOZPR [87]. The differential production cross section $m_{\ell\ell}^2 \frac{\mathrm{d}\sigma_{\mathrm{NNLO}}}{\mathrm{d}m_{\ell\ell}^2}$ calculated at NNLO using the MSTW2008NNLO PDF is given in table C.1 for dilepton masses $10\,\mathrm{GeV} < m_{\ell\ell} < 5000\,\mathrm{GeV}$. Table C.1 lists also the followoing mass-dependent cross section ratios (K-factors),

$$
\begin{aligned}
K_{\mathrm{NLO}}(m_{\ell\ell}) &= \tfrac{\mathrm{d}\sigma_{\mathrm{NLO}}}{\mathrm{d}m_{\ell\ell}^2}(\mathrm{MSTW2008NLO}) / \tfrac{\mathrm{d}\sigma_{\mathrm{LO}}}{\mathrm{d}m_{\ell\ell}^2}(\mathrm{MSTW2008LO}),\\
K_{\mathrm{NNLO}}(m_{\ell\ell}) &= \tfrac{\mathrm{d}\sigma_{\mathrm{NNLO}}}{\mathrm{d}m_{\ell\ell}^2}(\mathrm{MSTW2008NNLO}) / \tfrac{\mathrm{d}\sigma_{\mathrm{LO}}}{\mathrm{d}m_{\ell\ell}^2}(\mathrm{MSTW2008LO}),\\
K^{*}_{\mathrm{NNLO}}(m_{\ell\ell}) &= \tfrac{\mathrm{d}\sigma_{\mathrm{NNLO}}}{\mathrm{d}m_{\ell\ell}^2}(\mathrm{MSTW2008NNLO}) / \tfrac{\mathrm{d}\sigma_{\mathrm{LO}}}{\mathrm{d}m_{\ell\ell}^2}(\mathrm{MRST2007LO}^{*}),\\
K^{**}_{\mathrm{NNLO}}(m_{\ell\ell}) &= \tfrac{\mathrm{d}\sigma_{\mathrm{NNLO}}}{\mathrm{d}m_{\ell\ell}^2}(\mathrm{MSTW2008NNLO}) / \tfrac{\mathrm{d}\sigma_{\mathrm{LO}}}{\mathrm{d}m_{\ell\ell}^2}(\mathrm{MRST2007LO}^{**}),
\end{aligned}
$$

which are shown in figure C.1 as well. For reference, table C.2 lists in addition K-factors for various other PDF sets used in LO and NLO predictions. The NLO and NNLO K-factors $K_{\mathrm{NLO}}(m_{\ell\ell})$ and $K_{\mathrm{NNLO}}(m_{\ell\ell})$, respectively, which are defined based on PDF sets of the corresponding order, increase by approximately 25% for dilepton masses between 10 GeV and 400 GeV and decrease for larger masses. $K^{*}_{\mathrm{NNLO}}(m_{\ell\ell})$ and $K^{**}_{\mathrm{NNLO}}(m_{\ell\ell})$, which are based on LO predictions using the modified LO PDF sets MRST2007LO* (a.k.a. MRST2007lomod) and MRST2007LO** (a.k.a. MRSTMCal) [35], respectively, have only a modest dependence on $m_{\ell\ell}$ over a wide range of dilepton masses but decrease rapidly for masses beyond 1 TeV. Since the MRST2007LO** PDF set is used in the ATLAS MC11 production campaign, $K^{**}_{\mathrm{NNLO}}(m_{\ell\ell})$ defines an event specific weight for DY events generated with a LO event generator (e.g.

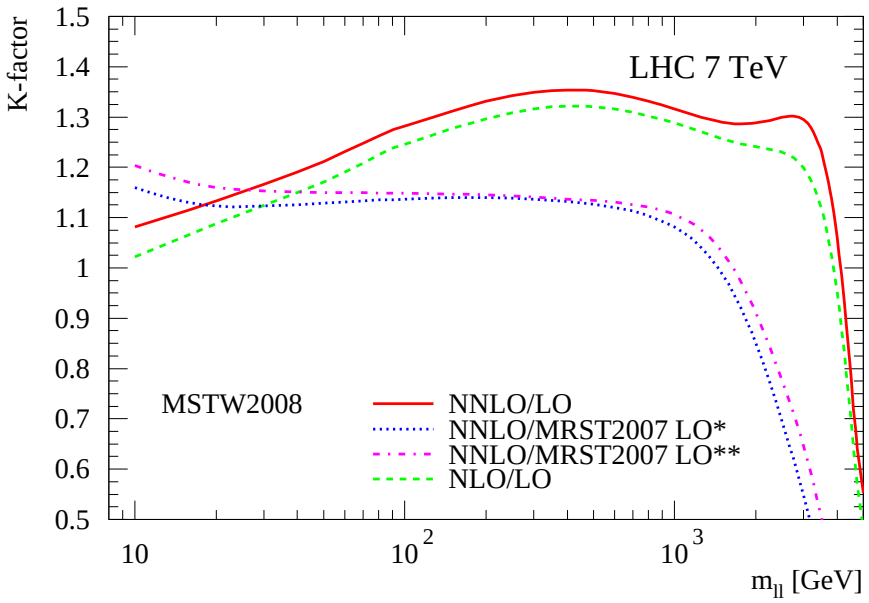

Figure C.1.: Cross section ratios (K-factors) for DY lepton-pair production as function of dilepton invariant mass $m_{\ell\ell}$, calculated with PHOZPR.

PYTHIA, HERWIG) to obtain a normalization and a dilepton invariant mass shape which is accurate to NNLO.

Table C.1.: NNLO DY lepton-pair production cross section $m_{\ell\ell}^2 \mathrm{d}\sigma_{\mathrm{NNLO}}/\mathrm{d}m_{\ell\ell}^2$ as function of dilepton mass $m_{\ell\ell}$ calculated with PHOZPR [87] and the MSTW2008NNLO PDF set, cross section ratios (K-factors) based on the MSTW2008 LO, NLO, and NNLO and MRST2007 LO* and LO** PDF sets.

$m_{\ell\ell}$ [GeV]	$m_{\ell\ell}^2 \frac{\mathrm{d}\sigma_{\mathrm{NNLO}}}{\mathrm{d}m_{\ell\ell}^2}$ [nb]	$\frac{\sigma_{\mathrm{NLO}}}{\sigma_{\mathrm{LO}}}$	$\frac{\sigma_{\mathrm{NNLO}}}{\sigma_{\mathrm{LO}}}$	$\frac{\sigma_{\mathrm{NNLO}}}{\sigma_{\mathrm{LO}}}$	$\frac{\sigma_{\mathrm{NNLO}}}{\sigma_{\mathrm{LO}}}$
	MSTW	MSTW	MSTW	MSTW/MRST	MSTW/MRST
	2008NNLO	2008NLO/LO	2008NNLO/LO	2008NNLO/2007LO*	2008NNLO/2007LO**
10.00	0.465E+01	1.022	1.081	1.166	1.212
20.00	0.917E+00	1.088	1.133	1.138	1.176
30.00	0.327E+00	1.124	1.166	1.142	1.173
40.00	0.154E+00	1.150	1.191	1.146	1.173
50.00	0.884E-01	1.171	1.212	1.149	1.172
60.00	0.633E-01	1.190	1.231	1.148	1.168
70.00	0.665E-01	1.208	1.248	1.144	1.161
80.00	0.155E+00	1.225	1.262	1.138	1.152
91.12	0.113E+02	1.239	1.275	1.136	1.149
100.00	0.236E+00	1.246	1.282	1.138	1.150
125.00	0.207E-01	1.263	1.299	1.145	1.154
150.00	0.784E-02	1.277	1.312	1.149	1.156
175.00	0.405E-02	1.287	1.323	1.151	1.156
200.00	0.239E-02	1.296	1.331	1.151	1.155
250.00	0.104E-02	1.308	1.342	1.149	1.152
300.00	0.528E-03	1.316	1.349	1.146	1.149
400.00	0.179E-03	1.322	1.354	1.139	1.142
500.00	0.750E-04	1.321	1.352	1.131	1.136
600.00	0.357E-04	1.316	1.347	1.123	1.130
700.00	0.185E-04	1.310	1.339	1.114	1.124
800.00	0.101E-04	1.302	1.332	1.104	1.118
900.00	0.582E-05	1.295	1.324	1.093	1.110
1000.00	0.346E-05	1.288	1.316	1.080	1.100
1250.00	0.105E-05	1.271	1.300	1.041	1.069
1500.00	0.353E-06	1.257	1.290	0.990	1.025
1750.00	0.127E-06	1.247	1.286	0.929	0.973
2000.00	0.473E-07	1.241	1.288	0.860	0.914
2250.00	0.180E-07	1.236	1.293	0.787	0.853
2500.00	0.687E-08	1.230	1.300	0.712	0.791
2750.00	0.259E-08	1.219	1.302	0.637	0.728
3000.00	0.949E-09	1.199	1.295	0.563	0.664
3250.00	0.333E-09	1.166	1.272	0.487	0.594
3500.00	0.111E-09	1.117	1.229	0.411	0.515
3750.00	0.342E-10	1.045	1.159	0.340	0.434
4000.00	0.973E-11	0.950	1.059	0.276	0.350
4250.00	0.250E-11	0.831	0.930	0.221	0.263
4500.00	0.576E-12	0.697	0.783	0.177	0.177
4750.00	0.120E-12	0.568	0.641	0.146	0.103
5000.00	0.246E-13	0.484	0.553	0.144	0.055

Table C.2.: *K*-factors to normalize LO and NLO predictions based on the CTEQ6L1, CTEQ6L, CTEQ6.6, CT10, and CT10W PDF sets to the NNLO prediction calculated with MSTW2008NNLO.

$m_{\ell\ell}$ [GeV]	$\frac{\sigma_{\mathrm{NNLO}}}{\sigma_{\mathrm{LO}}}$ CTEQ6L1	$\frac{\sigma_{\mathrm{NNLO}}}{\sigma_{\mathrm{LO}}}$ CTEQ6L	$\frac{\sigma_{\mathrm{NNLO}}}{\sigma_{\mathrm{NLO}}}$ CTEQ6.6	$\frac{\sigma_{\mathrm{NNLO}}}{\sigma_{\mathrm{NLO}}}$ CT10	$\frac{\sigma_{\mathrm{NNLO}}}{\sigma_{\mathrm{NLO}}}$ CT10W
10.00	1.249	1.352	0.968	1.011	1.009
20.00	1.236	1.337	1.001	1.030	1.030
30.00	1.245	1.340	1.017	1.037	1.038
40.00	1.256	1.345	1.026	1.041	1.042
50.00	1.267	1.351	1.032	1.042	1.043
60.00	1.278	1.358	1.034	1.041	1.042
70.00	1.291	1.366	1.032	1.038	1.038
80.00	1.302	1.374	1.029	1.035	1.034
91.12	1.311	1.379	1.030	1.035	1.032
100.00	1.316	1.380	1.033	1.036	1.034
125.00	1.325	1.381	1.044	1.040	1.037
150.00	1.334	1.383	1.051	1.042	1.040
175.00	1.341	1.385	1.056	1.044	1.041
200.00	1.348	1.386	1.060	1.046	1.042
250.00	1.358	1.387	1.067	1.049	1.044
300.00	1.365	1.386	1.072	1.052	1.046
400.00	1.375	1.382	1.081	1.057	1.050
500.00	1.380	1.374	1.089	1.063	1.054
600.00	1.383	1.365	1.095	1.068	1.058
700.00	1.384	1.355	1.101	1.073	1.063
800.00	1.385	1.344	1.106	1.077	1.067
900.00	1.385	1.333	1.110	1.081	1.072
1000.00	1.385	1.322	1.115	1.084	1.076
1250.00	1.386	1.296	1.123	1.093	1.087
1500.00	1.391	1.273	1.128	1.102	1.097
1750.00	1.403	1.255	1.128	1.112	1.107
2000.00	1.421	1.241	1.121	1.122	1.116
2250.00	1.441	1.228	1.106	1.131	1.126
2500.00	1.459	1.214	1.081	1.135	1.133
2750.00	1.466	1.195	1.047	1.130	1.139
3000.00	1.456	1.169	1.002	1.115	1.142
3250.00	1.424	1.135	0.945	1.087	1.138
3500.00	1.365	1.093	0.875	1.044	1.123
3750.00	1.279	1.043	0.788	0.984	1.091
4000.00	1.168	0.985	0.683	0.905	1.032
4250.00	1.038	0.921	0.565	0.809	0.943
4500.00	0.897	0.850	0.446	0.700	0.829
4750.00	0.764	0.783	0.345	0.598	0.712
5000.00	0.694	0.767	0.292	0.548	0.651

Table C.3.: Relative uncertainties on the NNLO prediction for SM γ/Z production as function of dilepton mass $m_{\ell\ell}$ due to variations of the factorization and renormalization scales, α_S, and PDFs (based on MSTW2008NNLO PDF uncertainty sets and based on the envelope of MSTW2008, NNPDF2.1, CT10, and CT10W uncertainty bands), at 68% and 90% C.L., respectively. Also shown are $K^{**}_{\mathrm{NNLO},Z'}$ for Z' production as function of $m_{\ell\ell}$ and its relative difference to $K^{**}_{\mathrm{NNLO},\gamma/Z}$ for γ/Z production: $\Delta K_{\gamma/Z,Z'} = K^{**}_{\mathrm{NNLO},Z'}/K^{**}_{\mathrm{NNLO},\gamma/Z} - 1$.

$m_{\ell\ell}$	scale unc.		68% C.L. uncertainties							90% C.L. uncertainties							$K^{**}_{\mathrm{NNLO},\gamma/Z}$	$\Delta K^{**}_{\gamma/Z,Z'}$
			α_S		MSTW2008: PDF			envelope: PDF		α_S		MSTW2008: PDF			envelope: PDF			
	Δ_r^+	Δ_r^-	Δ_r^+	Δ_r^-	Δ_r	Δ_r^+	Δ_r^-	Δ_r^+	Δ_r^-	Δ_r^+	Δ_r^-	Δ_r	Δ_r^+	Δ_r^-	Δ_r^+	Δ_r^-		
[GeV]	[%]	[%]	[%]	[%]	[%]	[%]	[%]	[%]	[%]	[%]	[%]	[%]	[%]	[%]	[%]	[%]		[%]
10.	2.5	-9.8	1.7	-1.5	5.5	7.5	-4.5	15.7	-4.5	3.9	-3.8	9.3	12.2	-8.8	23.5	-8.8	1.204	-0.7
20.	1.6	-3.9	1.5	-1.5	2.3	3.1	-2.0	8.2	-2.0	3.5	-3.7	4.5	5.5	-4.3	11.3	-4.3	1.160	-1.4
30.	1.3	-2.4	1.4	-1.4	1.8	2.1	-1.8	4.5	-1.8	3.2	-3.5	3.7	4.0	-3.7	7.5	-4.1	1.153	-1.7
40.	1.1	-1.7	1.3	-1.3	1.7	1.8	-1.7	3.0	-2.2	3.0	-3.3	3.5	3.6	-3.5	5.4	-4.2	1.151	-1.8
50.	0.9	-1.3	1.2	-1.2	1.7	1.7	-1.7	2.3	-2.4	2.8	-3.1	3.4	3.5	-3.3	4.4	-4.2	1.150	-1.8
60.	0.8	-1.1	1.2	-1.2	1.7	1.7	-1.6	1.9	-2.6	2.7	-3.0	3.3	3.5	-3.2	3.8	-4.1	1.150	-1.5
70.	0.7	-0.9	1.1	-1.1	1.7	1.7	-1.6	1.7	-2.7	2.5	-2.8	3.3	3.5	-3.2	3.5	-4.1	1.150	-1.0
80.	0.6	-0.8	1.1	-1.1	1.7	1.7	-1.6	1.7	-2.8	2.4	-2.7	3.3	3.5	-3.2	3.5	-4.1	1.149	-0.2
91.	0.6	-0.5	1.0	-1.0	1.6	1.7	-1.6	1.7	-2.8	2.3	-2.6	3.3	3.5	-3.1	3.5	-4.1	1.149	0.0
100.	0.4	-0.6	1.0	-1.0	1.6	1.7	-1.6	1.8	-2.9	2.2	-2.5	3.2	3.5	-3.1	3.5	-4.1	1.149	-0.1
125.	0.3	-0.5	0.9	-0.9	1.6	1.7	-1.5	1.8	-3.0	2.0	-2.3	3.2	3.5	-3.0	3.5	-4.1	1.148	-0.5
150.	0.3	-0.4	0.8	-0.8	1.6	1.7	-1.5	1.8	-3.1	1.7	-2.1	3.1	3.5	-3.0	3.5	-4.1	1.147	-0.8
175.	0.2	-0.3	0.7	-0.7	1.6	1.7	-1.5	1.7	-3.2	1.6	-1.9	3.2	3.5	-2.9	3.5	-4.2	1.146	-0.9
200.	0.2	-0.3	0.6	-0.7	1.6	1.7	-1.5	1.7	-3.4	1.4	-1.7	3.2	3.6	-2.9	3.6	-4.5	1.145	-0.9
250.	0.2	-0.4	0.5	-0.6	1.6	1.8	-1.4	1.9	-3.7	1.1	-1.4	3.3	3.7	-3.0	3.7	-4.8	1.143	-0.8
300.	0.3	-0.4	0.4	-0.4	1.6	1.8	-1.5	2.0	-4.1	0.8	-1.2	3.4	3.9	-3.1	3.9	-5.3	1.141	-0.7
400.	0.3	-0.5	0.2	-0.2	1.7	2.0	-1.5	2.0	-4.8	0.3	-0.7	3.6	4.2	-3.3	4.2	-6.4	1.137	-0.4
500.	0.4	-0.6	0.0	-0.1	1.8	2.1	-1.6	2.1	-5.5	0.0	-0.2	3.9	4.5	-3.5	4.5	-7.3	1.134	-0.2
600.	0.5	-0.7	0.1	-0.2	1.9	2.3	-1.7	2.3	-6.2	0.2	-0.6	4.1	4.8	-3.7	4.8	-8.2	1.131	0.0
700.	0.5	-0.8	0.2	-0.4	2.0	2.5	-1.7	2.5	-6.8	0.6	-0.9	4.4	5.1	-3.8	5.1	-9.0	1.126	0.2
800.	0.6	-0.9	0.4	-0.5	2.2	2.7	-1.8	2.7	-7.4	1.0	-1.3	4.6	5.5	-4.0	5.5	-9.8	1.121	0.3
900.	0.7	-1.0	0.5	-0.6	2.3	2.9	-1.8	2.9	-7.9	1.3	-1.6	5.0	6.0	-4.1	6.0	-10.5	1.115	0.4
1000.	0.7	-1.1	0.7	-0.8	2.5	3.2	-1.9	3.2	-8.4	1.7	-1.9	5.4	6.6	-4.3	6.6	-11.3	1.106	0.6
1250.	0.9	-1.4	1.0	-1.0	3.2	4.1	-2.3	4.6	-10.2	2.5	-2.4	6.7	8.4	-5.3	8.4	-13.9	1.076	0.6
1500.	1.1	-1.6	1.3	-1.2	4.2	5.4	-3.2	5.6	-12.3	3.3	-2.7	8.8	11.0	-7.0	11.0	-16.8	1.032	0.6
1750.	1.3	-1.9	1.5	-1.3	5.5	7.1	-4.4	7.1	-14.2	4.0	-2.7	11.6	14.5	-9.3	14.5	-19.6	0.975	0.2
2000.	1.5	-2.1	1.7	-1.2	7.3	9.2	-6.1	10.2	-15.9	4.6	-2.3	15.3	19.1	-12.3	19.1	-22.4	0.911	-0.3
2250.	1.6	-2.4	1.8	-1.1	9.5	11.7	-8.2	16.1	-17.4	5.0	-1.5	19.8	24.7	-16.0	28.1	-25.4	0.844	-1.0
2500.	1.9	-2.7	1.9	-0.9	11.9	14.5	-10.7	24.1	-18.6	5.4	-0.3	24.8	30.8	-20.3	39.8	-28.8	0.777	-1.8
2750.	2.1	-3.0	1.9	-0.5	14.5	17.4	-13.4	33.9	-28.3	5.7	0.0	30.1	37.2	-25.0	54.4	-60.1	0.711	-2.3
3000.	2.4	-3.4	1.9	-0.1	17.2	20.3	-16.2	46.6	-43.4	5.9	0.0	35.4	43.7	-29.6	73.1	-105.0	0.647	-2.6
3250.	2.8	-3.8	1.8	0.0	19.8	23.1	-18.9	64.4	-61.3	6.7	0.0	40.6	50.2	-34.1	99.8	-175.3	0.578	-2.7
3500.	3.2	-4.3	1.6	0.0	22.2	25.8	-21.3	91.2	-106.1	10.8	0.0	45.6	56.5	-38.1	139.8	-288.3	0.501	-2.7
3750.	3.6	-4.8	2.6	0.0	24.4	28.3	-23.5	150.7	-170.6	16.5	0.0	50.2	62.5	-41.6	241.9	-477.8	0.422	-2.8
4000.	4.0	-5.3	4.3	0.0	26.3	30.6	-25.3	296.9	-275.1	24.5	0.0	54.5	68.2	-44.5	472.6	-808.9	0.339	-3.3
4250.	4.3	-5.7	6.7	-0.4	27.9	32.4	-26.7	627.9	-500.5	35.2	0.0	58.5	73.7	-46.7	872.6	-1410.4	0.252	-4.1

Appendix D.

Electroweak corrections to the Drell-Yan cross section

In addition to higher order QCD corrections, electroweak (EW) corrections to the $\gamma/Z \to \ell^+\ell^-$ cross sections need to be considered. As calculations combining both QCD and EW higher order contributions are not available, these corrections are assumed to factorize. The EW corrections include contributions from final state photon radiation, EW loop corrections and processes with initial photons (being part of the proton's structure). For the MC background and signal samples, final state photon radiation (real QED correction) is accurately simulated using PHOTOS [98] and a full detector simulation. Therefore, this contribution needs to be excluded when defining a weight for the simulated samples to account for the remaining EW corrections.

The EW corrections were evaluated using the HORACE event generator v3.1 [88]. The cross section weights (correction factors) are defined as function of $m_{\ell\ell}$ as the following ratios of differential cross section predictions:

1. the ratio of the exact $\mathcal{O}(\alpha)$ calculation[1] over the LO prediction including only final state QED radiation in the parton shower approximation which parameterizes the correction due to EW loop contributions (figure D.1, left),

2. the ratio of the prediction including contributions with initial state photons over the one excluding these processes (with both calculations using the exact $\mathcal{O}(\alpha)$) which parameterizes the correction due to the photon contribution of the proton structure (figure D.1, right),

[1] Here $\mathcal{O}(\alpha)$ refers to the correction itself, which is at one-loop, not to the full ME^2. The full calculation is not $\mathcal{O}(\alpha^2)$ because the real corrections are not included.

3. the ratio of the exact $\mathcal{O}(\alpha)$ calculation including contributions with initial state photons over the prediction including only final state QED radiation in the parton shower approximation which is the product of the first two ratios (figure D.2).

The last ratio can be interpreted as an EW correction, which can be applied as additional event weight for simulated $\gamma/Z \to \ell^+\ell^-$. This correction factor is shown in figure D.2 for the electron and muon decay channels, respectively. For the differential cross section calculations the MRST2004QED PDF set [99] has been used. It provides a photon distribution function based on photon radiation and splitting kernels, and a lepton acceptance of $|\eta_\ell| < 2.5$ and $p_{T,\ell} > 20\,\text{GeV}$. As this acceptance does not properly match the data selection applied, the EW correction was recalculated for $|\eta_\ell| < 2.4$ and $p_{T,\ell} > 25\,\text{GeV}$, with a lower statistical precision. The ratio of both predictions, which is shown in figure D.3, agree within $\sim 0.2\%$.

While the EW correction can be directly applied as additional event weight for simulated $\gamma/Z \to \ell^+\ell^-$ events, in addition an effective correction factor for the expected selected $\gamma/Z \to \ell^+\ell^-$ event yield is determined by taking the ratio of the differential cross sections integrated over the selected invariant mass region (i.e. the range from the minimal $m_{\ell\ell}$ requirement up to infinity). These correction factors as function of the $m_{\ell\ell}$ cut are displayed in figure D.4 for electron and muon final states, respectively.

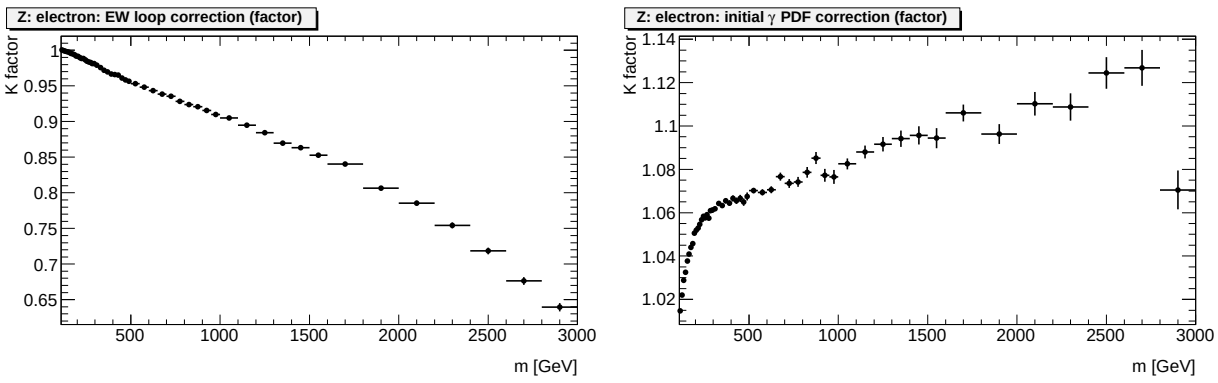

Figure D.1.: Correction factor (event weight) for the electron channel due to EW loop contributions (left) and due to photon induced processes (right).

The EW loop corrections, which were calculated using HORACE are partially canceled by the radiation of real W and Z bosons off the final state leptons [100]. This additional contribution is estimated based on reference [100] which presents corrections for $\gamma/Z \to \ell^+\ell^-$ production at $\sqrt{s} = 14$ TeV as function of $m_{\ell\ell}$ and p_T, respectively. These results are applied for $\sqrt{s} = 7$ TeV, assuming that they only depend on the center-of-mass energy of the hard interaction. Also, following reference [100], decays of the radiated W and Z bosons with charged leptons are not considered. The correction due to real radiation of weak bosons increases about linearly

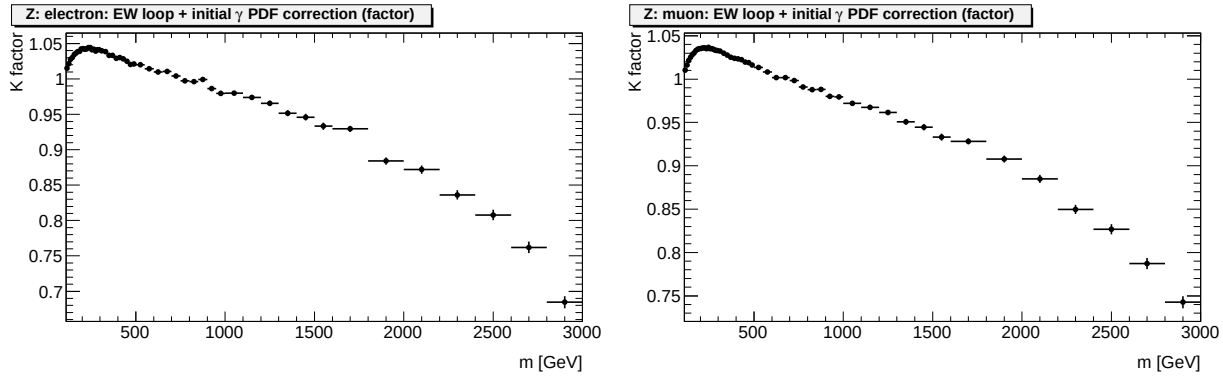

Figure D.2.: Correction factor (event weight) due to the combination of EW loop contributions and photon induced processes for electron (left) and muon (right) channels

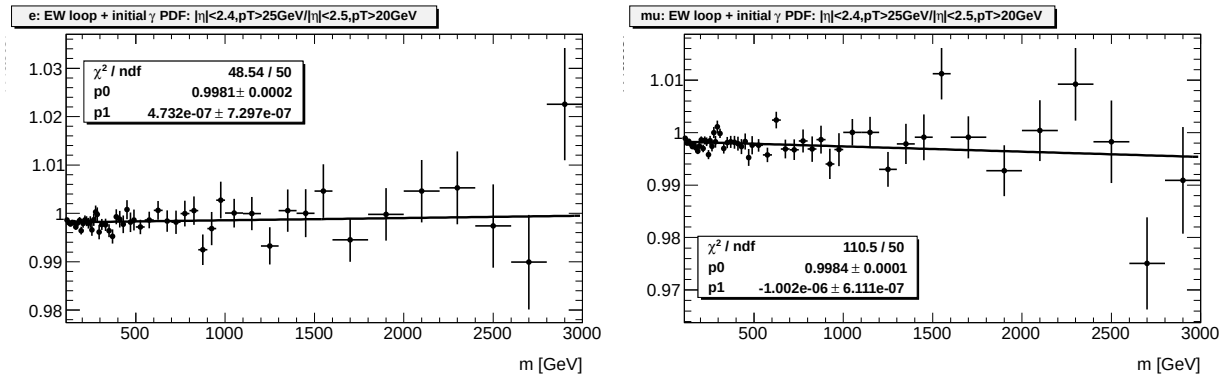

Figure D.3.: Ratio of the EW correction factors assuming different lepton acceptances (see text) for electron (left) and muon (right) channels.

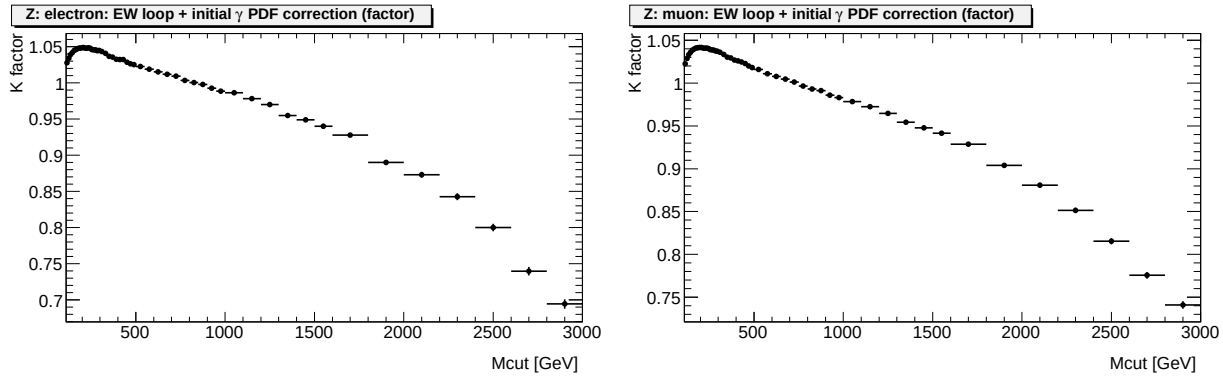

Figure D.4.: Correction factor on the expected integrated yield of $\gamma/Z \to e^+e^-$ (left) and $\gamma/Z \to \mu^+\mu^-$ (right) events with invariant masses $M > M_{\text{cut}}$ due to the combination of EW loop contributions and photon induced processes.

with dilepton mass (figure D.5) and is approximately 20% of the EW loop corrections at $m_{\ell\ell} = 1$ TeV.

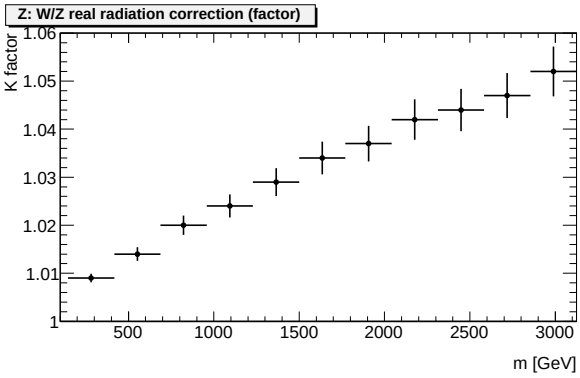

Figure D.5.: Correction factor due to weak boson radiation as function of $m_{\ell\ell}$ for $\gamma/Z \to \ell^+\ell^-$ production [100].

Finally an EW K-factor is derived by combining the corrections due to EW loops and initial photon processes (both obtained with HORACE) and due to weak boson radiation which is shown in figure D.6, separately for dielectron and dimuon final states. For 250 GeV $< m <$ 1750 GeV, the combined K-factor can be well approximated by a linear function,

- for $\gamma/Z \to e^+e^-$: $K_{ee} = 1.067 - 6.35 \times 10^{-2}\,\mathrm{TeV}^{-1} \times m\,,$
- for $\gamma/Z \to \mu^+\mu^-$: $K_{\mu\mu} = 1.060 - 6.09 \times 10^{-2}\,\mathrm{TeV}^{-1} \times m\,.$

Below 250 GeV, a cubic function is needed:

- for $\gamma/Z \to e^+e^-$: $K_{ee} = 0.841 + 2.58\,\mathrm{TeV}^{-1} \times m\, - 10.8\,\mathrm{TeV}^{-2} \times m^2\, + 15.4\,\mathrm{TeV}^{-3} \times m^3,$
- for $\gamma/Z \to \mu^+\mu^-$: $K_{\mu\mu} = 0.852 + 2.33\,\mathrm{TeV}^{-1} \times m\, - 9.53\,\mathrm{TeV}^{-2} \times m^2\, + 13.1\,\mathrm{TeV}^{-3} \times m^3;$

and above 1750 GeV, a quadratic function is needed:

- for $\gamma/Z \to e^+e^-$: $K_{ee} = 0.873 + 0.183 \times 10^{-3}\,\mathrm{TeV}^{-1} \times m\, - 0.0797\,\mathrm{TeV}^{-2} \times m^2,$
- for $\gamma/Z \to \mu^+\mu^-$: $K_{\mu\mu} = 0.931 + 0.114 \times 10^{-3}\,\mathrm{TeV}^{-1} \times m\, - 0.0571\,\mathrm{TeV}^{-2} \times m^2.$

A systematic uncertainty on the EW K-factor is estimated as 4.5%, taking into account uncertainties in the calculation of real boson radiation (1%), potential contributions from $\mathcal{O}(\alpha\alpha_s)$ corrections (1%) [89], higher order EW corrections (1.5%) [101], an assumed uncertainty of 10% on the contribution from photon induced processes (1%), and a difference in the definition of the EW scheme used in the event generation with PYTHIA and in the calculation of the EW corrections with HORACE (3%).

This K-factor is not applied in the σB limit for the Z'_{SSM} signal, although EW corrections of similar size can be expected. This calculation cannot be directly applied, as in this model the

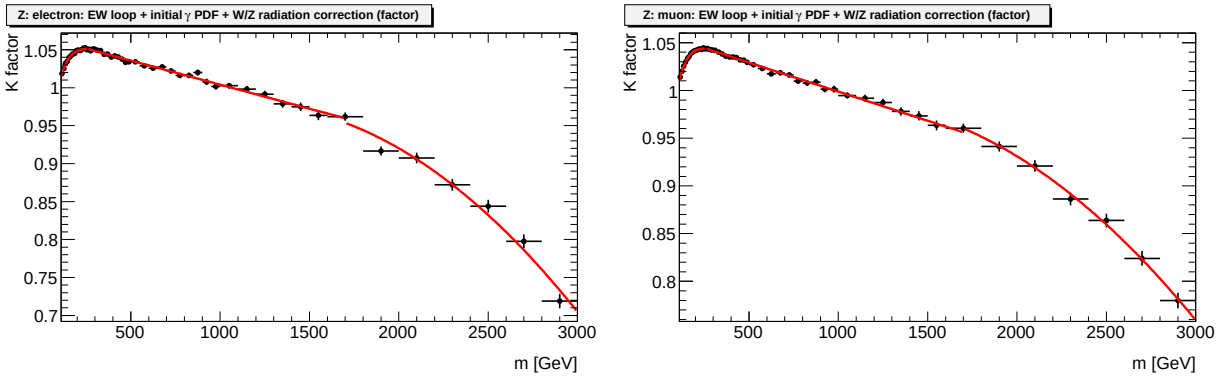

Figure D.6.: Electroweak K-factor for $\gamma/Z \to e^+e^-$ (left) and $\gamma/Z \to \mu^+\mu^-$ (right) production as function of dilepton mass taking into account corrections due to processes with initial photons, EW loops and real radiation of W and Z bosons.

triple gauge coupling $Z'W^+W^-$ vanishes in contrast to the standard model ZW^+W^- coupling. However, for the coupling limit, where the signals interfere with the DY, the EW correction has to be applied in order to match the low-end of the $m_{\ell\ell}$ shape where the DY dominates over the (heavy) Z'_{SSM} (or $\gamma_{\mathrm{KK}}/Z_{\mathrm{KK}}$) signal.

Appendix E.

Muon trigger efficiency

In this analysis, the muon trigger and reconstruction efficiencies are determined using the "tag-and-probe" method, which reconstructs $Z \to \mu\mu$ decays to select a very pure dimuon sample. In this section the procedure of how to measure muon trigger efficiency in both data and MC and to derive the data/MC scale factor (SF) are described. The trigger efficiency is defined as the fraction of events where the muon is matched to the corresponding high level trigger (HLT) objects.

The *tag* muon satisfies the baseline, single muon selection and should be classified as a *three-station* muon, as described in section 4.4. In addition, it has to be matched with an HLT object corresponding to the relevant event trigger, with a relatively tight matching requirement, $\Delta R < 0.1$. In other words, the *tag* is a *three-station* good muon[1] that has initiated the event trigger chain.

The *probe* muon also has to satisfy the *three-station* single muon selection. The invariant mass of the the *probe* muon and the *tag* muon must be within $|m_{\mu\mu}(\text{tag} + \text{probe}) - M_Z| < 10$ GeV, where their charges must be opposite. Then it is checked if the *probe* muon can be matched with an HLT object corresponding to the relevant event trigger, with a looser matching requirement of $\Delta R < 0.2$. If this matching requirement is satisfied then the *probe* is called "matched-*probe*". The distributions of the p_{T}, η and ϕ are made once for the matched-*probes* and once for all the *probes* (matched and unmatched). The ratio between the two distributions is the efficiency where this is done for data and MC in the exact same way.

The dimuon channel is used for this analysis, therefore there are two chances to pass a single-lepton trigger. It is necessary to define an event-based scale factor, which in this case is given

[1] The *two-stations* muons were checked as well but there are insufficient statistics for the efficiency study for this category.

by:

$$\mathrm{SF}_{\mu\mu} = \frac{1-[1-\epsilon_{\mu 1}(Z,\mathrm{data})][1-\epsilon_{\mu 2}(Z,\mathrm{data})]}{1-[1-\epsilon_{\mu 1}(Z,\mathrm{MC})][1-\epsilon_{\mu 2}(Z,\mathrm{MC})]} \tag{E.0.1}$$

This analysis uses a combination of the following single muon triggers:

- for period B to I, EF_mu22 or EF_mu22_MG or EF_mu40_MSonly_barrel.
- for period J to M, EF_mu22_medium or EF_mu22_MG_medium or EF_mu40_MSonly_barrel_medium are used, as the triggers used for period B to I were prescaled due to L1 trigger rate limitation.

For periods L3 and L4, trigger efficiencies in data at barrel region are considerably lower than the other periods due to a misconfiguration problem of RPC detector. For this reason, trigger efficiencies for period L3 and L4 are calculated separately.

Figure E.1 shows the single muon trigger efficiency and data/MC scale factor as a function of the offline muon p_{T} in the barrel and endcap regions.

Figure E.2 shows the trigger efficiency and data/MC scale factor as a function of the offline muon η, where the η regions are divided into 28 bins (-3.0, -2.4, -1.918, -1.623, -1.348, -1.2329, -1.1479, -1.05, -0.908, -0.791, -0.652, -.0.476, -0.324, -0.132, 0.0, 0.132, 0.324, 0.476, 0.652, 0.791, 0.908, 1.05, 1.1479, 1.2329, 1.348, 1.623, 1.918, 2.4, 3.0).

Figure E.3 shows the trigger efficiency and data/MC scale factor as a function of the offline muon ϕ in barrel and endcap regions. Barrel regions are divided into 16 ϕ bins (from $-15/16\pi$ to $17/16\pi$), and endcap regions are divided into 12 ϕ bins (from $-45/48\pi$ to $51/48\pi$). For both barrel and endcap regions, the binning choice stems from the geometry of the RPC and TGC detectors, respectively.

To estimate the systematic uncertainty on the trigger efficiency, the following sources are considered:

- vary the size of the Z mass window (± 5 GeV),
- vary the matching cone size for the offline muon and HLT trigger objects. The default cone size used are 0.1 for tagged muon and 0.2 for probe muon, and these studies are repeated using 0.3 for tag muon and 0.1 and 0.3 for probe muon.
- remove the isolation cut for tagged muon to estimate the QCD background effect.
- vary the tag muon p_{T} cut value (± 5 GeV).

- correct η and ϕ dependency respectively comparing MC Z'_{SSM} 2 TeV sample and $Z \to \mu\mu$ sample.

Total systematic uncertainty are defined as quadratic sum of these uncertainty contributions. The systematic uncertainties on trigger efficiencies are less than 1% for the barrel region and about 2.5% for the endcap region throughout all periods, and the systematic uncertainties on the scale factors are less than 0.01 throughout all periods.

Tables E.1, E.2 and E.3 show trigger efficiencies and data/MC scale factors for periods B to I, periods J to M (without periods L3 and L4) and period L3 and L4 respectively. Each of the values in the tables are obtained by a linear fitting of the p_{T} plateau region between 25 GeV and 300 GeV.

Table E.1.: Trigger efficiency and data/MC scale factor for periods B to I.

	Barrel efficiency	Endcap efficiency
data	$(85.02 \pm 0.07 \pm 0.17)\%$	$(86.19 \pm 0.07 \pm 2.36)\%$
MC	$(82.64 \pm 0.04 \pm 0.13)\%$	$(84.77 \pm 0.04 \pm 2.66)\%$
scale factor	$1.029 \pm 0.001 \pm 0.001$	$1.017 \pm 0.001 \pm 0.002$

Table E.2.: Trigger efficiency and data/MC scale factor for periods J to M (without periods L3 and L4).

	Barrel efficiency	Endcap efficiency
data	$(77.79 \pm 0.06 \pm 0.08)\%$	$(85.63 \pm 0.06 \pm 2.21)\%$
MC	$(79.05 \pm 0.04 \pm 0.10)\%$	$(84.72 \pm 0.04 \pm 2.36)\%$
scale factor	$0.984 \pm 0.001 \pm 0.001$	$1.011 \pm 0.001 \pm 0.002$

Table E.3.: Trigger efficiency and data/MC scale factor for periods L3 and L4.

	Barrel efficiency	Endcap efficiency
data	$(61.89 \pm 0.18 \pm 0.28)\%$	$(85.49 \pm 0.13 \pm 2.26)\%$
MC	$(79.05 \pm 0.04 \pm 0.10)\%$	$(84.72 \pm 0.04 \pm 2.26)\%$
scale factor	$0.783 \pm 0.002 \pm 0.003$	$1.009 \pm 0.002 \pm 0.002$

Table E.4, Table E.5 and Table E.6 show the event-based trigger efficiency and data/MC scale factor for periods B to I, periods J to M (without periods L3 and L4) and periods L3 and L4 respectively.

Table E.4.: Event-based trigger efficiency and scale factor with muon $p_T > 25$ GeV for barrel-barrel (BB), barrel-endcap (BE) and endcap-endcap (EE) events for periods B to I.

	BB efficiency	BE efficiency	EE efficiency
data	$(97.76 \pm 0.02 \pm 0.04)\%$	$(97.93 \pm 0.02 \pm 0.35)\%$	$(98.09 \pm 0.01 \pm 0.46)\%$
MC	$(96.99 \pm 0.01 \pm 0.03)\%$	$(97.36 \pm 0.01 \pm 0.46)\%$	$(97.68 \pm 0.01 \pm 0.57)\%$
scale factor	$1.008 \pm 0.000 \pm 0.001$	$1.006 \pm 0.000 \pm 0.006$	$1.004 \pm 0.000 \pm 0.008$

Table E.5.: Event-based trigger efficiency and scale factor with muon $p_T > 25$ GeV for barrel-barrel (BB), barrel-endcap (BE) and endcap-endcap (EE) events for periods J to M (without periods L3 and L4).

	BB efficiency	BE efficiency	EE efficiency
data	$(95.07 \pm 0.02 \pm 0.03)\%$	$(96.81 \pm 0.02 \pm 0.49)\%$	$(97.94 \pm 0.01 \pm 0.45)\%$
MC	$(95.61 \pm 0.01 \pm 0.03)\%$	$(96.80 \pm 0.01 \pm 0.49)\%$	$(97.67 \pm 0.01 \pm 0.51)\%$
scale factor	$0.994 \pm 0.000 \pm 0.000$	$1.000 \pm 0.000 \pm 0.007$	$1.003 \pm 0.000 \pm 0.007$

Table E.6.: Event-based trigger efficiency and scale factor with muon $p_T > 25$ GeV for barrel-barrel (BB), barrel-endcap (BE) and endcap-endcap (EE) events for periods L3 and L4.

	BB efficiency	BE efficiency	EE efficiency
data	$(85.47 \pm 0.09 \pm 0.15)\%$	$(94.47 \pm 0.06 \pm 0.86)\%$	$(97.89 \pm 0.03 \pm 0.46)\%$
MC	$(95.61 \pm 0.01 \pm 0.03)\%$	$(96.80 \pm 0.01 \pm 0.49)\%$	$(97.67 \pm 0.01 \pm 0.51)\%$
scale factor	$0.894 \pm 0.001 \pm 0.002$	$0.976 \pm 0.001 \pm 0.010$	$1.002 \pm 0.000 \pm 0.007$

To conclude, it is found that the SF is very close to one and is flat in p_{T} and therefore its influence should be anyhow small and independent of $m_{\mu\mu}$. The effect of this flat correction in $m_{\mu\mu}$ vanishes upon normalizing the backgrounds sum to the Z peak from data, as described in section 4.4. A systematic uncertainty is accounted for, however, as described here and in the text (chapter 5).

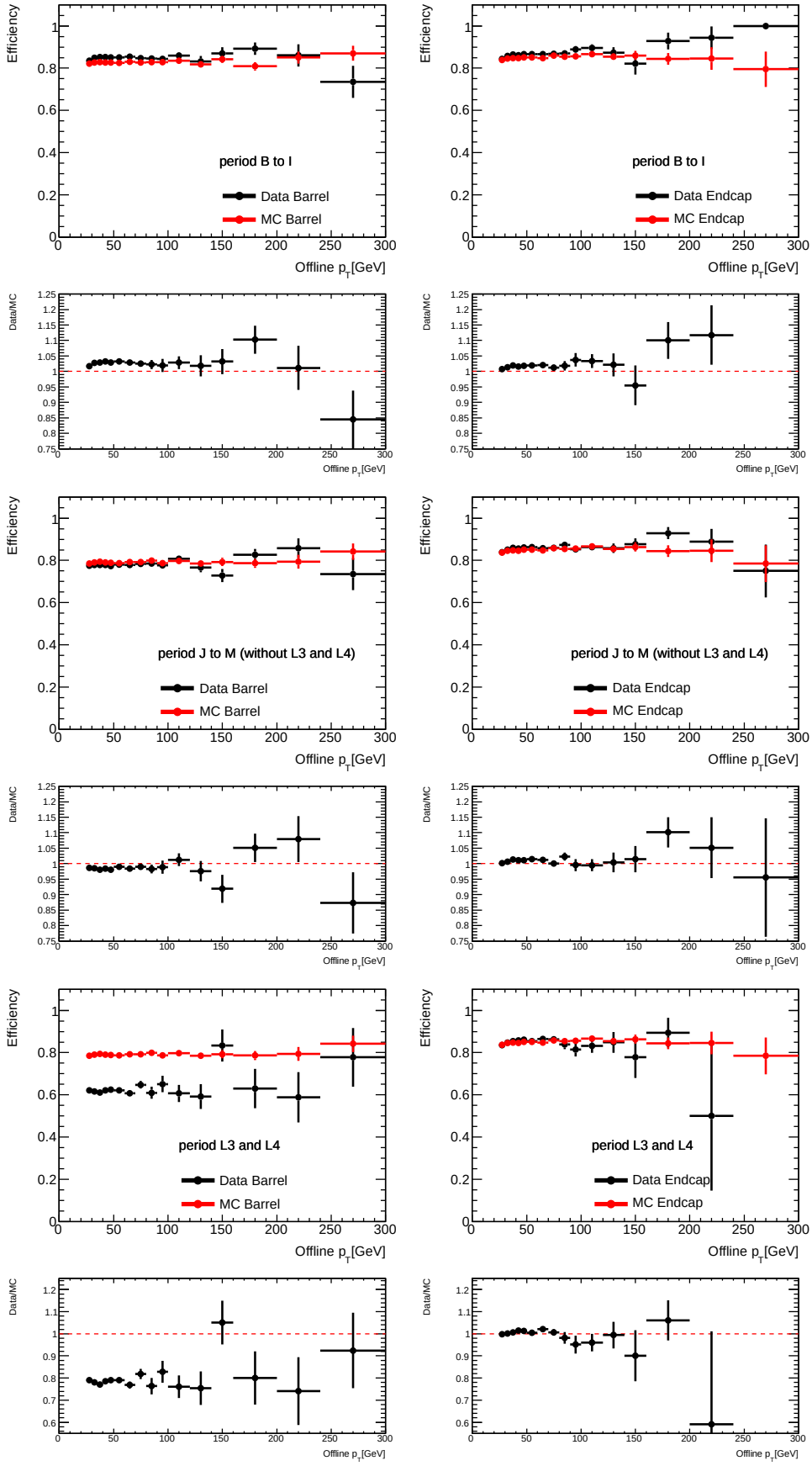

Figure E.1.: Muon trigger efficiency and data/MC scale factor as a function of muon p_{T} for barrel and endcap region.

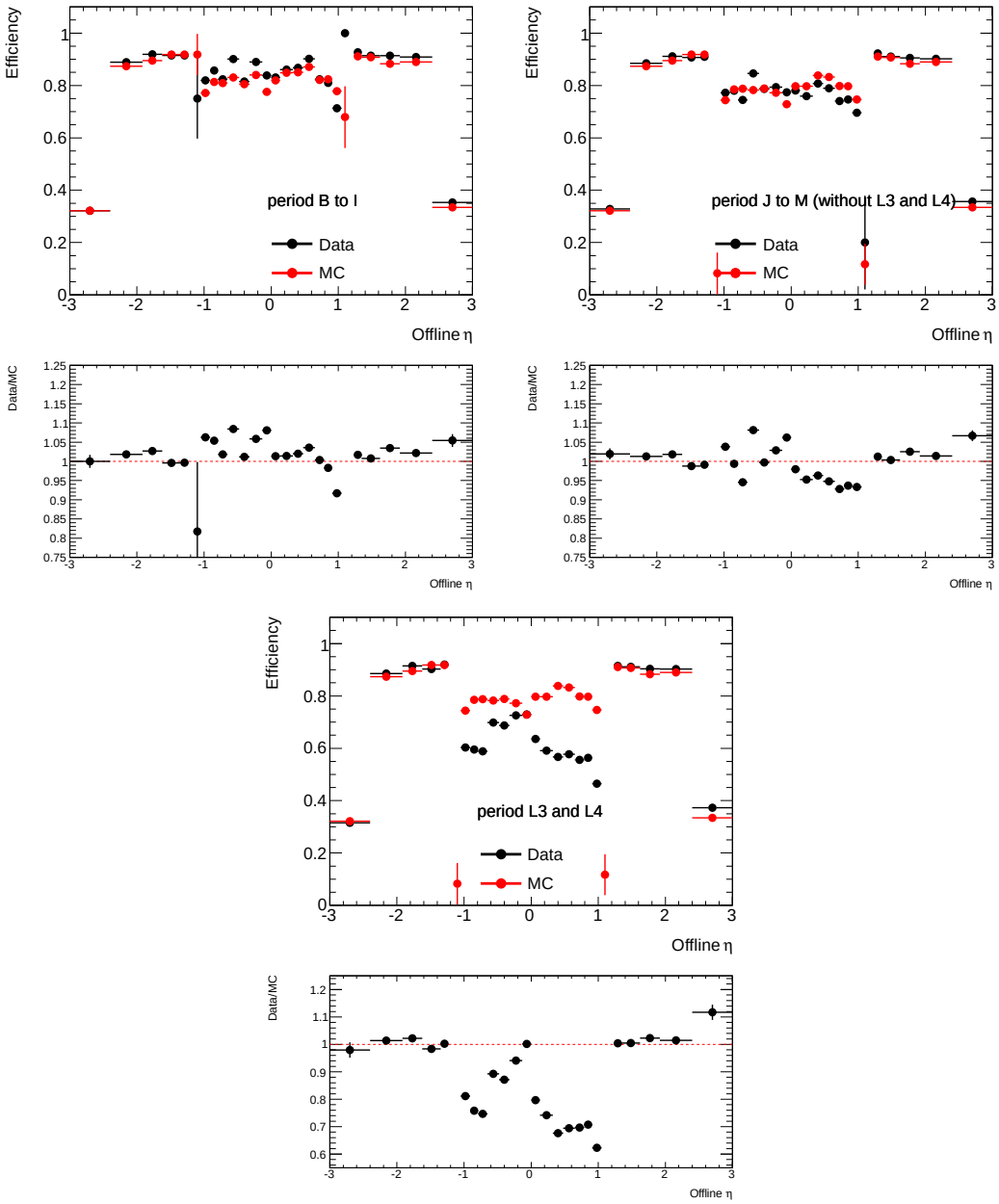

Figure E.2.: Muon trigger efficiency and data/MC scale factor as a function of muon η. Muons with $p_T > 25$ GeV are used.

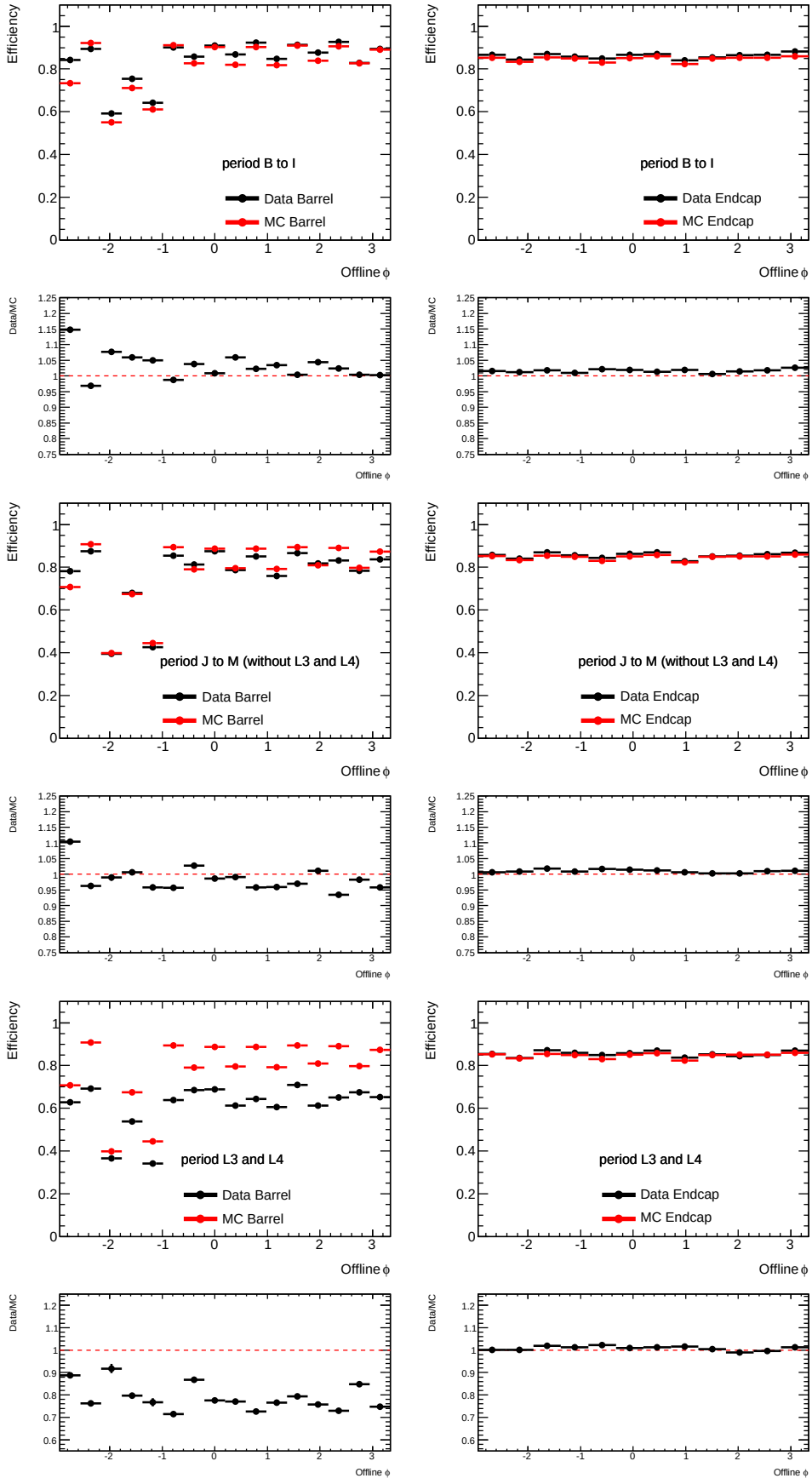

Figure E.3.: Muon trigger efficiency and data/MC scale factor as a function of muon ϕ for barrel and endcap regions. Muons with $p_{\mathrm{T}} > 25$ GeV are used.

Appendix F.

Muon reconstruction efficiency

In this section it is described how the "tag-and-probe" method allows to measure the muon reconstruction efficiency in both data and MC and derive the data/MC scale factors (SF) as a function of p_{T}, ϕ and η, and also separately in the various regions of the detector. For the implementation of the tag-and-probe method, events are selected with one good muon (the *tag* muon) and one charged particle track measured by the ID (the *probe* track).

The reconstructed *tag* muons follow the single muon criteria used in the baseline analysis, as described in section 4.4. In order to avoid bias from trigger, it is required that the *tag* muon will be matched to an HLT triggered object, using the same HLT triggers used in the analysis for the various data-taking periods as described in section 4.4.

The ad-hoc definition of the good ID *probe* tracks is required to have,

- $p_{\mathrm{T}} > 25$ GeV,
- $|z_0| < 10$ mm (same vertex as the *tag* muon),
- $|\eta| < 2.5$
- the sum of the p_{T} of all tracks in a cone of size $\Delta R < 0.4$ relative to the p_{T} of the track itself, must be less than 0.2.

To suppress the contamination from backgrounds, the invariant mass of the the candidate ID *probe* track and the *tag* muon must be within a small range around the Z peak, $81 < m_{\mu\mu} < 101$ GeV, and their charges must be opposite.

The efficiency is computed as the ratio between the distribution of all the ID *probe* tracks that were matched with a reconstructed muon within $\Delta R < 0.01$, over the same distribution of all the ID *probes* tracks (matched and unmatched).

The MC samples that were taken into account were the Z boson signal and the $t\bar{t}$, $Z \to \tau\tau$ and W boson backgrounds. The smearing of p_{T} of the reconstructed muons was applied to all MC samples as described in section 4.5.

Figure F.1 shows the muon reconstruction efficiency and data/MC scale factor as a function of muon p_{T}. Figure F.2 shows the efficiency and data/MC scale factor as a function of muon η and ϕ. Figure F.3 shows the efficiency and data/MC scale factors in the different regions of the detector. Tables F.1 and F.2 show the efficiencies and the scale factors obtained per region of the detector. Since the data-MC agreement is nearly flat, the data is averaged to obtain the scale factor shown in table F.2. The scale factors for periods B2-I and J, K, L, and M are listed in table F.3 and F.4.

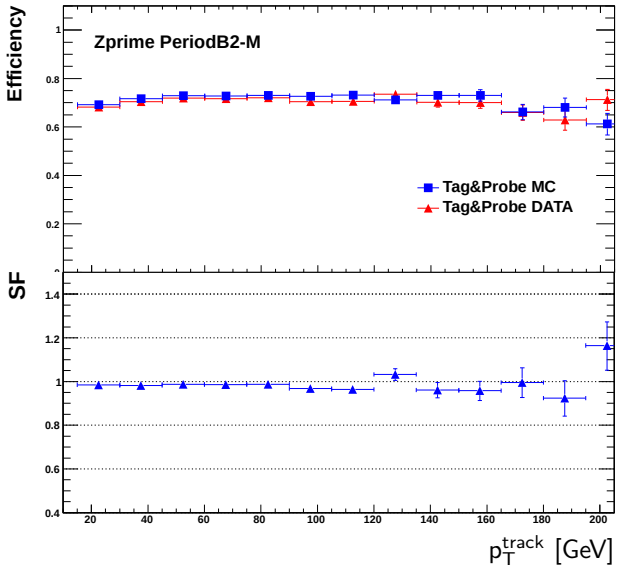

Figure F.1.: Muon efficiency and data/MC scale factor as a function of muon p_{T} for periods B2-M (barrel and endcap region are combined).

Table F.1.: Average reconstruction efficiency for muons with $p_T > 25$ GeV for Periods B2 to M.

	Tag-and-probe efficiency
Average efficiency Periods B2-M (data)	$(70.63 \pm 0.03^{+0.27}_{-0.11})\%$
Average efficiency Periods B2-I (data)	$(70.49 \pm 0.06^{+0.27}_{-0.11})\%$
Average efficiency Periods JKLM (data)	$(70.73 \pm 0.04^{+0.27}_{-0.11})\%$
Average efficiency (MC)	$(71.82 \pm 0.03)\%$

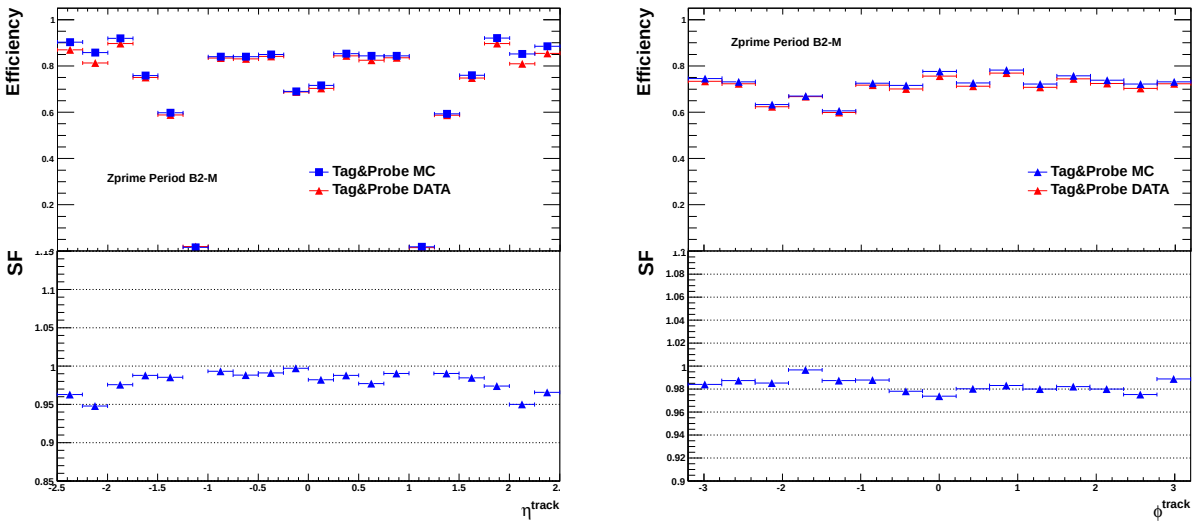

Figure F.2.: Muon efficiency and data/MC scale factor as a function of muon η (left) and ϕ (right) for barrel and endcap region for periods B2-M. Muons with $p_T > 25$ GeV are used.

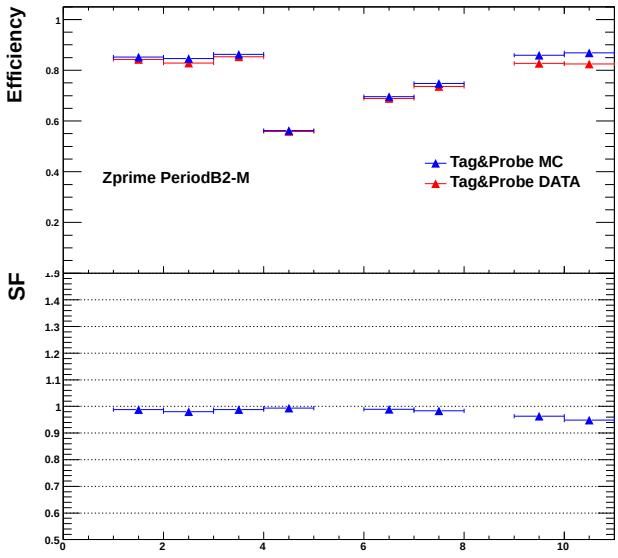

Figure F.3.: Muon efficiency and data/MC scale factor in the various regions of the detector for periods B2-M. Binning notation: 1= Barrel Large; 2=Barrel Small; 3=Barrel Overlap; 4=Feet; 6=Endcap Large; 7=Endcap Small; 9=CSC Large; 10=CSC Small.

The systematic uncertainties reported in the table were obtained considering the following sources:

1. Mass Window: The invariant mass range (Z peak) was varied from nominal value (81 GeV,101 GeV) to (83 GeV,99 GeV) and to (79 GeV,103 GeV).

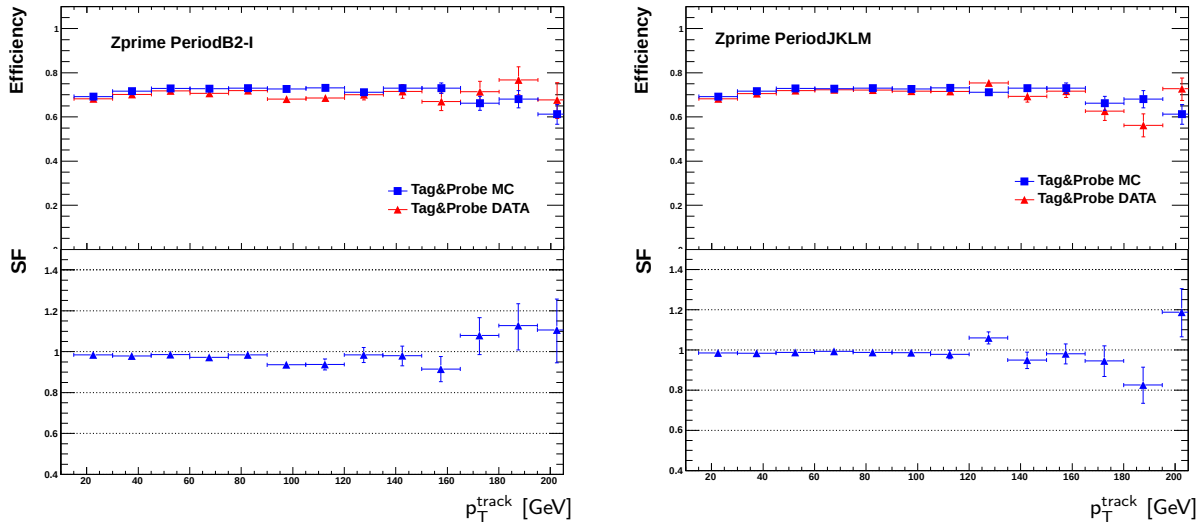

Figure F.4.: Muon efficiency and data/MC scale factor as a function of muon p_T for periods B2-I (left) and periods J, K, L and M (right) (barrel and endcap region are combined).

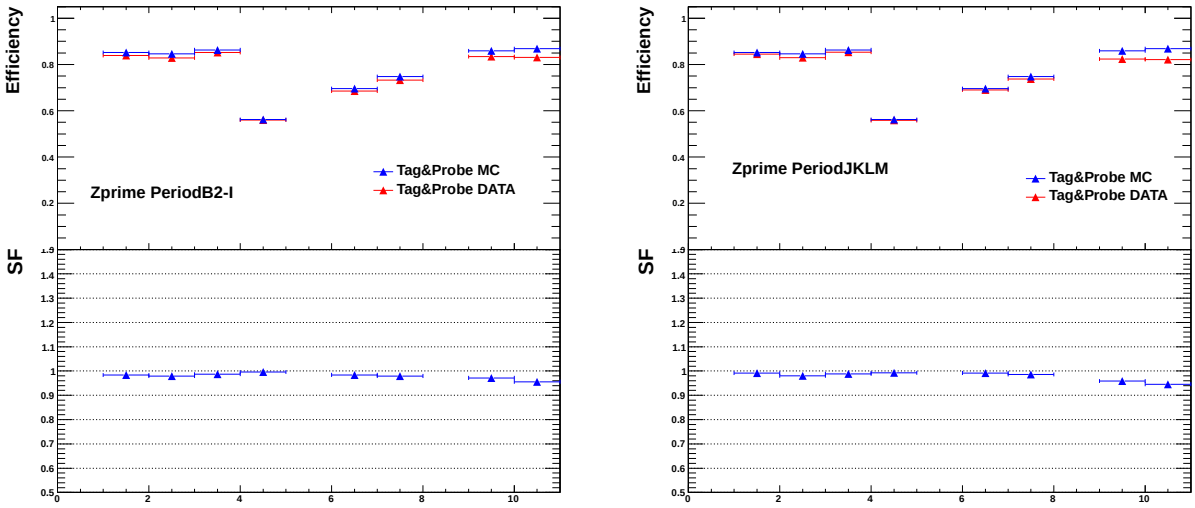

Figure F.5.: Muon efficiency and data/MC scale factor in the various regions of the detector for periods B2-I (left) and periods J, K, L and M (right). Binning notation: 1= Barrel Large; 2=Barrel Small; 3=Barrel Overlap; 4=Feet; 6=Endcap Large; 7=Endcap Small; 9=CSC Large; 10=CSC Small

2. Tag muon p_T: The p_T threshold was varied from the nominal value 25 GeV to 20 GeV and to 30 GeV.

3. Track isolation: The cone size for the isolation requirement is reduced from 0.4 to 0.3 and the isolation requirement itself is reduced from 0.2 to 0.05.

4. Background: The backgrounds were increased by 10%.

Table F.2.: Data/MC scale factors per region of the detector and average scale factor for muons with $p_{\mathrm{T}} > 25$ GeV for periods B2-M.

Detector region	SF $\pm$ (stat.) $\pm$ (syst.)
Barrel Large	$0.9885 \pm 0.0009^{+0.0003}_{-0.0006}$
Barrel Small	$0.9800 \pm 0.0015^{+0.0006}_{-0.0006}$
Barrel Overlap	$0.9879 \pm 0.0013^{+0.0009}_{-0.0006}$
Feet	$0.9939 \pm 0.0037^{+0.0005}_{-0.0007}$
Endcap Large	$0.9893 \pm 0.0020^{+0.0010}_{-0.0013}$
Endcap Small	$0.9835 \pm 0.0015^{+0.0003}_{-0.0007}$
CSC Large	$0.9633 \pm 0.0020^{+0.0003}_{-0.0011}$
CSC Small	$0.9492 \pm 0.0013^{+0.0003}_{-0.0011}$
Mean value	$0.9815 \pm 0.0006^{+0.0002}_{-0.0006}$

Table F.3.: Data/MC scale factors per region of the detector and average scale factor for muons with $p_T > 25$ GeV for periods B2-I.

Detector region	SF $\pm$ (stat.) $\pm$ (syst.)
Barrel Large	$0.9839 \pm 0.0013^{+0.0002}_{-0.0005}$
Barrel Small	$0.9795 \pm 0.0020^{+0.0007}_{-0.0009}$
Barrel Overlap	$0.9867 \pm 0.0018^{+0.0011}_{-0.0006}$
Feet	$0.9959 \pm 0.0050^{+0.0024}_{-0.0007}$
Endcap Large	$0.9842 \pm 0.0027^{+0.0008}_{-0.0008}$
Endcap Small	$0.9796 \pm 0.0020^{+0.0004}_{-0.0006}$
CSC Large	$0.9717 \pm 0.0028^{+0.0012}_{-0.0011}$
CSC Small	$0.9560 \pm 0.0019^{+0.0012}_{-0.0015}$
Mean value	$0.9799 \pm 0.0008^{+0.0002}_{-0.0004}$

The effects on the efficiency for each source of the systematic uncertainty are shown in tables F.5 and F.6 for MC and data respectively. Table F.7 shows the corresponding effects on the scale factors. The systematic uncertainties are not correlated and therefore are added in quadrature.

Table F.4.: Data/MC scale factors per region of the detector and average scale factor for muons with $p_T > 25$ GeV for periods J, K, L and M.

Detector region	SF $\pm$(stat.) $\pm$(syst.)
Barrel Large	$0.9911 \pm 0.0011^{+0.0006}_{-0.0007}$
Barrel Small	$0.9803 \pm 0.0017^{+0.0006}_{-0.0008}$
Barrel Overlap	$0.9886 \pm 0.0015^{+0.0009}_{-0.0006}$
Feet	$0.9926 \pm 0.0042^{+0.0008}_{-0.0013}$
Endcap Large	$0.9920 \pm 0.0022^{+0.0011}_{-0.0019}$
Endcap Small	$0.9856 \pm 0.0016^{+0.0002}_{-0.0010}$
CSC Large	$0.9590 \pm 0.0023^{+0.0008}_{-0.0012}$
CSC Small	$0.9458 \pm 0.0015^{+0.0002}_{-0.0012}$
Mean value	$0.9824 \pm 0.0007^{+0.0002}_{-0.0007}$

Table F.5.: Reconstruction efficiency due to each source variation in MC.

Source to vary	Tag-and-probe Efficiency
Mass window (81GeV,101GeV)→(83GeV,99GeV)	71.780%
Mass window (81GeV,101GeV)→(79GeV,103GeV)	71.837%
Tag muon p_{T} (25 GeV$p_{\mathrm{T}} \rightarrow$ 20 GeV)	72.091%
Tag muon p_{T} (25 GeV$p_{\mathrm{T}} \rightarrow$ 30 GeV)	71.714%
Track Isolation ptcone40→ptcone30	71.833%
Background (+10%)	71.817%

Table F.6.: Reconstruction efficiency due to each source variation in data periods B2-M.

Source to vary	Tag-and-probe Efficiency
Mass window (81GeV,101GeV)→(83GeV,99GeV)	70.586%
Mass window (81GeV,101GeV)→(79GeV,103GeV)	70.634%
Tag muon p_{T} (25 GeV$p_{\mathrm{T}} \rightarrow$ 20 GeV)	70.854%
Tag muon p_{T} (25 GeV$p_{\mathrm{T}} \rightarrow$ 30 GeV)	70.533%
Track Isolation ptcone40→ptcone30	70.648%

To conclude, the average scale factor for the full period B2-M is $0.9815 \pm 0.0006^{+0.0002}_{-0.0006}$ and the reconstruction efficiency for data is $71.63 \pm 0.03^{+0.27}_{-0.11}\%$ for this analysis. It is found that the SF is very close to one and is flat in p_{T}, and therefore its influence should be anyhow

Table F.7.: Average scale factor due to each source variation for periods B2-M.

Source to vary	Average SF
Mass window (81GeV,101GeV)→(83GeV,99GeV)	0.9815
Mass window (81GeV,101GeV)→(79GeV,103GeV)	0.9814
Tag muon p_{T} (25 GeVp_{T} → 20 GeV)	0.9809
Tag muon p_{T} (25 GeVp_{T} → 30 GeV)	0.9817
Track Isolation ptcone40→ptcone30	0.9816
Background (+10%)	0.9816

small and independent of $m_{\mu\mu}$. The small effect of the SF, being close but not exactly one, is vanished upon normalizing the backgrounds sum to the Z peak from data, as described in section 4.4. As in the trigger efficiency study, although the SF is eventually not applied on the MC samples, an uncertainty is accounted for as described here and in the text (chapter 5).

Appendix G.

Signal templates validation

G.1. Templates examples

The templates for Z'_{SSM} signals are shown in figure G.1. The 2D templates for $\gamma_{\mathrm{KK}}/Z_{\mathrm{KK}}$ signal plus backgrounds are shown in figures G.2 and G.3 for two example pole masses. Unlike in figure G.2 for a Z'_{SSM} with a mass of 2 TeV, the 4 TeV Z'_{SSM} is not shown in figure G.3 because it affects the $m_{\mu\mu}$ distribution only above 3 TeV which is the high end in this analysis.

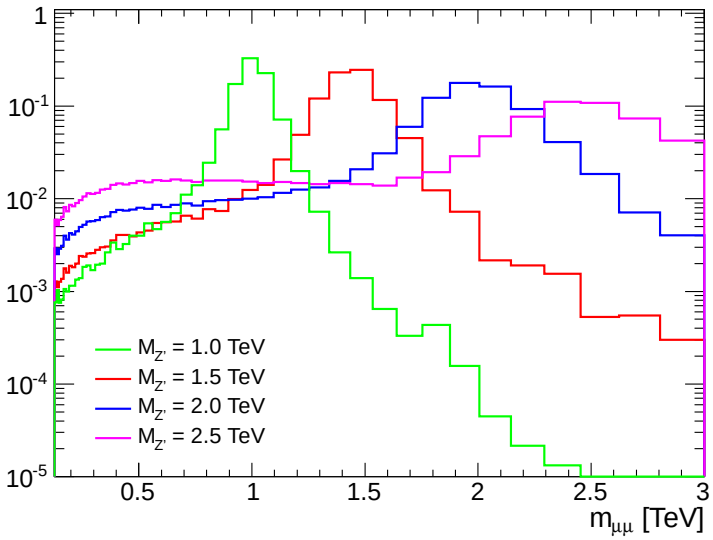

Figure G.1.: Dimuon $m_{\mu\mu}$ templates for few Z'_{SSM} pole masses as reweighted from the flat sample for the σB limits. These templates are normalized to unity.

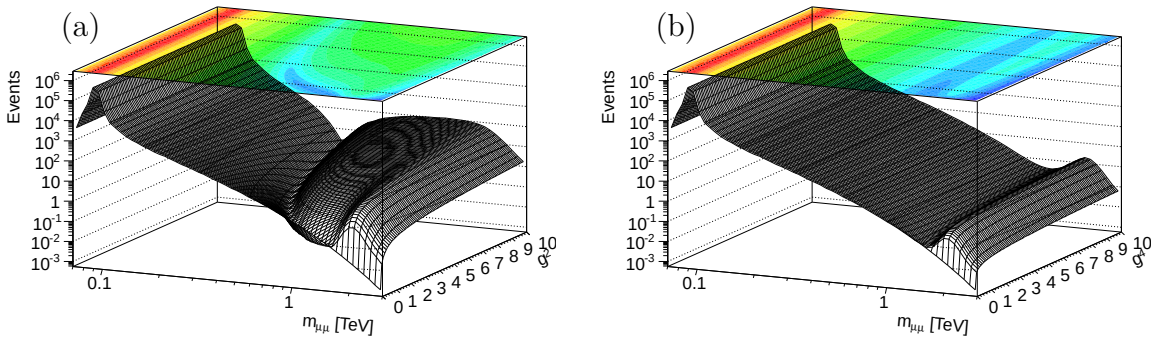

Figure G.2.: The nominal 2D templates ($m_{\mu\mu}$ vs. g^N) at 2 TeV. The KK template for g^2 in (a) and the Z'_{SSM} template for g^4 in (b).

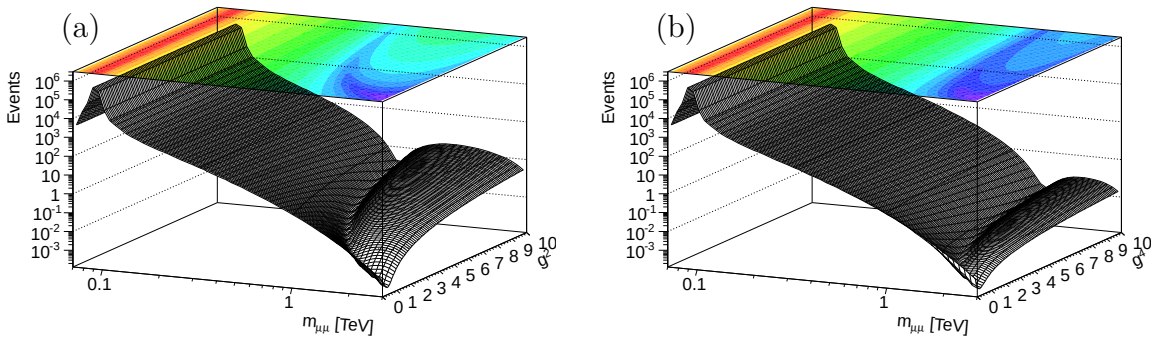

Figure G.3.: The nominal 2D templates ($m_{\mu\mu}$ vs. g^N) at 4 TeV. The KK template for g^2 in (a) and the KK template for g^4 in (b).

G.2. Template reweighting validation

Figure G.4 shows the validation of the dimuon templates for the Z'_{SSM} signal as obtained in the two reweighting frameworks. Namely, few of the official Z'_{SSM} samples can be compared with the reweighed samples from the flat sample (see equation 4.2.1) and from the binned DY samples (see equation 4.2.2). The first framework constructs only the Z'_{SSM} signal in the desired luminosity where the DY is added to it afterwards (with the same luminosity). The second framework, labeled here ME^2 (matrix-element-squared), constructs the full-interference structure. It can also produce the pure Z'_{SSM} with a greater accuracy comparing with the flat sample reweighting procedure because the analytic form is used and no approximations are done.

To conclude, the two frameworks give a very good agreement between the templates and the official Z'_{SSM} samples.

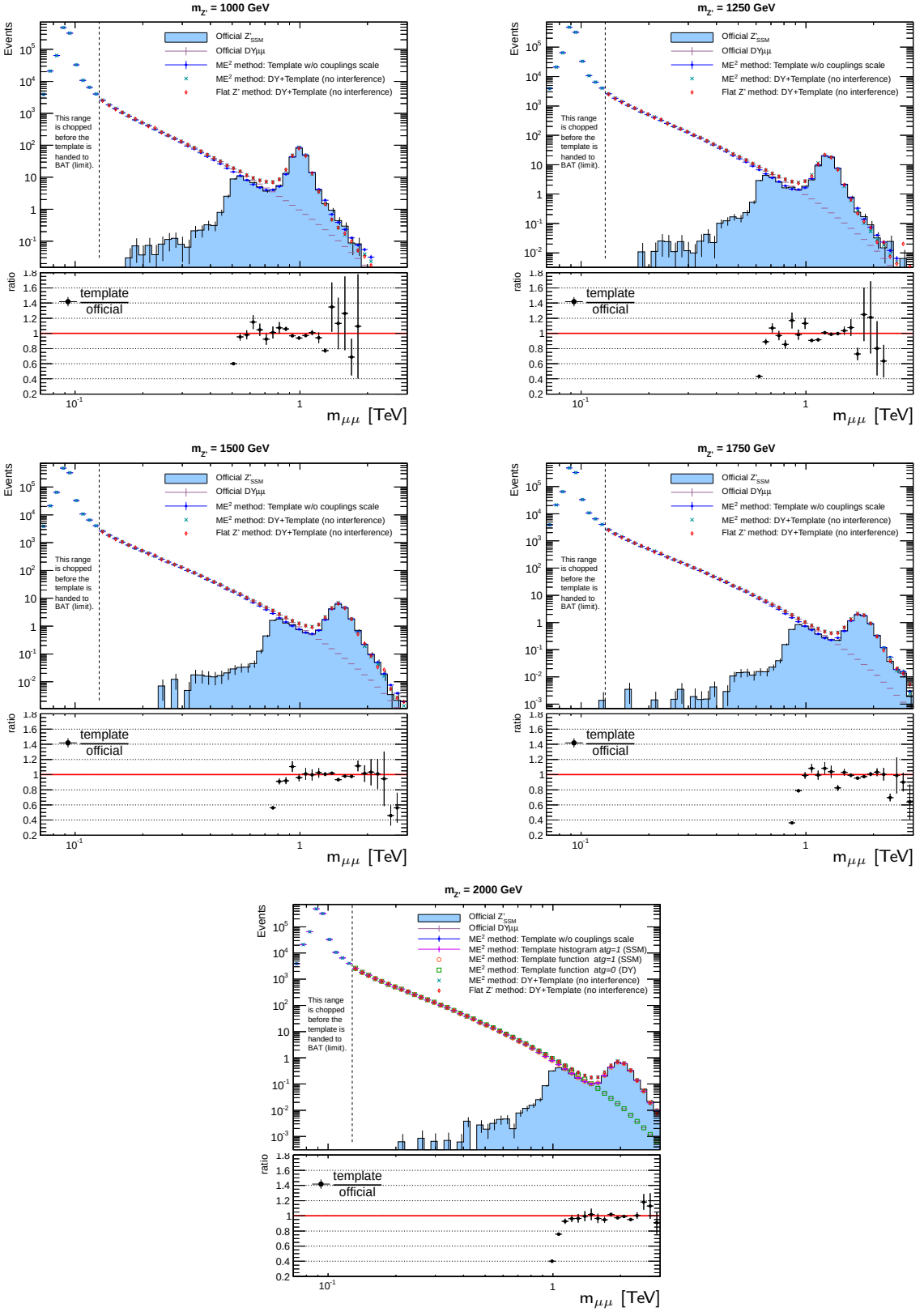

Figure G.4.: Dimuon invariant mass distribution after event selection, of Z'_{SSM} signals at five pole mass values: 1.0, 1.25, 1.5, 1.75 and 2 TeV. The bottom plot shows the ratio of the ME^2 template for $g = 1$, i.e. for Z'_{SSM} (blue points) over the official Z'_{SSM} sample (blue histogram).

Appendix H.

Highest mass dimuon event display

Figure H.1 shows a display of the measured dimuon event with the highest invariant mass.

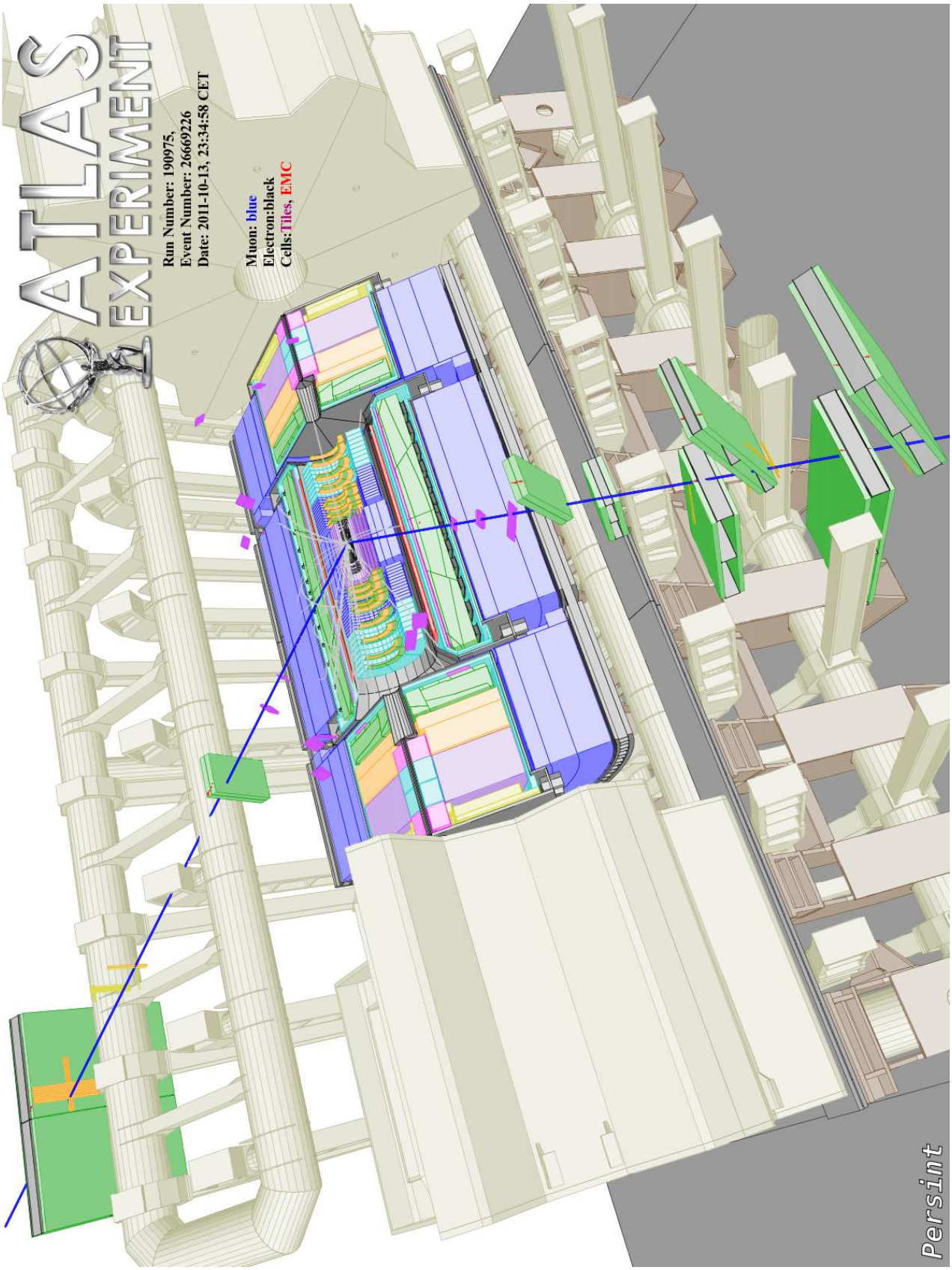

Figure H.1.: PERSINT display of the measured event with the highest dimuon invariant mass. The highest momentum muon has a p_{T} of 648 GeV and an (η, ϕ) of (-0.75, 0.49). The subleading muon has a p_{T} of 583 GeV and an (η, ϕ) of (-0.36, -2.60). The invariant mass of the pair is 1252 GeV.

Appendix I.

The TGC online monitoring

This appendix briefly describes my work on the TGC (L1 trigger) on-line monitoring (TGCOM) system. I was the muon-expert responsible for this service work within the ATLAS muon-community since the end of 2007 until 2012. The system was generally designed, developed and maintained in collaboration with Y. Benhammou, N. Taiblum and O. B. Ami from Tel Aviv University and D. Lellouch and L. Levinson from the Weizmann institute.

The code is stored and maintained together with the rest of the TGC DAQ code and it can be accessed under the TGC DAQ svn repository [102].

I.1. Introduction

The TGCOM system role is to provide real-time status indications[1] and to perform real-time data quality (DQ) analysis, based on the real time data extracted from the TGC detector which was introduced in detail chapter 3.

It is mainly a software built as a group of synchronized modules that run simultaneously inside ATLAS data taking software system located in the ATLAS detector site, point-1 (P1), as a part of the ATLAS DAQ and on-line monitoring framework. The various TGCOM outputs are aimed at the muon shifters at the ATLAS control room (ACR), as well as at the TGC experts that constantly monitor the detector. In addition, its output can be also preserved in the TGC and ATLAS data-base in order to determine the run DQ or the status of an item down to the lowest level detector unit (e.g., a strip channel) or up to the TGC detector as a whole.

[1] These are largely ROOT histograms.

The DQ analysis and the production of status flags rely on a considerably large sets of histograms being created per run. During a run, these histograms are being constantly filled with information coming directly from the TGC readout drivers (RODs) in the form of encoded events. The decoding and the filling parts are being performed by few instances of an application module named GNAM.

As mentioned in chapter 3 and as illustrated in the figures shown in section I.3, the TGC has many structural and readout fragmentation logics. This implies that a large set of histograms should be created in order to be able to fully monitor the detector, down to a single strip or wire channel. Alternatively, large groups of many of these items (to be monitored) that are supposed to have the same behavior can be projected onto the x or $x - y$ axes of a single histogram. The current set of histograms can be divided to several subsets, distinguished by their subject, e.g. occupancy, timing, rates, triggering etc.

These subsets of histograms are booked in the ATLAS pool of on-line DQ histograms and can be accessed by other processes and users. Particularly, there are several histogram viewers that allow convenient navigation between the many histograms. It is possible to perform custom DQ analysis on these histograms in order to extract discrete results that translate to alarms and can be written in the data-base. These results and alarms are called DQ flags.

I.2. Implementation

All TGCOM histograms are produced by the TGC on-line monitoring box (TomBox) which is located in P1. The TGCOM system components are in general:

- one ROD-sampler application that acts as a sampling server for all GNAM applications,
- several GNAM applications that receive and decode the TGC events while filling a set of histograms,
- one DQ agent with several data quality monitoring framework (DQMF) segments running several DQ algorithms.

The basic process, as illustrated in figure I.1, can be summarized in several basic steps:

1. book the set of histograms into the TDAQ pool of histograms in start-of-run (GNAMs),
2. pull and sample encoded event packets from the TGC RODs (ROD-sampler),

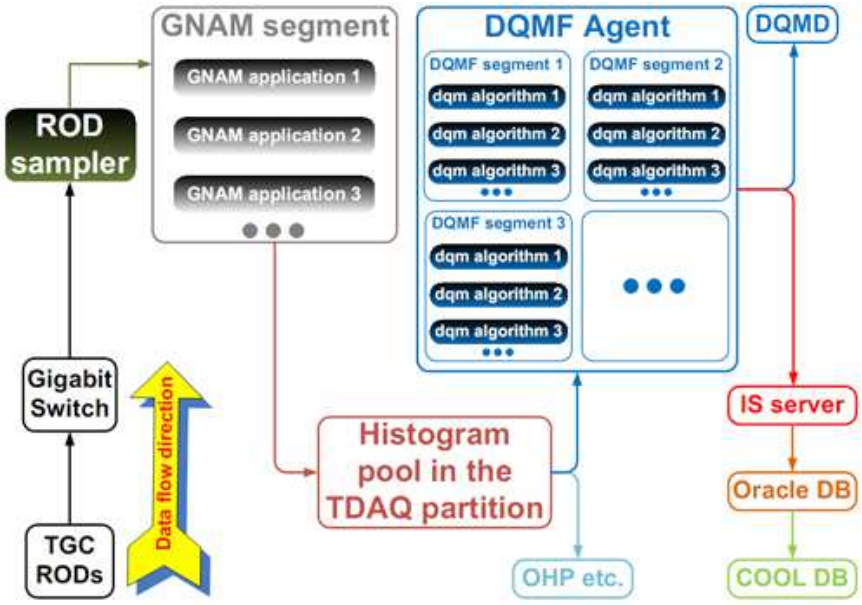

Figure I.1.: Schematic diagram of the data flow, main modules and stations in the overall monitoring scheme. The color-filled frames represent processes that rum within the TomBox whereas the empty frames represent external modules and stations. The process starts from the TGC RODs (bottom left). As illustrated, there can be several GNAM applications and DQMF segments running instantaneously.

3. decode and process these event packets while filling and updating the predefined set of histograms previously published in the TDAQ partition (GNAMs),
4. analyze the histograms that are constantly being updated in the TDAQ partition (DQMFs),
5. publish the DQ results in the data quality monitoring display (DQMD),
6. publish more DQ results in the TGC dedicated Information Service (IS) server as a set of `int` arrays. These are being read by another tool that translate the content and can register it both in the TGC Oracle data base and in the general ATLAS COOL data base (DQMF and GNAM),
7. view and inspect the histograms using the histogram presenters (DQMD and the on-line histogram presenter (OHP)).

One can use a variety of presenters to view the histograms that are published in the TDAQ partition. Currently, the tools used in practice are (the passive) OHP and (the active) DQMD.

I.3. Histograms

The histograms being produced and analyzed by TGCOM system mainly concern the detector status and trigger performance. Hit multiplicities are monitored as well as hit-rates, p_{T}-thresholds, trigger-sectors (see figure I.4), timing-performance etc. In that context, the system does not monitor the electronic signals of the detector (e.g. pulse height, charge distribution, rise/fall time, etc.). All information needed to fill these histogram is available either from the ROD or from the IS servers.

There are several histogram granularities that correspond to certain structural granularities or read-out logics of the TGC detector. In figures I.2, I.3 and I.4 one can see only a small part of the possible physical or logical fragmentations of the detector. As mentioned, each of the items e.g a chamber or a sub-sector can be associated with a histogram or a certain bin in a histogram such that as much information is monitored.

Looking on the TGCGnamHitProfile histograms for example (see figure I.6.(b) and (c)), one can see the contribution of a single strip or wire channel out of the tens of thousands that constitute the TGC chambers. This way it is possible to spot dead/hot channels and examine the general hit pattern behavior along a certain sub-sector. At the other end of the scale, looking on the histograms that are published in TGCGnamOverView/TGC_level (see e.g. figure I.7.(a) and I.10), one can have an overhead view of the entire TGC detector.

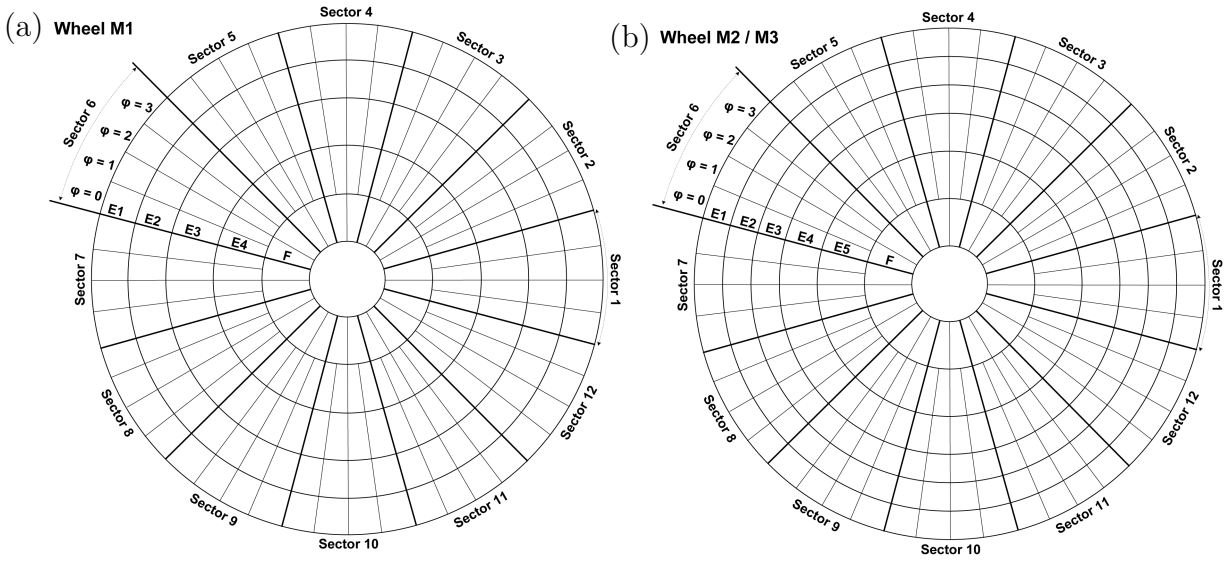

Figure I.2.: The TGC big wheels (single layer) layout. M1 in (a) and M2,3 in (b).

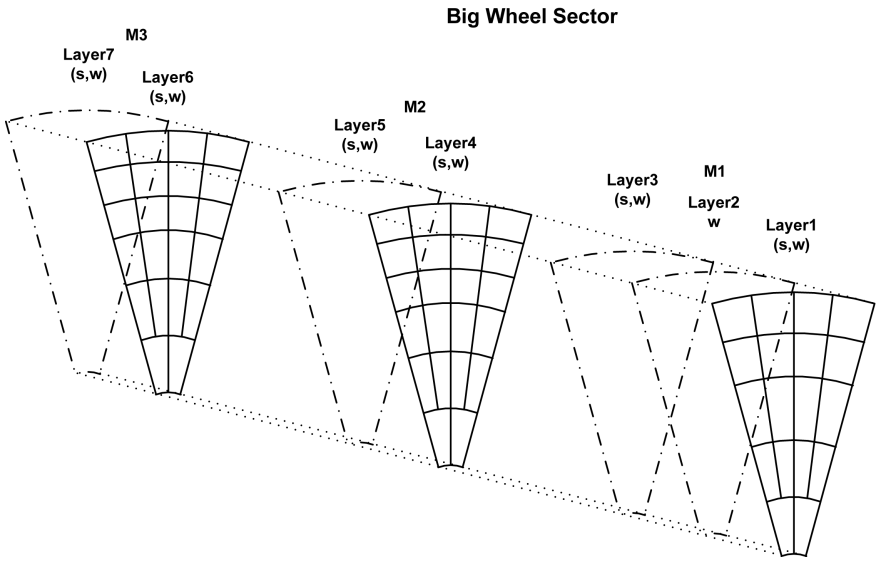

Figure I.3.: A complete sector layout (7 layers) of the three big TGC wheels.

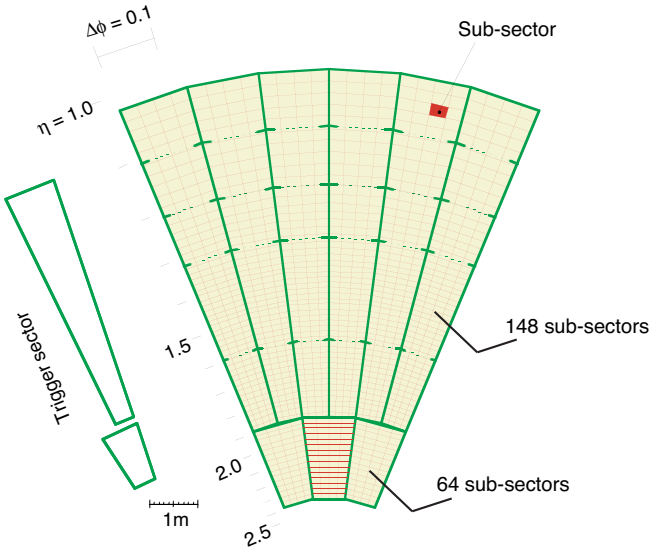

Figure I.4.: Segmentation of the L1 muon end-cap trigger.

I.4. TGC GNAM design review

As mentioned, the module that is responsible for decoding the TGC events and distributing this information to the various histograms is called GNAM. This abstract standard tool is part of the TDAQ software. Each of the ATLAS subsystems has implemented it according to its unique way of operation. In the TGC, it is implemented as an abstract class which is in charge of the decoding of events coming from the TGC ROD sampler. This class is called TGCGnamBase and it also has the other basic abstract methods of GNAM core.

The GNAM modules that do the work in practice, inherit from this class and have a name corresponding to the subject which is analyzed (e.g. TGCGnamHitProfile). Each of these modules are in charge of a certain subset of histograms from the publishing step to the filling and the destruction steps, corresponding to the run state.

I.5. TGC DQMF design review

The DQMF is a tool that was designed to systematically automate the very long list of online DQ tests The DQMF utilizes a set of custom algorithms to examine a certain subset of histograms. These algorithms require sets of input thresholds and tuning parameters. The algorithms output is a conventional traffic-light alert, i.e. the analyzed histogram label in the DQMD viewer will be colored in red if the DQ test failed (e.g. if a value exceeded its threshold), in green if the test went through or in yellow if the test was not successful but also did not fail.

For example, in the timing performance histograms, due to pile-up effects and the limited speed of the readout electronics, it is possible to have an event that contains hits associated with three bunch-crossings at once: *previous*, *current* and *next* bunch. Thus, the timing adjustment will be "good" if most of the hits in the examined item (down from a single chamber and up to a TGC side) will be associated with the *current* bunch while very few hits will accumulate the *previous* or *next* bunch. This can be realized in a single 1D histogram (per item) with three X bins corresponding to the three possible bunch-crossings. Therefore it is very easy to apply an algorithm that will check , for instance, if the two side bins heights are smaller than 10% of the central bin. If either of the side bins is higher than the 10% threshold in this example, the algorithm will issue a red alert that will be instantly seen in the DQMD viewer next to the faulty histogram. This type of histograms can be seen for example (for trigger-sector entries) in figure I.6.(a) as they appear in the DQMD viewer. Each green entry in that picture represents a DQ region where the lowest level DQ region is such a histogram corresponding to a single sector (1/12 of a 7-layer disc as shown in figure I.3).

Another trivial example is a simple comparison of the input histogram to a reference histogram. The comparison itself can utilize some known algorithms like the Kolmogorov test or a custom defined comparison tests.

While analyzing a subset of histograms, it is possible to publish the results in a dedicated IS server. This is done also by DQMF (and GNAM) in shape of `int` arrays that correspond

to several granularities. The IS arrays contain information about dead/hot channels, timing performance, etc.

The code which is responsible for that is embedded in several DQ algorithms. In order to preserve this information in a more "static" data base, one must translate this information and update the relevant slots in the data base. Otherwise, the information in the IS will be lost at the next start-of-run.

The overall DQMF proceeding is controlled by a set of xml files containing many definitions, parameters, linkings etc. These configuration files are responsible for the communication between the custom DQ algorithms library (TGCGnamDQMF) and the DQMF core libraries.

A detailed example of such algorithm, uses the logic of the assumption of uniform occupancy for special detector segmentations. In this case, it is obvious that all the chambers in a certain layer in a certain "η-ring" as the ones shown in figure I.2 (F,E1,E2,E3,E4,E5) should have a relatively uniform occupancy of items (such as hits, triggers, tracks etc.) since these are concentric rings around the beam axis. Therefore, if the channels of these chambers are projected one after the other on a single histogram x-axis (per η-ring), then it can be expected that the occupancies of all the channel will fluctuate around a certain average value. Then, a certain DQ algorithm can be written to spot dead and hot channels at the same time. The algorithm may work on a given η-ring histogram, basing on a comparison to an ad-hoc average, as follows:

1. sort the channels (bins) by their height and store the values in a vector;
2. mark the value of the "noisiest" and the "emptiest" channels (will be last and first entries of the vector correspondingly);
3. the "true" average of the bins heights may be biased by extreme bins ("hot" or "dead") channels. Therefore, remove the lowest and highest 10% of the channels from the vector according to the values found in the previous step (where the percentage is an external parameter);
4. calculate the reduced average of the remaining channels height from the reduced vector. In this step, non-existing/disabled/masked channels, which can be read from the data base, can be excluded from the average calculation;

5. calculate the Poisson probability to fluctuate to above or below this average (μ) given N^k_{obs} entries are observed per channel k of the histogram (no bin is ignored)

$$P_k\left(\mu|N^k_{\text{obs}}\right) = \frac{\mu^{N^k_{\text{obs}}}e^{-\mu}}{N^k_{\text{obs}}!} \tag{I.5.1}$$

6. determine a certain (external) Poisson threshold such that if the binned result from the previous step will be lower than this threshold, then the channel k is flagged as problematic, $P_k\left(\mu|N^k_{\text{obs}}\right) \leq P_{\text{threshold}}$;

7. decide if the channel is "dead" or "hot" according to its value - above or below the reduced average;

8. register the channel to the data base and count the bad channels. This number of bad channels is compared with some external threshold values in order to decide if the histogram pass the DQ test, if it fails or if it just needs the expert's attention.

The outcome of this algorithm is visualized in figure I.5 where the top histogram is the input (toy) η-ring with $\sim$4500 channels fluctuating around a certain value with few hot channels and few dead ones. It can be seen that the inclusive y-axis average is biased upwards where after removing the lowest- ans highest-10% the "true" (reduced) average is obtained and the channels can be flagged and classified according to it. The entire process is configurable with external values rather than hard-coded ones. Example of few such η-ring histograms from 2012 real data run can be seen in figure I.9 in linear y-axis scale where no special anomalies are seen.

I.6. TGCOM histogram examples

Representative examples of few of the TGCOM histograms are given below as viewed in the DQMD or OHP histogram presenters in the ACR. All examples shown here were taken during a certain run in August 2012.

Some histograms show the monitored quantities versus the luminosity block (LB) number. This enables to spot problems throughout the run either in real time or in retrospective. Examples of these LB-aware histograms are shown in figure I.8.

Some histograms are monitoring the status of the physical electronic elements of the TGC detector, such as the RODs themselves. These histograms are shown in figure I.10. Since

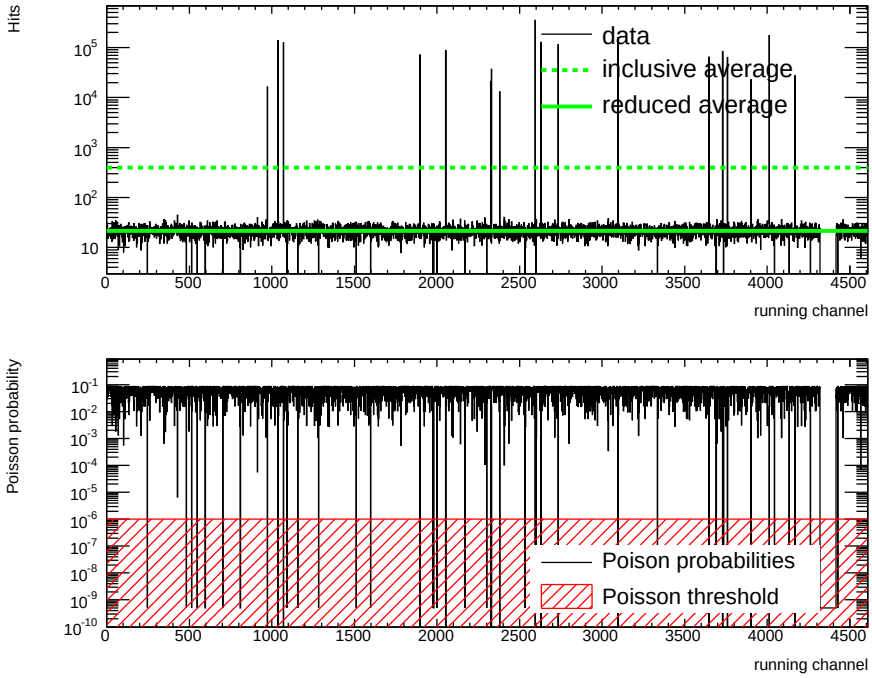

Figure I.5.: Illustration of the η-ring anomalies finder algorithm shown for a toy η-ring histogram (top). In the bottom plot, the Poisson probabilities are given according to equation I.5.1 where these are compared to some fixed threshold which is indicated as the flat red histogram. In both histograms, the x-axis label "running channel" represents the projection of all channels of all the chambers of a typical η-ring.

this type of histograms is important to spot immediate problems of the readout system, e.g. dropped RODs etc., then it is both LB-aware and also looking on the real-time status.

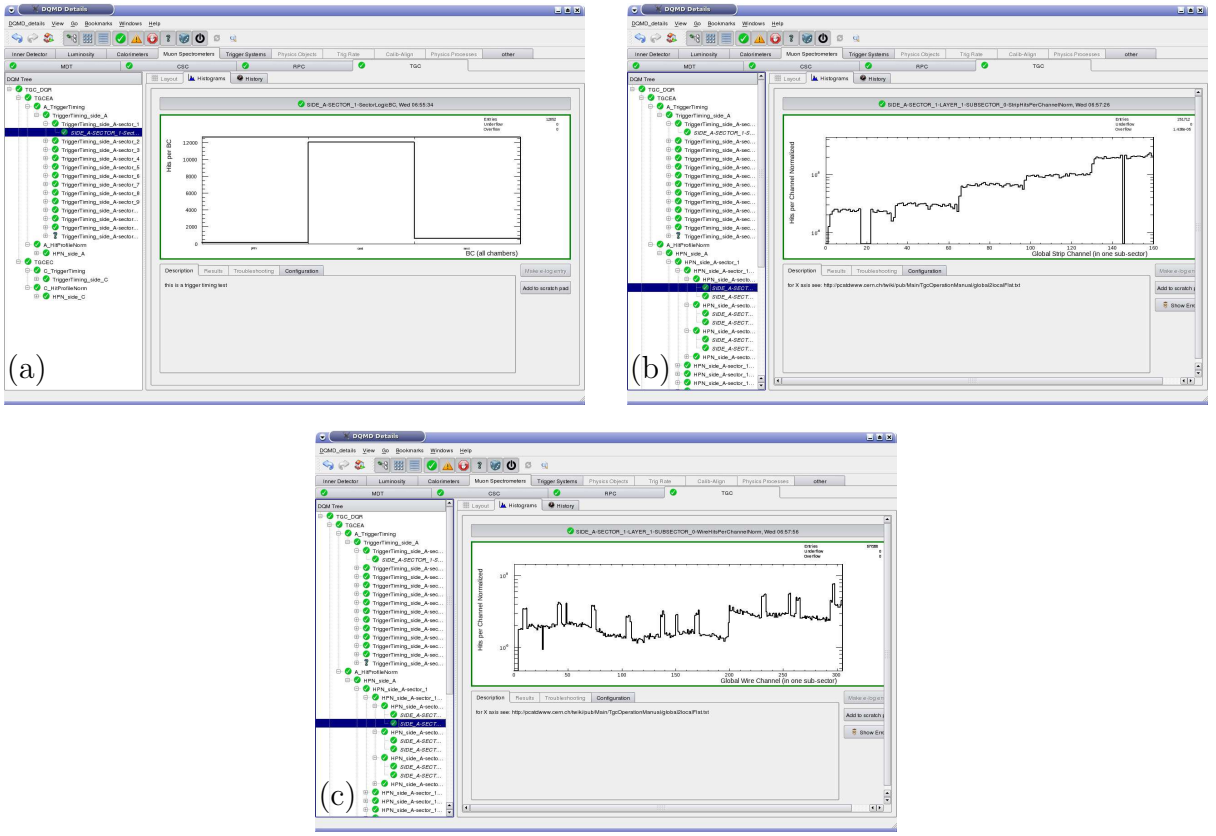

Figure I.6.: Example of few DQMD outputs. The set of sub-trigger-sectors (trigger ROI) timing histograms as described in the text is given in (a). The normalized hit profile histograms are given in (b) and (c), where this set of histograms is being filled only when there are no high-p_{T} TGC triggers fired in the sector where the hit to be filled came from. This enables to better monitor the noisy hits and therefore spot "hot" channels. This set is being checked relative to a static threshold. The x- axis is a projection of all the channels in a certain layer in a certain ϕ coordinate ($\phi = 0, 1, 2, 3$) as can be seen in figures I.2 and I.3.

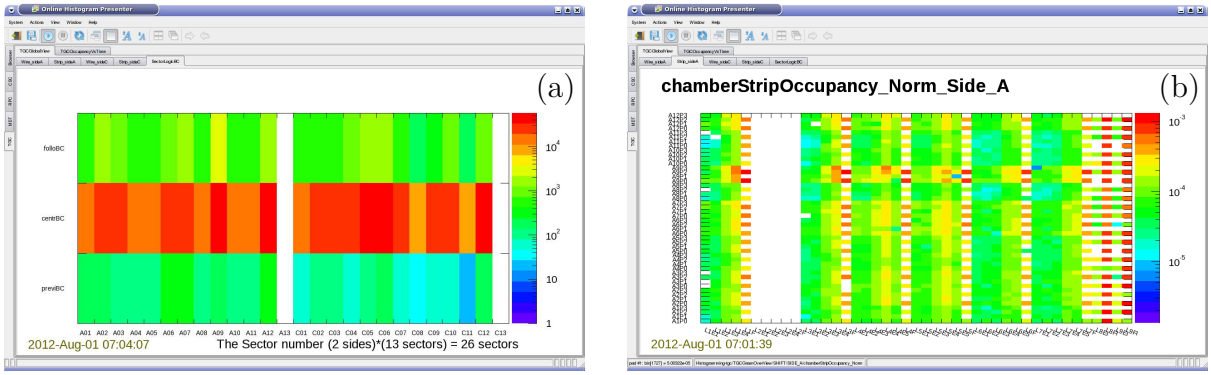

Figure I.7.: Example of a general TGC view in the OHP. The trigger timing for all the TGC sectors (projected on the x-axis) is shown in (a) where in (b) a chamber-level occupancy histogram with respect to a special variation of the TGC $\eta - \phi$ space is shown.

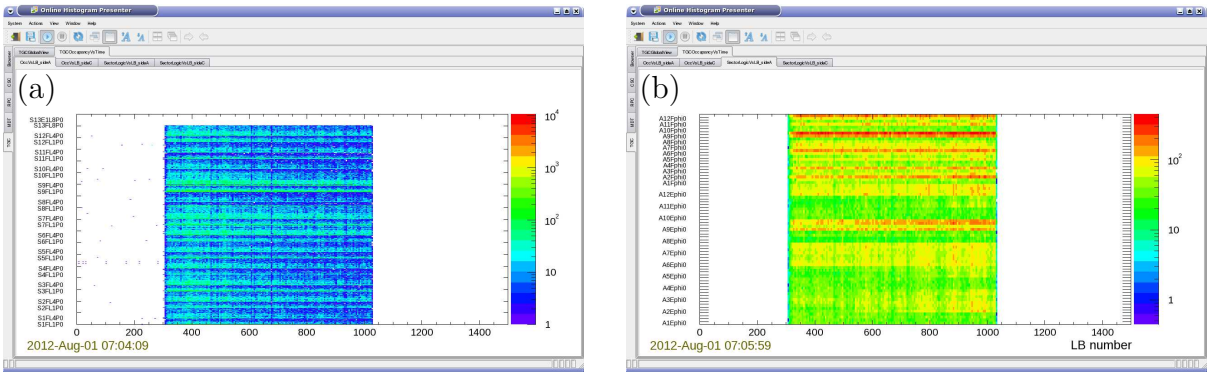

Figure I.8.: Example of a general TGC view in the OHP of LB-aware histograms. Chamber-level occupancy vs. LB number in (a) and chamber-level sub-trigger-sectors (trigger ROI) vs. LB number in (b). A continuous problem will manifest as a large "hole" or as an enhanced area across several bins in the y-axis throughout several LB numbers such that it will be very easy to detect.

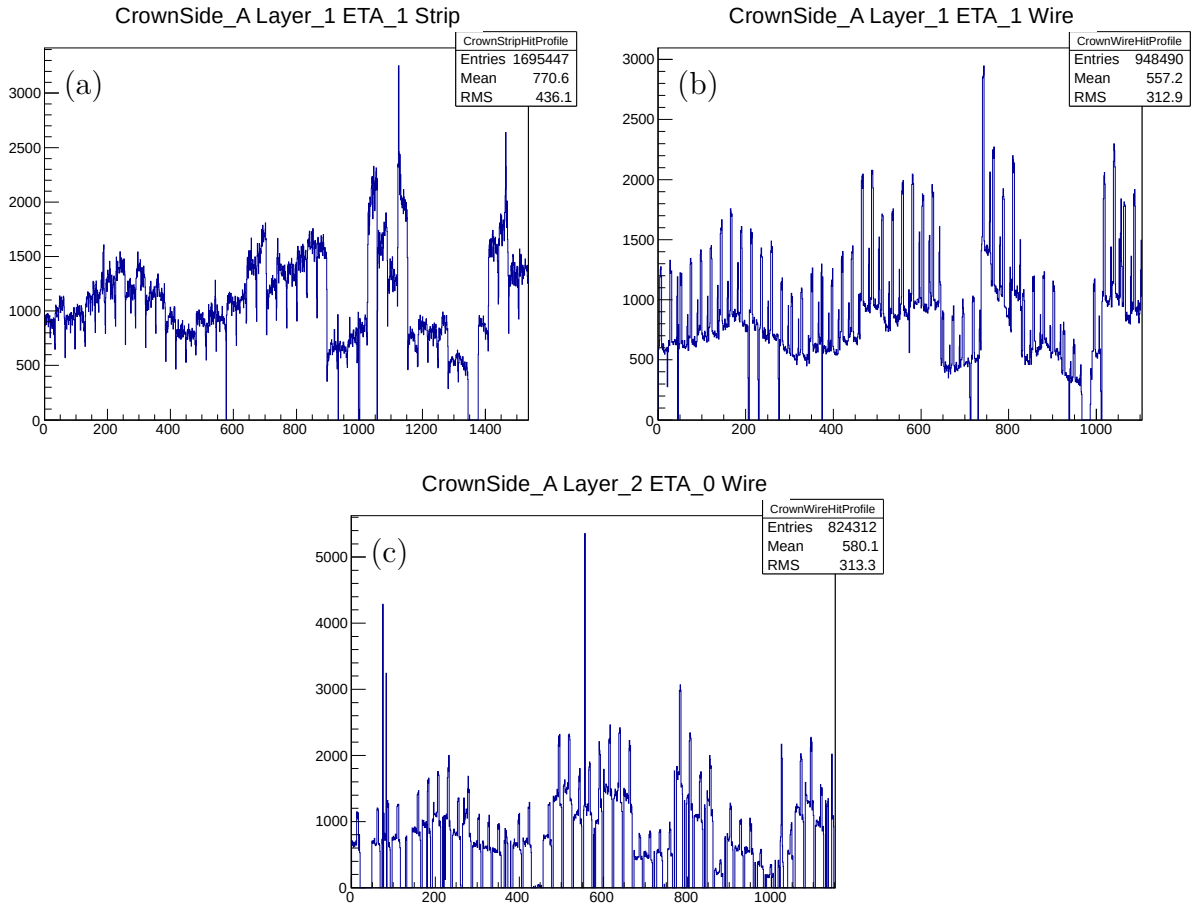

Figure I.9.: Examples of few "η-ring" histograms. See text in the previous section.

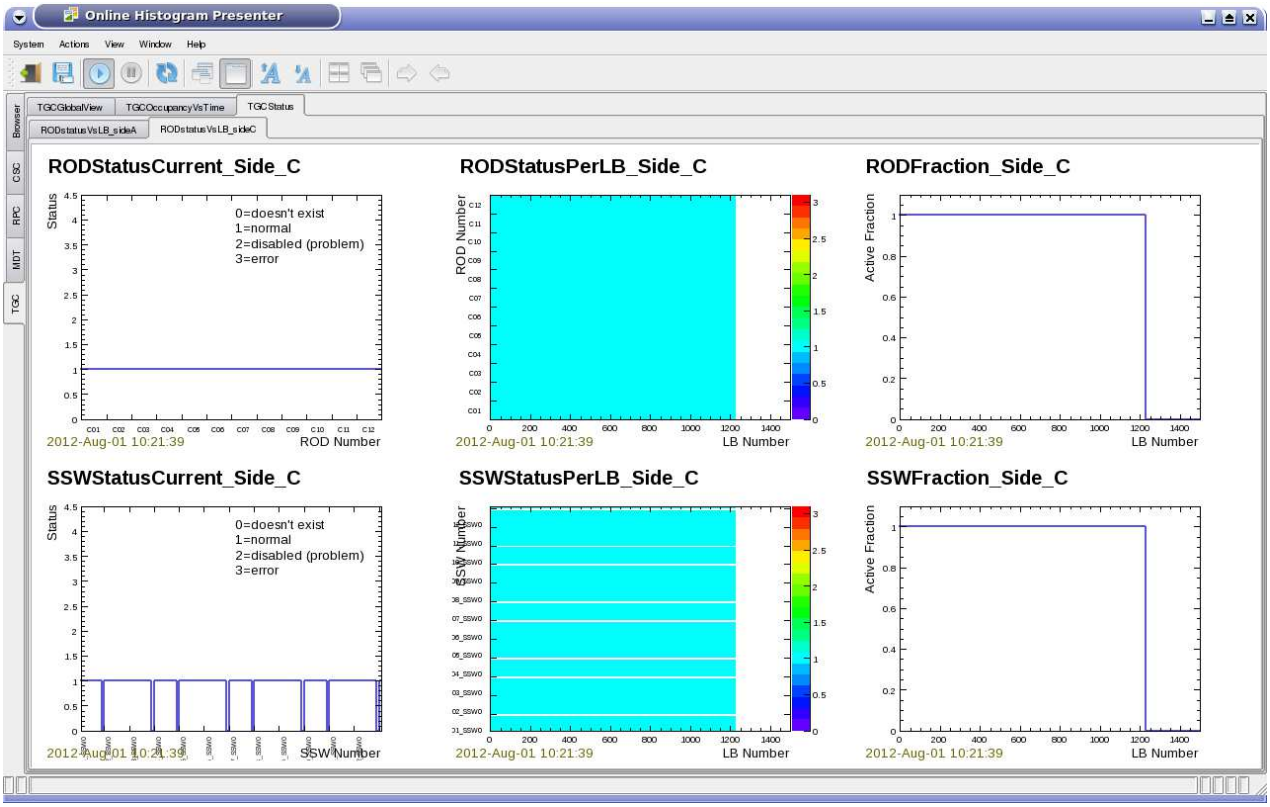

Figure I.10.: Example of a general TGC view in the OHP of detector's electronic elements status histograms.

Bibliography

[1] *Monte Carlo Net*, Http://www.montecarlonet.org/, 2008.

[2] G. Bella et al., *A search for heavy Kaluza-Klein electroweak gauge bosons at the LHC*, JHEP **09** (2010) 025.

[3] T. Sjöstrand, S. Mrenna, and P. Z. Skands, *A Brief Introduction to PYTHIA 8.1*, Comput. Phys. Commun. **178** (2008) 852–867.

[4] T. Sjöstrand, S. Mrenna, and P. Z. Skands, PYTHIA8 *web page*, http://home.thep.lu.se/ torbjorn/php8165/Welcome.php.

[5] ATLAS Collaboration, *Search for high-mass resonances decaying to dilepton final states in pp collisions at a center-of-mass energy of 7 TeV with the ATLAS detector*, . CERN-PH-EP-2012-190 (submitted to JHEP).

[6] ATLAS Collaboration, *Observation of a New Particle in the Search for the Standard Model Higgs Boson with the ATLAS Detector at the LHC*, Accepted by Phys. Let. B. (CERN-PH-EP-2012-218) (2012) , arXiv:1207.7214 [hep-ex].

[7] CMS Collaboration, *Observation of a new boson at a mass of 125 GeV with the CMS experiment at the LHC*, Submitted to Phys. Let. B. (CERN-PH-EP-2012-220) (2012) , arXiv:1207.7235 [hep-ex].

[8] H. Georgi and S. L. Glashow, *Unity of All Elementary Particle Forces*, Phys. Rev. Lett. **32** (1974) 438.

[9] P. Langacker, *Grand Unified Theories and Proton Decay*, Phys. Rept. **72** (1981) 185–385.

[10] P. Langacker, *The Physics of Heavy Z' Gauge Bosons*, Rev. Mod. Phys. **81** (2009) 1199–1228.

[11] T. G. Rizzo, *Indirect Searches for Z'-like Resonances at the LHC*, JHEP **08** (2009) 082.

[12] T. G. Rizzo, *Testing the nature of Kaluza-Klein excitations at future lepton colliders*, Phys. Rev. **D61** (2000) 055005.

[13] ATLAS Collaboration, G. Azuelos and G. Polesello, *Prospects of the detection of Kaluza-Klein excitations of gauge bosons in the ATLAS detector at the LHC*, SN-ATLAS-2003-023, 2003.

[14] K. Nakamura et al., *Review of particle physics*, J. Phys. **G37** (2010) 075021.

[15] ATLAS Collaboration, *Search for dilepton resonances in pp collisions at* $\sqrt{s} = 7$ *TeV with the ATLAS detector*, Phys. Rev. Lett. **107** (2011) 272002.

[16] ATLAS Collaboration, *Search for high mass dilepton resonances in 5* fb^{-1} *of pp collisions at* $\sqrt{s} = 7$ *TeV with the ATLAS detector*, Tech. Rep. ATLAS-CONF-2012-007, CERN, Geneva, Mar, 2012. http://cdsweb.cern.ch/record/1428547/.

[17] CMS Collaboration, *Search for Resonances in the Dilepton Mass Distribution in pp Collisions at* $\sqrt{s} = 7$ *TeV*, CMS PAS EXO-11-019, https://cdsweb.cern.ch/record/1369192/.

[18] D0 Collaboration, *Search for a heavy neutral gauge boson in the dielectron channel with 5.4* fb^{-1} *of* $p\bar{p}$ *collisions at* $\sqrt{s} = 1.96$ *TeV*, Phys. Lett. **B695** (2011) 88–94.

[19] CDF Collaboration, *Search for High Mass Resonances Decaying to Muon Pairs in* $\sqrt{s} = 1.96$ *TeV* $p\bar{p}$ *Collisions*, Phys. Rev. Lett. **106** (2011) 121801.

[20] OPAL Collaboration, *Tests of the standard model and constraints on new physics from measurements of fermion pair production at 189 GeV to 209 GeV at LEP*, Eur. Phys. J. **C33** (2004) 173–212.

[21] DELPHI Collaboration, *Measurement and interpretation of fermion-pair production at LEP energies above the Z resonance*, Eur. Phys. J. **C45** (2006) 589–632.

[22] L3 Collaboration, *Measurement of hadron and lepton-pair production in* e^+e^- *collisions at* $\sqrt{s} = 192$ *GeV to 208 GeV at LEP*, Eur. Phys. J. **C47** (2006) 1–19.

[23] ALEPH Collaboration, *Fermion pair production in* e^+e^- *collisions at 189-209 GeV and constraints on physics beyond the standard model*, Eur. Phys. J. **C49** (2007) 411–437.

[24] J. Erler, P. Langacker, S. Munir, and E. R. Pena, *Improved constraints on* Z' *bosons from electroweak precision data*, JHEP **0908** (2009) 017.

[25] A. Caldwell, D. Kollar, and K. Kröninger, *BAT - The Bayesian Analysis Toolkit*, Comput. Phys. Commun. **180** (2009) 2197.

[26] CMS Collaboration, *Search for narrow resonances in dilepton mass spectra in pp collisions at* $\sqrt{s} = 7$ *TeV*, arXiv:1206.1849 [hep-ex].

[27] CMS Collaboration, *Search for Resonances in the Dilepton Mass Distribution in pp Collisions at* $\sqrt{s} = 7$ *TeV*, JHEP **1105** (2011) 093.

[28] N. T. Hod, *My private svn repository*, http://code.google.com/p/z0analysis/source/checkout.

[29] F. Halzen and A. D. Martin, *Quarks & Leptons: An Introductory Course in Modern Particle Physics*. John Wiley & sons, 1984.

[30] M. Cvetic and P. Langacker, *Implications of Abelian Extended Gauge Structures From String Models*, Phys. Rev. D. **54** (1996) 3570.

[31] C. T. Hill and E. H. Simmons, *Strong Dynamics and Electroweak Symmetry Breaking*, Phys. Rept. **381** (2003) 235.

[32] N. Arkani-Hamed et al., *Electroweak symmetry breaking from dimensional deconstruction*, Phys. Lett. B. **513** (2001) 232–240.

[33] I. Antoniadis, *A Possible New Dimension At A Few Tev*, Phys. Lett. B. **246** (1990) 377.

[34] L. Randall and R. Sundrum, *A large mass hierarchy from a small extra dimension*, Phys. Rev. Lett. **83** (1999) 3370–3373.

[35] A. Sherstnev and R. S. Thorne, *Parton Distributions for LO Generators*, Eur. Phys. J. **C55** (2008) 553–575, arXiv:0711.2473 [hep-ph].

[36] D. Bardin et al., *Z LINE SHAPE*, . CERN-TH.5468/89, Scanned version.

[37] G. Bella et al., *Introduction to the MCnet Moses project and Heavy gauge bosons search at the LHC*, . arXiv:1004.1649v1.

[38] T. G. Rizzo, *Z' Phenomenology and the LHC*, . SLAC-PUB-12129 (arXiv:hep-ph/0610104v1).

[39] *The LEP Electroweak Working Group*, Www. http://lepewwg.web.cern.ch/LEPEWWG/.

[40] A. Leike, *The Phenomenology of extra neutral gauge bosons*, Phys. Rept. **317** (1999) 143–250, arXiv:hep-ph/9805494.

[41] J. L. Hewett and T. G. Rizzo, *Low-Energy Phenomenology of Superstring Inspired E(6) Models*, Phys. Rept. **183** (1989) 193.

[42] C. Ciobanu et al., *Z' generation with PYTHIA*, . FERMILAB-FN-0773, Link.

[43] T. G. Rizzo, *Distinguishing Kaluza-Klein Resonances From a Z' in Drell-Yan Processes at the LHC*, eConf **C010630** (2001) .

[44] F. Ledroit et al., *$Z' \to e^+e^-$ studies in full simulation (DC1)*, . ATL-PHYS-PUB-2005-010.

[45] G. Nordström, *On the possibility of unifying the electromagnetic and the gravitational fields*, Z. Phys. **15** (1914) 504–506.

[46] T. Kaluza, *On the Problem of Unity in Physics*, Sitzungsber.Preuss.Akad.Wiss.Berlin (Math.Phys.) (1921) 966–972.

[47] O. Klein, *Quantum Theory and Five-Dimensional Theory of Relativity*, Z. Phys. **37** (1926) 895.

[48] N. Arkani-Hamed et al., *The hierarchy problem and new dimensions at a millimeter*, Phys. Lett. B. **429** (1998) 263–272.

[49] N. Arkani-Hamed et al., *New Dimensions at a Millimeter to a Fermi and Superstrings at a TeV*, Phys. Lett. B. **436** (1998) 257–263.

[50] N. Arkani-Hamed et al., *Phenomenology, Astrophysics and Cosmology of Theories with Sub-Millimeter Dimensions and TeV Scale Quantum Gravity*, Phys.Rev. D. **59** (1999) 086004.

[51] L. Randall. and R. Sundrum, *An Alternative to Compactification*, Phys. Rev. Lett. **83** (1999) 3370.

[52] E. Witten, *Strong Coupling Expansion Of Calabi-Yau Compactification*, Nucl. Phys. B. **471** (1996) 135–158.

[53] P. Horava and E. Witten, *Eleven-Dimensional Supergravity on a Manifold with Boundary*, Nucl. Phys. B. **475** (1996) 94–114.

[54] E. Dudas et al., *Extra Spacetime Dimensions and Unification*, Phys. Lett. B. **436** (1998) 55–65.

[55] I. Antoniadis and K. Benakli, *Large dimensions and string physics in future colliders*, Int. J. Mod. Phys. A. **15** (2000) 4237–4286.

[56] A. Mück et al., *Minimal Higher-Dimensional Extensions of the Standard Model and Electroweak Observables*, Phys. Rev. D. **65** (2002) 085037.

[57] C. Csaki et al., *Gauge Theories on an Interval: Unitarity without a Higgs*, Phys. Rev. D. **69** (2004) 055006.

[58] D. M. Ghilencea et al., *Gauge corrections and FI-term in 5D KK theories*, Nucl. Phys. B. **619** (2001) 385–395.

[59] M. Kubo et al., *The Hosotani Mechanism in Bulk Gauge Theories with an Orbifold Extra Space S^1/Z_2*, Mod. Phys. Lett. A. **17** (2002) 2249–2264.

[60] L. Evans and P. B. (editors), *LHC Machine*, Jinst **3** (2008) no. S08001, .

[61] CMS Collaboration, *The CMS experiment at the CERN LHC*, Jinst **3** (2008) no. S08004, .

[62] LHCb Collaboration, *The LHCb Detector at the LHC*, Jinst **3** (2008) no. S08005, .

[63] TOTEM Collaboration, *The TOTEM Experiment at the CERN Large Hadron Collider*, Jinst **3** (2008) no. S08007, .

[64] ALICE Collaboration, *The ALICE experiment at the CERN LHC*, Jinst **3** (2008) no. S08002, .

[65] Tevatron Collaboration, A. D. Fermi National Accelerator Laboratory, Tevatron *luminosity*, Www. http://www.fnal.gov/pub/now/tevlum.html.

[66] ATLAS Collaboration, *The ATLAS Experiment at the CERN Large Hadron Collider*, Jinst **3** (2008) no. S08003, .

[67] ATLAS Collaboration, *The ATLAS Simulation Infrastructure*, Eur. Phys. J. **C70** (2010) 823–874.

[68] ATLAS Collaboration, *Atlas Computing: technical design report*, . ATLAS-TDR-017 (CERN-LHCC-2005-022).

[69] R. Brun and F. Rademakers, *ROOT - An Object Oriented Data Analysis Framework*, Nucl. Inst. & Meth. in Phys. Res. A. **389** (1997) 81–86. http://www.fnal.gov/pub/now/tevlum.html.

[70] S. Agostinelli et al., *GEANT4: A simulation toolkit*, Nucl. Instrum. Meth. **A506** (2003) 250.

[71] S. Hassani et al., *A muon identification and combined reconstruction procedure for the ATLAS detector at the LHC using the (MUONBOY, STACO, MuTag) reconstruction packages*, Nucl. Instrum. Meth. A **572** (2007) 77Ű79.

[72] D. Fassouliotis et al., *Muon Identification using the MUID package*, . ATL-MUON-2003-003 (link).

[73] ATLAS Collaboration, *Luminosity Determination in pp Collisions at* $\sqrt{s} = 7$ *TeV using the ATLAS Detector in 2011*, . ATLAS-CONF-2011-116.

[74] ATLAS Collaboration, *Report from the Luminosity Task Force*, . ATL-GEN-PUB-2006-002; ATL-COM-GEN-2006-003; CERN-ATL-COM-GEN-2006-003.

[75] T. Sjöstrand, S. Mrenna, and P. Skands, *PYTHIA 6.4 physics and manual*, JHEP **05** (2006) 026.

[76] G. Corcella et al., *HERWIG6: an event generator for hadron emission reactions with interfering gluons (including supersymmetric processes)*, JHEP **01** (2001) 010.

[77] G. Corcella et al., *HERWIG 6.5 release note*, arXiv:hep-ph/0210213.

[78] J. M. Butterworth, J. R. Forshaw, and M. H. Seymour, *Multiparton interactions in photoproduction at HERA*, Z. Phys. **C72** (1996) 637–646.

[79] E. Boos et al., *CompHEP 4.4: Automatic computations from Lagrangians to events*, Nucl. Instrum. Meth. **A534** (2004) 250–259.

[80] J. Alwall et al., *MadGraph/MadEvent v4: The New Web Generation*, JHEP **09** (2007) 028.

[81] S. Frixione and B. R. Webber, *Matching NLO QCD computations and parton shower simulations*, JHEP **06** (2002) 029.

[82] M. L. Mangano et al., *ALPGEN, a generator for hard multiparton processes in*

hadronic collisions, JHEP **07** (2003) 001.

[83] ATLAS Collaboration, *ATLAS tunes of PYTHIA 6 and Pythia 8 for MC11*, ATL-PHYS-PUB-2011-009, http://cdsweb.cern.ch/record/1399599/.

[84] P. M. Nadolsky et al., *Implications of CTEQ global analysis for collider observables*, Phys. Rev. **D78** (2008) 013004.

[85] ATLAS Collaboration, *New ATLAS event generator tunes to 2010 data*, ATL-PHYS-PUB-2011-008, https://cdsweb.cern.ch/record/1340273.

[86] H.-L. Lai, M. Guzzi, J. Huston, Z. Li, P. M. Nadolsky, et al., *New parton distributions for collider physics*, Phys. Rev. **D82** (2010) 074024, arXiv:1007.2241 [hep-ph].

[87] R. Hamberg, W. L. van Neerven, and T. Matsuura, *A Complete calculation of the order α_s^2 correction to the Drell-Yan K factor*, Nucl. Phys. **B359** (1991) 343–405.

[88] C. M. Carloni Calame et al., *Precision electroweak calculation of the production of a high transverse-momentum lepton pair at hadron colliders*, JHEP **10** (2007) 109, arXiv:0710.1722 [hep-ph].

[89] C. M. Carloni Calame et al., *Precision electroweak calculation of the charged current Drell-Yan process*, JHEP **0612** (2006) 016.

[90] ATLAS Collaboration, *Search for contact interactions in dilepton events from pp collisions at $\sqrt{s} = 7$ TeV with the ATLAS detector*, Phys. Lett. **B712** (2012) 40–58.

[91] ATLAS Collaboration, R. Blair et al., *ATLAS Standard Model Cross Section recommendations for 7 TeV LHC 2 running*, https://svnweb.cern.ch/trac/atlasgrp-/export/50132/Physics/StandardModel/xsectf/note/xsectf.pdf, 2010.

[92] ATLAS Collaboration, J. M. Butterworth et al., *Single and Diboson Production Cross Sections in pp collisions at $\sqrt{s} = 7$ TeV*, ATL-COM-PHYS-2010-695 (2010) .

[93] ATLAS Collaboration, *Muon Momentum Resolution in First Pass Reconstruction of pp Collision Data Recorded by ATLAS in 2010*, ATL-CONF-2011-046, https://cdsweb.cern.ch/record/1322424.

[94] ATLAS Collaboration, *Search for high mass dilepton resonances in pp collisions at $\sqrt{s} = 7$ TeV with the ATLAS experiment*, Phys. Lett. **B700** (2011) 163–180.

[95] G. Choudalakis, *On hypothesis testing, trials factor, hypertests and the BumpHunter*, arXiv:1101.0390v2 [hep-ph].

[96] G. Choudalakis and D. Casadei, *Plotting the Differences Between Data and Expectation*, arXiv:1111.2062 [physics.data-an].

[97] E. Eichten et al., *New Tests for Quark and Lepton Substructure*, Phys. Rev. Lett. **50** (1983) 811–814.

[98] P. Golonka and Z. Wąs, *PHOTOS Monte Carlo: a precision tool for QED corrections in Z and W decays*, Eur. Phys. J. **C45** (2006) 97–107.

[99] A. D. Martin, R. G. Roberts, W. J. Stirling, and R. S. Thorne, *Parton distributions incorporating QED contributions*, Eur. Phys. J. **C39** (2005) 155–161, arXiv:hep-ph/0411040.

[100] U. Baur, *Weak Boson Emission in Hadron Collider Processes*, Phys. Rev. **D75** (2007) 013005, arXiv:hep-ph/0611241.

[101] TeV4LHC-Top and Electroweak Working Group Collaboration, C. E. Gerber et al., *Tevatron-for-LHC Report: Top and Electroweak Physics*, arXiv:0705.3251 [hep-ph].

[102] D. Lellouch and N. T. Hod, *TGC DAQ svn repository*, https://svnweb.cern.ch/trac/muondaq/browser/TGCGnam.

List of Figures

List of Tables